CONTROL OF DIFFERENTIAL MOTION BETWEEN ADJACENT ADVANCED LIGO SEISMIC ISOLATION PLATFORMS

A DISSERTATION
SUBMITTED TO THE DEPARTMENT OF
MECHANICAL ENGINEERING
AND THE COMMITTEE ON GRADUATE STUDIES
OF STANFORD UNIVERSITY
IN PARTIAL FULFILLMENT OF THE REQUIREMENTS
FOR THE DEGREE OF
DOCTOR OF PHILOSOPHY

Daniel E. Clark
March 2013

I certify that I have read this dissertation and that, in my opinion, it is fully adequate in scope and quality as a dissertation for the degree of Doctor of Philosophy.

Daniel DeBra, Primary Adviser

I certify that I have read this dissertation and that, in my opinion, it is fully adequate in scope and quality as a dissertation for the degree of Doctor of Philosophy.

David Beach, Co-Adviser

I certify that I have read this dissertation and that, in my opinion, it is fully adequate in scope and quality as a dissertation for the degree of Doctor of Philosophy.

Brian Lantz

Approved for the Stanford University Committee on Graduate Studies.

Patricia J. Gumport, Vice Provost Graduate Education

This signature page was generated electronically upon submission of this dissertation in electronic format. An original signed hard copy of the signature page is on file in University Archives.

Abstract

Gravitational wave detection will provide further insight into areas that are inaccessible by traditional electromagnetic astronomy methods such as black holes (Baker et al., 2006). The Laser Interferometer Gravitational-wave Observatory (LIGO) is a large project designed to detect directly gravitational waves from astrophysical sources through the use of three, long-baseline interferometers and is funded by the National Science Foundation (NSF). We have demonstrated a prototype system, the Seismic Platform Interferometer (SPI), which could improve the operational reliability of the observatory.

Initial LIGO, operating for 1 year of science data collection, had no known event detections. To improve the estimated detection event rate by a factor of about 1,000, the LIGO project is currently installing the Advanced LIGO (aLIGO) upgrade increasing the sensitivity of the detectors (Harry and LSC, 2010), (Shoemaker, 2009), and (Fritschel, 2009). Commissioning work for aLIGO has already started with the upgrade scheduled to come on-line in 2015.

Several significant changes are being made to improve the detectors' performance. One of these changes is the installation of an upgraded seismic isolation system. This is necessary to increase the attenuation of ground motion to the suspended optics to 10 orders of magnitude at 10 Hz – an order of magnitude improvement over current LIGO. Seismic isolation starts with quiet Hydraulic External Pre-Isolators (HEPI) outside the vacuum system, Internal Seismic Isolation (ISI) platforms inside the vacuum envelope, and then as many as four stages of pendulums culminating at the final proof mass optic.

As part of aLIGO, thirty Internal Seismic Isolation (ISI) platforms, actively controlled in six degrees of freedom, are being installed to support and align each of the optics that are part of the interferometer. These platforms are controlled relative to inertial space utilizing seismometers. At low frequencies, however, the horizontal feedback seismometers cannot distinguish horizontal accelerations from the component of gravity, g, due to tilt. The ratio of a horizontal seismometer's sensitivity to rotation (signal per radian of angle) to the sensitivity to translation (signal per m) at a particular frequency (denoted ω in rad/s) is represented by:

$$\frac{\text{rotation response}}{\text{translation response}} = \frac{-g}{\omega^2} \tag{1}$$

This tilt-horizontal coupling is one of the factors limiting the low frequency performance of the ISI system (Lantz et al., 2009).

Several solutions could address the problems caused by the tilt-horizontal coupling in the feedback inertial sensors. One set of solutions involves measuring the tilt independently and then subtracting its effect from the horizontal inertial sensors' signal. Possible solutions in this set include measuring tilt rate with a ring laser gyroscope and integrating to obtain the tilt.

Alternatively, two or more linear inertial sensors (accelerometer or seismometer) could be spatially arranged in such a way as to obtain tilt from the difference of their signals. One method would involve two horizontally separated vertical inertial sensors. In this arrangement, tilt is the differential signal between the two instruments. A vertical seismometer with immunity to atmospheric pressure changes was designed and prototyped for this purpose.

We have developed and demonstrated a different approach to address the excess motion at low frequency imposed by the tilt-horizontal coupling in the inertial sensors. An auxiliary sensor, the Seismic Platform Interferometer (SPI) was designed, prototyped, and demonstrated in the Stanford Engineering Test Facility (ETF) measuring and controlling the differential displacement between adjacent platforms at low frequencies.

The dynamic range requirement of subsequent sensors, such as the main LIGO

interferometer, is reduced by controlling this motion. While LIGO was operational, motion reduction would help simplify lock acquisition of the main interferometer as it effectively offloads some of the necessary control to isolation stages closer to the ground. This offloading is also helpful in that these stages utilize actuators that are better impedance matched to control low frequency motion and zero frequency offsets and alignments than actuators acting directly on the test masses, optics, and suspension systems.

In order to sense the excess motion resulting from tilt coupling into the horizontal control loops, the SPI needs to measure the differential length between platforms. The measurement of differential pitch and yaw also becomes necessary because the attachment point for the suspension to the optics is not co-located at the center of rotation of the platform but is approximately 1 m above it and up to 1 m to the side.

The SPI prototype signal was then used to control the differential motion of two actively controlled isolation platforms in the ETF. These platforms were separated by a distance of 8.9 m with one being a two-stage system and the other a single stage platform. The two-stage platform served as the host platform.

Both of the platforms were locked together at low frequencies through the prototype SPI in differential length, pitch, and yaw signal by controlling the remote platform. The differential displacement motion reduction was recorded on two independent GS-13 seismometers and displayed an order of magnitude reduction between the frequencies of 100 mHz to 5 Hz.

The SPI prototype demonstrated success in measuring and controlling differential pitch, yaw, and length between two active seismic isolation platforms. The in-loop RMS differential motions were reduced by 11 times in pitch, 24 times in yaw, and 4,418 times in length by the SPI enabled control. The SPI therefore provides a solution to induced, unwanted motion at low frequency caused by the tilt-horizontal coupling in the feedback seismometers of the active ISI platforms in Advanced LIGO. It is recommended that an SPI system be implemented in aLIGO.

The work contained in this thesis does not necessarily reflect the scientific opinion of the LIGO Scientific Collaboration (LSC) as it was not required to be technically reviewed by the LSC.

Acknowledgement

The author would like officially to acknowledge the support of the work contained in this thesis by the National Science Foundation grants NSF PHY-10 68596, NSF PHY-07 57896, and NSF PHY-05 02641 along with the support of the LIGO Scientific Collaboration. This thesis has been assigned the internal LIGO document control center identification of LIGO-P1300043.

The results of this thesis and corresponding work could not have been achieved without the many people who have been instrumental in my life throughout the years. These people have been influential in instructing, mentoring, counseling, and encouraging me.

Firstly, I would like to express my deepest gratitude to my advisor, Professor Dan DeBra. His time, effort, and patient teaching has been the basis for this work. His professional, yet kind manner has always been appreciated throughout the time I have known him. He has an attention to detail that is surpassed by few, critical to precision engineering, yet at the same time is able to keep the big picture of a project or task in mind. He is truly a gentleman that I greatly respect.

Secondly, Dr. Brian Lantz has been vital in the theory, preparation, and experimental validation of the work contained in this thesis. Without him this would not have been possible. Dr. Lantz oversees the day-to-day operation of the Advanced LIGO seismic isolation efforts at Stanford and is a key leader in many aspects of the LIGO project. Even with all of his responsibilities, he has always been approachable, taking the time to come to the lab and explain any aspect, theory, or design in such a way as to make it clear. His carefully articulated words and patience in explaining things are most deft. I sincerely thank him for his influence on my life and work.

Many many hours have been invested by him in my success.

Professor Dave Beach, along with Craig Milroy, has been a special inspiration to me, both through classroom instruction and through the direction of the Product Realization Laboratory. They exemplify precision engineering from product design to manufacturability.

Additional members of my oral exam committee deserve my heartfelt thanks: Professor Roger Howe, Professor Mark Cutkosky, and Professor Leo Hollberg.

Many others, both associated with the Stanford LIGO team and Ginzton Laboratory at Stanford University have been helpful in so many ways. I would like to thank Professor Robert Byer, Professor Fejer, and Dr. Roger Route for their wisdom and experience with experimental laboratory research. Everyone in the Byer/Fejer group were most helpful and appreciated including, among others, Vivian Drew, Dr. Karel Urbanek, Dr. Carsten Langrock, Dr. Ashot Markosyan, and Nick Leindecker. Mike Hennessey and Jim Perales, who have many years of experience in managing the laboratory building and experimental equipment, have also provided invaluable assistance over the years.

I would also like to take the chance to thank my fellow students who have worked on the LIGO project at Stanford. There are many, among whom are Tarmigan Casebolt, John Ulmen, Graham Allan, Doug Beck, Andre Keiser, Alireza Marandi, Jimson Tseng, Ruslan Kurdyumov, Tej Bhadbhade, Chris Kucharczyk, Brett Shapiro, Riccardo Bassiri, Angie Lin, Charles Celerier, and Marvin Andersen.

Brian O'Reilly and Jeff Kissel, both from the LIGO Scientific Collaboration, have also been helpful throughout my involvement with LIGO. I wish to thank them.

Several people, prior to my involvement in the LIGO project at Stanford University have provided instruction and mentorship throughout the years. Dr. Aubrey Sykes was a constant source of encouragement, along with Dr. Matthew Heun, Dr. Steven VanderLeest, and Dr. Ned Nielson, professors at Calvin College. The late Don Amborski, missionary pilot in Zambia, positively influenced my formative years and I wish to express my gratitude for him.

Right now, I would like to express my thanks to two very special people in my life. These people have bridged the gap between the technical, scientific, academic fields

and the personal, home environment. A special thanks to my father, Dr. James Alan Clark, and mother, Susan Jane Vetter Clark. Without their constant encouragement, teaching, training, and attention, I would never be where I am today. I appreciate their creative, detailed approach to problems. They instilled in me care for and curiosity in the world around us.

My grandparents deserve special appreciation: the late Dr. Robert and Eme Clark for their love for science and nature and Rev. Eugene and Joan Vetter for their interest in physics, their practical outlook, and their contribution to my hands-on training from as far back as I can remember.

My siblings have also been critical to my survival. I thank my sisters Christel, along with her husband Veniamin, and Lisa Marie, with her husband Derek, for sharing their lives with me and encouraging me during my time in school. I thank my niece Tavifa, and nephews Mark and Benjamin for their diversion from school and reminder of life beyond the laboratory.

I also thank the youth at my Baptist church on Astoria Street in Sacramento who welcomed me in their weekend activities and supported me with their love and prayers.

Finally and most importantly, I thank God for what His son Jesus Christ means to me. I hope to glorify and honor Him in everything I do.

> *"And I gave my heart to seek and search out by wisdom concerning all things that are done under heaven: this sore travail hath God given to the sons of man to be exercised therewith."* Holy Bible - Ecclesiastes 1.13

> *"It is the glory of God to conceal a thing: but the honour of kings is to search out a matter."* Holy Bible - Proverbs 25.2

Contents

List of Tables

List of Figures

Chapter 1

Introduction

The detection of gravitational waves will allow investigations into areas of science that are currently inaccessible, one area being further insight into black holes, for example (Baker et al., 2006). Several observational facilities have been constructed in multiple countries with the sole purpose of the direct detection of gravitational waves. The Laser Interferometer Gravitational-wave Observatory (LIGO) is one such project. Detection of gravitational waves by LIGO is dependent on stringent seismic vibration attenuation within an ultra-high vacuum envelope. To this end, this work addresses the low frequency seismic isolation requirements and active alignment between adjacent platforms using an auxiliary interferometer.

1.1 Gravitational Waves

Einstein's theory of general relativity first predicted gravitational waves in 1916 and provided a causal explanation for the gravitational force to an accelerating mass (Einstein, 1918), (Einstein, 1916). These gravitational waves are predicted to travel at the speed of light, expressed with a wave equation, in contrast to Newton's theory of gravity's instantaneous attraction at a distance. While there have been no known, direct observations of gravitational waves, careful measurements of the orbital frequency decay of neutron star binary systems, such as the PSR B1913+16 by Hulse and Taylor, resulted in an indirect observation of energy loss consistent to a few

percent with the predictions of energy converted through the generation of resulting gravitational waves (Hulse and Taylor, 1975), (Taylor and Weisberg, 1982), (Taylor and Weisberg, 1989).

1.1.1 Visualizing Gravitational Waves

Gravitational waves can be visualized as disturbances to space-time caused by an accelerating mass. According to the theory, this can be visualized by the mass distorting the space-time fabric (as depicted in **Figure 1.1** inset) on which it sits while this space-time fabric dictates the movement of the mass. When massive astrophysical objects accelerate, they create the gravitational waves, or "ripples" in the space-time mesh, which then are theorized to radiate away, traveling at the speed of light, from the disturbance source. Passing gravitational waves distort the space-time metric in a detector and can be measured. A gravitational wave can be sensed with correlated detectors at multiple locations, which can provide information as to the wave's source.

1.1.2 Polarization of Gravitational Waves

Gravitational waves induce a differential strain in space-time they pass through, in a plane orthogonal to the direction of travel. Gravitational waves, similar to electromagnetic waves, have two types of polarization of their differential planar strain waves, plus (h_+), and cross (h_x), (Blair, 1991). As an h_+ gravitational wave travels, space-time will stretch in one dimension while it shrinks correspondingly in the other orthogonal dimension. If, for example, the space-time metric is depicted in **Figure 1.2** (a) and is then subjected to a passing gravitational wave (b) that is traveling along a direction parallel to the longitudinal axis of the bar z, the x and y dimensions of the bar will become distorted. These distortions of the space-time metric correspond to different points along the period of the gravitational wave. If the space-time metric were sectioned at these points, we would discover contours as in (c) for the corresponding h_+ and h_x polarizations. As depicted, the h_+ and h_x polarizations are rotated 45° with respect to each other.

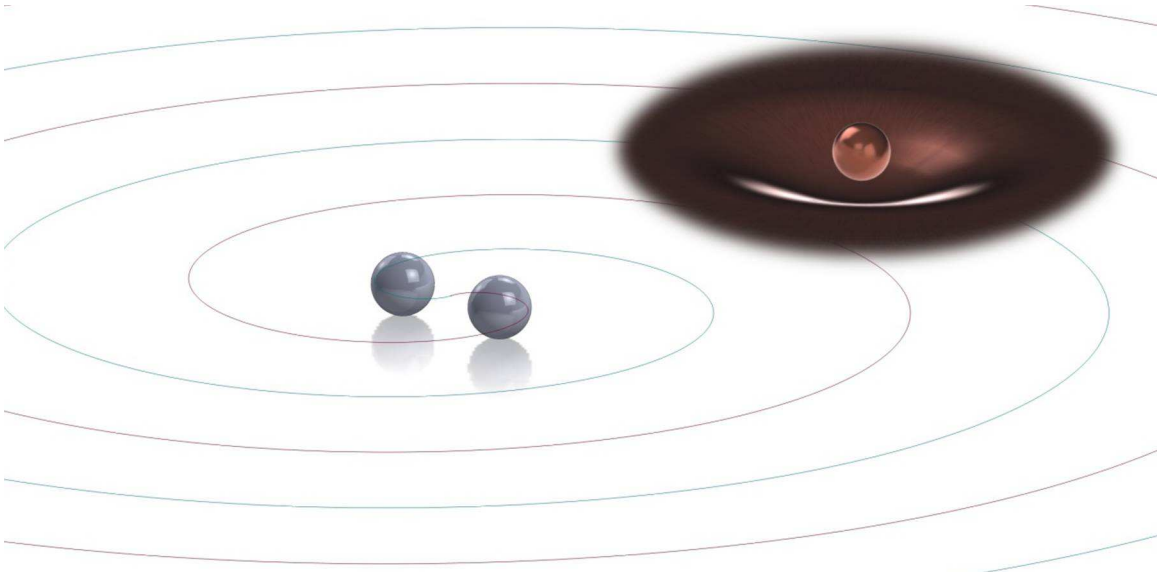

Figure 1.1: Depiction of space-time curvature caused by a mass (inset). When two massive objects, such as binary black holes or coalescing neutron stars, are rotating around each other, the disturbances in the space-time metric generates gravitational waves which can be visualized as radiating ripples.

1.1.3 Amplitudes of Gravitational Waves

Gravitational waves are predicted to be generated by astro-physical events such as supernovae, inspiraling black holes or binary neutron stars (Saulson, 1994a). The amplitude of gravitational waves, generated by a pair of coalescing neutron stars, traveling perpendicular to the $x-y$ plane is shown in **Equation 1.1** (Saulson, 1994b). M is the mass of each neutron star, $2r_o$ is the separation between the two stars, $f_{orbital}$ is their orbital frequency, and D_c is the distance from the observer to the center of the neutron star system. The amount of strain induced in space-time rapidly diminishes with distance from the source.

$$h_{xx} = \frac{32\pi^2 G}{D_c^4} M r_o^2 f_{orbital}^2 \cos\left(4\pi f_{orbital} t\right) \tag{1.1}$$

$$h_{yy} = -h_{xx} \tag{1.2}$$

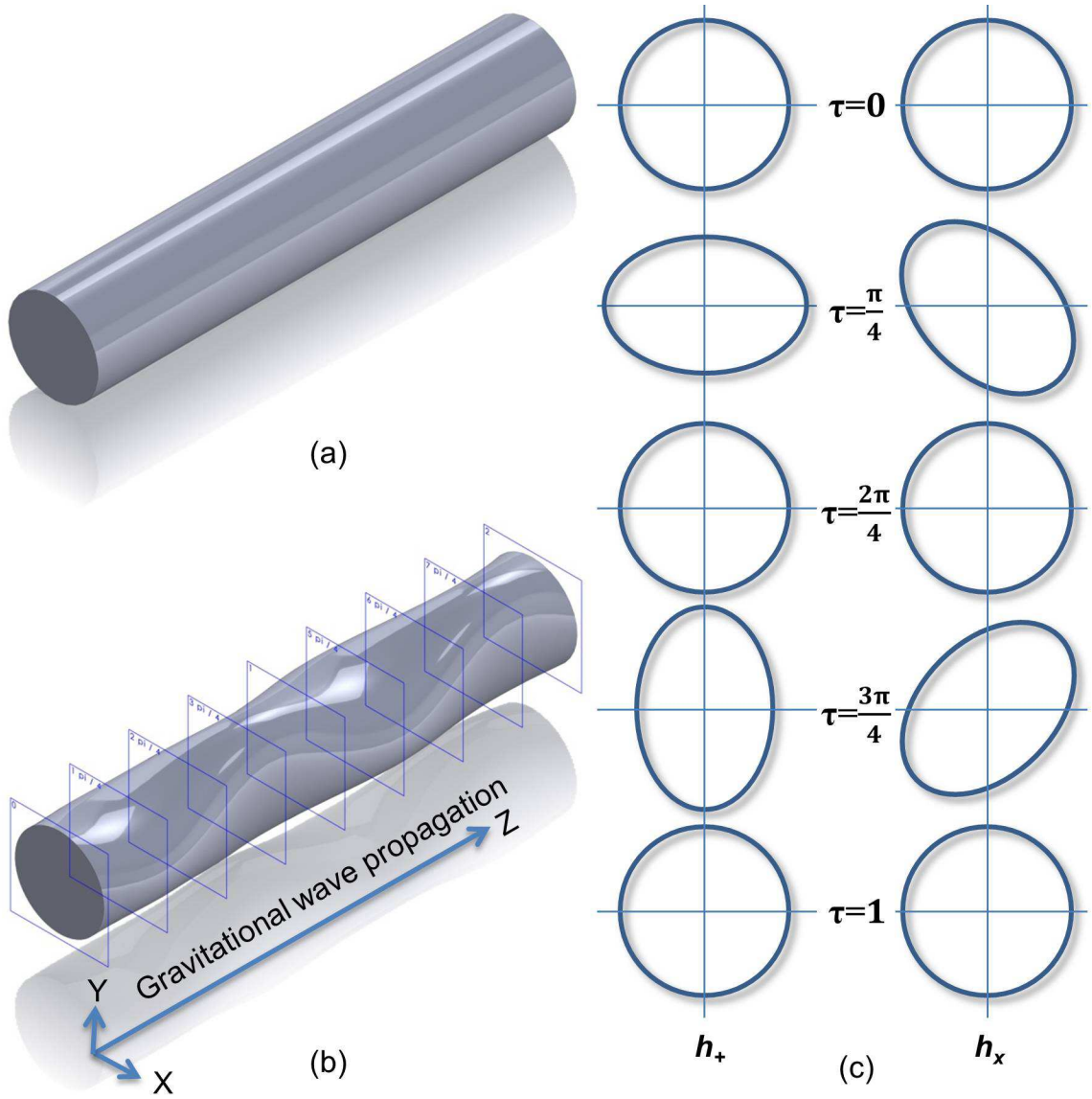

Figure 1.2: A passing gravitational wave propagating along the z axis of a space-time metric (undisturbed in (a)) strains the space-time metric as depicted in (b), distorting the $x-y$ cross sections corresponding to different points along the gravitational wave's period. The strain induced by a passing gravitational wave is dependent on the wave's polarization. The h_+ orientation is depicted in (b). For an h_x wave, the axes of maximum strain would be rotated by 45°.

Substituting $f^2_{orbital} = GM/16\pi^2 r_o^3$ in **Equation 1.1**, the characteristic strain on earth for a 1.4 solar mass neutron star system at 15 Mpc (corresponding to being in the Virgo cluster) and orbiting at about 350 Hz is calculated at $h_{xx} = 10^{-21}$.

The gravitational wave sources mentioned are some selected examples but must not be considered all-inclusive. Future discoveries may easily expand this list and are difficult to predict. These sources can, however, be divided into different classes by the various methods used for their discovery in a detector's data including: 1) the burst group, such as supernovae, 2) the inspiral group, such as when binary inspiral stars coalesce, 3) the cw-band group, such as pulsars, and 4) the stochastic background group, which is made up of many weaker sources blended together (Ju et al., 2000).

1.2 Detection of Gravitational Waves

Bar detectors marked the beginning of scientific devices specifically built and operated in an attempt to measure gravitational waves with some of the first detectors being built and operated in the United States (Weber, 1969), (Weber, 1970), (Forward, 1965). Several operational bar detectors are still in service in places such as Italy, Switzerland, Australia, and the U.S. (Ju et al., 2000). These detectors operate on the principle that as a gravitational wave travels through the bar it will excite the specifically designed natural resonant modes of that bar. These bars are designed to have high Q factors, meaning a long decay time, at those resonant frequencies. This allows the signal to then be integrated over a period of time so that strain sensitivities can be obtained down to a few $10^{-19}/\sqrt{\text{Hz}}$ at the bar's resonant frequency.

A slightly different measurement approach but one that still measures the strain induced by a gravitational wave, would be to utilize a laser interferometer. This could be ground based, such as multiple interferometric gravitational wave detectors currently installed or being installed around the world, or space based, such as the proposed Laser Interferometer Space Antenna (LISA).

1.2.1 Laser Interferometric Detection

A laser interferometer is especially well suited to gravitational wave detection because the differential strain induced in the plane orthogonal to the wave's propagation direction can be differentially measured by a Michelson interferometer (**Figure 1.3**). Rainer Weiss worked out the requirements in the 1970s for just such a system (Weiss, 1972). By the late 1970s, an operational laser interferometric detector was operating at the Hughes Research Laboratories (Forward, 1978). The current operationally maintained, ground-based, gravitational wave interferometers include the 300 meter Japanese operated TAMA, the 600 meter German-English collaborative GEO-600, the Italian-French 3 km VIRGO, and the three 4 km Advanced LIGO detectors, two sited in the U.S. and one proposed to be located in India (IndIGO, 2011). There are also some future earth-based gravitational wave observatories proposed such as AIGA in Western Australia and a cryogenic observatory, KAGRA, in Japan. The space-based LISA mission would provide an interferometer that is not bound by some of the restrictions imposed on earth-based systems and would be able to detect gravitational waves at significantly lower frequencies utilizing $5 \cdot 10^6$ km arms (Center, 2009).

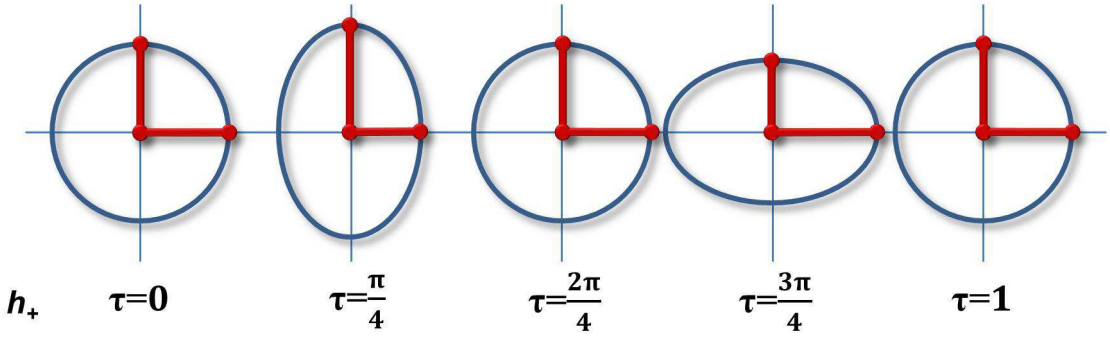

Figure 1.3: A laser interferometer, such as a Michelson type, is well suited for detection of gravitational waves. If the mirrors at the ends of the interferometer's arms are as depicted on the perimeter of the blue circle with the beam splitter located in the middle, then, as a gravitational wave passes, the resulting strain induced in space-time can be measured by a differential arm length change. This resulting differential arm length measurement can then be recorded as the gravitational wave signal.

1.2.2 LIGO

The Laser Interferometer Gravitational-wave Observatory (LIGO) currently has two observatory sites, one located on the Hanford Nuclear Reservation near Richland, Washington, and one near Livingston, Louisiana. The observatories housed three interferometer instruments: one at the Livingston site called L1 and two at the Hanford site, H1 and H2 respectively for Initial LIGO. For Advanced LIGO (aLIGO) one of the interferometers from Hanford is proposed be relocated to a new observatory site to be constructed in India (IndIGO, 2011). In order to learn the most from a gravitational wave detection, it is important that the instruments be located with a large separation distance allowing for time-of-arrival triangulation and source localization. This geographical separation also helps reduce the possibility of local disturbances such as lightning and seismic noise from being mistakenly interpreted as a gravitational wave signal. The LIGO observatories are currently going through a sensitivity upgrade called aLIGO.

Since a passing gravitational wave generates a strain, as the interferometer's arms are lengthened, the motion induced by a given strain also increases. The aLIGO interferometers will all utilize 4 km long arms. Another method used by aLIGO to increase sensitivity is to resonate the light in each arm in a Fabry-Perot cavity. This can be recognized by visualizing the extra round-trips of the light in the resonate cavity as effectively lengthening the arms. Thus the strain sensitivity of the interferometer increases. This does not happen without some expense, as it only increases sensitivity for sources that generate gravitational waves that have periods longer than the light storage time of the cavities in the science frequency band, which was 0.84 milliseconds (ms) in initial LIGO but expected to be around 1.7 ms for aLIGO (Shoemaker, 2009).

Each observatory maintains a single ultra-high vacuum (UHV) system (**Figure 1.4**). The vacuum system includes the 4 km long beam tubes named the x and y arms and the chambers that house the main and auxiliary optics. Since the Hanford observatory had two instruments, they shared the same beam tubes but had individual optic chambers. This meant that H2 (the second instrument for Initial LIGO at Hanford) also required additional folding mirrors to allow its light to be coupled into the tubes. All of the main interferometer optics are suspended down from inverted

optics platforms in the Beam Splitter Chambers (BSCs) whereas the auxiliary optics are mounted to supports on top of the Horizontal Access Module (HAM) chambers' platform (**Figure 1.5**).

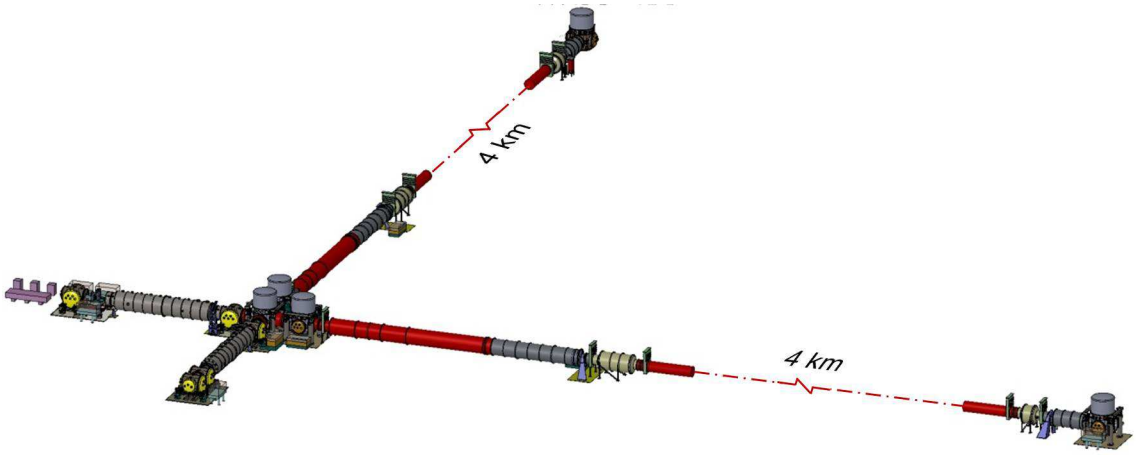

Figure 1.4: The LIGO vacuum envelope. The HAM chambers are rendered with yellow domes and the BSCs are rendered with blue domes.

Because of the UHV levels necessary for aLIGO, any object placed in the chambers must meet strict cleanliness and outgassing requirements. These requirements are essential so that the high vacuum levels can be obtained and fouling of the interferometer optics can be prevented.

In principle, aLIGO is a Michelson interferometer but in actuality there are many more optical filters and resonators used to clean and condition the input light as well as the signal light at the output (**Figure 1.6**). The high power light (180 W continuous wave (CW) at 1,064 nm) is introduced into the vacuum system from the Pre-Stabilized Laser (PSL). Once inside the vacuum system, it is conditioned in a resonant cavity, the input mode cleaner, before passing through a power recycling mirror that is designed to keep a higher power of the light on the beam splitter. Once past the power recycling mirror, the light is split at the beam splitter and sent to each 4 km long arm. When the light enters the arm it is transmitted through the input test mass, which forms one end of the Fabry-Perot arm cavity. The other end of the cavity is the end test mass. The finesse of the arm cavity is chosen so that the light remains resonant in the arms for approximately several hundred round trips.

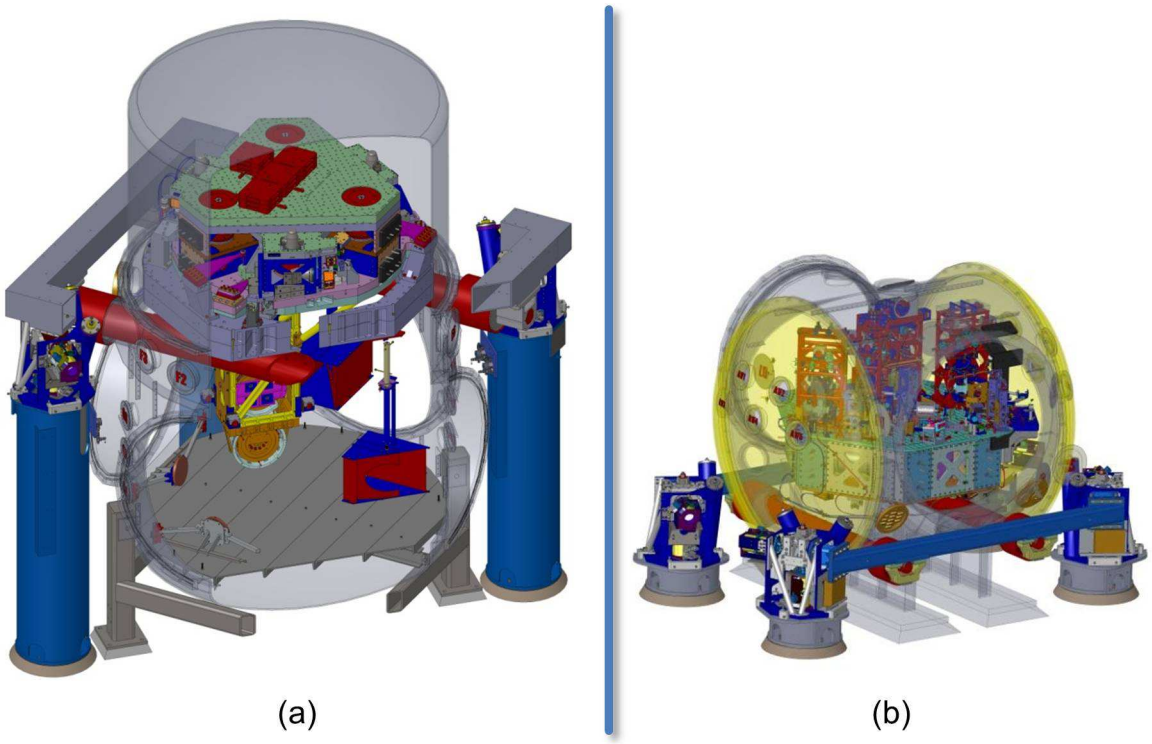

Figure 1.5: Cross sections of the two types of chambers used in Advanced LIGO (aLIGO), (a) the Beam Splitter Chamber (BSC) houses all of the main optics such as beam-splitters and the input and end test masses, (b) the Horizontal Access Module (HAM) chamber houses the auxiliary input and output optics. There are 5 BSC and 6 HAM chambers per interferometer.

As the light exits the arm cavities, it is recombined on the beam splitter and sent to the signal-recycling cavity. After resonating in the signal-recycling cavity, the light enters the output mode cleaner where it is finally monitored on photodetectors. A good description of the optical components that LIGO uses has been described by Black (Black and Gutenkunst, 2003)

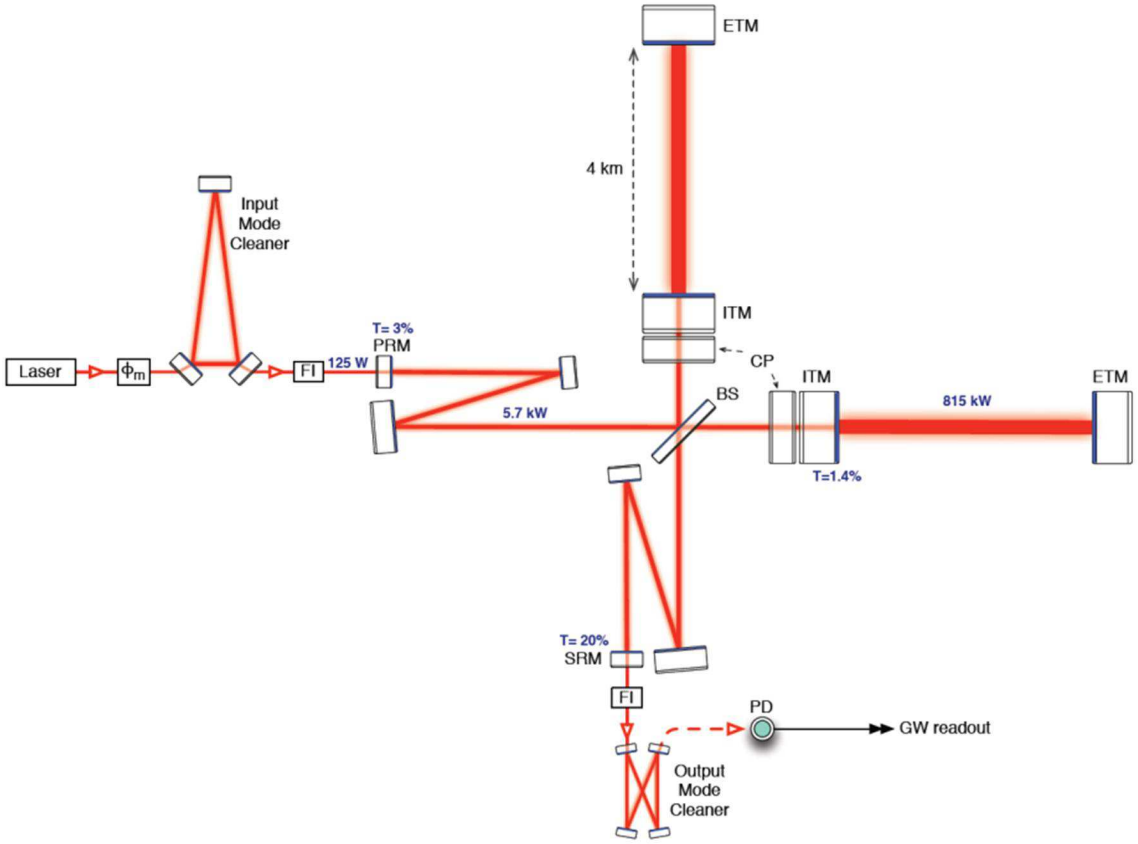

Figure 1.6: The Advanced LIGO (aLIGO) light path schematic. (Fritschel, 2009)

The signals from the photodetectors are subsequently digitized and recorded in the LIGO computer system (known as the Control and Data acquisition System (CDS)) along with other state variables and sensor information for future analysis (Bork et al., 2001). The Experimental Physics and Industrial Control System (EPICS) and its user interface, the Motif Editor and Display Manager (MEDM) provide the real-time interface for operations from the control room.

Many noise sources have the potential to degrade the sensitivity of LIGO. Some of the prominent sources include seismic coupling at lower frequencies, thermal noise of the Brownian motion on the mirror surfaces at the mid frequencies and shot noise at the higher frequencies of the science band. These predicted sources are displayed relative to frequency for aLIGO in **Figure 1.7**.

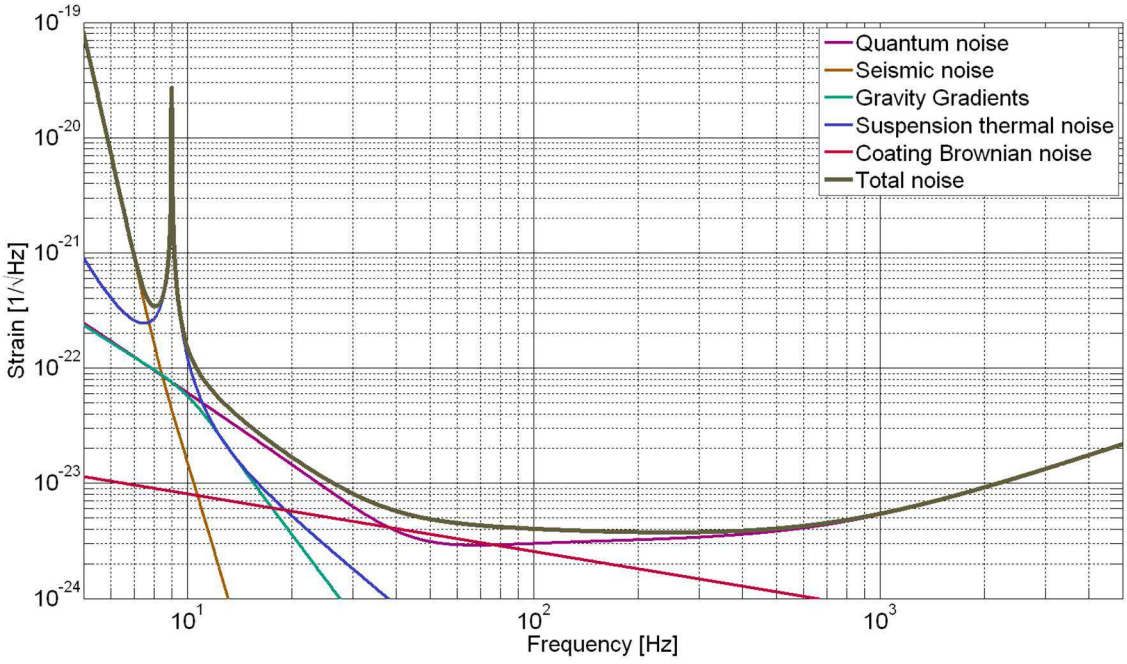

Figure 1.7: Advanced LIGO (aLIGO) design noise limiting sources as a function of frequency. Seismic noise is the limiting factor below 10 Hz. The noise sources, in general, have been carefully engineered to be below the quantum noise levels in the science band from 10 Hz to several kHz (Fritschel, 2009).

Since the largest non-quantum noise source degrading aLIGO sensitivity at low frequencies is seismic noise, great effort has been expended in order to reduce these disturbances below the quantum noise level at the interferometer optics above 10 Hz. Natural and anthropogenic ground vibrations at the observatory sites are about 10 orders of magnitude greater than the tolerable motion at the optics at 10 Hz. For aLIGO to operate at its design sensitivity, vibration isolation of an unprecedented 10 orders of magnitude at 10 Hz and more at higher frequencies is required (**Figure 1.8**). The systems necessary to achieve this are introduced in more detail in the

following section.

1.3 Seismic Isolation Systems in LIGO

In order for aLIGO to reach the design sensitivity levels that it needs to allow for the regular detection of gravitational waves (and subsequent astronomy), the test masses in the arm cavities must be isolated from ground vibrations. This seismic isolation needs to attenuate the ground motion by as much as ten orders of magnitude.

The system that LIGO utilizes, in order to isolate to these levels, is composed of three different subsystems. First, outside the vacuum chamber, the Hydraulic External Pre-Isolator (HEPI) provides low frequency isolation and alignment. The alignment of each subsequent stage is provided by the next outer stage. HEPI, as the outermost stage in the isolation chain, must provide the zero frequency steady state alignment as well as low frequency isolation. Because of good impedance matching of the hydraulics to the load, HEPI is well suited to carry the biases from the subsequent isolation systems that it supports. This allows offloading of static loads and alignment of supported subsystems back to HEPI. The Internal Seismic Isolation (ISI) platform is an in-vacuum subsystem that sits on support tubes that are controlled by HEPI. Finally, attached to the ISI is the suspensions (SUS) subsystem that is typically comprised of a multiple spring-mass pendulum system which terminates with the optic.

The approach taken at GEO and VIRGO has been one of utilizing large, soft springs to attain isolation through passive means. By utilizing anti-springs and unique spring structures to cancel stiffness and reduce the natural frequency of the system, large attenuation ratios have been achieved. The approach at LIGO has been different in that LIGO has chosen to use a stiffer suspension system, that results in a more compact structure and then add isolation through active control. This is better suited to correct for small variations in material properties and has the benefit of providing the ability to actively control and point the optical support structure.

Different targets have been established for each of these subsystems and are plotted in **Figure 1.8**. The ground motion curve is the 50^{th} percentile of the ground motion

measured on the technical slab (the floor) at the LIGO Livingston Observatory (LLO) in Louisiana. HEPI, which sits on top of the blue piers, supports the lilac crossbeams that support the red tubes in the computer aided drafting (CAD) drawing. Motion in the 0.1 to 5 Hz band is reduced by HEPI. The BSC ISI or HAM ISI sitting on these tubes reduces the motion of the optical table. The support tubes (red) penetrate the vacuum shell, which is sealed with a flexible bellows (not shown in **Figure 1.8**). The various suspensions (SUS) are attached to the optical table and provide the remaining attenuation necessary.

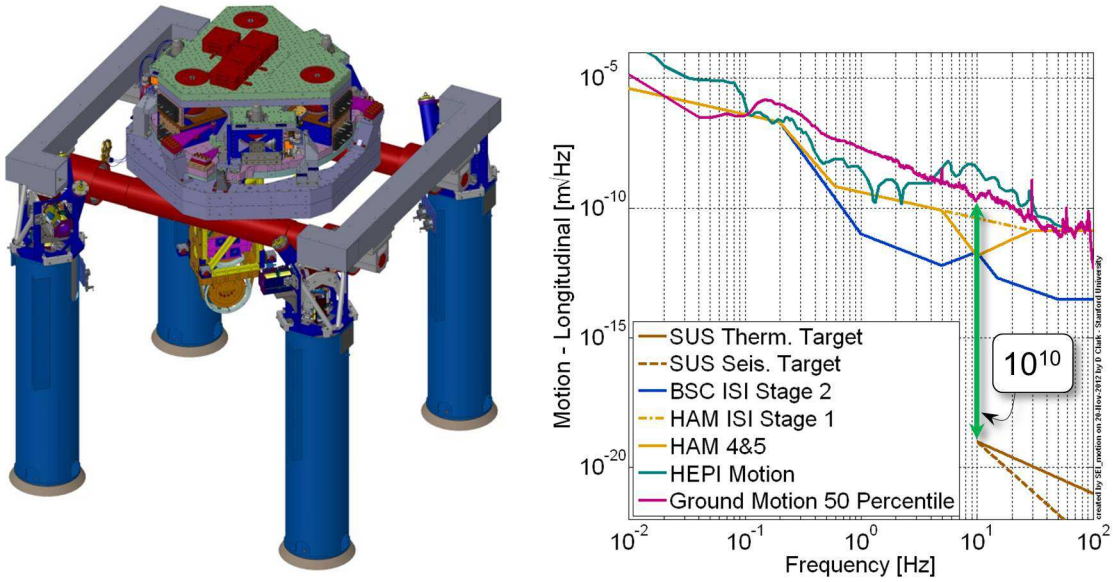

Figure 1.8: Seismic Isolation Requirements. Advanced LIGO (aLIGO) isolation requirements from the ground attach points to the proof masses and optics. The isolation is obtained in three steps: (a) an external hydraulic stage (HEPI), (b) the in-vacuum isolation system (ISI), and (c) the suspension system (SUS). HEPI data, (Wen, 2006)

1.3.1 Hydraulic External Pre-Isolators

HEPI was implemented in initial LIGO at the LLO after a large research and development investment by the LIGO group at Stanford (Hardham, 2005). Because of the large, low frequency disturbances of the ground at LLO, HEPI significantly increased

the instrument's duty cycle. HEPI is currently in the process of being installed in Hanford as part of the aLIGO upgrade.

The system utilizes linear, quiet hydraulic actuators to control support tubes for the ISI. Two tubes are utilized for each chamber with each end of a given tube being supported by a crossbar that is supported on each end by a HEPI pier. A single HEPI pier contains two actuators, two maraging steel, counter-wound offload springs, two inductive displacement sensors, and two inertial Sercel L-4C (L-4C) seismometers (**Figure 1.9**).

Hydraulics was used for the actuation medium because of better impedance matching to the static loads and forces on this outermost isolation system. The control of actuator position is done by a Wheatstone bridge configured laminar flow valve with the actuator itself damping high frequencies through an integral resistive and capacitive hydraulic flow path across the actuator chambers. The hydraulic supply flow is also carefully pressure-fluctuation filtered after the pump and in the distribution manifolds with resistive and capacitive hydraulic networks.

The main frequency control band for HEPI starts at zero frequency and rolls off with an upper-unity gain frequency as high as 5 Hz (Abbott et al., 2004) (Wen, 2009). HEPI creates a stable platform, reducing low frequency ground disturbances from being passed on to the next subsystem in the seismic isolation chain, the Internal Seismic Isolation (ISI) subsystem. It also has the capability of carrying large zero-frequency offsets for the alignment and pointing of the subsequent, supported subsystems and provides a stiff, well damped structure to support the ISI.

1.3.2 Internal Seismic Isolation Platforms

The ISI system is composed of large, six degree of freedom, passive isolation and active isolation and alignment platforms. These platforms have either two stages, as utilized in the BSCs, or a single stage as used in the HAM chambers (**Figure 1.10**).

In practice, below 10 Hz two or three orders of magnitude of isolation is required of the ISI platform. This requirement dictates the use of one or two active stages that are implemented in the BSC and HAM respectively. Both structures utilize capacitive

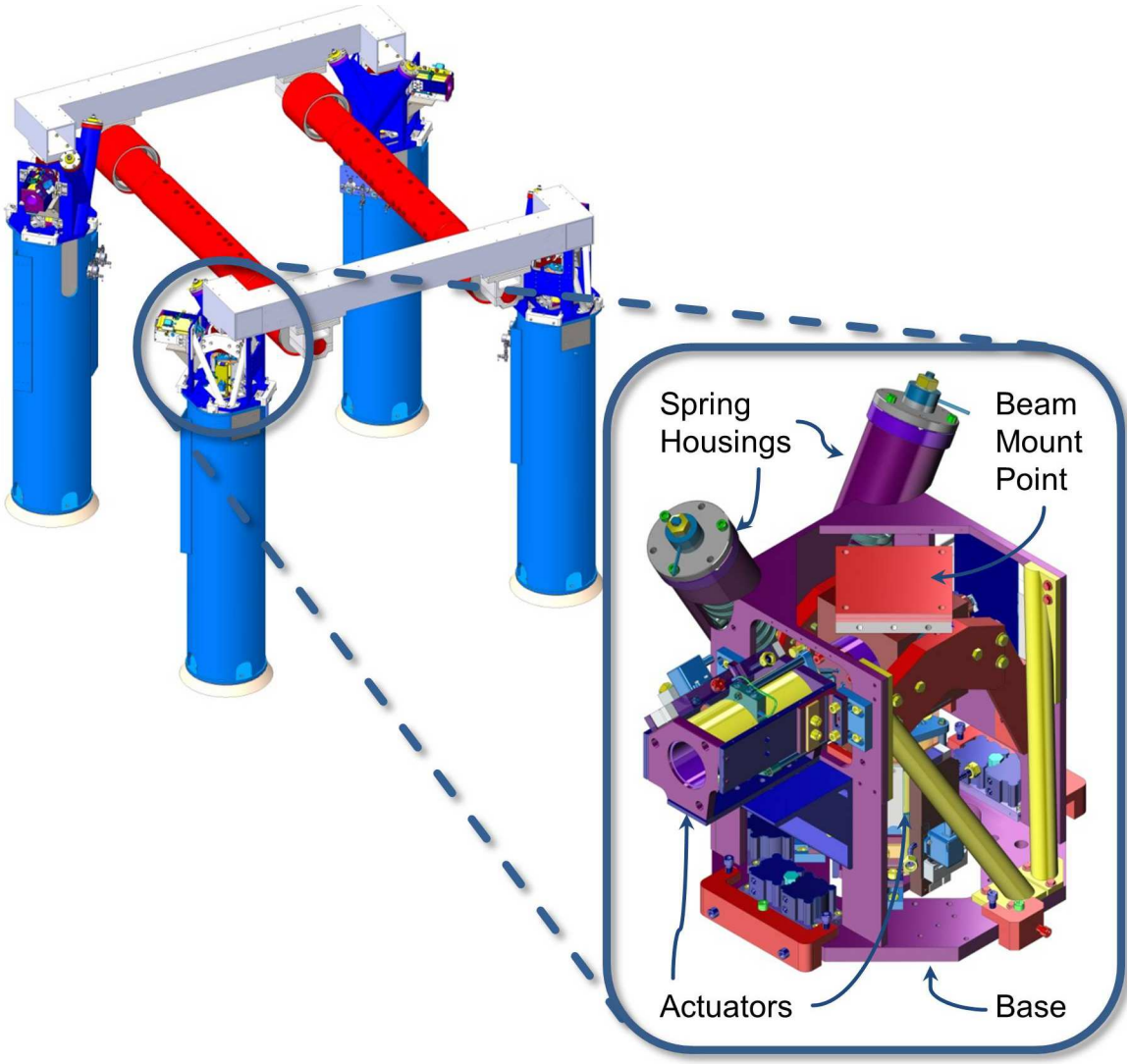

Figure 1.9: HEPI CAD diagram. The HEPI units for one BSC are displayed including the crossbeams and support tubes (shown in red) that support the next stage of isolation. The inset shows one of the four HEPI modules that are used on each chamber. The V-shaped tubular structures hold the maraging steel offload springs. The horizontal actuator is clearly visible while the vertical actuator is barely visible inside the structure.

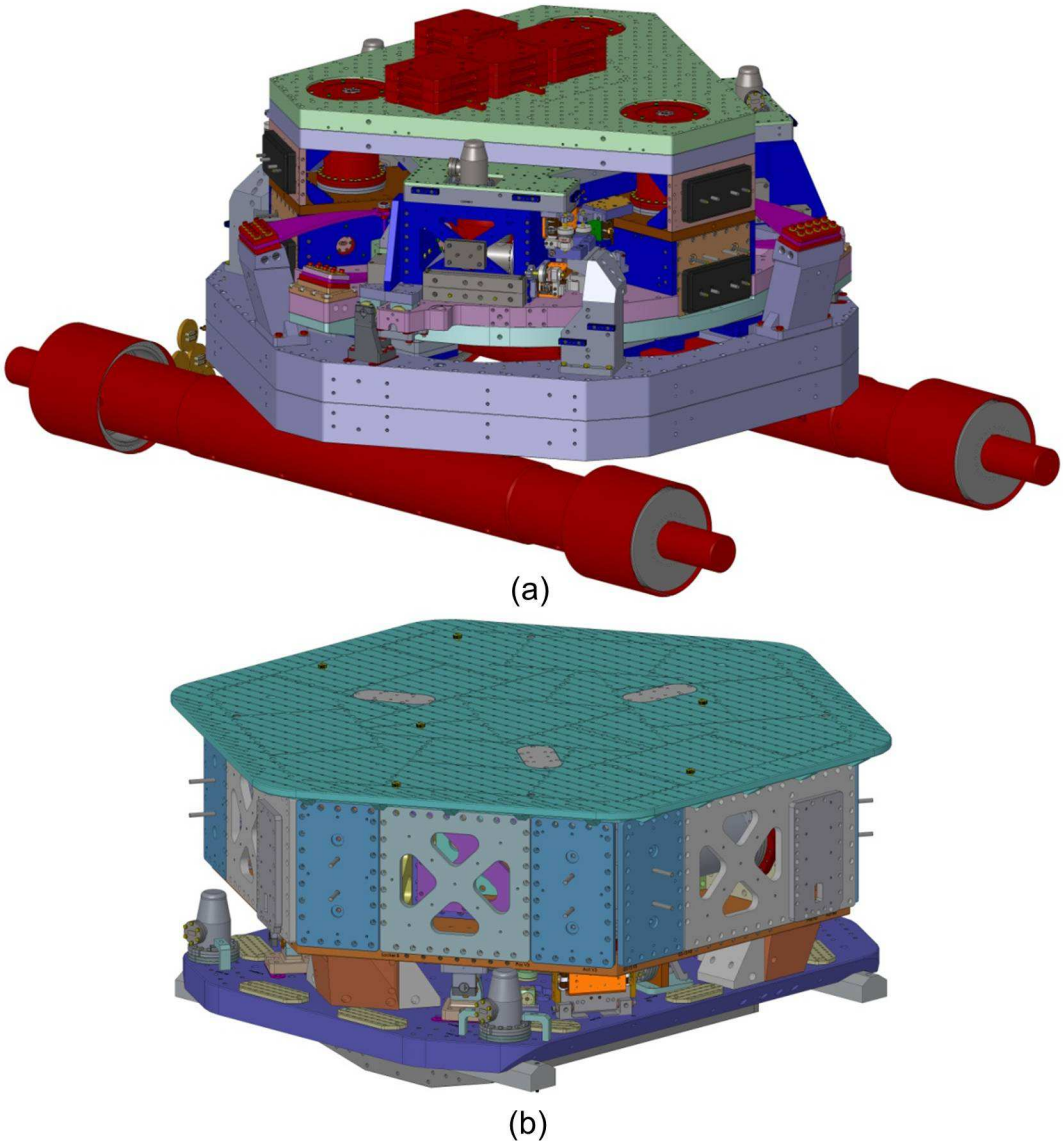

Figure 1.10: The Internal Seismic Isolation (ISI) subsystem CAD models. This subsystem is the second in a series of three isolation systems necessary for Advanced LIGO (aLIGO) to operate at its design sensitivity. The ISI is actively controlled in all degrees of freedom in each of its stages. The BSCs house a two stage version (a) whereas the HAM chamber's relaxed requirements allow them to utilize a single stage (b).

position sensors (CPSs) for low frequency control and then blend to inertial sensors at high frequencies creating a virtual sensor used to obtain the isolation (see Section 2.3 for additional information on this process).

It is interesting to note that the BSC SUS subsystem interfaces to the ISI at the underside of the platform whereas the HAM SUS components are placed on top. So for the BSC and HAM the optics table is on the bottom and top of their respective ISI platforms.

In the ISI design, care has been taken to mitigate against cross-coupled control terms. For example, co-locating the actuators and the sensors allows for a simplified single-input single-output (SISO) control scheme. Designing the platform so that the lower zero-moment plane is close to the sensing and actuation plane for each stage helps decouple the horizontal and tilt motions (Coyne et al., 2006).

The performance goals for the ISI platforms are shown in **Figure 1.11**. This includes the target for the ISI optics table, which is the interface point to the suspension systems and already accounts for the isolation provided by HEPI.

The Stanford University Engineering Test Facility (ETF) contains two vacuum chambers separated by 10 m that each houses an ISI prototype. The Technology Demonstrator Platform (Tech Demo) is a two stage, active, full degree of freedom controlled platform while the Rapid Prototype Platform (RPP) is currently configured as a single stage platform where all of the degrees of freedom can be independently controlled and are actively damped through feedback inertial sensors (**Figure 1.12**).

1.3.3 Pendulum Isolation Chain

The suspensions subsystem interfaces with the ISI and provides further isolation through multiple mass-spring stages down to the critical, main interferometer optics (**Figure 1.13**). In the most critical application, at the input and end test masses for the arm's Fabry-Perot cavities, the suspension system is composed of a four stage pendulum supporting both an optic and a reaction mass. Since the ISI is actively controlled in all degrees-of-freedom, most static control effort required by the SUS can then be offloaded up the isolation chain to the ISI and ultimately to the HEPI,

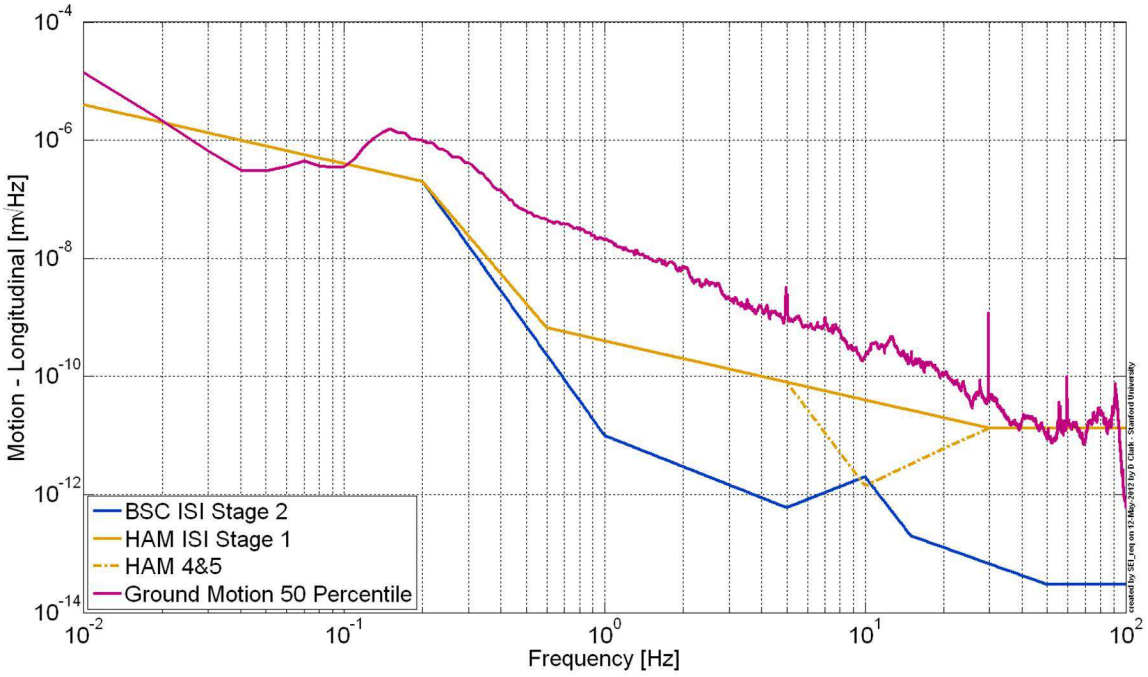

Figure 1.11: Advanced LIGO (aLIGO) performance goals for the ISI systems. The requirements for both the double stage ISI, used in the BSCs, and the single stage ISI, used in the HAM chambers are shown relative to the input motion.

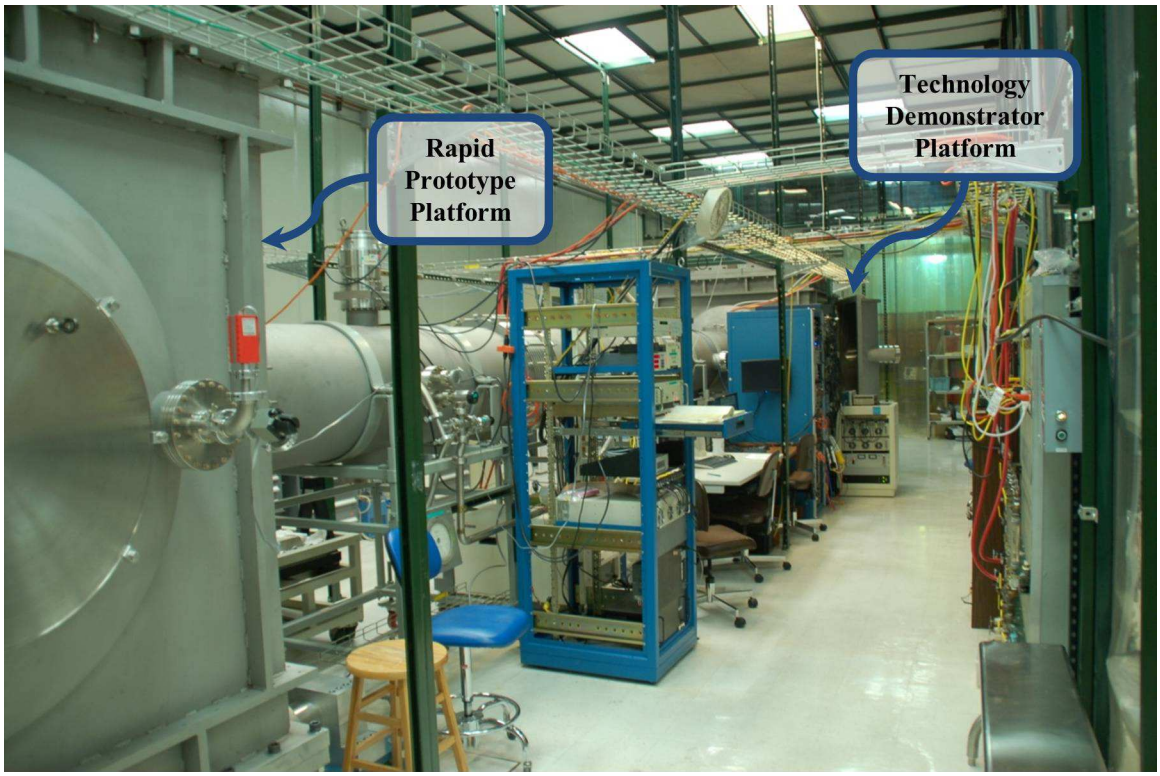

Figure 1.12: The Stanford University Engineering Test Facility (ETF). The fully controlled and isolated two-stage Technology Demonstrator Platform (Tech Demo) and the single-stage Rapid Prototype Platform (RPP) separated by 10 m.

both of which have higher authority levels and are better suited to carrying static pointing and positioning loads.

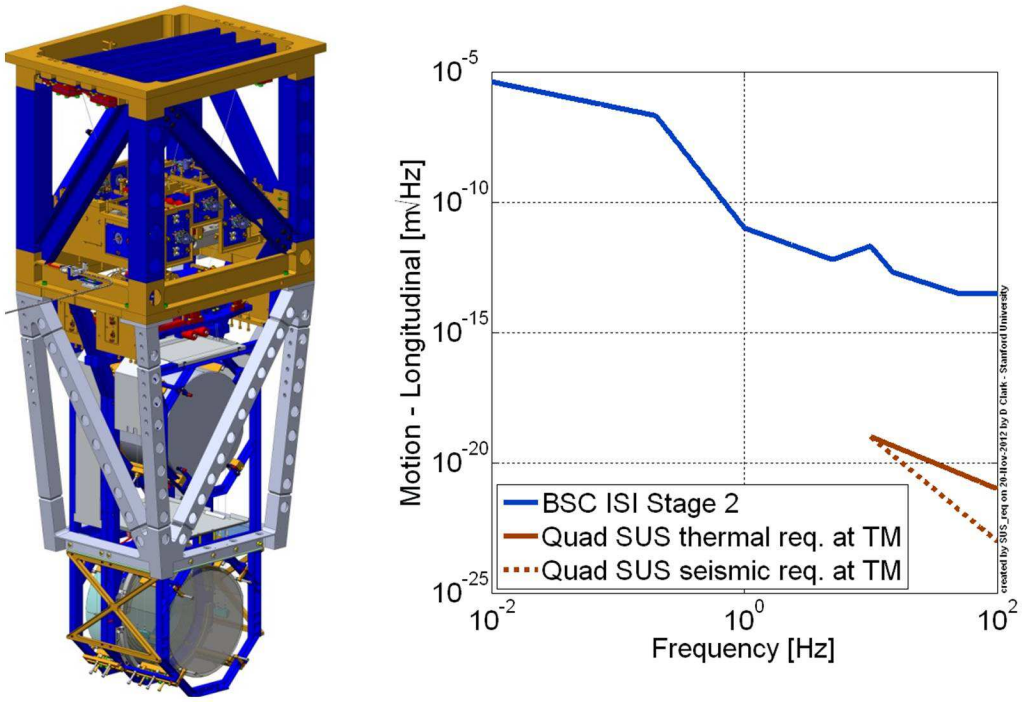

Figure 1.13: The suspensions (SUS) system CAD model for the input test mass shows the four stages that support both the appropriate test mass and its corresponding reaction mass. The top stage is controlled while the subsequent three stages are passive (Barton et al., 2008).

Finally, in an effort to reduce the Johnson-Brownian noise of the last suspension stage, the optic and stage directly above it in the suspension chain are made from high-Q fused silica with welded, glass connecting fibers. This monolithic system composed of the final two stages in the suspension is critical in reducing this noise source. Saulson provides a good description of thermal noise issues in suspension systems (Saulson, 1990).

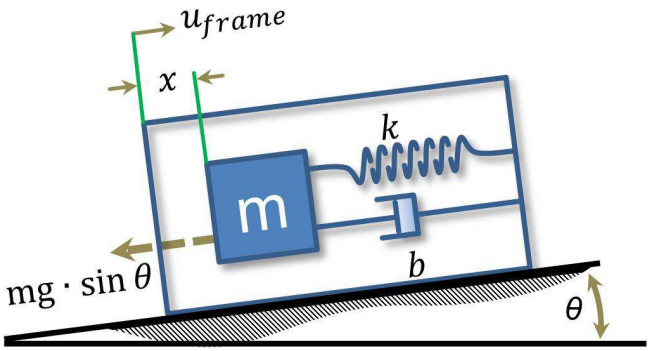

Figure 1.14: Tilt-horizontal coupling in horizontal seismometers. This causes low frequency tilt to be added to the translation signal causing ambiguity as to what is translation and what is rotation.

1.4 Tilt-Horizontal Coupling

Inertial-type sensors are the backbone of the sensors used for ISI platform isolation. However, the horizontal sensors can couple gravitational acceleration g into the output signal by the tilt of the instrument frame. It has been stated that this tilt-horizontal coupling in the horizontal inertial sensors is "the most challenging problem for the low-frequency seismic isolation systems" (Hua, 2005). This is described by Lantz (Lantz et al., 2009) and briefly reviewed below. Referencing **Figure 1.14**, the basic equation describing the system can be written as follows where u_{frame} is the instrument's frame position with respect to inertial space and x is the distance between the proof mass and the instrument frame. In **Equation 1.3** θ is the ground tilt, b is the instrument damping, k is the spring constant, and mass, m, is constrained to move along the axis x.

$$m(\ddot{x} - \ddot{u}_{frame}) = -b\dot{x} - kx + mg\sin\theta \tag{1.3}$$

If small angles are assumed ($\sin\theta \approx \theta$) then **Equation 1.3** simplifies as follows:

$$\ddot{x} = \ddot{u} - \frac{b}{m}\dot{x} - \frac{k}{m}x + g\theta \tag{1.4}$$

Taking the Laplace transform leaves:

$$x \cdot s^2 = u \cdot s^2 - \frac{b}{m} x \cdot s - \frac{k}{m} x + g\theta \tag{1.5}$$

$$x = u \cdot -\frac{b}{m} x \cdot \frac{1}{s} - \frac{k}{m} x \cdot \frac{1}{s^2} + g\theta \frac{1}{s^2} \tag{1.6}$$

$$x(1 + \frac{b}{m}\frac{1}{s} + \frac{k}{m}\frac{1}{s^2}) = u - g\theta \tag{1.7}$$

Taking the Fourier transform so that $s = i\omega$ leads to a sensitivity to rotation and sensitivity to translation ratio as follows:

$$\frac{\text{rotation response (seismometer signal / } \theta \text{ in radians)}}{\text{translation response (seismometer signal / m)}} = -\frac{g}{\omega^2} \tag{1.8}$$

Where ω is any given frequency in radians/sec. This demonstrates that as ω is decreased (low frequencies) the seismometer's signal resulting from instrument tilt rapidly becomes a complicating factor making pure inertial measurements at low frequencies difficult.

In the LIGO seismic isolation subsystem, the tilt-horizontal coupling in the inertial sensors is one reason why the current platform performance does not meet the target at low frequencies as displayed in **Figure 1.15**. This work addresses some of the complications that arise from the tilt-horizontal coupling in the LIGO seismic isolation system inertial sensors.

1.5 Previous Work

Seismic vibration isolation has been an area of scientific interest for decades. Vibration isolation has hampered precision measurements as noted by Forward from the Hughes Research Laboratories in his patent in 1964 on a gradiometer. Forward also did his thesis work on gravitational wave detectors (Forward, 1964), (Forward, 1965). Later, he describes using large granite masses on air springs as the base for his purpose-built gravitational-wave interferometer experiment (Forward, 1978).

Other pioneering work was pursued in the quest for detecting gravity anomalies by people, among others, Milton Trageser of the Charles Stark Draper Laboratory

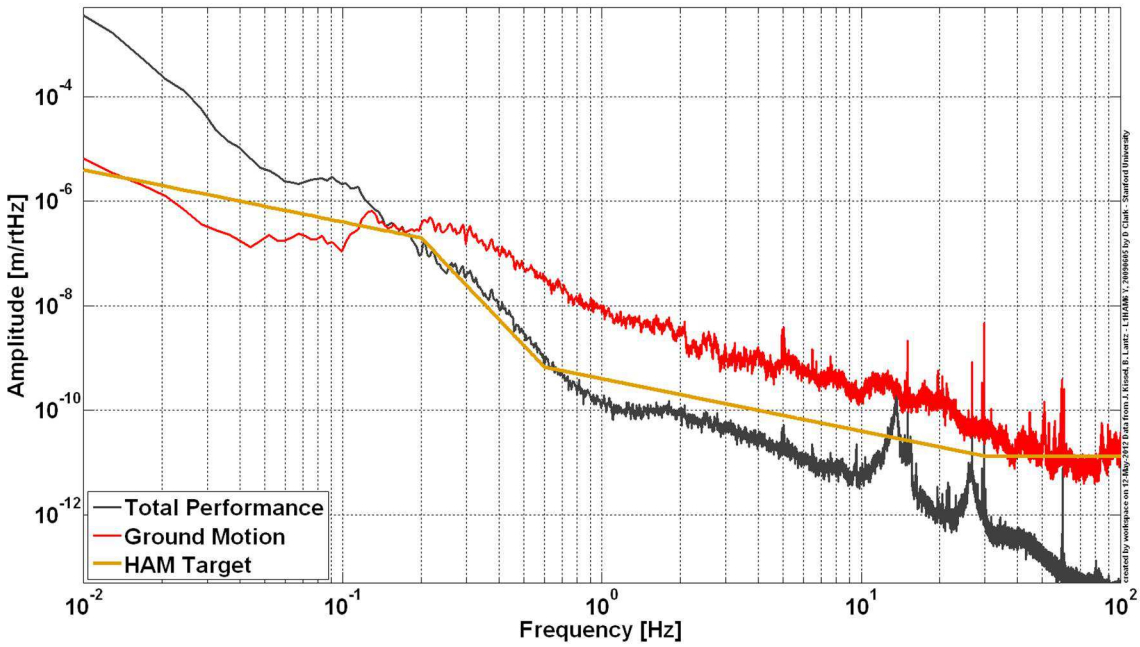

Figure 1.15: Measured data of the performance of the HAM 6 ISI in the LLO shows that performance goals at low frequency are not met; if the tilt were able to be differentiated from the horizontal seismometer signals, the low frequency performance could be improved. Data measured by Kissel (Kissel, 2009)).

and Ernest Metzger from the Bell Aerospace Textron (Ahn et al., 1984), (Metzger, 1986), (Metzger, 1987). There is still ongoing work at Stanford in the Kasevich research group studying gravity anomalies with an atom interferometer, which also has vibration isolation as a concern (Dimopoulos et al., 2007) (Dimopoulos et al., 2008).

Work such as the active 1 Hz seismic isolation development at Joint Institute for Laboratory Astrophysics (JILA) has laid the groundwork for the active isolation systems currently in use at LIGO (Richman et al., 1998). This was followed by the first active, all degree of freedom controlled platform which demonstrated control at the secondary micro seismic peak at Stanford (Hua, 2005). These have all influenced the Advanced LIGO (aLIGO) seismic isolation subsystem design leading to the current isolation platforms.

Other areas of research have revolved around the suspension systems that support the interferometer optics. Drever has suggested exotic isolation systems such as active magnetic suspension systems (Varvella et al., 2004).

The differential control of platforms that this work addresses is also not a new consideration. Robertson has proposed such a system for the suspension points of optics (Robertson et al., 1982) with an experimental system later being developed in Japan (Aso et al., 2006).

1.6 Outline of the Thesis

The tilt-horizontal coupling is something that intrinsically plagues horizontal inertial sensors. This work explores a few parallel considerations in Chapter 2, some of which might be worth pursuing. One method for measuring tilt, and then subtracting its effect from a corresponding horizontal inertial sensor's signal, is to spatially separate two vertical inertial sensors. This is described along with a novel, vertical seismometer design that exhibits decreased coupling to changes in air density in Chapter 3. A different approach would be to measure angular velocity with a ring laser gyroscope and then integrating the output.

A different solution, but toward the same goal, involves measuring the relative

displacement between platforms by an auxiliary instrument. The motion that the inertial sensors' tilt-horizontal coupling creates in the controlled platforms would then be independently measurable and controllable. The Seismic Platform Interferometer (SPI) addresses this and is defined in Chapter 4. The experimental setup and instrument noise budget are contained in Chapter 5. The results of the implementation and control of internal active seismic isolation systems in the Stanford ETF is discussed in Chapter 6. Finally, Chapter 7 contains ideas and concerns for future implementation of the SPI in aLIGO or similar environments.

1.7 Research Contributions

The primary contributions of this work involve methods to mitigate the effect of tilt-horizontal coupling of inertial sensors such as those used by LIGO in the seismic isolation systems. These include:

1. Experimental demonstration of differential length, pitch, and yaw control between two platforms, the Rapid Prototype Platform (RPP) and the Technology Demonstrator Platform (Tech Demo). Estimations of the noise floor for the instrument as demonstrated are listed in **Table 1.1**.

Table 1.1: Differential length, pitch, and yaw expected noise floor relative to the first stage platform target in the LIGO vertex.

Noise Floor and Target	**0.01 Hz**	**0.1 Hz**	**1 Hz**	**10 Hz**
Optical lever pitch and yaw (rad/$\sqrt{\text{Hz}}$)	$1.7 \cdot 10^{-7}$	$1.9 \cdot 10^{-8}$	$6.3 \cdot 10^{-10}$	$1.3 \cdot 10^{-10}$
Optical lever target, HAM 4-5	$5.5 \cdot 10^{-6}$	$5.5 \cdot 10^{-7}$	$5.5 \cdot 10^{-10}$	$5.5 \cdot 10^{-11}$
Length sensing noise floor (m/$\sqrt{\text{Hz}}$)	$4.5 \cdot 10^{-9}$	$5 \cdot 10^{-10}$	$6 \cdot 10^{-11}$	$9.5 \cdot 10^{-12}$
Length target, HAM 4-5	$5.5 \cdot 10^{-6}$	$5.5 \cdot 10^{-7}$	$5.5 \cdot 10^{-10}$	$4 \cdot 5.5^{-11}$

2. The implementation of a Mach-Zehnder interferometer and optical levers for differential tip and tilt sensing between the Tech Demo and RPP in the Stanford ETF.

3. The characterization of the laser frequency noise of a possible laser source as necessary for items 1 and 2 above.

4. A vertical seismometer design that decouples pressure variations and could be extended to provide sensing for resolving ground tilt through an array.

5. Integration of an aLIGO compatible UHV feedthrough for 1.550 μm polarization maintaining (PM) fiber.

Chapter 2

Tilt Sensing

A tilt sensor is desirable for Advanced LIGO (aLIGO) because tilt-horizontal coupling in the inertial sensors used in the Internal Seismic Isolation (ISI) platforms create excess noise at low frequencies (Section 1.4). This excess noise not only limits the seismic isolation performance but also makes it more difficult to return the instrument to science mode after interferometer lock-loss events such as earthquakes.

The aLIGO in-vacuum, active, seismic isolation platforms have multiple sensors. These sensors can be classified in two groups, relative position and inertial. The position sensors measure displacement between two objects. The sensors that are used in the aLIGO seismic isolation subsystem operate by measuring either the capacitance or inductance between two surfaces, providing good information down to zero frequency. This is then converted to displacement in a calibrated read-out unit. In the Internal Seismic Isolation (ISI) subsystem, capacitive position sensors measure the location of each stage relative to its support in all six degrees of freedom.

2.1 Inertial Sensors

The ISI also uses inertial sensors to measure its instrument vibration relative to inertial space. Several models of inertial sensors are used in the aLIGO isolation systems. These include the 240 second period Trillium T-240, which is an active feedback seismometer, and the passive, one second period, velocity-sensitive seismometers Geotech

GS-13 and Sercel L-4C. An inherent difficulty with inertial sensors, as described in Section 2.1.1, is that their noise floor rapidly increases below the instrument's natural frequency.

2.1.1 Principles of Operation

The inertial sensors used in aLIGO utilize an internal proof mass that is a reference to inertial space. On earth, the proof mass must be supported to counteract mg forces and practically constrained to move in only one dimension (these constraints are not necessarily applicable in space where drag-free satellites can reposition themselves around an inertial proof mass (DeBra, 1999), (DeBra, 1998)). The free dimension left unconstrained on the proof mass becomes the instrument's sensitive axis.

The natural frequency (ω_n) of the instrument is defined by the spring-mass system. For a vertical seismometer this is composed of the proof mass and the equivalent spring, k, of the offload springs (used to offset the mg force) and the restoring force coming from the constraint flexure stiffness. The horizontal seismometers do not need the offload springs so their natural frequency is typically only a result of the proof mass and the constraint flexure stiffness.

At frequencies above ω_n, the inertial mass remains stable relative to the inertial reference frame and least affected by motion of the instrument frame. This results in the best signal to noise ratio (SNR) for the instrument. In contrast, at frequencies much lower than ω_n the proof mass simply tracks the motion of the sensor's frame. In the extreme, this results in zero signal at zero frequency.

The equations for a vertical inertial seismometer such as the type used in aLIGO are as follows with a schematic representation in **Figure 2.1**.

$$m_{proof}(\ddot{x} + \ddot{u}) + b\dot{x} + k(x - x_0) - m_{proof}g = 0 \tag{2.1}$$

Where x is the difference between the proof mass and the instrument case, u is the case relative to inertial space, and b is the damping. If we define the initial starting position x_0 of the proof mass to be the equilibrium position counteracting the mg force, then $mg = -kx_0$ simplifying to:

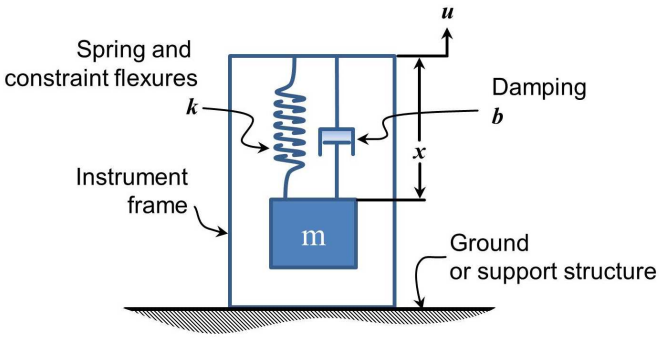

Figure 2.1: Sketch of the dynamic elements of a vertical seismometer.

$$m_{proof}(\ddot{x} + \ddot{u}) + b\dot{x} + kx = 0 \tag{2.2}$$

Then dividing through by the mass and subtracting the induced acceleration on the case:

$$\ddot{x} + \frac{b}{m_{proof}}\dot{x} + \frac{k}{m_{proof}}x = -\ddot{u} \tag{2.3}$$

From this form, we can set $\omega_n = \sqrt{\frac{k}{m_{proof}}}$ and $\frac{b}{m_{proof}} = 2\zeta = \frac{1}{Q}$ and obtain the following form:

$$\ddot{x} + 2\zeta\dot{x} + \omega_n^2 x = -\ddot{u} \tag{2.4}$$

By taking the Laplace transform and rearranging, the following familiar transfer function is reached:

$$\frac{u(s)}{x(s)} = \frac{-s^2}{s^2 + 2\zeta s + \omega_n^2} \tag{2.5}$$

Now, the readout methods on the 1 Hz seismometers in aLIGO measure the proof mass velocity instead of position ($V \propto \dot{x}$), which changes the transfer function to:

$$\frac{\dot{u}(s)}{\dot{x}(s)} = \frac{-s^2}{s^2 + 2\zeta s + \omega_n^2} \tag{2.6}$$

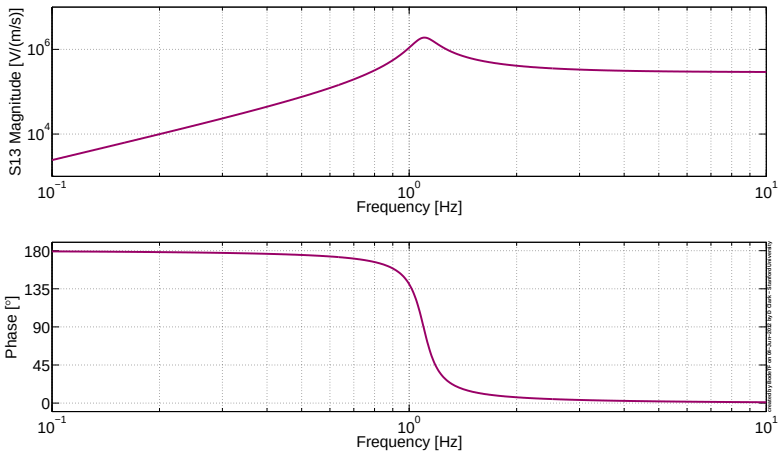

Figure 2.2: Geotech S-13 seismometer Bode plot. This is a 1 Hz vertical seismometer that was used as a reference instrument for the prototype seismometer discussed in Chapter 3. Advanced LIGO uses the Geotech GS-13 model extensively for active feedback of the isolation platforms. The GS-13 is similar in construction to the Geotech S-13 but differs in that the "G" model has a larger generator constant. LIGO also installs custom internal preamplifiers in the GS-13.

Or in terms of displacement this can be corrected by integrating the velocity to yield:

$$\frac{u(s)}{\dot{x}(s)} = \frac{-s^2}{s^2 + 2\zeta s + \omega_n^2} \cdot \frac{1}{s} \tag{2.7}$$

$$\frac{u(s)}{\dot{x}(s)} = \frac{-s}{s^2 + 2\zeta s + \omega_n^2} \tag{2.8}$$

A typical 1 Hz velocity-readout seismometer response is represented in **Figure 2.2**. At frequencies above the natural frequency the velocity response of the proof mass is directly related to the ground velocity. At frequencies below the natural frequency the response rapidly decreases and quickly approaches the noise floor of the readout electronics. Most analog to digital converters (ADCs) that aLIGO uses exhibit a form of $1/f$ noise coloring at low frequencies, which further challenges low frequency measurements.

2.2 Sensor Locations

In the aLIGO seismic isolation subsystem, sensors continuously measure all six degrees of freedom for each platform. The sensors and actuators have been carefully placed in three groups around the platform. For example, as much as practical, the sensors and actuators have been co-located in order to make the control algorithms easier. Taking the single stage of the HAM ISI platform as displayed in **Figure 2.3**, the sensor groupings are shown. These groups are located around the outer perimeter approximately 120 ° from each other containing both horizontal and vertical sensors and actuators. The horizontal sensors are aligned tangential to the perimeter and perpendicular with a line extending radially from the center of the platform.

These actuators and sensors are located in what is called the sensor coordinate basis (V_1, V_2, V_3, H_1, H_2, H_3). In **Figure 2.3** only the H_1 and V_1 inertial sensor axis are shown. Before the control laws are applied, however, all of these sensor and actuator locations are transformed to a platform-global Cartesian coordinate system (X, Y, Z, RX, RY, RZ), which allows standardization from one platform to the next and simplifies the interface with the Interferometer Sensing and Control (ISC) subsystem.

2.3 Sensor Blending

The seismic isolation subsystem in aLIGO performs different functions at different frequencies. This is one reason why different classes of sensors such as displacement and inertial are used. For example, at frequencies above 0.2 Hz, the main objective is to obtain the most isolation relative to inertial space as possible. Since this is exactly what inertial sensors excel at, they are used for the control signal at high frequencies. The platforms, however, must still be able to be positioned and oriented at low frequencies. For this task the position sensors are used.

Ultimately, the SUS subsystem offloads any zero frequency holding biases to the next outer ISI stage. The ISI then, in turn, transfers its zero frequency biases to the HEPI subsystem, which is much better suited to holding zero frequency terms.

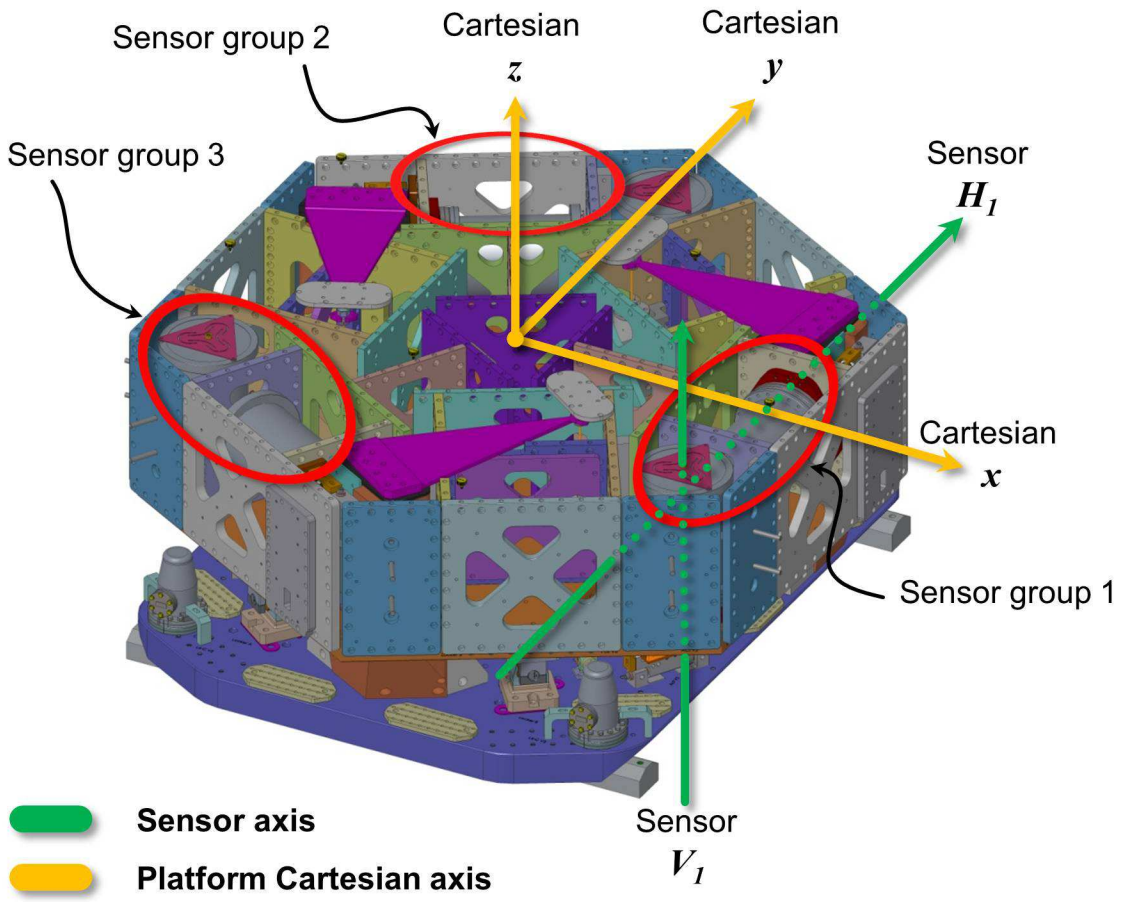

Figure 2.3: Sensor groups are located around the perimeter of the platform as shown above on a HAM ISI platform model with the optics table removed for illustration. Each group contains both position and inertial sensors and voice coil actuators for two degrees of freedom. The sensor coordinate basis is displayed only for the sensor group 1's inertial sensors. The signals are all transformed into the Cartesian coordinate system before reaching the controllers.

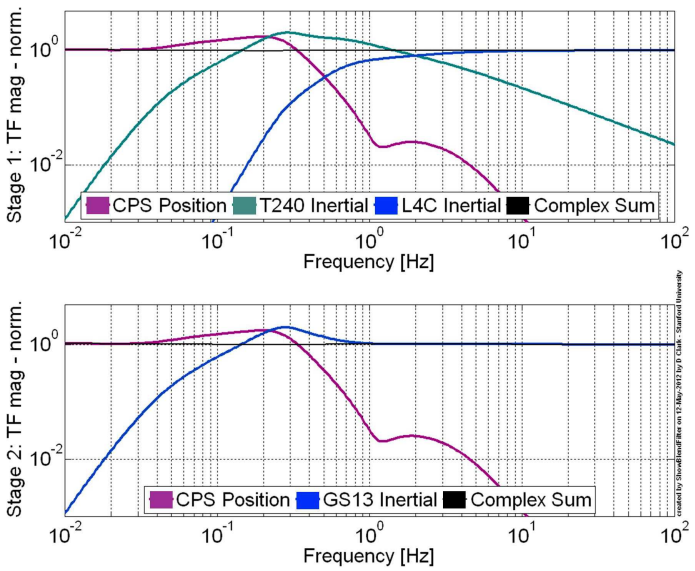

Figure 2.4: The blend filters for the first stage of the BSC ISI shows the blending of the capacitive position sensors and two inertial sensors, the T-240 and the L-4C respectively (a). The HAM and the second stage of the BSC utilize a single fade between the capacitive position sensors and the GS-13 inertial sensors (b).

The provision of different sensor information as a function of frequency to the controllers is generated by filtering. In the aLIGO control scheme, the position sensors are combined with the inertial sensors creating a combined virtual sensor. This is created for each sensing axis by first calibrating and normalizing the gains of the position and inertial sensors. The calibrated position sensor is then aggressively low-pass filtered and added to a complimentary high-pass filter for the calibrated inertial sensor. Care is taken to ensure that the complex addition of the two filters add to one across all frequencies. This effect can be seen in **Figure 2.4**. In this plot the magnitude of the individual sensor's signal actually peaks above one in order to compensate for the phase that is not shown.

The final stage of an internal seismic isolation platform (stage two of the BSC or the only stage in the HAM) utilizes just a single position sensor and inertial sensor for any given control axis. The first stage of the BSC platform, however, uses position sensors, low frequency inertial sensors, and high frequency inertial sensors. In this

case, the blend filter must combine all three sensors to create the virtual "super-sensor" signal as used by the controller.

In the overall control sense, it is the inertial sensors that provide the sensing necessary for active isolation. The position sensors, measuring displacement from their stage to the underlying structure, are necessary to provide the low frequency pointing and positioning but cannot provide isolation. In fact, if the control gain were increased using only the position sensors, the platform would do nothing more than just track the ground motion! Because inertial isolation is really the goal, it is advantageous to reduce the blend frequency. A practical lower limit for the blend frequency, however, is set by the noise of the inertial sensors and tilt-horizontal coupling in the horizontal sensors. This was discussed in Section 1.4 and is the motivation for the work covered in the rest of this chapter.

2.4 Methods to Resolve Tilt

Referring back to Section 1.4, we understand that an accelerometer is a specific force meter that, for a vertically oriented instrument, measures the combination of the forces necessary to balance both accelerations and weight (which is the mg force resulting from gravity acting on a proof mass). Since tilting of a horizontal accelerometer couples in a component of gravity, one cannot use the output of a horizontal inertial instrument without also accounting for tilt. This is reviewed in the following equation and illustrated graphically in **Figure 2.5**:

$$S_{signal} \propto \frac{gsin\theta}{\omega^2} \tag{2.9}$$

If θ (the tilt of the horizontal inertial sensors) can be found, then it could be fed-forward correcting the horizontal inertial sensor's signal. This would allow the use of a lower blend frequency resulting in greater isolation of the system. In order for the tilt measurements to be useful in correcting for the tilt-horizontal coupling in aLIGO, it must be able to be resolved to the target levels required (Lantz et al., 2009). The rest of this chapter discusses three possible ways in which θ can be quantified and

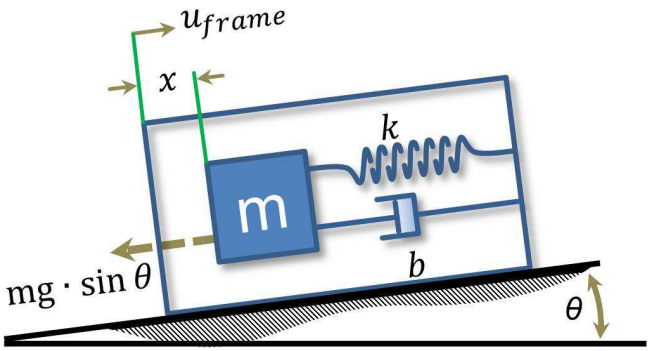

Figure 2.5: Tilt-horizontal coupling is a concern in the horizontal inertial sensors at low frequencies.

then used to correct a horizontal inertial sensor's signal.

2.4.1 Direct Measurements

2.4.1.1 Measuring θ

First, measuring tilt, θ, directly results in an elegant solution. Tilt has been successfully measured at low frequencies in boreholes by researchers at JILA (Levine et al., 1989), (Kohl and Levine, 1993), with insight on their design provided by Kohl (Kohl and Levine, 1995). The primary purpose was to resolve tidal and secular tilt of the crust where their work demonstrates the desire for sensitive, low-frequency tilt measurements. An experimental "walk-off" tilt-meter was developed and tested in Australia with an impressive noise floor of $10^{-11}\,\mathrm{rad}/\sqrt{\mathrm{Hz}}$ at 1 Hz (Zhou et al., 2001), (Cheng et al., 2002). Other LIGO tilt-meter work is currently being conducted at the University of Washington and CalTech (Venkateswara, 2011), (Dergachev and DeSalvo, 2012).

2.4.1.2 Measuring $\dot{\theta}$

It should also be noted that θ does not need to be measured directly, measuring $\dot{\theta}$ (angular velocity) or for that matter $\ddot{\theta}$ (angular acceleration) and then integrating the appropriate number of times would result in resolving theta for frequencies greater

than zero. ring laser gyroscopes (RLGs), for instance, typically measure angular velocity by interfering two counter-propagating beams around an enclosed space. If such an instrument could be constructed with sensitivities exceeding the requirements, then the output would simply have to be integrated to obtain theta (**Figure 2.6**). Measurements to these levels ($2 \cdot 10^{-11}$ $\frac{\text{rad}}{\text{s}}$)/$\sqrt{\text{Hz}}$ at 10^{-2} Hz) are not trivial as any local ground tilts are orders of magnitude below the earth's rotation rate ($\omega_{earth} \approx 73\,\frac{\mu\text{rad}}{\text{s}}$). This requires the instrument to have a large dynamic range. Low noise floor, low frequency ring laser gyroscopes have been constructed for geophysical monitoring such as the 0.75 and 1 m^2 units installed in Cashmere cavern near Christchurch, New Zealand (Bilger et al., 1993), (Stedman, 1997), larger 16 m^2 instruments such as the G-ring in Wettzell, Germany (Schreiber et al., 2004) and one documented by Rowe in the United States (Rowe et al., 1999), and a large 834 m^2 ring, the UG-2, also sited in Cashmere cavern (Hurst et al., 2009).

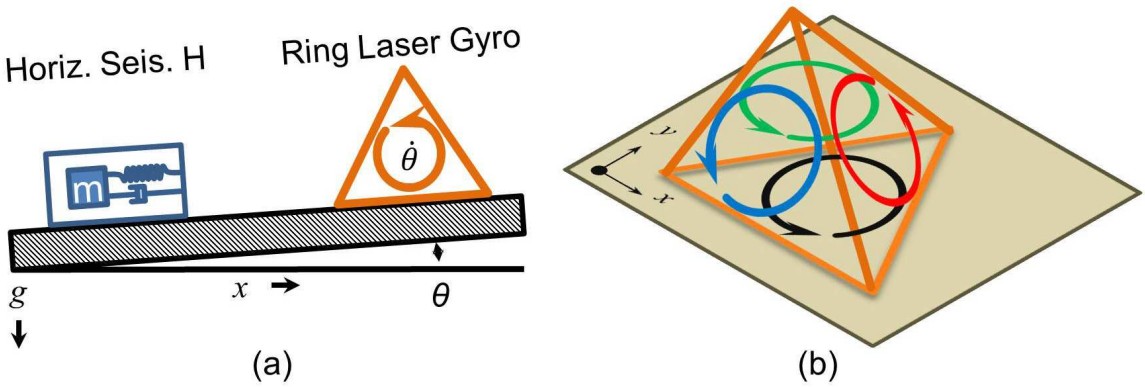

Figure 2.6: If $\dot{\theta}$ were measured by a Ring Laser Gyroscope as shown in (a), then the tilt-horizontal coupling in the seismometer could be corrected. If multiple RLGs were integrated onto a single tetrahedron, with the four RLGs represented in red, green, blue and black in (b), the extra information provided (4 signals for 3 degrees of freedom) could be used for error checking and providing a real-time indication of instrument stability.

If a ring laser gyro were pursued for aLIGO applications, several possibilities for optimization might be worth considering. One area of possible tuning lies in the gyro's ring design. The scale factor of an RLG is related to the ratio of the area enclosed by the laser beams divided by the perimeter, represented below as (Loukianov, 1999):

$$ScaleFactor_{RLG} \propto \frac{Area_{enclosed}}{Distance_{perimeter}} \tag{2.10}$$

It is easy to realize that a ring in the shape of a circle maximizes this ratio but has other practical drawbacks such as the infinite number of mirrors required (in the limit case). Another practical concern is that commercially available mirrors are optimized for a particular angle of incidence (AOI) of the light. It might be difficult to obtain mirrors optimized to an angle that is approaching that of being parallel with the mirror surface, which would be required for rings with many mirrors. While square rings display a nice working range in the $\frac{A_{enclosed}}{D_{perimeter}}$ ratio and commercial mirrors are readily available for AOI of 45 °, several advantages to a triangular ring should also be considered:

- A triangular ring defines a single plane of measurement.
- Precision triangular structures are typically easier to construct kinematically thus maintaining high tolerances and reducing internal strains and stresses.
- A minimum number of critical components is required for establishing an RLG.

It could also be advantageous to integrate multiple RLGs on a single structure. For instance, four RLGs could be arranged on the four faces of a tetrahedron (as shown in schematic form in **Figure 2.6**(b)). If the tetrahedron support structure were made from a suitably stiff material, such as possibly granite, this would result in four instruments measuring three degrees of freedom. The extra information could be used for self-checks on the four instruments and their scale factors. The earth's rotation provides a sufficiently large signal that could be used for just such self-checks. For a large multi-ring gyroscope to measure the gravitomagnetic effects, Bosi proposes a system where three square RLGs are formed around the edges of an octahedron. By sharing the end mirrors, comparisons can be made among the other rings. A second octahedron, intermeshed in the original sensor, would provide additional information (Bosi et al., 2011).

Figure 2.7 compares the range of current experimental RLGs against the requirements for Advanced LIGO (aLIGO). Commercial RLGs are available approaching this range in roughly the $50k to $200k price range (Barbour and Schmidt, 2001).

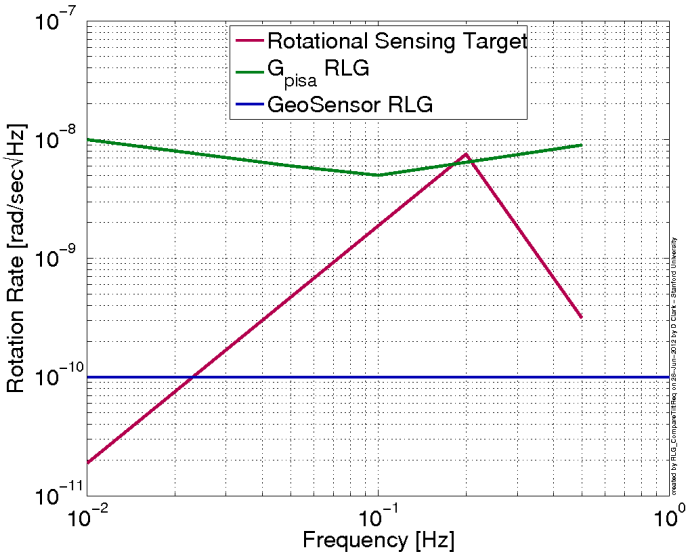

Figure 2.7: Several experimental Ring Laser Gyroscopes are plotted relative to the rotation sensing target for Advanced LIGO. The G_{pisa} ring is 1.82 m^2 and is located at the Virgo observatory (Belfi et al., 2012), while the GEOsensor is a 2.56 m^2 ring that is located in Piñion Flats Observatory (Schreiber et al., 2009). The GEOsensor has a reported sensitivity of 10^{-10} rad/s/$\sqrt{\text{Hz}}$ without a specified frequency and is assumed flat across this frequency range for comparison purposes.

2.4.1.3 Measuring $\ddot{\theta}$

Measuring $\ddot{\theta}$ and double integrating it could also provide the θ term necessary for correcting tilt-horizontal coupling in the horizontal inertial sensors. DeSalvo describes some efforts in angular accelerometer construction in (DeSalvo, 2009).

2.4.2 Horizontal Seismometers on a Pendulum

A second method to deduce pure horizontal acceleration is through the use of two horizontal accelerometers suspended on a single pendulum. This is shown in schematic form in **Figure 2.8**. It is important to note that the distance from each accelerometer

to the pivot point must be different (i.e. $L_1 \neq L_2$). The equations governing the seismometer's signals for each of the accelerometers are then listed below where ϕ is the pendulum angle relative to inertial space, x is translation of the pivot with respect to inertial space, and θ, as before, is the angle from the ground to the horizontal inertial reference axis.

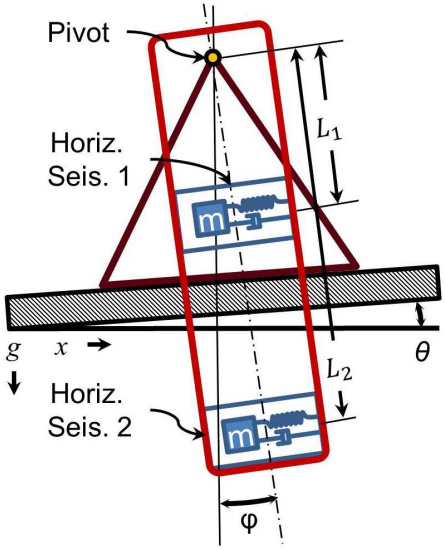

Figure 2.8: Two horizontal seismometers located on a pendulum separated by different heights. This allows the angle ϕ to be resolved and it can then be used to correct the seismometer's output to read x acceleration.

To simplify the analysis, we have chosen to use force-feedback accelerometers. This means that the proof mass of the instrument does not change position relative to the case regardless of acceleration. The individual seismometers, S_1 and S_2 then are sensitive as follows:

$$S_1 = \ddot{x}\cos\phi + \ddot{z}\sin\phi + L_1\ddot{\phi} - g\sin\phi \tag{2.11}$$

Now assuming small angles of ϕ so that $\sin a \approx a$ and $\cos a \approx 1$ this linearizes to:

$$S_1 = \ddot{x} + \ddot{z}\phi + L_1\ddot{\phi} - g\phi \tag{2.12}$$

Similarly S_2 differs only in the length from the pivot to the seismometer and is:

$$S_2 = \ddot{x} + \ddot{z}\phi + L_2\ddot{\phi} - g\phi \tag{2.13}$$

If these two seismometer signals are subtracted, then most of the terms drop out leaving the following expression for $\ddot{\phi}$:

$$\ddot{\phi} = \frac{S_1 - S_2}{L_1 - L_2} \tag{2.14}$$

From this it is clear that a large separation distance between instruments is helpful. There is a practical limit, however, in the physical size and in the ability to create suitably stiff structures.

Once $\ddot{\phi}$ is known, it can be used in either of the seismometer signals to calculate $\ddot{x}$ assuming the $\ddot{z}\phi$ term is negligible such as:

$$\ddot{x} = S_1 - L_1\ddot{\phi} + g\phi \tag{2.15}$$

$$\ddot{x} = S_1 - L_1 \cdot \frac{S_1 - S_2}{L_1 - L_2} + g \cdot \int\int \frac{S_1 - S_2}{L_1 - L_2}\, dt^2 \tag{2.16}$$

So instead of measuring ground tilt θ, this method relies on the measurement of an artificial angle ϕ, which is the pendulum angle relative to local g and subtracting this tilt effect from the accelerometer signals.

The equation of motion of the pendulum can then be written as the sum of the individual torques, τ about the pivot, where I is the moment of inertia of the pendulum (including the seismometers) about the pivot point.

$$\sum \tau = I\alpha \tag{2.17}$$

The length to the total pendulum center of mass is denoted L_p. Also, in this equation $\alpha = \ddot{\phi}$, which is the angular acceleration about the pivot. In the case of the pendulum the torques include the weight of the pendulum, horizontal acceleration of the ground at the pivot (which can be modeled as horizontal acceleration of the pendulum in the opposite direction), and the difference in the pendulum angle ϕ, and the ground tilt θ multiplied by the pivot flexure stiffness. This results in:

$$\ddot{x} m_{pend} L_p \cos\phi - g m_{pend} L_p \sin\phi - k_{pivot}(\phi - \theta) = I\ddot{\phi} \tag{2.18}$$

From this the coupling of ground tilt θ and ground horizontal acceleration $\ddot{x}$ to pendulum angle ϕ can be determined where:

$$\frac{\phi(s)}{\theta(s)} = \frac{k_{pivot}}{Is^2 + (gm_{pend}L_p - k_{pivot})} \tag{2.19}$$

$$\frac{\phi(s)}{x(s)} = \frac{m_{pend}L_p s^2}{Is^2 + (gm_{pend}L_p - k_{pivot})} \tag{2.20}$$

If such an instrument were to be constructed, a well defined flexure or other precision pivot should be used. Flexure arrangements provide other options as to the virtual pivot point that can be located far above or below the actual geometrical constraints of the instrument. The flexure stiffness relates coupling of θ to ϕ. This can be imagined in the two limit cases. Firstly, if $k_{pivot} = \text{inf}$, then the pendulum angle ϕ must track the ground tilt θ. This results in a design that is simply two vertically separated horizontal seismometers. Note that this case is similar to horizontally separated vertical seismometers as described in Section 2.4.3. In the other extreme, when $k_{pivot} = 0$ ground tilt θ cannot couple into the system at all. This is desirable but cannot be implemented.

Since ground tilt θ could be much larger than the horizontal ground acceleration $\ddot{x}$, a low k_{pivot} (and natural frequency of the pendulum) allows mechanically filtering out of the ground tilt signal from the sensors. Research on a system with the same objective is currently being conducted at Massachusetts Institute of Technology (MIT) (Matichard, 2012). This is illustrated in the following example.

Assume a pendulum system were built using two Trillium T-240 seismometers mounted with an $L_1 = 0.25$ m and $L_2 = 1.25$ m on a pendulum structure that has a mass of 10 kg. The supported mass is then 38 kg. Then, for convenience, we assume a flexure design adopted from the design as described in Appendix A. A suitable round notch flexure could be made from beryllium copper with a notch diameter of 0.5 in. (12.7 mm), a web thickness of 0.001 in. (0.025 mm), and a length of 1.0 in.

(25.4 mm). This flexure provides a static safety factor of 9 and allows the pendulum angle ϕ to swing up to $\pm 18\,^{\circ}$. Using these numbers, the transfer function from θ to ϕ becomes:

$$\frac{\phi(s)}{\theta(s)} = \frac{0.0091}{(27.96)s^2 + (9.81)(38)(0.717 - 0.0091)} \tag{2.21}$$

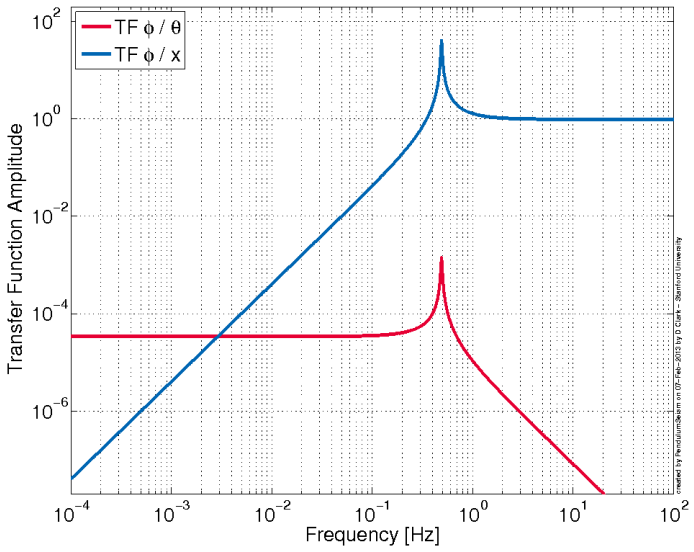

Figure 2.9: Transfer function from ground tilt θ to pendulum angle ϕ is minimized. The horizontal displacement x also affects the pendulum angle as shown.

After adding an arbitrary damping term (although reasonable based on the damping seen in the GS-13 BeCu flexures), this is then plotted in **Figure 2.9**, which demonstrates the low coupling of ground tilt onto the pendulum. At low frequencies, the decoupling is based on the k_{pivot} term. At frequencies above the pendulum natural frequency the inertia of the pendulum decouples θ. By choosing a low stiffness flexure as the pivot, the ground tilt can be mechanically decoupled by as much as $4 \cdot 10^{-5}$ in this example at frequencies below 0.1 Hz.

The ground horizontal acceleration couples in two ways, one is displayed here, which is that $\ddot{x}$ affects the pendulum angle ϕ. The other way couples directly into the sensor signal as was shown above in Equation 2.12.

For this example system, assuming an instrument noise equivalent to the measured

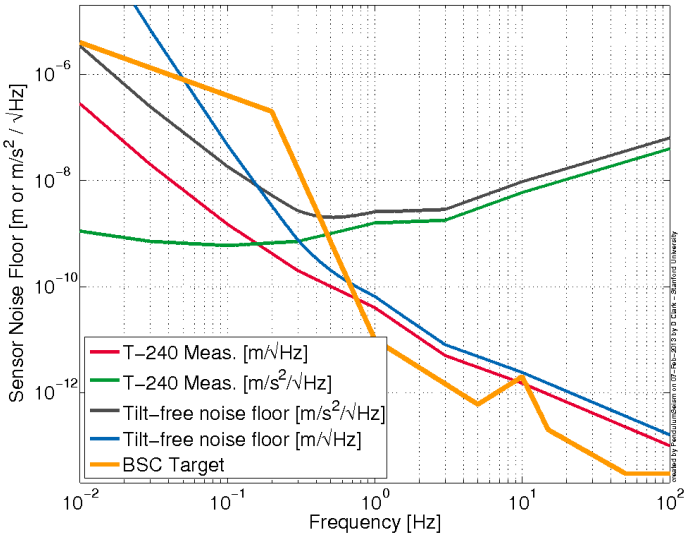

Figure 2.10: Noise performance of the described example system relative to the performance target in the x axis.

noise of the T-240 seismometers as quantified in Appendix B, the system's tilt-free horizontal noise floor is predicted in **Figure 2.10**. This accounts for the instrument noise but assumes exact matching and calibration of the scale factors, which may not be stable enough over time.

Finally, the lengths L_1 and L_2 could be optimized based on the sensors' noise performance. In the example both sensors were located below the pivot but one option, increasing sensitivity, could be to set the distance L_1 to be negative (above the pivot point).

2.4.3 Horizontally Separated Vertical Seismometers

A third method relies on two or more horizontally separated vertical seismometers. Assuming these instruments are calibrated to each other, the common mode signal from the seismometers can be interpreted as the average vertical motion. However, their differential signal can be related to tilt over the lever arm of their separation. This is visually shown in **Figure 2.11**.

For the seismometers depicted in **Figure 2.11**, the instruments' responses can

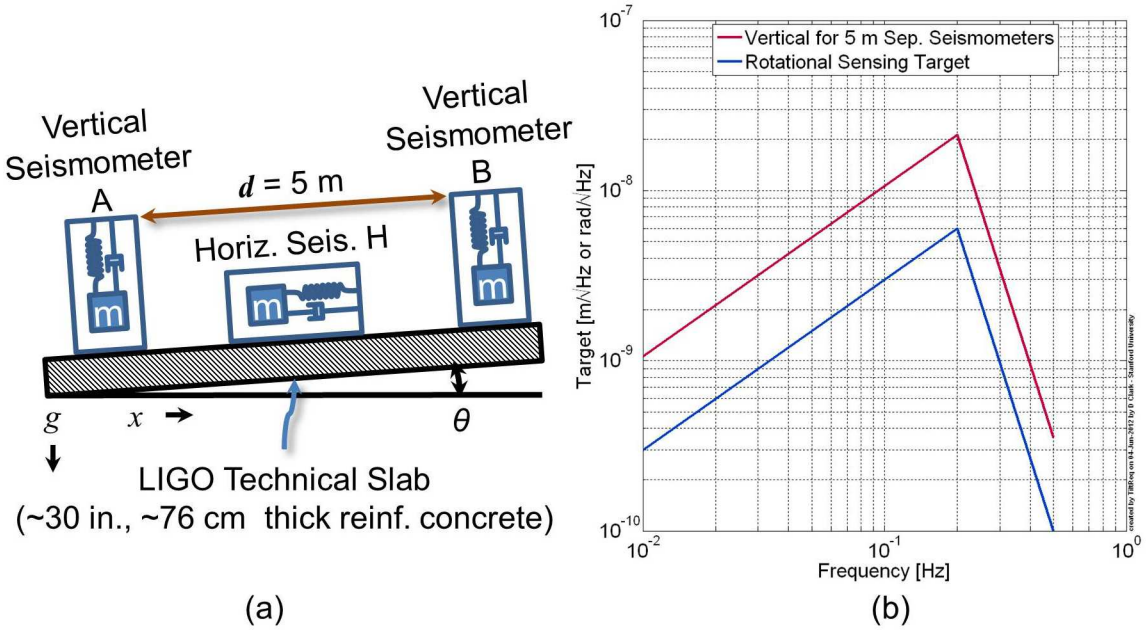

Figure 2.11: The signal from two vertical seismometers, separated by $d = 5$ m, can be subtracted from each other to resolve tilt of the slab (a). The distortions of the reinforced, technical slab must be small over this separation distance. The rotational sensing requirements to improve the aLIGO isolation systems are plotted in (b) along with the vertical motion that a seismometer would need to resolve if positioned in a configuration such as (a) (Lantz et al., 2009).

be simplified as follows where the signal is related to both a horizontal acceleration $\ddot{x}$, or a vertical acceleration $\ddot{z}$. The earth's gravitational acceleration g also couples into the seismometer output by $\sin\theta$ for the horizontal instrument and $\cos\theta$ in the vertical case.

$$S_H \propto \ddot{x} + g\sin\theta \tag{2.22}$$

$$S_{V_A} \propto \ddot{z} + g\cos\theta \tag{2.23}$$

Assuming that the rotation of the slab happens at seismometer S_{V_A}, then seismometer S_{V_B} rotates by θ but also moves vertically by the amount $z_\theta = d\sin\theta$. If we assume small angles for θ such that $\sin\theta \approx \theta$ then this additional term is added to S_{V_B}:

$$S_{V_B} \propto \ddot{z} + g\cos\theta + d\cdot\ddot{\theta} \tag{2.24}$$

Subtracting the two vertical seismometer signals allows $\ddot{\theta}$ to be solved as:

$$\ddot{\theta} = \frac{S_{V_B} - S_{V_A}}{d} \tag{2.25}$$

Which can then be double integrated to obtain θ. Once θ is known, it can be substituted in the equation for S_H yielding:

$$S_H = \ddot{x} + g\theta - g\int\int (S_{V_B} - S_{V_A})dt^2 \tag{2.26}$$

Which then simplifies to:

$$S_H = \ddot{x} \tag{2.27}$$

This result, a horizontal inertial sensor's signal that had been compensated for tilt-horizontal coupling, is exactly what is desired for control input.

2.4.3.1 Tilt-Vertical Coupling

In contrast to a horizontal seismometer's coupling that is of the form in **Equation 1.8**, a tilt-vertical coupling of θ is not so problematic. This is because earth's gravitational attraction g, couples in as a function of $\cos\theta$ in this case.

$$m(\ddot{x} - \ddot{u_{frame}}) = -b\dot{x} - kx + kx_0 - mg\cos\theta \tag{2.28}$$

Then for small θ, we can substitute $\cos\theta \approx 1 - \frac{\theta^2}{2}$ which yields:

$$m(\ddot{x} - \ddot{u_{frame}}) = -b\dot{x} - kx + kx_0 - mg(1 - \frac{\theta^2}{2}) \tag{2.29}$$

$$m(\ddot{x} - \ddot{u_{frame}}) = -b\dot{x} - kx + kx_0 - mg - mg\frac{\theta^2}{2} \tag{2.30}$$

In most vertical seismometers the offload spring force kx_0 counteracts the mg force resulting at equilibrium and can be subsequently ignored:

$$m(\ddot{x} - \ddot{u_{frame}}) = -b\dot{x} - kx - mg\frac{\theta^2}{2} \tag{2.31}$$

Finally, by taking the Fourier transform and looking at the term of interest we find that:

$$x \propto \frac{\theta^2 g}{\omega^2} \tag{2.32}$$

So if the vertical seismometers experience small tilt angles, the tilt-vertical coupling is second order (represented by θ^2) and is ignored in our further analysis.

2.4.3.2 Horizontal-Vertical Coupling

Similarly, a vertical seismometer's coupling to horizontal motion when tilted is related as:

$$m(\ddot{x} - \ddot{u_{frame}}) = -b\dot{x} - kx + kx_0 - mg\cos\theta + m\ddot{y}_{horiz}\sin\theta \tag{2.33}$$

Which, after applying the small angle approximation and the Fourier transform, simplifies to the relationship:

$$\ddot{x} \propto \frac{\ddot{y}_{horiz}\theta}{\omega^2} \tag{2.34}$$

Here the horizontal to vertical coupling is related more directly (directly proportional to changes in θ). However, if the tilt angle is assumed small, coupled with small horizontal accelerations (typically much smaller than the g that couples in to a horizontal sensor through tilt), this term likewise can be considered negligible compared to the other linear terms.

2.4.3.3 Separation Distance

The necessary separation between two vertical seismometers is determined both by the desired tilt resolution and by the individual seismometer's noise floor. This is because the tilt sensing signal is proportional to the separation distance d. If seismometers with better noise performance are used, this separation distance can be decreased while still maintaining the same level of sensing to θ. A short separation distance is preferable because with small d, it is more likely that the two seismometers (S_{V_A} and S_{V_B}) are measuring common vertical motion and common tilt. There is a concern that if the separation distance is too large, the individual seismometers will lose their correlation due to mounting surface and foundation distortion.

Lantz documents the tilt-requirement for a tilt sensor that would be necessary to meet the aLIGO ISI target requirements (Lantz et al., 2009). In **Figure 2.11**, the tilt requirement is plotted as the radian root of the mean-square spectral density vs. frequency and is compared to the displacement root of the mean-square spectral density required for two vertical seismometers at a separation distance of 5 m. **Figure 2.12** shows what the resolvable tilt would be assuming the noise characteristics for the Trillium T-240 seismometer as recorded in Appendix B.

Just as was the case for the two horizontal seismometers on the pendulum, the scale factors of the vertical instruments would also have to be calibrated to each other. This is important because if the scale factors are not calibrated, or if the calibration

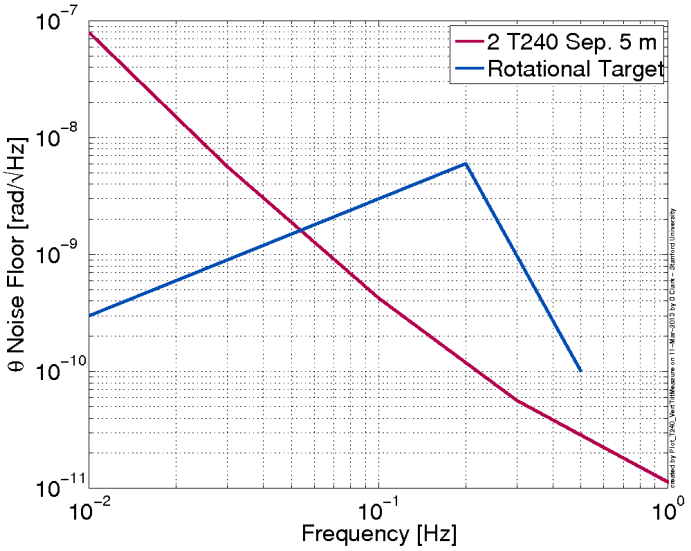

Figure 2.12: Two Trillium T-240 seismometers, if placed 5 m apart on a stiff mounting structure or foundation, would be able to resolve tilt to the levels plotted. This is compared to the requirements for a sensor as documented by Lantz (Lantz et al., 2009).

changes over time, then common mode vertical motion will appear as tilt once the seismometer signals are subtracted. It is unknown how stable the scale factors would be over time but the system should remain sensitive in the frequency range of interest if the scale factors are maintained within 0.002 of each other (Lantz et al., 2009).

So once a target sensitivity for the seismometers is quantified, the need arises to acquire a seismometer that is able to meet these requirements yet remain small, reliable, and not too costly. Ideally for aLIGO, multiple arrays of vertical seismometers would be used enabling the measurement of local tilt in both directions to provide relevant sensing for every isolation platform. One possible design for such a seismometer is explored in Chapter 3.

2.4.4 Comparison of Methods

Because of the tilt-horizontal coupling of local gravity g into the horizontal inertial sensors, aLIGO ISI subsystem's low frequency performance is limited. Several methods have been described in Sections 2.4.1, 2.4.2, and 2.4.3 of ways to extract pure

horizontal motion from these horizontal sensors. Each of the methods described has their own set of advantages and challenges as described below.

- Direct measurement of θ (Section 2.4.1.1): Experimental instruments meet the requirement at 1 Hz but the low frequency performance is unclear. It is hard to estimate what the costs would be for this type of sensor.

- Direct measurement of $\dot{\theta}$ (Section 2.4.1.2): The GEOsensor meets the requirement for aLIGO down to 0.022 Hz although might be difficult to operate for on-line measurements due to mode hopping of the laser in the cavity approximately once every hour. The cost is unknown, although a large 51 m^2, less sensitive, ring laser was estimated to cost \$16k in 2004 (Dunn et al., 2009).

- Direct measurement of $\ddot{\theta}$ (Section 2.4.1.3): This work on a dumbbell style sensor is ongoing with experimental sensitivities yet to be documented (DeSalvo, 2009).

- Two horizontal seismometers separated vertically on a pendulum (Section 2.4.2): If commercial low frequency seismometers were used as sensors, the cost would be in the \$35k range and could be expected to provide useful data meeting the requirements above 50 mHz range.

- Two horizontally separated vertical seismometers (Section 2.4.3): If two commercial, low frequency sensors were used on a suitable structure, tilt could be resolved to the aLIGO requirement for frequencies above 0.055 Hz at an approximate cost of \$30k.

Of the methods described, we decided to pursue the method in Section 2.4.3 by designing a cost effective vertical seismometer as described in Chapter 3.

Chapter 3

A Vertical Seismometer Design for Tilt Sensing

Seismometers, by necessity, are precision instruments. As such, careful attention must be paid in the design stage in order for them to reach the sensitivities required. In our case, we would like a seismometer design that would allow us to measure ground tilt, θ where two vertical seismometers are separated spatially as described in Section 2.4.3. In this case, the maximum sensitivity to θ is set by the largest separation distance between seismometers where the ground slab still behaves as a contiguous base. Also, since the tilt that the seismometers must detect is at low frequency, the seismometers must be sensitive to low frequency motion. In practice for aLIGO this is most critical in the range of about 10 mHz to 1 Hz.

In order for a sensor to be useful to aLIGO, it must be cost effective, robust, stable, meet the required sensitivity, and minimally couple in disturbances from the surrounding environment. The environmental disturbances could include things such as magnetic fields, temperature, pressure, acoustics, etc. As is the case in the design of many precision machines, design trades must be made to optimize it to the requirements. For example, Invar, a material well known for its good dimensional stability over a range of temperatures, has slight magnetic susceptibility. Trades such as these are discussed in the context of a new seismometer design.

Most vertical seismometers have a few universal items. These include the proof

mass, which becomes the reference to inertial space, a biasing mechanism to counteract the mg force due to the earth's gravitational acceleration, and a constraint mechanism to constrain the proof mass to move only in the desired direction.

In any seismometer, the proof mass is the critical part providing the point of reference. Often the position, velocity, or acceleration measurements are between the instrument's structure and this proof mass. For a vertical seismometer, ideally the proof mass would only be acted upon by the force through the vertical motion of the support structure and the offload springs. This is not always the case. However, fortunately some of the couplings are second order or very small such as the tilt-vertical coupling.

Buoyancy on the proof mass, however, is one force to which most vertical seismometers are susceptible and is coupled by the following: $F_{\text{buoyancy}} = V_{\text{pm}}\rho_{\text{air}}g$ where V_{pm} is the volume of the proof mass. This means that the buoyant force exerted on the proof mass changes with changes in air density, ρ_{air}. Some vertical seismometers are placed in a vacuum chamber, which reduces this coupling such as the extremely sensitive Streckeisen STS-1 (Wielandt and Streckeisen, 1982). In the interest of cost and space efficiency, we propose a novel vertical seismometer design that in theory is immune to fluctuations in air density.

As illustrated in **Figure 3.1**, if a proof mass for a vertical seismometer is constructed such that the center of mass and center of geometry are separated, then the two forces can also be separated. This is because inertially the point of reference is the center of mass, whereas F_{buoyancy} acts on the volumetric center or centroid of the proof mass. Moreover, if the proof mass is constrained to rotation instead of translation, then the centroid can be collocated at the pivot location (reducing r_{buoyancy} to 0). This means that any variations in F_{buoyancy} are supported by the seismometer's structure. If the pivot point and the centroid are exactly collocated and assuming a suitably stiff structure, air density changes will not be coupled into the sensor.

In the actual implementation it is not possible to have an entirely loss-less, zero stiffness, rotational pivot. However, there are better ways to implement it than others. Precision instrument designers have long used flexures to avoid stick-slip that is inherent with typical bearings (Smith, 2000). This design lends itself well to a type

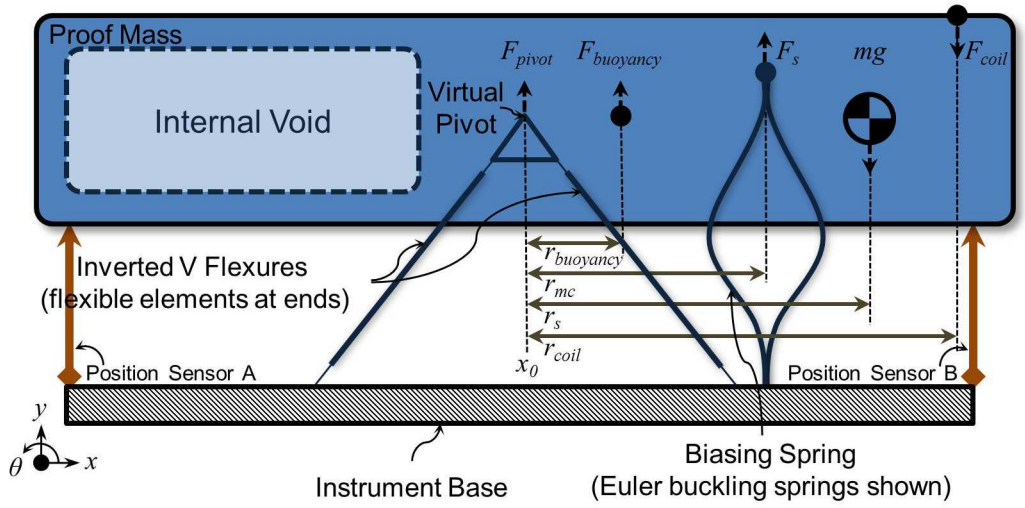

Figure 3.1: A vertical seismometer concept showing a method to decouple the center of mass from the centroid of the proof mass. Then, if the centroid of the proof mass is designed to be at the virtual pivot point, the instrument becomes immune to variations in atmospheric pressure affecting ρ_{air}.

of cross flexure where the end and pivot points are well constrained and accurately defined.

Perhaps the biggest possible disturbances come from changes in temperature. While it would be ideal to remove any temperature changes on the instrument, this might not be practical from a cost and size standpoint for an array of multiple seismometers for tilt sensing. These temperature fluctuations have the potential to couple in several ways and must be either reduced or characterized in the design. Firstly, most engineering materials have a non-zero coefficient of thermal expansion (CTE). Secondly, temperature gradients in the structure can distort the structure, often to a greater degree than the problems introduced by simple expansion. This often introduces stresses and if care is not taken in the design of the metrology loop, can often lead to temperature induced Abbè offset errors. Thirdly, in addition to most materials changing their size with temperature, the Young's modulus, E is also affected by temperature. This dE/dT is often a problem in biasing springs counteracting the mg force due to earth's gravity in vertical seismometers. For example, the Young's modulus of BeCu is reported to change by $-350 \cdot 10^{-6}/°\text{C}$ contrasted with a coefficient of

thermal expansion of $17 \cdot 10^{-6}/°\text{C}$ (CDA, 1962).

Vertical seismometers need a biasing method to carry the zero frequency mg force. While coil springs perhaps first come to mind, they have several disadvantages. These include, among other things, a torque applied about the longitudinal axis at the spring ends (often a function of their displacement) and several natural frequency internal modes. For the seismometer, two biasing springs were investigated. One method involves a curved flexure strip spring while the other method utilizes an Euler buckling spring.

3.1 Prototype Seismometer

A prototype vertical seismometer has been constructed and tested in the Stanford Engineering Test Facility (ETF). A proof mass of 8.9 kg was machined out of brass stock with an internal void created near one end. This void separated the centroid of the bar from the center of mass by about 1 in. (25.4 mm). Brass was chosen as the material for the prototype because of its ease of machining, low susceptibility to magnetic field, high density, and high thermal conductivity. Finally, since the prototype was intended to operate in air, strict vacuum compatibility requirements were not a concern. **Figure 3.1** shows a mechanical schematic of the prototype seismometer.

This proof mass was then constrained to rotation about the centroid by a set of four BeCu flexures. Flexures were chosen to support the mass over other bearings and methods because of their high repeatability and the lack of stick-slip nonlinearities other systems are prone to. BeCu has long been a material of choice for situations with high strain and has been desirable for precision instrument design where susceptibility to magnetic field is a concern. Two of these flexures were combined in an inverted V fashion to support each side of the proof mass bar. Each of the flexures combined two flexible portions - one on each end. It then follows that each inverted V configuration, composed of two flexures, is only rotationally flexible about the z-axis and stiff in all other degrees of freedom. The clamped ends are arranged in such a way as to project the inverted V to a virtual pivot point. The geometry constraints were such that

along with rotation about that pivot, some slight, second order vertical displacement also occurs. The virtual pivot location is plotted as a function of proof mass angle γ in **Figure 3.2**.

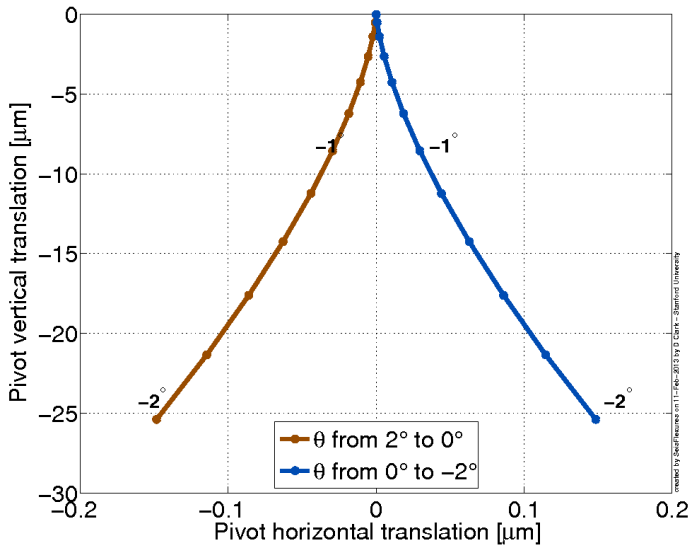

Figure 3.2: The prototype seismometer utilizes flexures to constrain the proof mass to rotation about a virtual pivot. Plotted here is the calculated second-order motion of the virtual pivot in the $x - y$ directions for various angles of the proof mass γ. Note the unequal axis scales.

Since there are two stacked inverted V flexure groups, care had to be taken in the construction to avoid over constraint of the proof mass. The flexures used in the prototype were wire electro-discharge machined (EDM) from BeCu sheet. The wire EDM was helpful in maintaining close tolerances and reducing any sheared edge and micro-burrs that might result from more traditional cutting methods.

For low frequency operation, it is important to have a seismometer with a low natural frequency. In the case of the prototype this natural frequency can be expressed in the form $\omega_n = \sqrt{\frac{k_{total}}{I_{pivot}}}$ where k_{total} is rotational stiffness and I_{pivot} is the rotational inertia about the pivot. The rotational stiffness is the sum of the flexure stiffness and the bias spring stiffness. It follows that for a low natural frequency and a fixed rotational inertia it is helpful to have a low stiffness for the proof mass bias springs.

One method to provide the biasing is through a flexible spring strip. This would

be cut from a suitable material in the shape of a rectangle and then bent with both ends attached in clamps. One end would attach to the proof mass and the other end would attach to the seismometer frame. Using the dimensions from the prototype seismometer for example, this can be analyzed as follows:

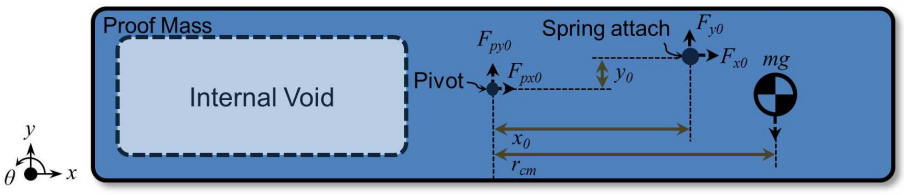

Figure 3.3: Spring strip attachment point relative to the pivot point and center of mass.

Setting arbitrary attachment points for the spring and variables defined in **Figure 3.3** to form a general solution, the forces and moments can be summed as follows.

$$\sum F_x = 0 = F_{px0} + F_{x0} \tag{3.1}$$

$$\sum F_y = 0 = F_{py0} + F_{y0} - mg \tag{3.2}$$

$$\sum M = 0 = M_0 + M_{p0} + F_{y0}x_0 - F_{x0}y_0 - mgr_{cm} \tag{3.3}$$

The end conditions can then be set so that the pivot point is not subject to a horizontal force. $F_{px0} = 0$ so then F_{x0} must also be 0. F_{py0} can be set to carry a slight fraction of the mg force to put the support flexures under slight tension (denoted β). This leads to $F_{y0} = mg - F_{py0}$ and after substitution, $F_{y0} = mg - \beta mg$. M_{p0} was also chosen to be 0 which results in $M_0 = -F_{y0}x_0 + mgr_{cm}$.

This leads to the starting end conditions for the spring strip which can then be defined as:

$$F_{sx0} = -F_{x0} = 0 \tag{3.4}$$

$$F_{sy0} = -F_{y0} = \beta mg + mg \tag{3.5}$$

$$M_{s0} = -M_0 = F_{y0}x_0 - mgr_{cm} \tag{3.6}$$

If the launch angle of the spring strip is defined to be vertical, the geometry of the spring can be determined by integrating back along the spring. This is useful because the resulting attachment location of the spring to the instrument frame can be determined analytically.

The shape is obtained by realizing that for a given point on the spring,

$$M_s = M_0 + F_{x0}(y - y_0) - F_{y0}(x - x_0) \tag{3.7}$$

and

$$M_s = EI\frac{d\theta}{ds} \qquad \tan\theta = \frac{dy}{dx} \qquad \sin\theta = \frac{dy}{ds} \qquad \cos\theta = \frac{dx}{ds} \tag{3.8}$$

Some resulting steel spring strip geometries of the specified dimensions are shown in **Figure 3.4**. The final conditions were set such that the spring strip was clamped to both the structure and the proof mass vertically. This does not have to be the case, however, as the conditions for other spring strip launch angles could easily be solved with this analysis. Other end conditions could be helpful in minimizing the overall size of the instrument. Once solved, the attachment points can be easily located on an instrument. Since the loaded profile, as shown in **Figure 3.4**, is already known, a rectangular spring strip can be cut with the corresponding width, thickness, and length. The necessary clamp points for the spring strip are also clearly defined, which would further simplify instrument assembly.

Other methods to reduce the natural frequency of the system still require that the same mg force on the proof mass be supported. Reducing the F/x slope, which is the spring constant, improves the natural frequency. One method to reduce this is to employ springs and anti-springs (Chin et al., 2005). Other anti-spring development

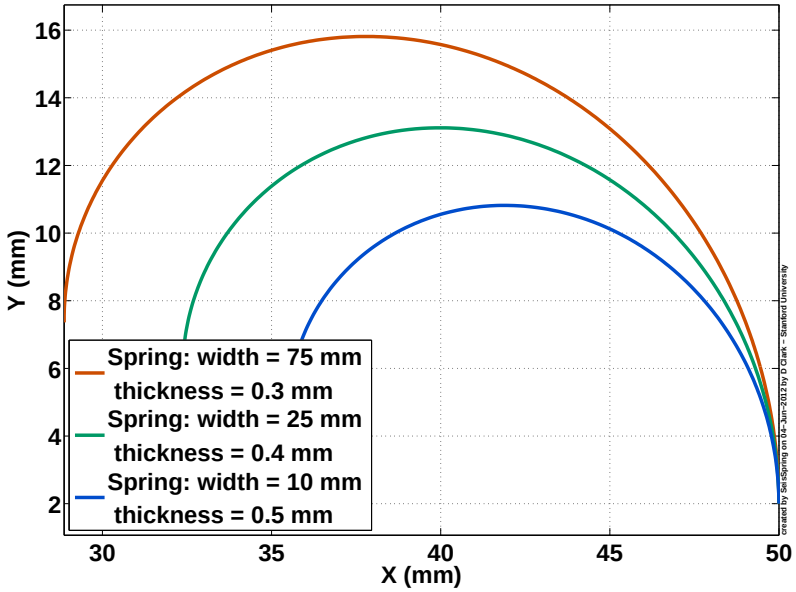

Figure 3.4: The curves shown above would provide the force and moments necessary on the proof mass to offload the mg force. The strips would be cut from sheet stock of a suitable material with the thickness and width as shown in the legend. The required length of the spring strip can be determined from this graph with the clamp locations easily defined. This analysis allows the attachment point to be determined for a given rectangular spring geometry and end conditions such as launch angles.

work to reduce the natural frequency was accomplished for an early LIGO seismic isolation prototype using Geometric Anti-Springs (GASs) described by Mantovani (Mantovani and DeSalvo, 2005) with hysteretic measurements reported in (DeSalvo et al., 2005) and improvements to the GAS in (Stochino et al., 2007). An overview of the prototype platform is provided in (Stochino et al., 2009). Alternatively, the base of the spring could be positioned such that the spring force is not directed exactly opposite of the mg force but rather interacts with the geometry and constraints of the proof mass. These options are sketched in **Figure 3.5**.

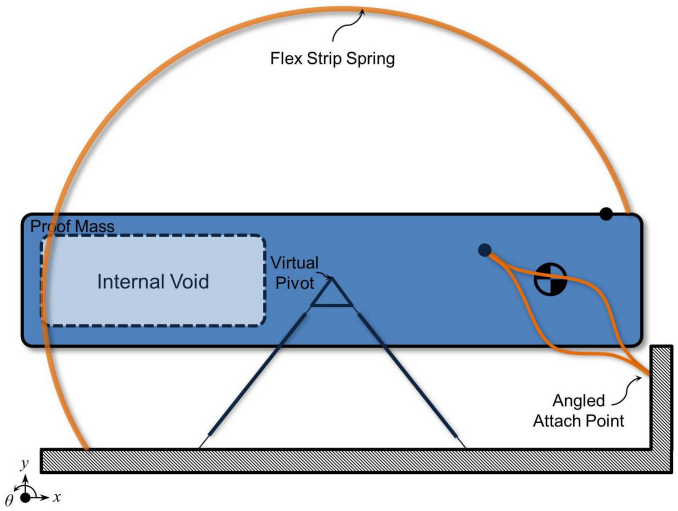

Figure 3.5: Possible spring biasing options for low natural frequencies. One option is to use a spring strip tuned to the correct end conditions and evaluated as shown in Figure 3.4. The other method would involve rotating the spring base up so that the spring acts against the pivoting constraints of the proof mass.

The method ultimately used for biasing the proof mass in the prototype seismometer was a set of four Euler buckling springs. These were created by placing wire EDM cut BeCu strips in compression to a point after Euler buckling but still in elastic deformation. These springs are unique in that their F/x curve is not linear; initially the curve is extremely steep until buckling and then changes to a shallow slope. This allows these springs to carry a high bias force while still exhibiting a low effective spring constant. These springs have been studied by Winterflood and others providing an in-depth analysis and application of these springs for seismic isolation purposes

(Winterflood et al., 2002a), (Winterflood et al., 2002b) and (Winterflood, 2001). An overview of different biasing techniques including nonlinear springs is provided by Ibrahim (Ibrahim, 2008).

Sensing of the ground disturbance by seismometers can be accomplished either passively or actively. The passive readout scheme simply measures the proof mass position, velocity, or acceleration relative to the instrument structure. The active method involves sensing the proof mass position, velocity, or acceleration and then centering the proof mass through a feedback loop. It is this feedback drive to the proof mass that corresponds to the ground disturbance. An advantage of the active readout is that the proof mass is constrained to a smaller range of motion increasing linearity and dynamic range. The prototype seismometer sensed the proof mass angle through a differential pair of optical-shadow position sensors at opposite ends of the mass. Feedback was provided by a voice coil that acted on a permanent magnet affixed to the proof mass. The structural and metrology loops of the instrument are shown in schematic form in **Figure 3.6**.

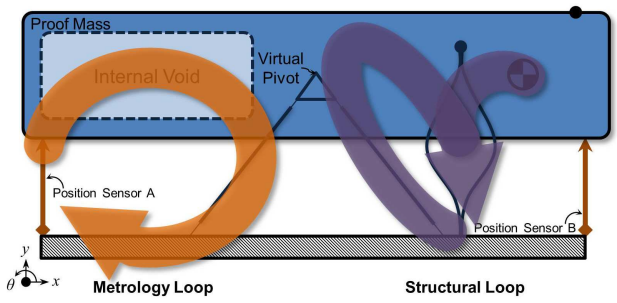

Figure 3.6: The metrology loop forms about the proof mass, supporting flexures, and base of the prototype seismometer returning to the optical-shadow position sensor (left half highlighted in orange). The structural loop that includes the biasing springs and the support flexures carries both the mg load and the disturbances (right and shown in purple). The common path for these loops is through the support flexures.

Referencing **Figure 3.1**, the equations of motion for this type of seismometer are as follows where θ_{gnd} is the ground angle, γ is the angle of the proof mass relative to the frame (defined in the same direction as θ_{gnd}), b is the pivot damping, and m is the proof mass:

$$I\ddot{\gamma} = \sum M_{pivot} \tag{3.9}$$

$$I\ddot{\gamma} = F_s r_s - mgr_{mc} + F_{coil} r_{coil} - k_{pivot}\gamma + k_{pivot}\theta_{gnd} + F_{buoyancy} r_{cob} - b\dot{\gamma} + F_{gnd} r_{mc} \tag{3.10}$$

Substituting ma for the F_{gnd}:

$$I\ddot{\gamma} = F_s r_s - mgr_{mc} + F_{coil} r_{coil} - k_{pivot}\gamma + F_{buoyancy} r_{cob} - b\dot{\gamma} + mr_{mc}\ddot{y}_{gnd} + k_{pivot}\theta_{gnd} \tag{3.11}$$

Then by mechanical design r_{cob} is set to zero and analyzing with no feedback:

$$I\ddot{\gamma} = F_s r_s - mgr_{mc} + F_{coil} r_{coil} - k_{pivot}\gamma - b\dot{\gamma} + mr_{mc}\ddot{y}_{gnd} + k_{pivot}\theta_{gnd} \tag{3.12}$$

Then because the moment of inertia, I, is at the hinge axis instead of at the mass center, the parallel axis theorem applies and yields:

$$I = I_{mc} + mr_{mc}^2 \tag{3.13}$$

Now F_s for small angles is $\gamma k_s r_s$ and assuming that mgr_{mc} is offset by the spring,

$$I\ddot{\gamma} = \gamma K_s r_s^2 - mgr_{mc} + F_{coil} r_{coil} - k_{pivot}\gamma - b\dot{\gamma} + mr_{mc}\ddot{y}_{gnd} + k_{pivot}\theta_{gnd} \tag{3.14}$$

Collecting terms:

$$I\ddot{\gamma} + b\dot{\gamma} + (k_{pivot} - k_s r_s^2)\gamma = mr_{mc}\ddot{y}_{gnd} + k_{pivot}\theta_{gnd} \tag{3.15}$$

And converting to the transfer function form:

$$\frac{\gamma}{y_{gnd}} = \frac{mr_{mc}s^2}{Is^2 + bs + (k_{pivot} - k_s r_s^2)} \tag{3.16}$$

The prototype actually utilizes position sensors at the ends of the proof mass so the displacement at the end can be converted to γ for small angles as $\gamma = x_{sensor} r_{sensor}$.

Substituting this yields:

$$\frac{y_{sensor}}{y_{gnd}} = \frac{m r_{mc} s^2}{I r_{sensor} s^2 + b r_{sensor} s + (k_{pivot} r_{sensor} - k_s r_s^2 r_{sensor})} \tag{3.17}$$

Assuming the parameters of a seismometer results in a magnitude Bode plot as shown in the top of **Figure 3.7** (the geometrical values chosen were similar to the prototype but with an arbitrarily lower natural frequency of 0.15 Hz). Using this response, an instrument sensitivity noise floor can be calculated. Assuming that the 0.25 mm range aLIGO capacitive position sensor could be used to measure the proof mass on each end at $r_{sensor} = 6$ in. (15.2 cm) from the virtual pivot, the noise floor of vertical motion can be calculated since the sensor noise is documented in (Lantz, 2009d). Then assuming that two such instruments were located 5 m from each other, the position readout sensor noise can be plotted in terms of rotation noise against the requirement (**Figure 3.7** lower plot). In this example, the seismometer is not quite sensitive enough to reach the lower frequency end of the target. Reducing the natural frequency or increasing the gain would help. By mounting both instruments on a suitably stiff structure, an assumption in this analysis, θ_{gnd} is common mode between the instruments and itself is not contained in the difference signal. The θ_{gnd} is obtained, though, from the differential y_{gnd} information.

3.2 Results

The completed prototype seismometer (shown in **Figure 3.8**) was then operated in the active feedback mode and validated against a commercial Geotech S-13 seismometer. For the tests, both instruments were installed in a vault prepared in the floor of the Stanford Hansen Experimental Physics Laboratory, End Station II. The S-13 is a 1 Hz natural frequency seismometer utilizing a velocity readout coil. The prototype seismometer had a natural frequency of about 0.7 Hz for this data. The spectra of the two instruments are compared to each other in **Figure 3.9** along with the coherence.

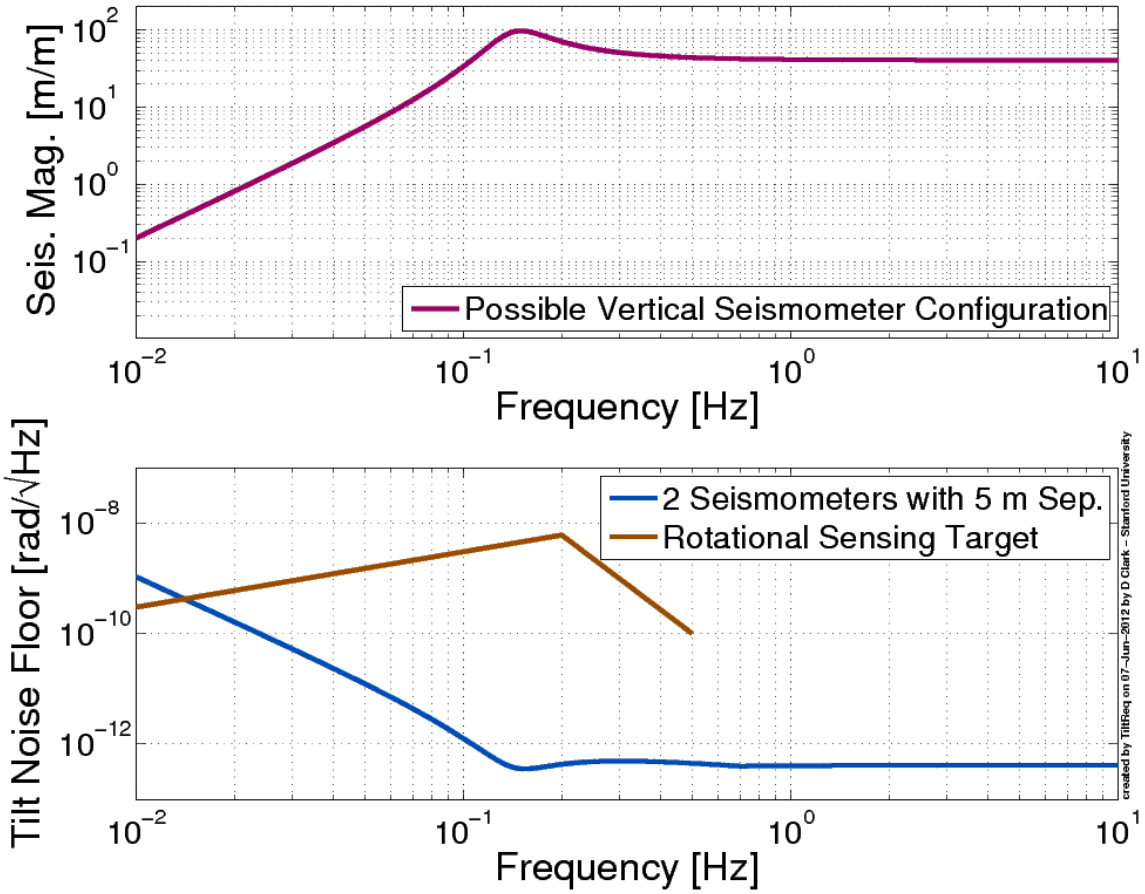

Figure 3.7: Assuming a ground motion to seismometer sensor motion magnitude transfer function as shown above, the noise floor for a given sensor can be converted to rotational sensitivity. This is plotted below along with the rotational target curve.

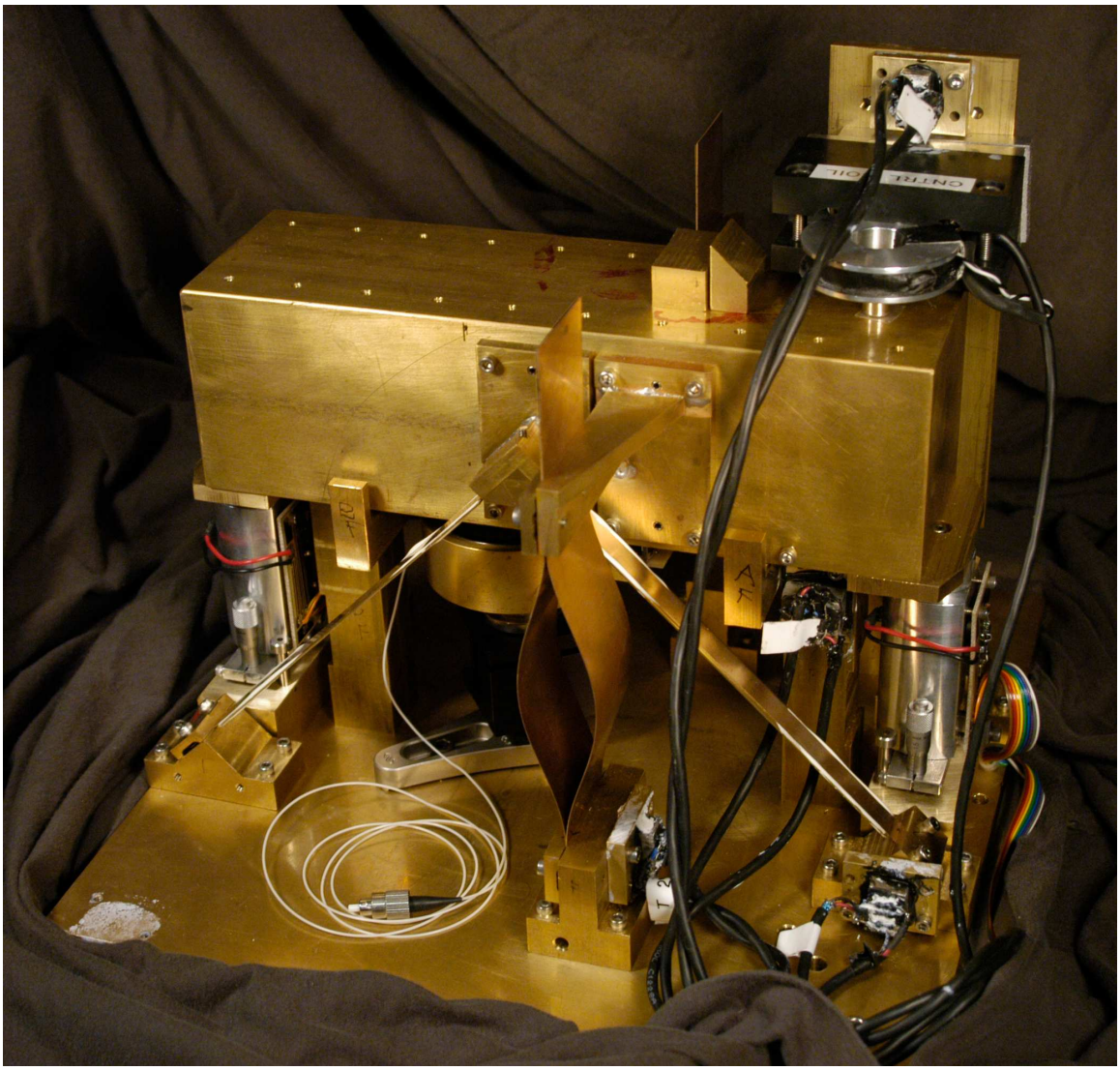

Figure 3.8: Picture of the vertical seismometer prototype as constructed.

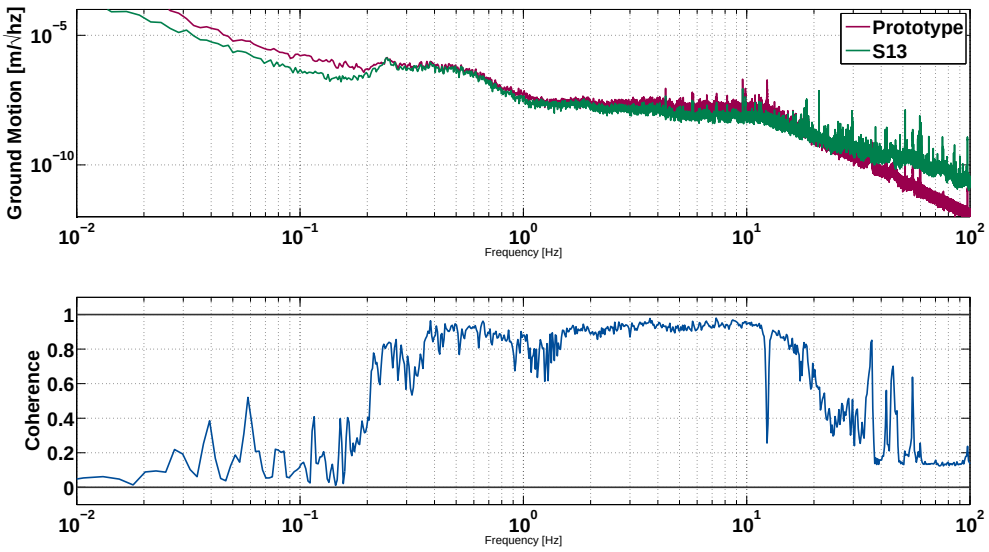

Figure 3.9: Measured amplitude spectral density plot of the Stanford HEPL End Station 2 vault. The prototype vertical seismometer compared to a Geotech S-13 seismometer.

A magnitude 5.4 Mw earthquake on the northern California coast (USGS Event Code: nc40193932) was also recorded by the prototype and is plotted in **Figure 3.10**.

Temperature proved to strongly couple into the seismometer signal as displayed in **Figure 3.11**. The building heating, ventilation, and air conditioning (HVAC) swings are obvious in the time series data as well as a lower frequency drift. The upper plot in **Figure 3.12** shows a shorter time series of the witness S-13 seismometer and the control signal required to keep the proof mass of the prototype vertical seismometer centered. On the lower plot, one of the temperature sensors and the pressure sensor are plotted. In the pressure trace it is detectable when the laboratory building personnel access door is opened (seen as reductions in pressure spikes) yet these are not readily detectable in the seismometer trace. While the total atmospheric pressure can also be seen to slowly rise over the length of the recording it is difficult with this data to prove that there is no pressure coupling to seismometer signal.

The seismometer signal is, however, strongly coupled to the temperature trace, as mentioned earlier. What follows is an investigation of temperature induced noise and

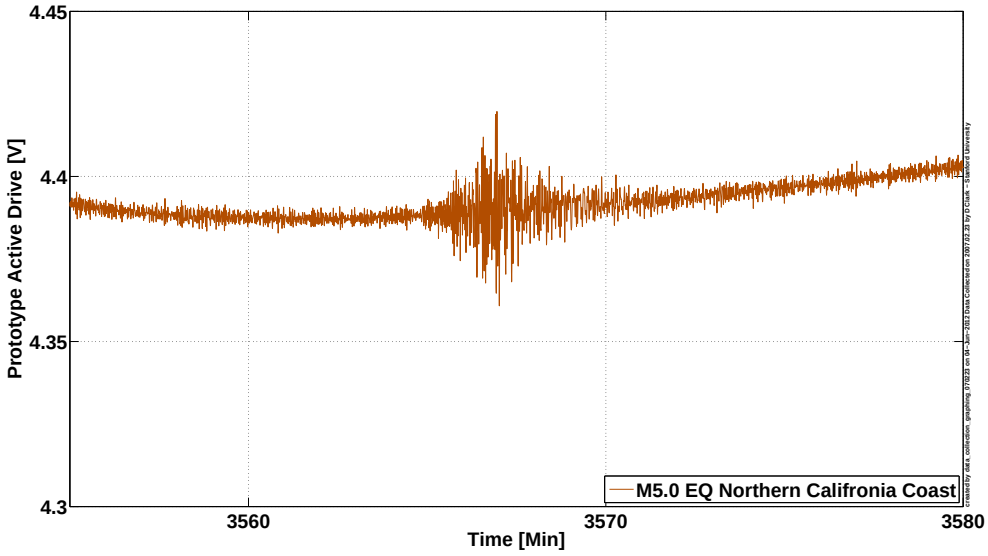

Figure 3.10: Vertical seismometer prototype recording of a 5.4 Mw northern California earthquake.

methods to compensate or correct for this.

Insulation of the instrument can help reduce the effect by low-pass filtering the temperature fluctuations to frequencies below those of interest. However, this becomes increasingly difficult as the lowest frequency for a tilt-sensing seismometer is in the range of 10 mHz. At these frequencies, it is unlikely that insulation alone would be practical.

Since a large proportion of the temperature coupling is likely through the dE/dT of the bias springs, other materials were investigated. There are many well-known alloys that exhibit low or matched coefficient of thermal expansions (CTEs) (dL/dT) such as Invar, and other superalloys but finding zero to low dE/dT materials is more difficult. One material, Ni-Span-C is purported to have a flat dE/dT curve at room temperature (SMC, 2004). The slope can actually be tuned slightly positive or negative by changing the composition. One drawback to Ni-Span-C is that it is not as immune to magnetic disturbances as BeCu. It was also difficult to locate sheet stock in small quantities for testing.

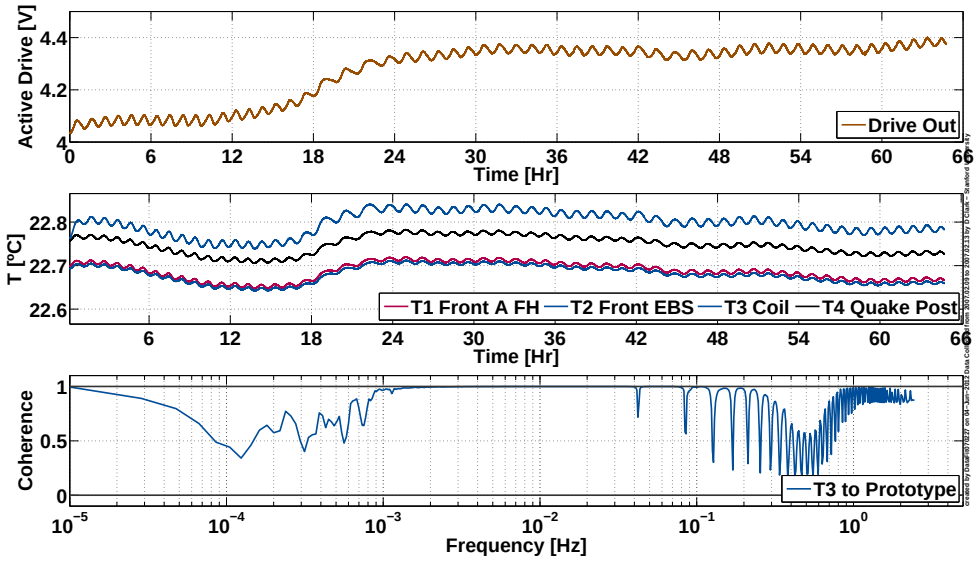

Figure 3.11: The vertical seismometer active control signal required to keep the proof mass centered is visibly very similar to the four temperature sensor signals. The building HVAC system induced temperature swings are quite visible rippling throughout the entire time period.

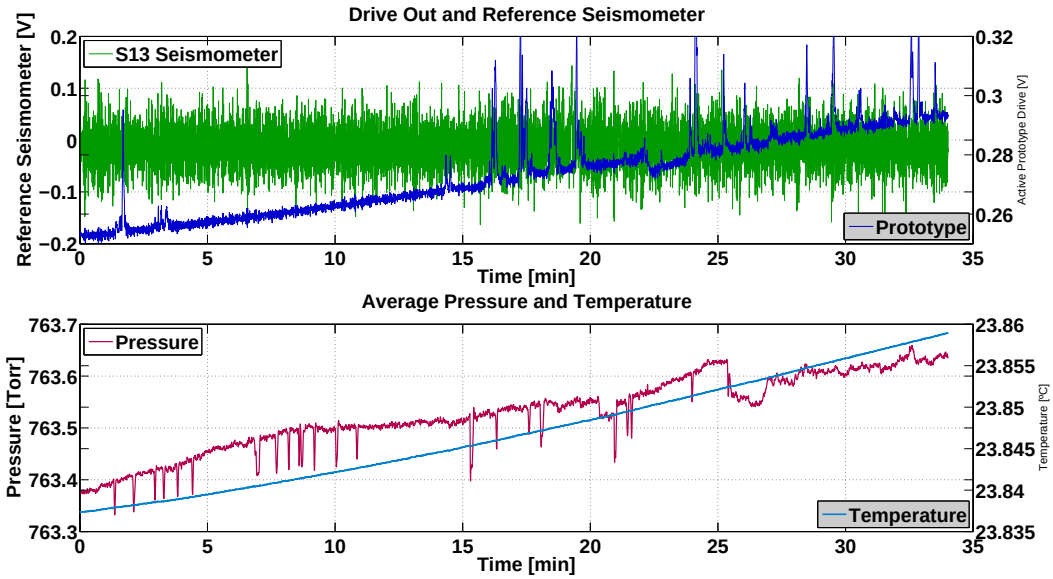

Figure 3.12: The vertical seismometer active control signal plotted with the S-13 witness signal. The temperature and pressure are plotted below.

Other methods to correct for the spring sag with temperature would be to compensate the springs themselves by combining them with other materials with different coefficients of thermal expansion, or altering the spring attachment points in a way that alters the position or orientation as a function of temperature. It is unclear how this can be accomplished while still maintaining isolation to magnetic disturbances.

The overall expansion of the instrument as a function of temperature is likely to be less of a concern because of the differential sensing of the proof mass position. Temperature gradients could certainly be problematic though. For the prototype seismometer, temperature gradients were reduced through the use of brass (with a high heat conductivity) and limited contact points (three spheres) between the base of the instrument and the ground.

These are all methods to reduce the effect of temperature on the instrument. Another less elegant solution is to measure the temperature and characterize the instrument's response as a function of temperature. The effect of the temperature on the instrument's signal could then be predicted and subtracted.

3.3 Conclusion

The prototype seismometer, as built, demonstrated several techniques that could be utilized in creating a cost-effective, low frequency, vertical seismometer for ground tilt measurements. The decoupling of air pressure variations is one novel way that helps this style of instrument to meet these goals. While the prototype did not have an adequately low noise floor to be useful in this sense, if the instrument were developed fully, an array of such sensors could provide the necessary information to correct the tilt-horizontal coupling of the aLIGO seismic isolation system horizontal seismometers. This in turn could lead to lower blend frequencies and higher isolation levels at low frequencies.

While being able to measure ground tilt, θ, and then correct for tilt-horizontal coupling in the inertial sensors is fundamentally very interesting, there are three reasons why this research was not continued. Firstly, the development time-line, roughly estimated at 5 years, would have to be expedited in order to benefit aLIGO. Secondly, the required instrument sensitivity for the examples was assuming a horizontal separation distance of 5 m. It is unclear how reasonable it is to assume a stable mounting structure that would allow for this separation distance, especially when the chambers themselves may be tilting on the technical slab. Of course, reducing this distance would require more sensitive instruments which easily complicates the design. Even small changes in temperature across the concrete technical slab at the observatories would induce localized tilt. For example, assuming a technical slab thickness of $t = 0.75$ m and a CTE of the concrete to be similar to steel, temperature differentials of 13 mK across the thickness of the slab are estimated to induce an angle of approximately 1 μrad across 5 m. Thirdly, measuring the differential displacement between adjacent optical platforms and then controlling them to track each other at low frequency sidesteps the problems caused by the tilt-horizontal coupling. This concept was subsequently pursued in the design and implementation of a prototype sensor and is the basis for the rest of this thesis as it continues in Chapter 4.

Chapter 4

Seismic Platform to Platform Differential Sensing

In this chapter a different approach is proposed, linking the adjacent platforms together through the use of an auxiliary sensor–the Seismic Platform Interferometer (SPI). At low frequencies, the performance of the ISI control loops is limited by artificial horizontal motion imposed on the system by tilt-horizontal coupling (Section 1.4). This tilt-horizontal coupling increases with a decrease in frequency. The control loop's ability to impose horizontal motion on a system whose disturbance was initially tilt results in excess, undesired motion. Chapters 2 and 3 addressed methods to measure the tilt independently and then correct the horizontal displacement sensor's signal by the appropriate factor. The SPI measures the differential length, pitch, and yaw between adjacent platforms enabling the control of these degrees of freedom. This chapter contains the design constraints and required noise floor for an effective SPI while Chapters 5, 6, and 7 discuss a prototype, control, and conclusions respectively.

4.1 Differential vs. Absolute Isolation

In Advanced LIGO there are nine seismic isolation platforms for each interferometer located in the corner station. These platforms support everything from the main

beamsplitter and input test mass optics in the BSCs to auxiliary input and output optics for beam shaping and signal conditioning in the HAM chambers (Section 1.2.2). Each significant optic is supported on a pendulum system that is bolted to the isolation platform (Section 1.3.3). At frequencies below about 0.2 Hz, the tilt-horizontal coupling reduces the absolute isolation from ground motion that can be achieved in the actively controlled platforms. The goal of the SPI is to enable differential measurements between adjacent platforms thus enabling differential control. Most sensors are limited in their dynamic range. In some situations reducing the differential motion enough can make an impossible measurement merely difficult. The SPI would control the differential motion thus relaxing the dynamic range requirements of other sensors. While the LIGO interferometer has already operated without the SPI, controlling the differential motion will help improve performance in two ways. It will assist in acquiring the lock of the main interferometer. It will also help by effectively offloading some low frequency control to stages closer to the ground. These stages utilize actuators that are better impedance matched to provide low frequency control and zero frequency offsets and pointing than the actuators acting directly on, or close to, the optics.

Ideally, absolute control relative to the inertial reference frame is an elegant solution. If the absolute motion of platforms are controlled to the inertial reference frame, then the differential motion between the platforms will also be held small. This is difficult to actually implement because of a lack of good, low frequency inertial sensors that are immune to tilt. The reverse however, is not necessarily true. Platforms could be well controlled differentially but still have large motion as a group relative to inertial space. In other words, a formation of platforms could be controlled to track to each other (requiring that they all travel in unison) while the formation as a whole has freedom to move globally in the absolute, inertial frame. These resulting extra degrees of freedom are discussed in Section 4.5.

If all of the optics on the platforms were supported by the same suspension systems and if all of the suspension systems could be tuned to precisely the same natural frequencies in their stages, then differential control would sufficiently stabilize the optics relative to each other at all frequencies. This is not the case in aLIGO. For

example, the triple pendulum suspension system on HAM 4 has a first predicted resonant frequency of 0.685 Hz while the adjacent HAM 5 triple suspension system has a first predicted resonance of 0.677 Hz. So for these two adjacent platforms, below the lowest natural frequency of the suspensions the common mode motion of the supporting platforms will become common mode motion at the optic. This results in the optics tracking each other, which is desired. At and above the lowest natural frequency, however, common mode motion of the supporting platforms will become amplified, especially near the suspension resonant frequencies and result in differential motion between the supported optics. This extra differential motion near and above the first natural resonances is undesirable.

Control at frequencies above the natural resonances of the suspension in practice is not necessary because motion induced at the suspension support is attenuated by the suspension pendulum chain before reaching the optic. It is the differential motion between optics that is required to be small so it will not affect the science signal. **Figure 4.1** displays the differential motion between optics as a result of a common mode input motion on two adjacent platforms but with different suspension systems.

As a result, the SPI is beneficial at frequencies below the natural frequencies of the suspension systems (0.5 Hz). It is around these frequencies where tilt-horizontal coupling in the isolation system's horizontal seismometers becomes problematic (Section 1.4).

4.2 Mounting Locations

There are several possible mounting locations for the SPI. An interferometric sensor was proposed by Robertson that would measure the differential length between corresponding second to last (penultimate) masses in adjacent suspensions pendulum chains (Robertson N. A., 1981). This was further investigated by a group at the University of Tokyo (Aso et al., 2006). A disadvantage is that the sensor noise requirements at this location are very strict, almost as small as the displacement levels necessary at the optics (**Figure 1.13**). An alternative mount location and the one recommended for the SPI is on the first stage of the ISI. This has several advantages

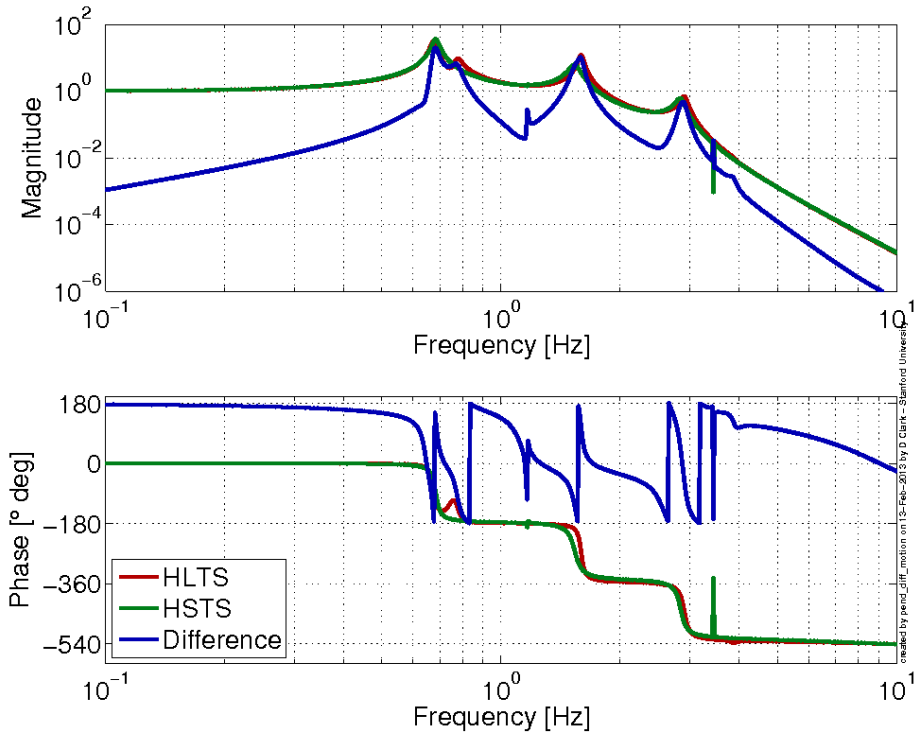

Figure 4.1: Simulated transfer functions of the two suspension subsystems on HAM 4 and 5. The magnitude is the motion at the optic relative to a given input motion at the suspension attachment point. The difference trace is the differential motion at the optic caused by a common mode motion input. From this we see common mode motion at low frequencies does not significantly affect the differential motion at the optic. At high frequencies, since the pendulums provide excellent passive isolation, the differential mode motion at the optic is also small.

including:

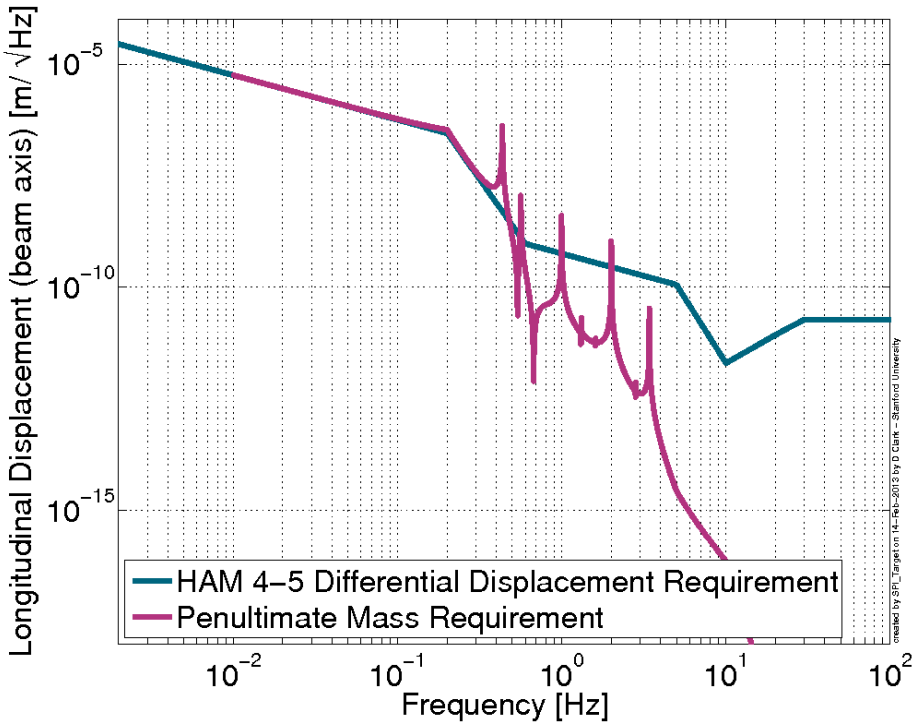

Figure 4.2: Comparison of two SPI mount points in terms of allowable sensor noise. Mounting the SPI to the ISI first stage has several advantages. The pink trace shows the equivalent noise performance that an SPI mounted on a penultimate mass (in the quad suspension system used for the input and end test masses) would have to attain in order to be equivalent.

- The sensor noise requirement of the SPI needs to satisfy the motion target of the ISI stage to which it is mounted (**Figure 4.2**). This is relaxed from an SPI mounted to the penultimate mass.

- The available mounting positions are greater on the platform than on the suspension system or its frame allowing greater flexibility in physical size and mass.

- Accessing the mounting location with power and signal cables is also simpler for an SPI mounted on the platform than on the suspension or its support structure.

- The ISI platform is already equipped with sensors and actuators to control all six degrees of freedom so implementation of control from the SPI signal would be simplified.

The SPI mount point is then the optics table on the single stage HAM ISI and the intermediate stage one on the BSC ISI. The mounting point performance requirement then dictates the maximum SPI sensor noise for the frequencies of operation.

4.3 SPI Sensing Dimensions

Two critical differential measurements between adjacent optics in aLIGO are the differential length between them along the beam path and the differential yaw. Differential pitch at the optic is also important but in practice the suspension system decouples pitch well along the suspension chain (Barton et al., 2008). Even though differential pitch control is not necessary to maintain the optic's pitch, it is necessary as part of the differential length requirement. This is because the SPI mounts on the ISI platform but the suspension point is approximately 1 m above the table surface (**Figure 4.3**). It is this separation from the center of rotation of the ISI to the attachment point of the suspension isolation system that necessitates SPI differential pitch sensing. This is because γ_{pitch} couples to suspension point motion as:

$$\sin \gamma_{\text{pitch}} \cdot L_{\text{from SPI to SUS point}} = L_{\text{displacement at SUS point}} \tag{4.1}$$

Thus defined, the SPI will provide sensing for differential length, differential pitch, and differential yaw between adjacent ISI platforms.

4.4 Accuracy and Range Needs

Since the SPI will be mounted on the first stage of the ISI platforms, the SPI requirements are set by the motion requirements of that stage. These are documented as the HAM motion targets and are more stringent for the HAM 4 to 5 case than for the other platforms (Lantz, 2010). Since the common mode motion of platforms is really

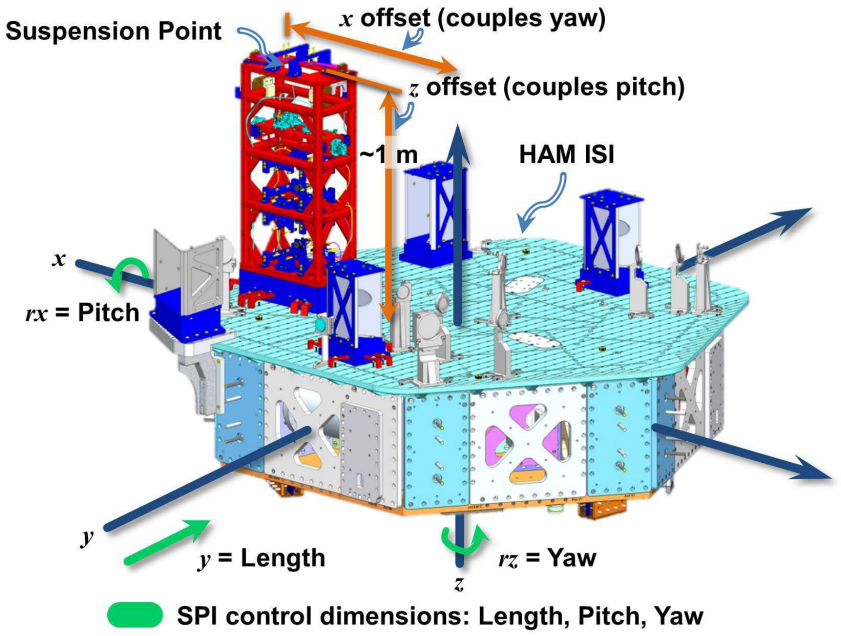

Figure 4.3: CAD of HAM 4 ISI platform displaying the suspension support point that is approximately 1 m above the platform. This necessitates the control of the differential pitch because the platform rotates about its center of mass at high frequencies and the center of stiffness at low frequencies both of which are within a few cm of the x and y axes in the figure.

only of interest below the natural frequencies of the suspension subsystems, control above 0.5 Hz is not necessary. Allowing for roll-off of the control and to avoid the introduction of sensor noise the SPI should still remain sensitive to 5 Hz above which point it is assumed that the sensor signal could be aggressively filtered. Because we want control to be retained to 0.5 Hz, the SPI requirement in this extra decade is simply to allow for this roll-off.

The isolation system is almost entirely controlled to track the ground motion at low frequencies around a few mHz so the ideal frequency band for the SPI ranges from approximately $5 \cdot 10^{-3}$ to 5 Hz. The requirements for the SPI sensor can then be determined and are plotted in **Figure 4.4**.

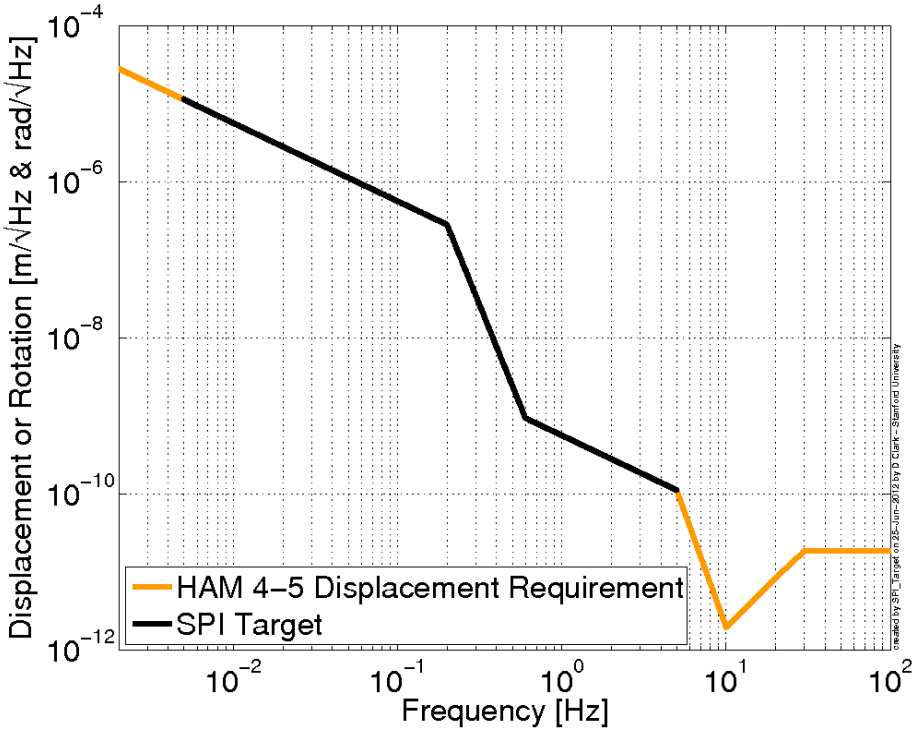

Figure 4.4: The SPI differential length, pitch and yaw sensing required accuracy as a function of frequency overlaid in black on the first stage ISI requirements.

Specific requirements that relate individually to the length, pitch and yaw sensing are described as follows in Section 4.4.1 and 4.4.2. Vacuum cleanliness is also important with requirements defined in Section 4.4.3.

4.4.1 SPI Differential Length Sensing

An interferometer was chosen for length sensing because it has good resolution even at large and varied standoff distances (distance between some chambers can be as little as $\approx$ 1 m or as great as 14 m). Initial work at Stanford conducted by John Ulman and Brian Lantz investigated balanced arm interferometers where the sensing and reference arms are the same length. This configuration is desirable because frequency changes in the laser used in the interferometer are common between the two arms and do not contribute to the measurement noise. Due to the long distances, however, between adjacent platforms (HAM 4 and HAM 5 are 14 m apart) the reference arm would also have to be long. A single mode fiber was tested as the reference arm of an interferometer. By coiling the fiber the overall size of the reference can be considerably reduced. After their investigation they concluded that apparent length of the fiber is difficult to stabilize to the levels necessary in the SPI frequency range. This is because noise in the fiber reference arm directly couples as noise in the length measurement and does not meet the specifications in **Figure 4.4**.

If the interferometer does not utilize a balanced reference arm, then the frequency noise of the laser must be taken into account. For mismatched arm lengths of an interferometer, the laser frequency noise, ΔF, couples into the interferometer's output appearing as differential length changes, ΔL, by the following equation where L_1 and L_2 are the interferometer's sensing and reference arm respectively and F_0 is the center frequency of the laser used.

$$\frac{\Delta L}{L_1 - L_2} = \frac{\Delta F}{F_0} \tag{4.2}$$

Which can be rewritten defining the frequency stability requirements as:

$$\Delta F_{\text{allowable}} = \frac{\Delta L_{\text{allowable}} \cdot c/\lambda}{L_1 - L_2} \tag{4.3}$$

The specification for laser frequency noise is determined by assuming optical path length dimension of $L_1 = 28$ m (14 m between HAM 4 and 5 as the worst case scenario). In practice if a short reference arm of $L_2 = 20$ cm is assumed, $L_2 = 20\,\text{cm} << L_1 = 28\,\text{m}$ so that $L_1 - L_2 \approx L_1$. The maximum laser frequency noise over the SPI

frequency range is plotted in **Figure 4.5**.

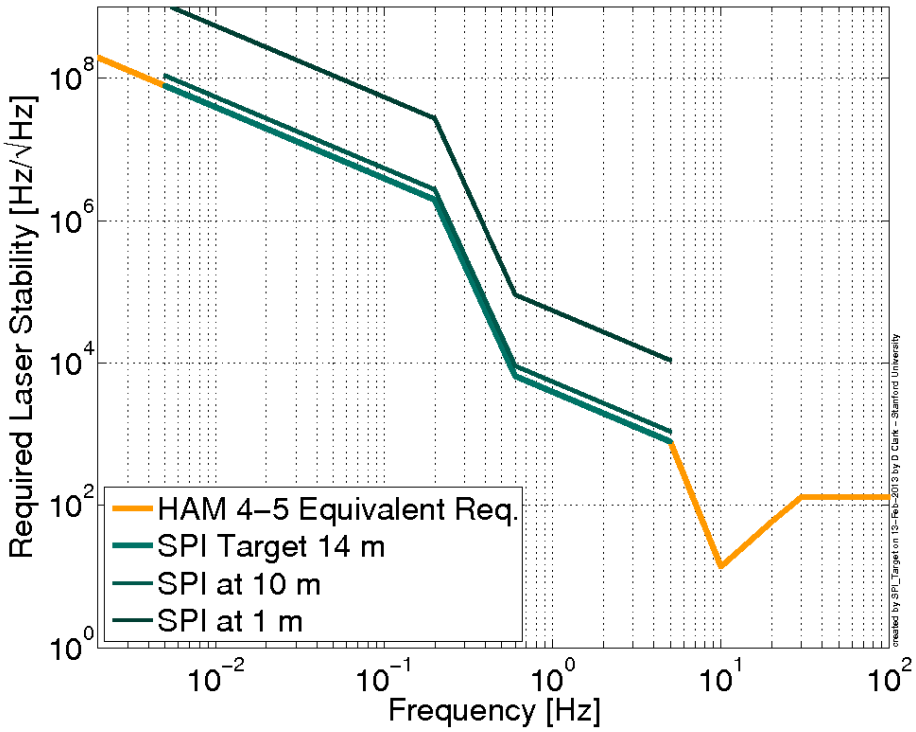

Figure 4.5: The SPI laser frequency stability requirement to meet the SPI noise requirement for operation between HAM 4 and 5 is shown. As expected, the frequency stability requirements relax as the length between platforms decreases.

4.4.2 SPI Differential Pitch and Yaw Sensing

The SPI will measure differential pitch and yaw with an optical lever. An optical lever simply measures the lateral or vertical displacement of a laser beam at some known distance from the source. For small angles γ, this can be approximated by $\gamma = \frac{d_{\text{offset at sensor}}}{L_{\text{distance from sensor to source}}}$. Ideally, the optical lever would use the same beam as the length sensing interferometer, simplifying the layout. Using this beam for the optical levers requires that it be optically anchored to the platform it is launched from. Several methods for how this could be done follow:

- Couple a beam of light through a cavity that is mechanically mounted on the

platform before launching the measurement beam.

- Sense the movements of a beam of light used for the measurement beam and actively control it through steering mirrors locking the beam to the platform.
- Sense the movements of a measurement beam and actively subtract the launch light angle from the measurement.
- Launch the beam into free space from a fiber that is anchored to the platform.

As discussed in Chapter 5, launching from a fiber was chosen for the prototype SPI. Choosing the fiber launch also necessitates a vacuum fiber feedthrough.

4.4.3 Vacuum Requirements

Since aLIGO operates at ultra-high vacuum (UHV) levels, in the range of 10^{-9} Torr ($1.3 \cdot 10^{-7}$ Pa), strict requirements have been set for what is allowed into the vacuum system. A list of permissible materials along with a required clean, bake and inspection sequence is provided by (Coyne, 2009a) and (Coyne, 2009b). In order for the SPI to be useful in aLIGO it must be able to be installed and operated in the aLIGO vacuum envelope by conforming to these requirements.

4.5 Control Scheme

Since the HAM and BSC ISIs are six degree of freedom, actively controlled isolation platforms, the implementation of control becomes a matter of blending the SPI signals with those of other sensors used by the control loops. Before blending, the SPI signal must be calibrated and filtered to limit its authority to the proper range.

For any given number of platforms SPI differential control leaves an extra degree of freedom. This is the global position of the formation of isolation platforms that are locked together by SPIs. This extra degree of freedom could be defined in various ways. Several methods are outlined below with their advantages and disadvantages discussed.

- Setting one platform as the master platform. All other platforms then track the master platform. This is simple to implement but may impose a cascading or slingshot effect on platforms that are several platforms removed from the master platform. The position of the master platform can be chosen but several platforms removed may have trouble remaining centered in the control envelope. A possible advantage is that if a good low frequency inertial sensor could be implemented, then that single sensor could control the master platform and all others would remained locked to it and take advantage of the sensor.

- The required differential motions necessary to satisfy the SPI control could be summed and then distributed to all of the platforms in such a way as to minimize any particular platform's motion. This allows the platforms to all move as little as possible. However, "walk-off" could be a problem in that the control scheme may keep commanding a particular platform to keep moving toward its physical stop while still satisfying the minimum motion control goal. Of course, this becomes problematic when any of the platforms contact their physical stop.

- Lastly, one could combine aspects of the other methods using a weighting technique. For example, the relative "stiffness" of a platform to motion could be a function of its own position relative to its hard limit stops. This could counteract the "walk-off" problems of the previous scheme. So for any particular platform, if it were required by the SPI to move in a particular direction, the closer it is to its limits the more control it offloads to surrounding platforms to maintain the SPI sensed differential displacements.

For the simplest case of two adjacent platforms the control method is not likely to be as important as it will be in the aLIGO corner station with the integrating of multiple systems. Of the platforms in the corner station, yaw must be controlled globally amongst all of the platforms. Differential length and pitch however, are decoupled between platforms along the x and y arm because of their orthogonality. This means that platforms in the x arm do not need to adjust their orientation based on a differential length or pitch change of a platform in the y arm and vice-versa.

4.6 SPI Purpose

The SPI will counteract the effect of tilt-horizontal coupling in the horizontal inertial sensors in the Advanced LIGO (aLIGO) corner station. The SPI, measuring differential length, pitch, and yaw will allow control of these dimensions between adjacent ISI platforms. The target frequency range for the SPI (from $5 \cdot 10^{-3}$ to 5 Hz) with target sensitivities for the most stringent configuration of HAM 4 to 5 are documented in **Table 4.1**.

Table 4.1: Differential length, pitch, and yaw resolution targets for the Seismic Platform Interferometer as a function of frequency.

Noise Floor and Target	**0.01**	**0.1**	**1**	**10**	**Hz**
Length target, HAM 4-5	$4 \cdot 10^{-6}$	$4 \cdot 10^{-7}$	$4 \cdot 10^{-10}$	$4 \cdot 10^{-11}$	$\frac{\text{m}}{\sqrt{\text{Hz}}}$
Optical lever target, HAM 4-5	$4 \cdot 10^{-6}$	$4 \cdot 10^{-7}$	$4 \cdot 10^{-10}$	$4 \cdot 10^{-11}$	$\frac{\text{rad}}{\sqrt{\text{Hz}}}$

Chapter 5

Seismic Platform Interferometer Prototype Design

The Seismic Platform Interferometer (SPI) prototype design and construction is described. It is an instrument that measures differential length, pitch, and yaw between seismic isolation platforms and was integrated as a prototype. The differential measurements are sufficient because if the differential mode motion between adjacent mirror support suspensions is controlled at frequencies below the suspension system's natural frequency, then the differential mirror motion will also be reduced even if common mode motion exists. This is what set the instrument's frequency range as described in Section 4.4.1. The SPI is helpful in improving the low frequency performance of the aLIGO Internal Seismic Isolation (ISI) subsystem in that it maintains a fixed differential length between two adjacent platforms, thereby counteracting the errors introduced from tilt-horizontal coupling in the platform control loops. The SPI prototype was installed in the Stanford Engineering Test Facility (ETF) and tested. The prototype design and construction to meet the design requirements as specified in **Chapter 4** are described in this chapter.

The SPI measures the differential length through a Mach-Zehnder (MZ) configured interferometer, while the differential pitch and yaw are measured by an optical lever. The MZ interferometer configuration differs from the Michaelson configuration in that two beamsplitters are used in the MZ interferometer (IFO). This makes

alignment simpler when commissioning the instrument because it is possible to individually adjust the splitting ratios on each beamsplitter. The SPI was installed measuring the three differential variables between two active isolation platforms that are housed in the vacuum envelope of the ETF. The SPI, with associated launch and measurement optics and electronics, is located on a host platform, and a single mirror is all that is necessary on a remote platform. In the ETF, the host platform for the SPI was chosen to be the Tech Demo, a two stage, all degree of freedom controlled (in each stage), active platform (Giaime and Lantz, 2003). The remote platform was the Rapid Prototype Platform (RPP), a first generation prototype of a six degree of freedom actively controlled platform, which for the tests was being actively damped relative to inertial space in all degrees of freedom. The control of the RPP is described in Appendix F.

In operation, the prototype SPI provided real-time length, pitch, and yaw sensing between the Tech Demo and the RPP in the vacuum system.

5.1 SPI Prototype Mount Location

The SPI prototype is designed to measure three differential degrees of freedom between adjacent seismic isolation platforms as described in Chapter 4. The SPI host platform contains the majority of the measurement instrumentation including the laser beam launching, receiving and interferometer with its associated optics and electronics. The remote platform only contains a single mirror. This configuration is not the only possibility. For example, placing detectors on the remote platform might be useful, but this complicates the integration because the single mirror on the remote platform would have to be replaced with optics and associated electronics. The added complexity might be worthwhile if it, for example, simplified the initial alignment of the instrument. These items would also need vacuum feedthroughs for the electronic signals. With the current design, all of the electronics and all of the optics except the single mirror are located on the host platform. This means that vacuum feedthroughs only have to be located on one chamber.

Finally, since all measurements are differential, it does not matter which platform becomes host and which one is the remote. This gives more flexibility in the implementation in Advanced LIGO (aLIGO) by providing the ability to place the items on the platforms which have available space and easiest accessibility for vacuum feedthroughs and access.

5.1.1 SPI Host: Technology Demonstrator Platform

The Technology Demonstrator Platform (Tech Demo) was chosen as the host platform for the SPI prototype. This platform provides a large optical table surface at a height coincident with a beam tube connecting its vacuum envelope to the RPP. The Tech Demo is a testbed prototype platform for the aLIGO ISI platforms, which shares with them most of the design and control concepts.

The Tech Demo platform is composed of two active stages, which are controlled in all degrees of freedom. The sensors on the first stage consist of capacitive position sensors, Streckeisen STS-2 seismometers, and Sercel L-4C seismometers, the signals of which are all blended together to create the input to the isolation controllers (sensor blending was described in Section 2.3). The second stage consists of capacitive position sensors and Geotech GS-13 seismometers; the signals of which are likewise blended together, creating one virtual sensor across all frequencies. The Tech Demo optical table is displayed in **Figure 5.1** and its isolation performance is described in more detail in **Chapter 6** (Lantz, 2005), (Hua and Lantz, 2005).

5.1.2 SPI Remote: Rapid Prototype Platform

The Rapid Prototype Platform (RPP) is separated from the Tech Demo by 10 m on center but 8.9 m between their platform edges. The RPP serves as the remote platform for the SPI prototype. The platform was recommissioned to provide inertial damping and control for a single active stage and is documented in detail in **Appendix F**.

The control signals obtained from the SPI were ultimately fed into the RPP, locking it to track the motion of the Tech Demo. Since better sensors on the Tech

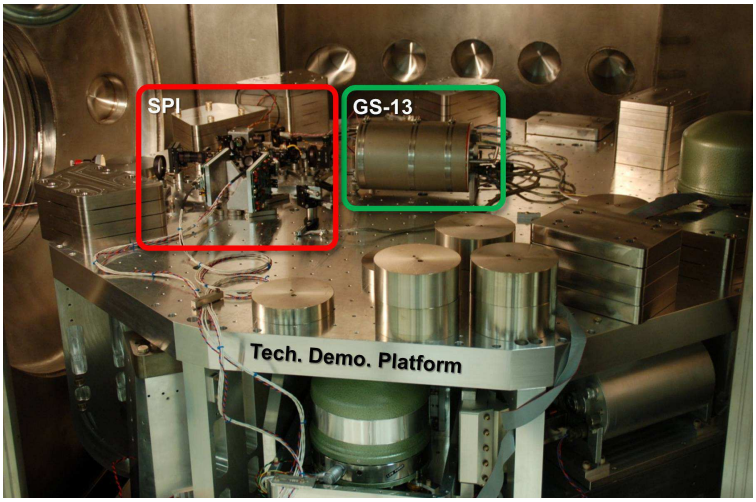

Figure 5.1: The two-stage, active Technology Demonstrator Platform (Tech Demo) in the Stanford Engineering Test Facility (ETF). The Tech Demo served as the host platform for the SPI prototype, which is visible to the left on the platform surface. A GS-13 seismometer used to validate the SPI is centered on the platform.

Demo give it better performance, it was hoped that the RPP performance would increase as a result of the SPI link to the Tech Demo.

5.2 Laser Source

Because of the SPI prototype's unbalanced arm configuration, the laser source frequency must be extremely stable and meet the requirements specified in **Figure 4.5**. A fiber based laser at 1.533 μm was selected because 1) it provides greater frequency separation from the 1.064 μm light used in the aLIGO main interferometer, 2) it was thought that fiber components could be obtained more readily for the 1.5 μm telecommunications band, and 3) because of laser safety concerns in the lab.

The laser used is an Orbits Lightwave 10 mW polarization maintaining (PM) fiber coupled laser. The PM fiber supports a single mode and is critical in reducing induced polarization wander of the light transmitted through the fiber. A fiber-coupled optical isolator was connected directly after the laser to reduce back reflections entering the laser and affecting the stability.

The laser is internally temperature-controlled but was also placed in a thermal enclosure (with insulation and additional thermal mass). The laser can be operated in constant current or constant power modes. Constant current operation was selected because the frequency stability was thought to be greater when operating in this mode. The operating setpoint was selected through RS-232 communications with the laser control unit and chosen to provide a maximum front to back ratio of power. This was set after allowing the laser to warm up and stabilize for twelve hours. This yielded power outputs around 8 mW into the fiber.

5.2.1 Vacuum Feedthrough

The laser light needs to be introduced into the vacuum chamber before it can be used by the SPI. There are two ways to accomplish: free-space coupling the light into the chamber through a viewport or through a fiber vacuum feedthrough. A vacuum feedthrough was preferred for several reasons, including 1) fiber delivery eliminates problems caused by changes of the index of refraction, n, of air outside the vacuum system, and 2) the light can be easily launched from fiber once on the host platform.

A 1.5 μm PM fiber vacuum feedthrough was constructed and tested because no commercially available aLIGO vacuum compatible feedthroughs were available. The SPI prototype feedthrough consisted of a PM fiber that was metalized and then hermetically sealed into a stainless steel KF flange. The assembly was leak checked with no indicated leak to our system's sensing floor of 10^{-9} $\frac{\text{Torr}\cdot\text{L}}{\text{s}}$ ($1.33 \cdot 10^{-10}$ $\frac{\text{Pa}\cdot\text{m}^3}{\text{s}}$). An in-vacuum section of PM fiber was spliced on, completing the feedthrough. The construction and testing of the feedthrough is described in detail in Appendix G.

5.2.2 Fiber Launch

The differential angle sensing of the SPI requires that the light launched from the host platform be coupled to its motion. There are several ways in which this might be accomplished as were discussed in Section 4.4.2. For the prototype, it was chosen to fiber couple the light from the laser and launch it into free-space from the host platform.

5.2.3 SPI Laser Beam Diameter

Assuming Gaussian beam propagation, the larger the launch beam diameter the less divergence. The launch diameter cannot be too great or optics in the chain will start to clip the beam, resulting in loss of interferometer contrast. Since the SPI prototype uses 1 in. (25.4 mm) diameter optics for the interferometer, the maximum beam radius at any of the optics should then be limited to 0.25 in. (6.35 mm) and preferably smaller to keep the beam Gaussian. The free-space coupler used in the prototype provided a beam waist radius of 1.5 mm. Assuming a planar wavefront at the free-space coupler, the divergence of the beam is documented in **Table 5.1** following the formula relating the beam waist, r_{waist}, at any specified distance:

$$r_{waist} = r_{launch} \cdot \sqrt{1 + (\frac{\lambda \cdot Distance}{\pi r_{launch}^2})^2} \tag{5.1}$$

While a 1.5 mm beam waist radius was used in the SPI prototype in the ETF, this would not be appropriate for an SPI operating between HAM 4 to HAM 5 as the divergence would be too great, exceeding the 1 in. (25.4 mm) optic diameters.

Table 5.1: Beam waist radii (from peak to $1/e^2$ level) for a free-space coupled 1.5 μm laser beam with an initial beam waist radius of 1.5 mm at various distances. The SPI prototype utilized 1 in. (25.4 mm) optics, which would pose a clipping problem if the beam waist approached 0.5 in. (12.7 mm) in radius.

Location	**Launch Point**		**ETF remote**	**ETF return**	**HAM 4 to 5**
Distance	0.0 m	1.0 m	8.9 m	17.8 m	55.6 m
Waist Radius	1.500 mm	1.533 mm	3.206 mm	5.861 mm	17.761 mm

The SPI angular sensing operates under the assumption of a Gaussian beam distribution. To verify the beam profile, the light launched from the fiber by the free-space coupler was measured (**Figure 5.2**). A slice of the profile was then fit against a Gaussian curve (**Figure 5.3**) showing that the beam profile is 94.7 % Gaussian in the prototype where the % Gaussian was determined by the following equation:

$$\%_{\text{Gaussian}} = \frac{Area_{\text{Gaussian fit}} - Area_{|\text{residual}|}}{Area_{\text{Gaussian fit}}} \tag{5.2}$$

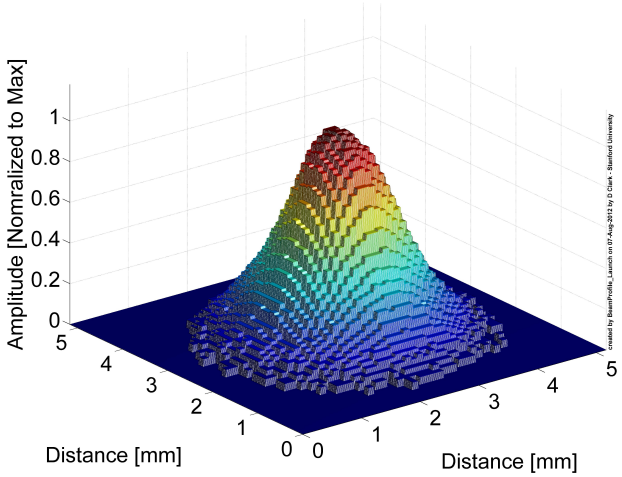

Figure 5.2: Measured beam profile of the launched laser light used by the SPI prototype.

5.3 Schematic Layout

The SPI prototype is schematically shown in **Figure 5.4**. Laser light originates from a source outside the vacuum chamber and is introduced into the vacuum system through a UHV feedthrough that is, in principle, compatible with aLIGO. The light is then launched into free space through a fiber coupler on the Tech Demo. After stray polarization is removed by a polarizing beam splitter, the light travels through the first beam splitter of the Mach-Zehnder (MZ) interferometer (IFO) and to the remote mirror on the RPP. The light returns from the RPP and is scaled through a telescope to bring it back to the corresponding spot size as the light in the reference arm of the interferometer. Before the telescope about 4% of the return light is directed to a quad photodetector (QPD) which monitors the differential angle between the Tech Demo and the RPP. The rest of the returning light gets recombined on the second beam splitter of the MZ IFO with the light from the reference arm. The reference arm light is directed by a steering mirror that is piezo-actuated and can be used either to lock the IFO at the mid-fringe or to modulate the reference arm light. Both outputs from the second beam splitter are monitored differentially on two photodetectors.

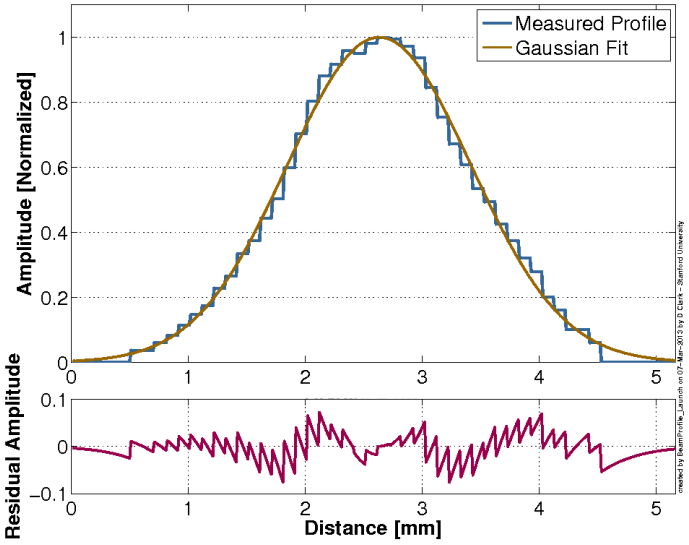

Figure 5.3: Beam profile slice and comparison with a Gaussian curve with the residual plotted below. The SPI angle sensing relies on the assumption that the launched beam is at least symmetrical. This beam slice was 94.8 % Gaussian.

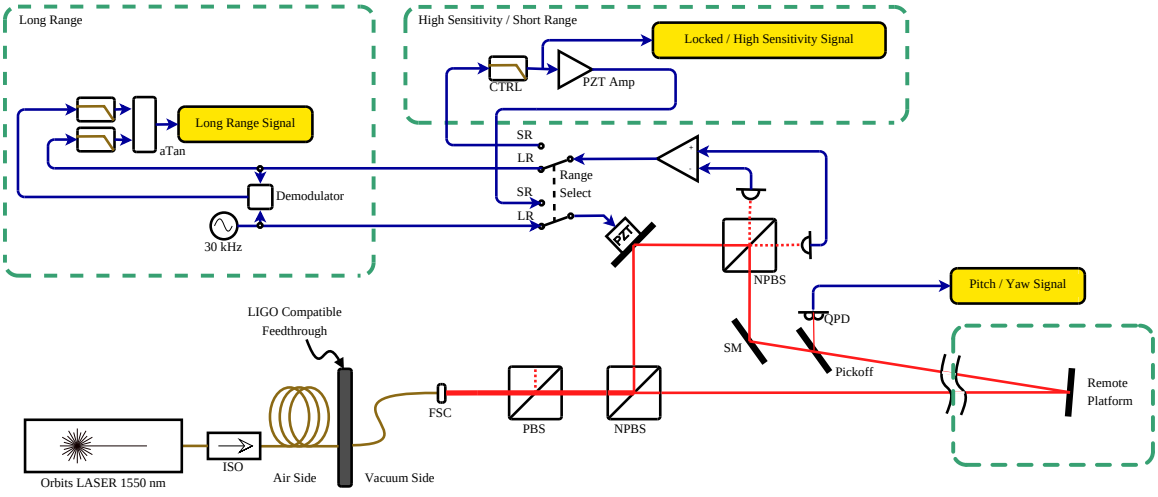

Figure 5.4: The SPI prototype in simplified schematic form. The host and the remote platforms are indicated with the majority of the SPI components located on the host platform. The remote platform only requires a single mirror.

A photo of the SPI prototype on the Tech Demo with components annotated is displayed in **Figure 5.5**. This also shows the additional steering mirrors, irises, and lenses that are not shown in the schematic. The purposes of the beam paths are then annotated in **Figure 5.6**.

5.4 Measurement Method

The SPI measures differential length, pitch, and yaw with two different methods. The length sensing is measured by an interferometer and the differential angle between platforms in pitch and yaw is measured by an optical lever.

5.4.1 Length Sensing

The SPI length sensing uses a Mach-Zehnder (MZ) configuration interferometer. This involves splitting the input light into two arms, one a short reference arm (11 cm) and the other a long sensing arm (8.9 m between the platforms). Because of divergence of the beam as described in **Table 5.1**, a telescope decreases the return sensing beam waist to approximately match that of the reference arm at the recombination beam splitter. The telescope consists of an $f = 50$ mm lens and an $f = -25$ mm lens separated by 50 mm in the direction of the beam propagation.

The SPI prototype interferometer was tested with two different sensing modes, mid-fringe locking and fringe counting. It was thought it would be necessary to automatically switch operation from the mid-fringe locking mode (in order to reach the required sensitivity) and the fringe counting mode (in order to achieve the necessary dynamic range). Ultimately, the fringe counting mode provided enough resolution that it was sufficient to operate the prototype continuously in this mode reducing complexity. However both methods are described below for completeness.

5.4.1.1 Mid-Fringe Locking

The mid-fringe locking mode of the interferometer involves locking the reference, short arm, in a multiple of the laser wavelength, to the long arm. This is realized

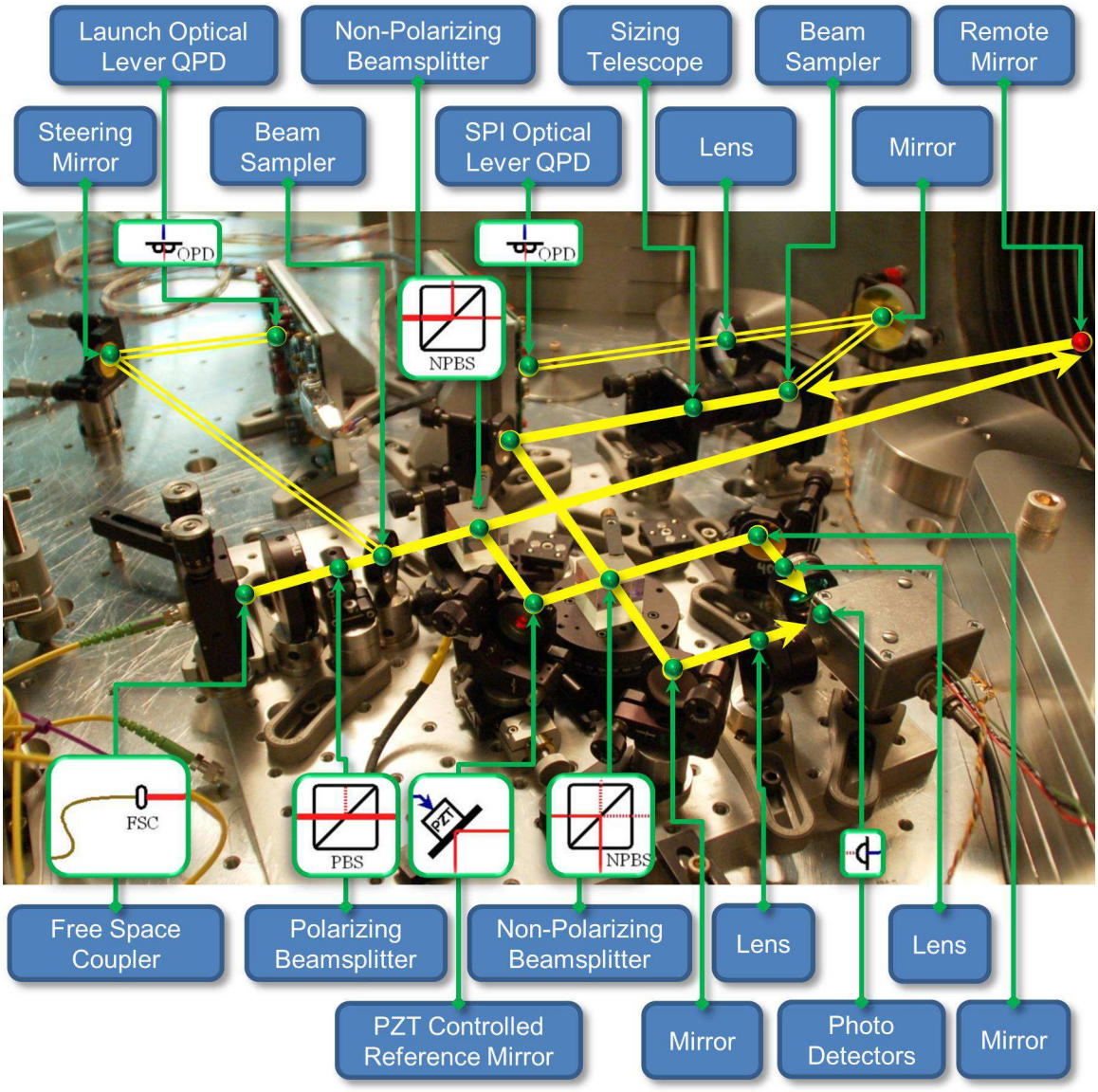

Figure 5.5: An annotated picture of the SPI prototype components on the host platform. Items not shown include the laser source, fiber isolator, fiber vacuum feedthrough, and remote platform mirror. Doubled thin lines represent rays used by optical levers for angular sensing.

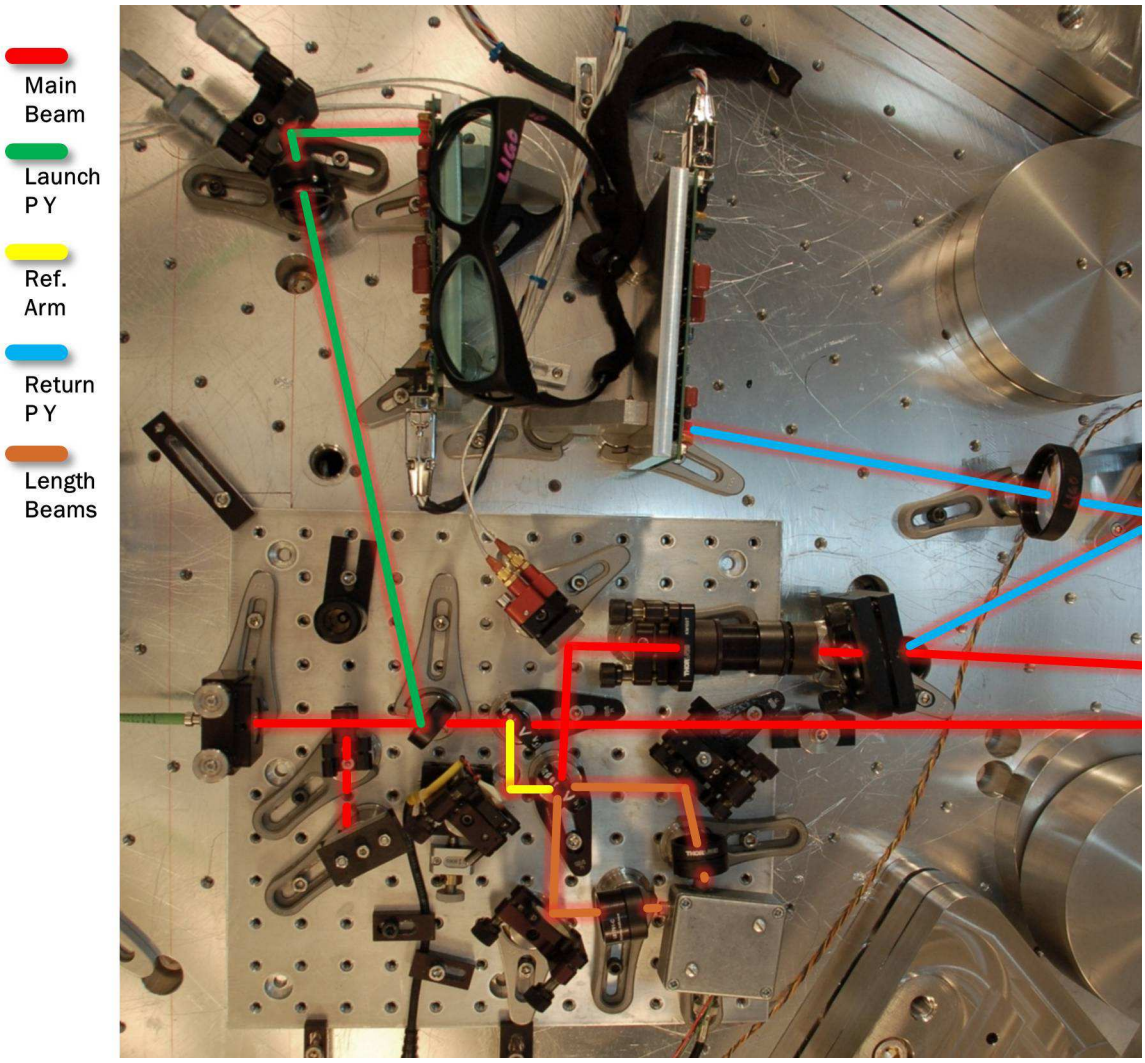

Figure 5.6: This photo displays the purpose of the beam paths in the prototype interferometer.

through the electrical actuation of the piezo-electric transducer (PZT) on the folding mirror in the reference arm. Motion of the PZT is translated to changes in the optical path length of the reference arm. The amount of optical path length change in the reference arm is equivalent to the optical path length change in the sensing arm and can then be measured.

Both optical outputs of the second beam splitter are directed onto individual photodetectors. These photodetectors are then subtracted in the preamplifier resulting in a balanced detector. This mode results in high sensitivity because the control signal to the PZT, often in hundreds of volts, is monitored while the control loop keeps the interferometer locked to the mid-fringe **Figure 5.7**.

The fringe locking is accomplished by a controller that takes the balanced photodetector output and controls a high voltage amplifier driving the PZT in the reference arm. Initially this controller was implemented in analog electronics but was later switched to a digital filter in the aLIGO real-time control computer (CDS which is described in more detail in Section 5.6). The transfer function of this locking controller is:

$$G(s) = \frac{-40}{0.1592s + 1}\frac{\mathrm{V}}{\mathrm{V}} \tag{5.3}$$

While the mid-fringe locking method results in excellent resolution, its sensing arm range is limited to the maximum displacement of the PZT in the reference arm (about 2 μm). An increase in range then requires larger actuation range PZTs or higher voltage and ultra stable amplifiers. A disadvantage of the mid-fringe mode is that if induced platform-to-platform motion does overcome the control authority of the reference arm PZT, the interferometer could re-lock to the mid-fringe at a different fringe thus losing its point of reference.

5.4.1.2 Fringe Counting

Because an infinite amount of control authority is not available from the control system, the amount of optical path length change that can be accommodated by the prototype in the mid-fringe locking mode is limited. In practice, this means that if the

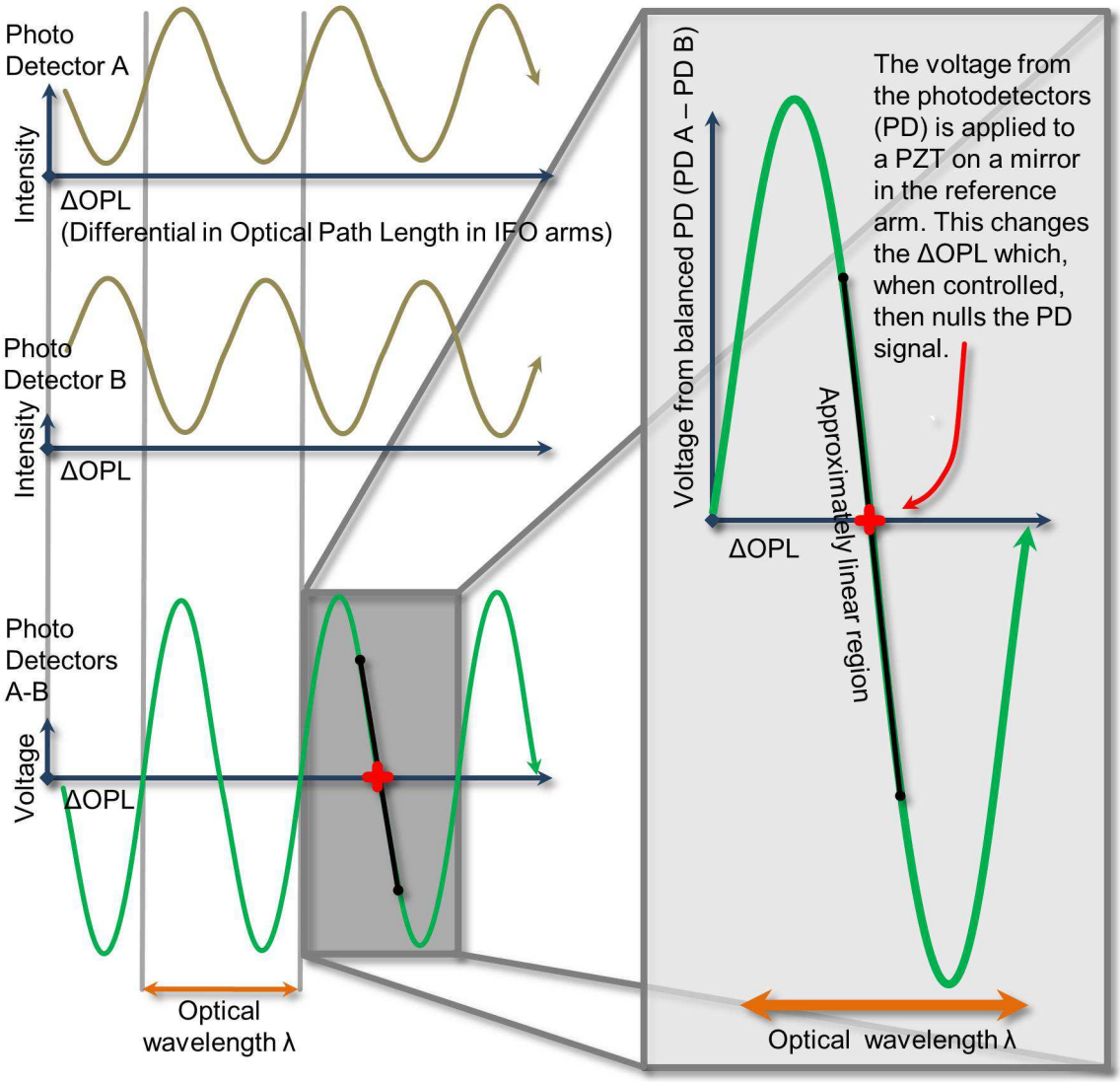

Figure 5.7: The mid-fringe locking of the interferometer. The length signal is obtained by monitoring the drive level to the PZT in the reference arm required to keep the interferometer at the mid-fringe position. Because of the balanced detection, this method is not sensitive to laser amplitude fluctuations. One limitation is that the maximum sensing length is determined by the maximum PZT actuation range on the reference arm. If large displacements, larger than the PZT actuation range, are encountered, the interferometer "jumps" fringes and re-locks on an unknown fringe. This results in a loss of position information which would be a multiple of the wavelength.

differential motion between the platforms exceeds one micron, then the control loop is forced to unlock and the actual differential displacement is then unknown as the interferometer jumps through fringes re-locking on an unknown, arbitrary fringe. The fringe counting mode allows the interferometer to remain in the unlocked state while counting the fringes it passes through. This provides a large dynamic range which is not limited in length. If the wavelength of the light is nominally 1.5 μm, then a change in the differential platform position of 750 nm results in the interferometer's operating point being located on a different fringe. The ability to count fringes and travel large distances is critical when the platforms linked by the SPI are not under complete isolation, such as when recovering from an earthquake.

To locate the position along the interferometer's operating curve in the fringe counting mode two signals are necessary. One signal is provided by low pass filtering the voltage from the balanced photodetectors at 100 Hz (subsequently referred to as the cosine signal). The other signal, which provides the slope of the curve where the interferometer is operating, is determined by band pass filtering the balanced photodetectors' signal from 3 to 30 kHz and then demodulating with a lock-in amplifier (this signal is referred to as the sine signal).

The signal can be modulated in several places, 1) modulating the laser frequency, 2) modulating the PZT in the sensing arm, or 3) modulating the PZT in the reference arm. For the prototype, modulating the light in the reference arm was chosen at 10 kHz. Higher modulation rates would allow higher velocities to be sensed but the dynamics of the PZT used limited the maximum rate. In practice, the SPI prototype's maximum velocity has not been exceeded when operating in fringe counting mode during typical platform operations (even with RMS motions in the range of 8 μm).

The distance between adjacent platforms can then be determined from the phase angle, ϕ, which is calculated from the two signals as:

$$\phi = \arctan \frac{\text{Sine Signal}}{\text{Cosine Signal}} \tag{5.4}$$

This phase angle, ϕ, can then be converted to a distance through the following relationship:

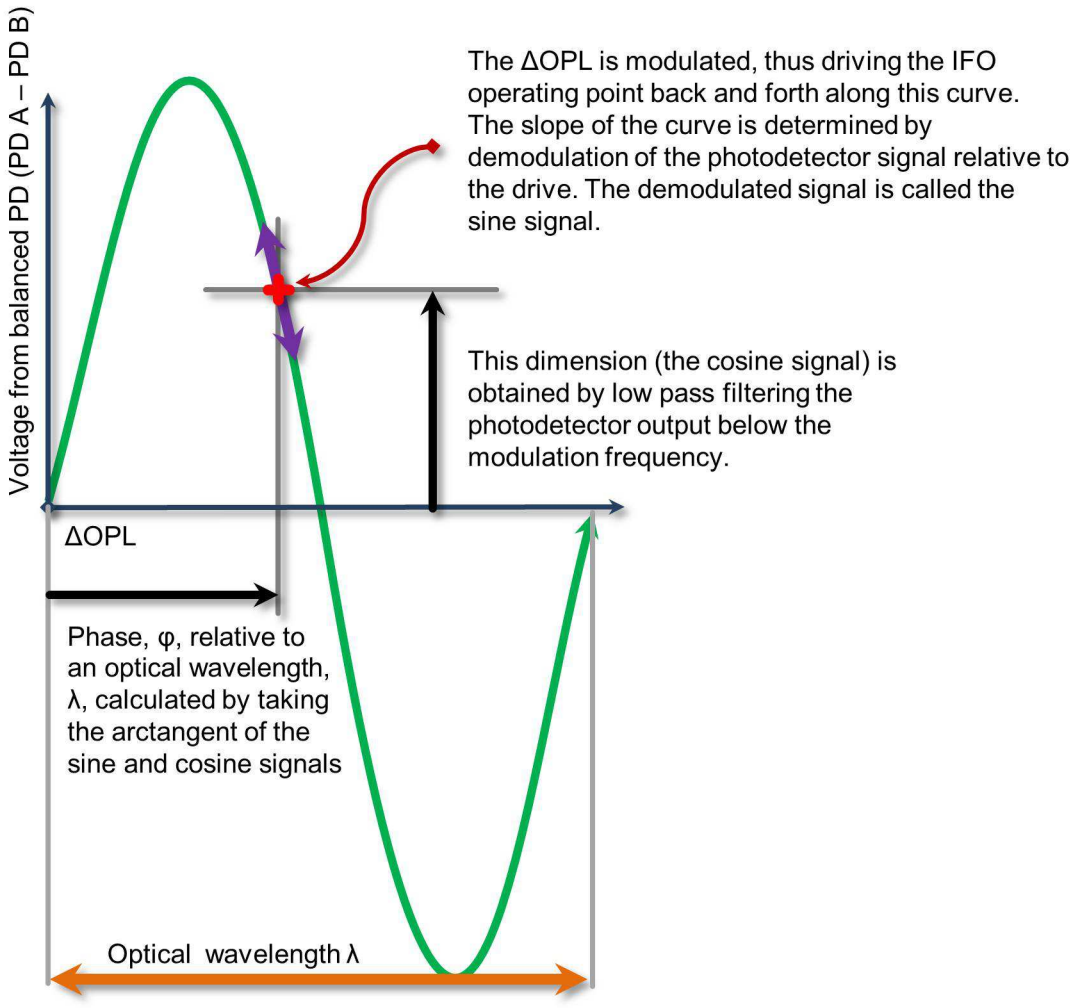

Figure 5.8: The fringe counting technique modulates the light in the reference arm so that the position along the interferometer operating curve can be determined. This measurement mode is not limited in range like the mid-fringe locking mode but is limited in measurement velocity as a function of the modulation frequency.

$$Displacement = \phi \cdot \frac{\lambda}{4\pi} = \phi \cdot 123.345 \frac{\text{nm}}{\text{rad}} \tag{5.5}$$

5.4.2 Pitch and Yaw Sensing

The SPI prototype measures pitch and yaw between adjacent platforms using an optical lever. For small angles, γ, this can be approximated by:

$$\gamma = \frac{d_{\text{offset at sensor}}}{L_{\text{distance from sensor to source}}} \tag{5.6}$$

For the prototype, the $d_{\text{offset at sensor}}$ is measured as x and y motion of an incident laser beam on a quad photodetector (QPD). The details of the circuit board and the analog math are contained in Appendix E.

In the prototype, while one QPD measures the return light from the remote platform, a similar QPD monitors a fraction of the light (4%) launched from the fiber through the free-space coupler. This allows beam wander and amplitude changes of the launched light to be recorded.

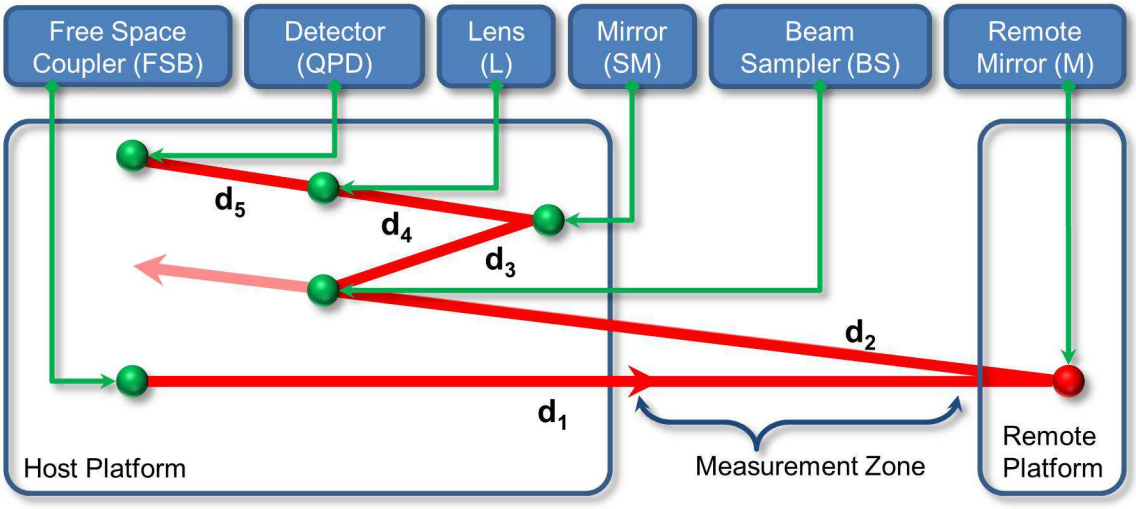

Figure 5.9: Schematic diagram of the differential pitch and yaw angle sensing of the SPI. The beam sampler (BS) allows the majority of the light to proceed and be recombined in the second beam splitter of the MZ interferometer (**Figure 5.5**).

Table 5.2: The SPI optical lever angular sensing optical parameters. These are used to determine the system's ABCD matrix, which describes the response at the QPD for a given input. ABCD matrices are also known as ray-transfer matrices (Goodman, 2005). Variables refer to labels in **Figure 5.9**.

Distance	**m**	Location	**Object**	**Focal Length mm**
d_1	8.700	To Remote		
d_2	8.700	To Host		
d_3	0.105	To Steering Mirror		
d_4	0.120	To Lens	Lens (L)	150
d_5	0.230	To QPD		

Simple ray tracing can be done with ABCD matrices (Goodman, 2005). Referencing **Figure 5.9**, the optical parameters for the optical lever angle sensing are documented in **Table 5.2**. By combining these distances and focal lengths into discrete ABCD matrices and multiplying, the complete system can be described as follows:

$$\begin{pmatrix} r_{detector}\,(\mathrm{m}) \\ \theta_{detector}\,(\mathrm{rad}) \end{pmatrix} = \begin{pmatrix} -116.500 & 17.625\,\mathrm{m} \\ -6.667\,\frac{1}{\mathrm{m}} & 1.000 \end{pmatrix} \begin{pmatrix} r_{launch}\,(\mathrm{m}) \\ \theta_{launch}\,(\mathrm{rad}) \end{pmatrix} \tag{5.7}$$

If the incident beam is called the z axis, the QPD measures the fractional difference of light on its quadrants in the x and y directions. This means that the QPD is sensitive to displacement across the face, which is then converted into angles by Equation 5.6. The angle of the light on the detector is not measurable so the term $\theta_{detector}$ can be ignored. Using this matrix, a 1 μrad differential angle between the two platforms results in 17.6 μm of displacement at the QPD.

The incident spot size on the QPD is a critical design factor. As the spot size of the incident beam on the QPD is reduced, higher resolutions can be obtained. This, however, must be balanced because once the beam is completely contained in a quadrant, no additional information can be obtained that limits the dynamic range. Also, since the QPD contains small null zones between quadrants (≈ 59 μm), it is necessary that the spot size still remain large relative to these zones. Finally, it is an assumption that all of the light from the incident beam is contained within the

four quadrants. The QPD detector used in the SPI prototype has a diameter of approximately 3 mm. The return beam from the host platform was focused to be 1 mm in diameter at the QPD.

As mentioned in Section 5.2.3, another assumption for the operation of the angle sensor is that the incident beam is Gaussian. If the beam is not Gaussian (or at least symmetrical), then it is difficult to accurately determine the center of the beam. The beam profile of the launched beam from the free-space coupler was shown in **Figures 5.2** and **5.3**.

The angle sensing of the prototype was then calibrated to match the calibrated sensors and actuators of the Tech Demo. Calibration is important, allowing the experimental results to be directly compared to the requirements.

5.5 Considered Noise Sources

While the target resolutions for the SPI are tabulated in **Table 4.1**, it is still important to quantify the noise sources that make up the noise floor, thus creating a noise budget. This is useful because it helps determine the limiting factors and, if improvements were made to the instrument, in which areas they would be most helpful.

5.5.1 Shot Noise

The photodetectors used for both interferometric and optical lever sensing experience shot noise. This is a fundamental limit set by photon counting with the noise being proportional to the square root of the light power. In the following equation, i is the current in the photodiode resulting from the light and e is the elementary charge $\approx 1.6 \cdot 10^{-19}$ C.

$$n_{shot} = \sqrt{i \cdot e \cdot 2} \tag{5.8}$$

This noise level was calculated for the interferometer assuming 10 mW of incident light on the photodetectors as follows:

$$n_{shot}\,(\mathrm{m}) = \sqrt{10\,(\mathrm{mW}) \cdot 1\,(\frac{\mathrm{A}}{\mathrm{W}}) \cdot 1.6 \cdot 10^{-19}\,(\mathrm{C}) \cdot 2} = 5.66 \cdot 10^{-11} \frac{\mathrm{V}}{\sqrt{\mathrm{Hz}}} \tag{5.9}$$

In practice, because of losses in the isolator, fiber, and optical components, the incident light is in the range of 5 to 8 mW. Likewise, the angle sensor shot noise was also computed assuming a maximum power of 3.7 % (the beam sampler pickoff) of the 5 mW maximum in the return beam from the remote platform. In both cases, the actual shot noise is likely less than predicted. The values reported give the maximum shot noise in terms of displacement that might be seen by the SPI as $n_{shot} = 2.79 \cdot 10^{-14} \frac{\mathrm{m}}{\sqrt{\mathrm{Hz}}}$ for length and $n_{shot} = 1.04 \cdot 10^{-10} \frac{\mathrm{rad}}{\sqrt{\mathrm{Hz}}}$ for pitch and yaw.

5.5.2 Laser Frequency Noise

Since the SPI prototype is an unbalanced arm interferometer (the reference and measurement arms are not nominally the same length), any frequency drift in the laser or phase noise of the light in the delivery fiber will show up as a displacement signal at the output. This is what defined the laser frequency noise requirement in **Section 4.4.1**.

The frequency stability of the laser source was tested by operating a Mach-Zehnder (MZ) configured interferometer with a fixed arm length mismatch of 2.85 m. Both the reference arm and the measurement arms of the interferometer were defined by fixed mirrors located on the Tech Demo. Under the assumption that apparent length mismatch in the arms of the interferometer is caused by frequency fluctuations of the laser, this frequency stability can be quantified. This is an upper limit to the frequency noise because temperature changes of the Tech Demo platform cause the entire platform to change dimensionally, which results in real length changes in the arms of the test interferometer.

The measured frequency stability can also be projected for different mismatches in arm lengths. For the interferometric sensing and assuming a fixed length reference arm, this noise source scales proportionally with separation distances between platforms. This means the longer the separation distance, the higher the frequency noise

contribution.

The frequency stability of the laser is plotted in **Figure 5.10** compared to the frequency stability requirements for an SPI operating between HAMs 4 and 5. In the analysis, the best linear fit to the test interferometer length signal over the entire recorded data was removed. This removes the temperature coupling to the expansion of the platform and any other noise source that consistently affects the signal over the measurement time.

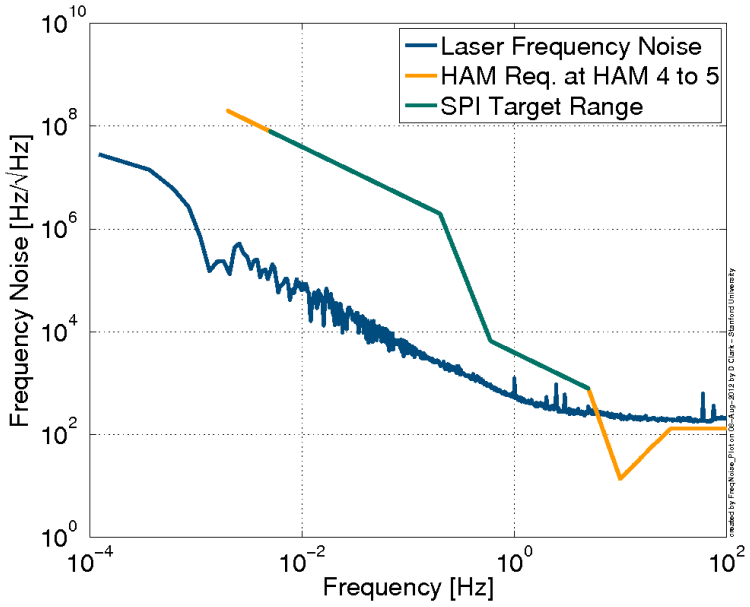

Figure 5.10: The laser frequency noise measured by a fixed arm length difference interferometer located on the Tech Demo platform in vacuum. The SPI target frequency range ends right before a notch in the HAM requirements. This large notch is actually only necessary for the HAM 4 to 5, which is the most strict case.

These tests indicate that the frequency noise of the laser is stable enough for the SPI to reach the target even for the distances between HAMs 4 to 5. The distance from HAMs 4 to 5 represents the largest distance where the SPI is expected to operate, at 27.8 m and is plotted for reference. The angular sensing does not experience any coupling of the laser frequency noise.

5.5.3 Laser Amplitude Noise

The amplitude stability of the laser was also measured. This should not be an applicable noise source for the length sensing mode. Even in the mid-fringe mode the output from the photodetector circuit is the difference of signal between two photodetectors so optical power fluctuations are common mode to both detectors and the balanced output remains constant. It does matter, however, for uncontrolled angle sensing optical levers.

The laser amplitude was measured directly on a photodetector over a measurement duration of 3 hours along with the temperature change of the laser housing shown in **Figure 5.11**. While there seems to be a strong correlation between the housing temperature and the laser power output it is difficult to determine which one is affecting the other. For example, mode hops internal to the laser could be causing fluctuations in the power resulting in changes to the heat loading of the laser. Or conversely, the temperature of the housing could be inducing changes in the laser power output.

The relative intensity noise (RIN) of the laser is one way to quantify the amplitude stability of a laser and is plotted in **Figure 5.12**.

Because we measure both interference beams we expect the length sensing interferometer to be insensitive to power fluctuations. While it is not expected that laser amplitude fluctuations would couple into just one signal, in the fringe counting interferometer an $x - y$ scatter plot of the sine and cosine signals shows a drift in the sine term (**Figure 5.13**). In this plot, the sine and cosine terms would trace out an ellipse if the interferometer experiences great enough displacements. Because this data was recorded while the platform was under isolation control, just a portion of the arc is visible. The colors progress with experiment time and throughout the 40 minute data set the radius of the arc traced out obviously decreases over time as the sine signal decreases from 5.62 to 5.46. This change over time is not well understood. Because the sine signal is obtained by modulating the reference arm and then demodulating the interferometer output, changes in the modulation drive amplitude, PZT dynamics, or electronic gains could be possible causes of change over time in the sine signal.

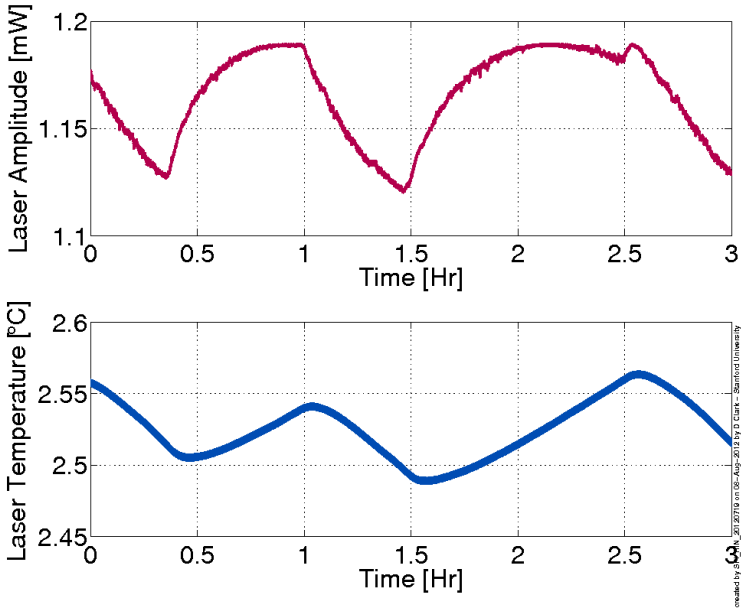

Figure 5.11: Power output of the laser source and temperature fluctuations of the laser housing. It is difficult from this to determine what is the cause and what is the effect.

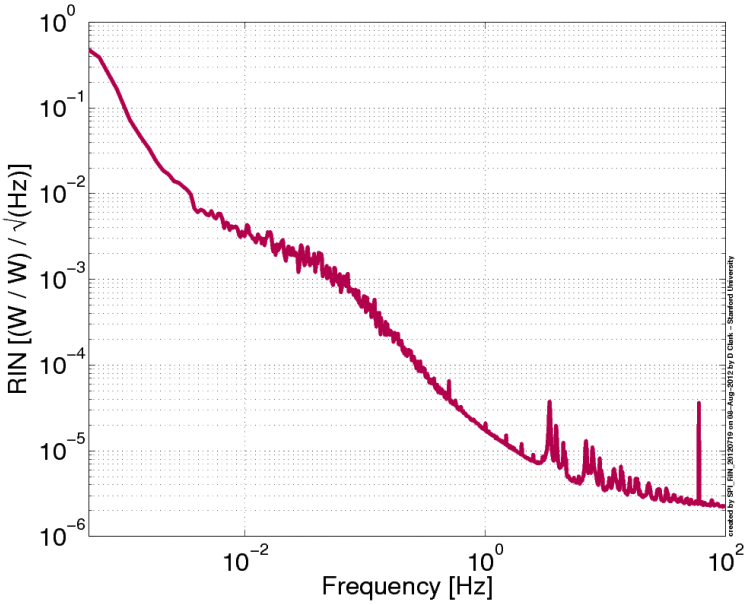

Figure 5.12: The Relative Intensity Noise (RIN) of the laser as tested. This is obtained by taking the recorded data, dividing by the average power before calculating the root of the mean square spectral density.

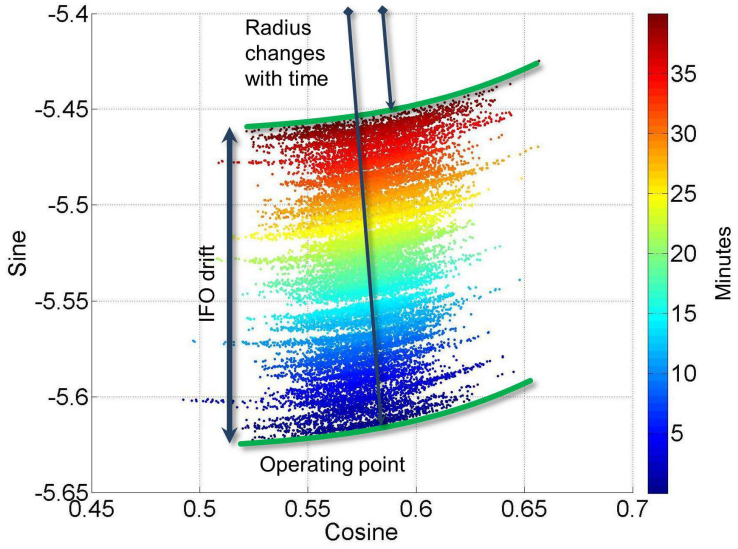

Figure 5.13: A 40 minutes long data segment recorded from the prototype SPI in fringe counting mode shows the radius of the arc segment traced by the sine and cosine signals decreasing through time. In this example the sine signal reduces by 3% while the cosine signal fluctuations remain roughly constant. Dark blue colors on the plot correspond to the data at the start of the experiment with dark red colors corresponding to the end after 40 minutes.

While under optical angle feedback control in pitch and yaw, the SPI is impervious to amplitude noise (**Figure 5.14** (a)). However, when the optical beam is not controlled to the center of the QPD, amplitude noise starts to affect the output angle signal. This is shown in schematic form in **Figure 5.14** (b) where a change in an off-center beam appears as change in position (which is interpreted as a change in the angle) due to the higher proportion of signal in quadrant **B**.

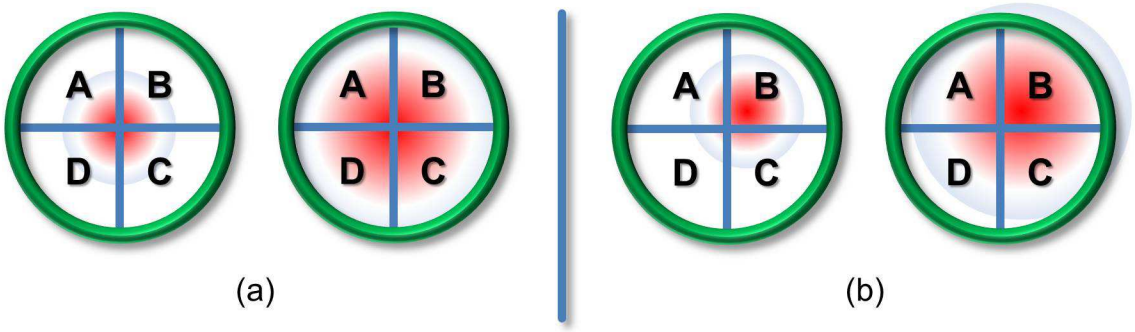

Figure 5.14: An incident beam is shown on the quadrants of the QPD. If the beam is centered on the detector, then amplitude fluctuations of the incident light affect all quadrants equally and the noise coupling is small (a). As the beam is offset on the detector, any changes in amplitude become apparent position changes (b). This error could be reduced by normalizing to the total beam power on all quadrants but this was not done in the analog circuitry (Appendix E). Instead, this error effect was corrected in real-time by the control software.

The prototype SPI has a launch laser beam monitor. The incident beam on this QPD is not actively controlled to the center so RIN affects the measurements. To correct for this, the incident laser power was summed over all of the quadrants and then the expected effect subtracted from the angle signals. The expected effect is estimated by taking the sum of the power in all quadrants, low-pass filtering it, and then multiplying by a scale factor. The scale factor used was determined by taking the best linear fit between the QPD sum data and the respective angle data (pitch or yaw) over a range of angles.

From these measurements, the RIN of the laser is not likely to be a limiting factor in either the length sensing or the closed loop angle measurements of the SPI. The launch angle open loop measurements are affected by RIN but these effects are

reduced by the real-time subtraction of the expected coupling.

5.5.4 Electronics Noise

Electronics are plagued with multiple sources of excess noise, from the Johnson-Nyquist noise of passive resistors to the noises associated with operational amplifiers. Throughout the design and construction of the SPI prototype, care has been taken to reduce the effect of electronics noise by using low-noise pre-amplifiers that are suitably matched to the impedances of the input. Extra care taken limited the majority of the noise contribution to the first amplifier stage.

5.5.4.1 Photodetector Circuit

The interferometric photodetector circuit's main noise source is the transimpedence pre-amplifier's voltage and current noise coupled through the feedback resistor. The feedback resistor itself exhibits Johnson noise but is designed to be less of a contribution than that of the operational amplifier. The noise of the circuit was measured with a spectrum analyzer in the dark state with the photodetectors covered.

5.5.4.2 PZT Amplifier

piezo-electric transducers (PZTs) require high voltages for actuation. The PZT installed in the prototype SPI exhibits a range of about 2 μm over 300 V. The high voltage from the DC power supply is controlled by a high voltage operational amplifier. The electronics noise contribution of this amplifier circuit was measured and plotted. The voltage gain of the PZT amplifier is: $G(s) = 550\frac{\mathrm{V}}{\mathrm{V}}$.

5.5.4.3 Analog to Digital Converter

The SPI prototype data was recorded in the aLIGO CDS computer system. This utilized a 16 bit A/D system after an anti-aliasing filter. The ADC electronics noise was measured to verify that it was not a contributor to the overall noise of the system.

5.5.4.4 Air Current Induced Electronics Noise

The SPI utilizes pre-amplifier circuitry both for the interferometer fringe sensing and for the angle sensing at the QPD. Tests of operational amplifiers have indicated that potting circuit boards reduces low frequency noise, which was also mentioned in a semiconductor data sheet (LTC, 1995). This is likely because potting decreases the effect of convective air currents of components on the board. This is not a noise source of concern because the SPI is operated under vacuum.

5.5.5 Laser Beam Launch Stability

As long as the interferometer contrast ratio remains high, the differential distance sensing between adjacent platforms is not affected by the directional launch stability of the free-space coupled light. The contrast ratio is defined as the ratio of high to low voltage on an individual photodetector across a fringe. This is not the case for angle sensing. Measurements were made of the fiber-launched light on the QPD and are included in the angle sensing noise budget (as documented in Appendix G). This is the largest noise contribution to the SPI angle sensing. Since these are angular measurements, this launch noise should be constant regardless of the separation between measurement platforms.

5.5.6 Optical Fiber Noise

In order to maintain the low phase noise of the laser, it is critical that the delivery fiber be kept still. Earlier tests of a balanced arm interferometer which utilized single mode (SM) fiber for the reference arm indicated that phase noise can be a significant problem in optical fiber. The fiber used in the prototype is all polarization maintaining (PM) single-mode fiber. While this fiber is less susceptible to changes in polarizations due to mechanical disturbance, it is desirable to reduce fiber motion as much as practical. As an added precaution, any light in the off-axis polarization is removed by a polarizing beam splitter. Additionally, any noise introduced by the fiber in the SPI prototype would already be coupled into the laser frequency noise measurement as shown in **Figure 5.10**.

5.5.7 Mechanically Induced Noise

The SPI components are mounted on an aluminum, 25 mm thick optical breadboard. The high thermal conductivity of the aluminum helps reduce temperature gradients across the board, however, the high CTE of aluminum is detrimental to geometrical stability. Optic mounting posts were intentionally kept short to reduce Abbé offset and to increase the stiffness of the structural loop. The breadboard is located on the optical platform of the Tech Demo, which is in vacuum limiting convective thermal disturbances. The platform's optical table has a very high thermal resistance to the outside through two sets of three maraging steel flexures. This results in the majority of the heat transfer coming through radiative coupling to the vacuum vessel. This also helps limit thermally introduced mechanical noise of the system to lower frequency with characteristic times of: $\tau \approx 40$ hours.

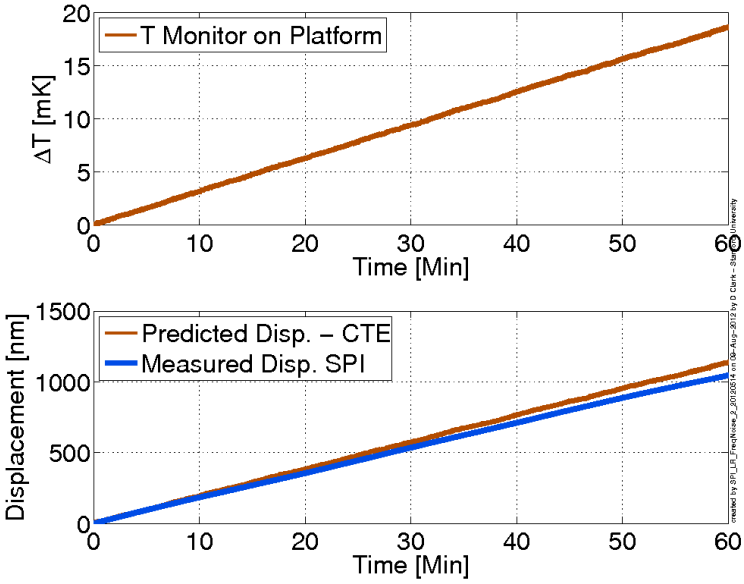

Figure 5.15: Temperature change of the Tech Demo platform and corresponding differential interferometer arm length change with a 2.58 m difference in nominally fixed arms. This change in differential arm length is compared against what would be expected for the corresponding temperature change and the coefficient of thermal expansion for Al-6061.

During the laser frequency stability tests, the temperature induced arm length

growth was quite evident (**Figure 5.15**). For this plot, thermal changes couple in to the arm length difference between the reference arm and a fixed length arm used to measure frequency stability ($\Delta OPL = 3.01\,\mathrm{m}$). With temperature monitors on the Tech Demo platform a characteristic plot of the temperature stability was calculated using several hours of data at vacuum (**Figure 5.16**). By applying the temperature change, the coefficient of thermal expansion for Al-6061, and the geometries of the test interferometer, a prediction of the effect on the prototype interferometer can be made. The effect of this temperature noise can be predicted in terms of interferometer length changes through the relationship: $Displacement = T_{\mathrm{stability}} \cdot CTE \cdot L_{\mathrm{reference\ arm}}$ where the $L_{\mathrm{reference\ arm}}$ for the SPI prototype is 11 cm. The temperature only affects the reference arm because in the other interferometer arm, as the measurement arm between the Tech Demo and the RPP, any changes are assumed real as the measurement is referenced to the beamsplitter locations.

In practice the interferometer does not experience as large a change in length as would be expected consistent with the discrepancy in this test of 9 %. For implementation in aLIGO, other materials such as Invar might be a better choice reducing this noise source.

5.5.8 Changes in the Index of Refraction of Air

Temperature, pressure, humidity, CO_2 content, and contaminants such as hydrocarbons all have an effect on the index of refraction, n, of the air. The overall effect of air has been measured by the unbalanced arm IFO during the characterization of the frequency noise of the laser (**Figure 5.17**). The excess phase noise at low frequency is evident in the difference from the air to vacuum cases. The air and vacuum measurements do not converge at high frequency because the contrast of the interferometer for the air tests was slightly better. Since both the prototype and the aLIGO SPI are to be operated at vacuum this noise source is not a concern.

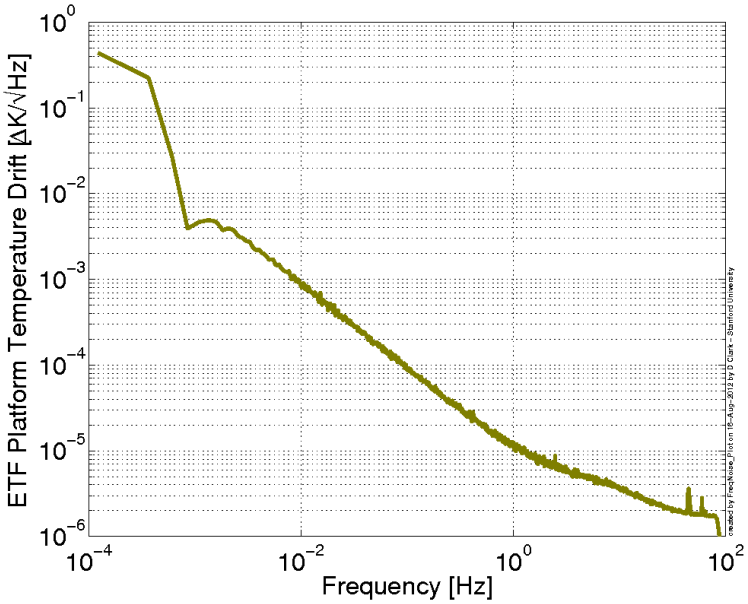

Figure 5.16: The temperature stability of the Tech Demo platform as measured over several hours by a sensor directly underneath the optical breadboard. The induced length change from the expansion of the aluminum can then be predicted for a reference arm length of 11 cm.

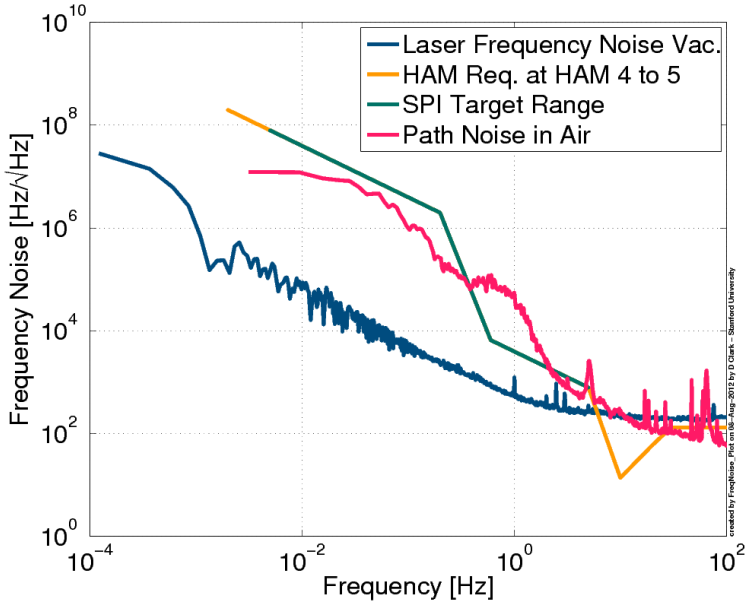

Figure 5.17: The index of refraction of air, n, causes phase changes in the arms of the interferometer creating substantial noise at low frequency (over 3.01 m ΔOPL). The SPI will be operated at vacuum so this noise source is not a concern. The SPI target frequency range ends just short of a notch in the requirements for the HAM 4 to 5.

5.5.9 Length Sensing Noise Budget

The above noise sources affecting the SPI length sensing were measured or calculated and plotted together for comparison (**Figure 5.18**). All of the noises were referenced to displacement distance between platforms and compared with the SPI requirement for sensitivity. Of the noise sources considered, most remain fixed regardless of the separation distance between platforms. The one exception is the laser frequency noise which increases proportionally with differential arm lengths of the interferometer. Since this is likely the limiting noise source, two curves were plotted. One curve represents the laser frequency noise contribution to the prototype operating with an 8.9 m separation distance between platforms in the ETF. The other curve is what the frequency noise contribution is expected to be for the greater HAM 4 to HAM 5 distance in aLIGO. Along with frequency noise, the geometrical stability of the short reference arm, as influenced by temperature, is also a significant concern. For the SPI prototype this reference arm was 11 cm long on an aluminum optical breadboard. The expansion of this plate over time with temperature induces as much noise into the prototype measurement as the laser noise.

Even for the stringent case of HAM 4 to HAM 5, the SPI length sensor should work well over the SPI frequency range. All of the noise sources quantified are well below the requirement at low frequency and have at least a factor of 5 at higher frequencies. The SPI length sensor should provide accurate information meeting the requirements.

5.5.10 Angle Sensing Noise Budget

The pitch and yaw measurements of the SPI are accomplished through optical lever angle sensing. Because of the principles of operation of the optical levers, many noise sources critical to the length sensing do not apply. The noise sources have been measured or calculated and are plotted relative to the angle sensing SPI requirements in **Figure 5.19**. The angular nature of the measurement along with the noise sources mean that they should remain constant regardless of the separation distance between the host and remote platform. One exception to this is that the contributions of

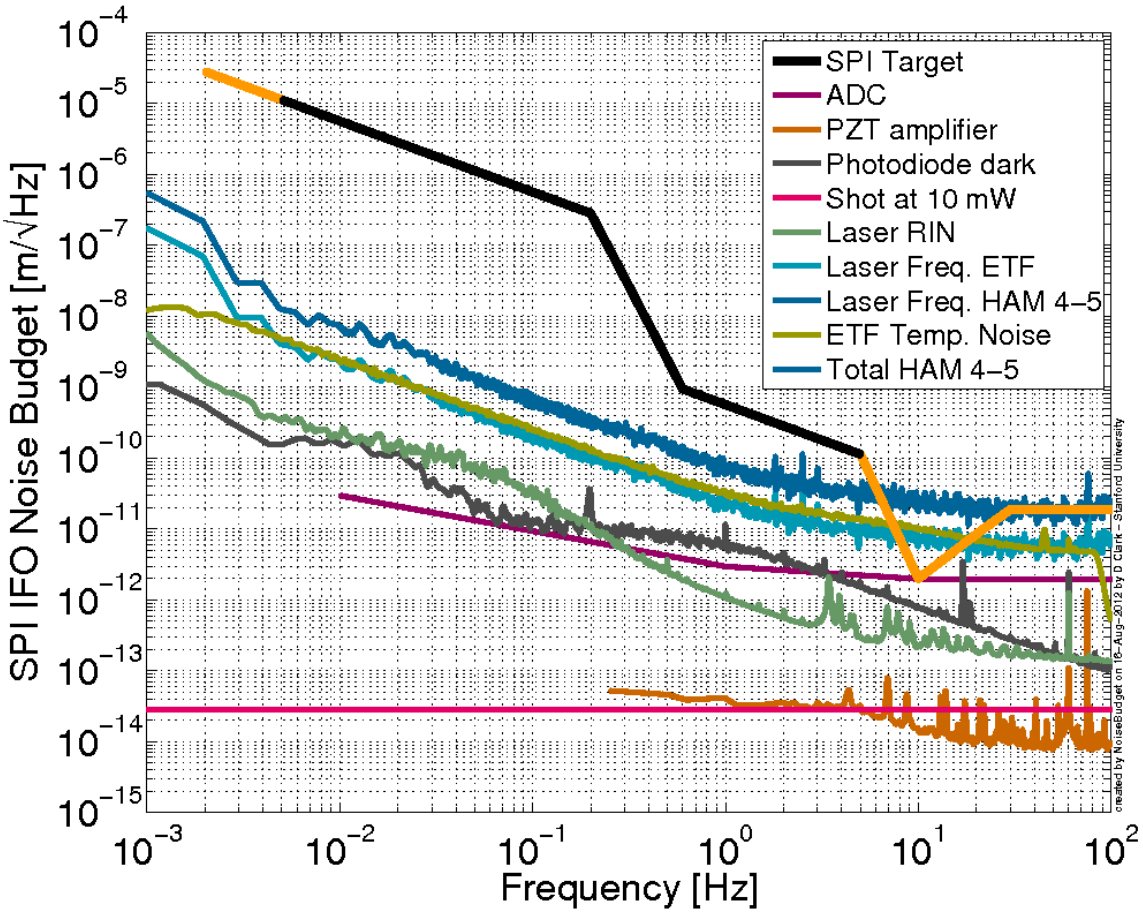

Figure 5.18: Length sensing interferometric noise budget. Measured noise sources affecting the interferometer signal are plotted in terms of sensing distance relative to the SPI target. Most noise sources are fixed regardless of the arm length of the sensing arm. One exception is the laser frequency noise that scales proportionally with the difference of the sensing to reference arm. The frequency noise is plotted twice, once for the ETF platform to platform sensing arm distance and again for the HAM 4 to HAM 5 distance in aLIGO. The SPI target frequency range ends just short of a significant notch in the HAM 4 to 5 requirement curve.

electronics noise of the QPD circuitry would decrease with added differential platform displacement.

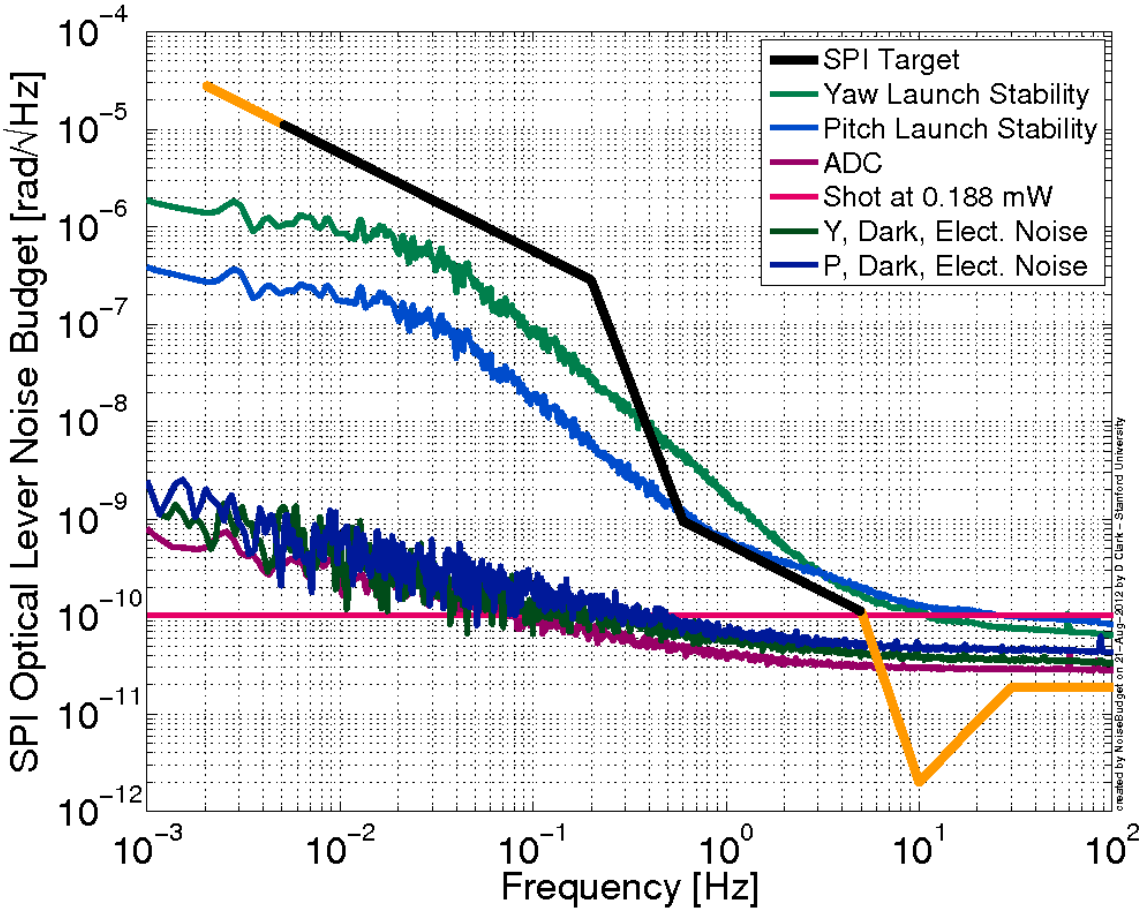

Figure 5.19: Angle sensing, pitch and yaw, noise budget. The largest source of contributing noise is the measured launch stability of the light from the fiber. These noise sources should remain constant regardless of platform to platform distances. The exception to this is electronics noise of the QPD circuitry whose effect would decrease with added separation distance.

Of the optical lever noise sources measured, the largest is the apparent launch stability of the light from the fiber which is orders of magnitude larger at lower frequency than the measured, dark noise of the sensor (electronics noise). It is unclear what all of the mechanisms are for the large apparent launch noise, which was investigated further and documented in Appendix G. One possible noise source is from reflected

light from the length sensor as shown in **Figure 7.1**. Regardless, below 0.4 Hz, the angle sensor meets the SPI sensing target. Unfortunately, at higher frequencies this is not the case. This noise plot indicates work is needed to improve the SPI angle sensors.

5.6 Control and Data Acquisition System

Most of the real-time control of the aLIGO systems is done through the Control and Data acquisition System (CDS). CDS is responsible for both the high speed real-time control (up to 64 kHz) and the recording of important process and data channels (Bork et al., 2001).

The SPI prototype was implemented using the aLIGO CDS as its control method so that compatibility for future deployment in aLIGO could be established. Since the Tech Demo is currently running on the CDS, integration with the Tech Demo control diagrams were simplified. During the commissioning of the RPP, it was switched from a dSPACE platform to run on the CDS (Appendix F).

Control flow in CDS is defined through a Matlab Simulink model file in which only certain blocks are supported. This model is then built by the Real-time Code Generator (RCG) before it is deployed on a dedicated Linux based platform.

An advantage of CDS is that several models can be run simultaneously on different processor cores of the Linux front-end computer. For the SPI prototype, the control and data recording was handled as part of the Tech Demo control model. Information from the SPI was then passed to the RPP, which was controlled separately.

5.6.1 Implementation of Arctangent

The arctangent is necessary for calculating the phase, ϕ, in the fringe counting length sensing mode of the SPI. Initially this mode was prototyped using dSPACE as the real-time control software. However, when the SPI control was implemented in the aLIGO CDS, blocks such as atan, unwrap, and sample and hold blocks were not supported. That meant that inline C functions had to be written. Because these are

inline functions, standard libraries such as math.h could not be included.

A splined approximation to the function was adapted for the C89 standard and implemented. This was tested and verified to have the same output from the real-time inline function as the offline Matlab function provided (**Figure 5.20**).

One problem encountered was that CDS had difficulty whenever the arctangent function needed to divide by a small number. This error was corrected by taking the quotient and divisor of the input and inverting them if the quotient was larger than the divisor. If the reciprocal of the input was used, then the output of the arctangent function was phase shifted by $\pi/2$ in order to maintain the correct relationship. This is represented as follows:

$$\phi = \arctan(\frac{a}{b}) = \arctan(\frac{b}{a}) - \frac{\pi}{2} \tag{5.10}$$

Where a is the cosine signal and b is the sine signal from the photodetector and demodulator respectively.

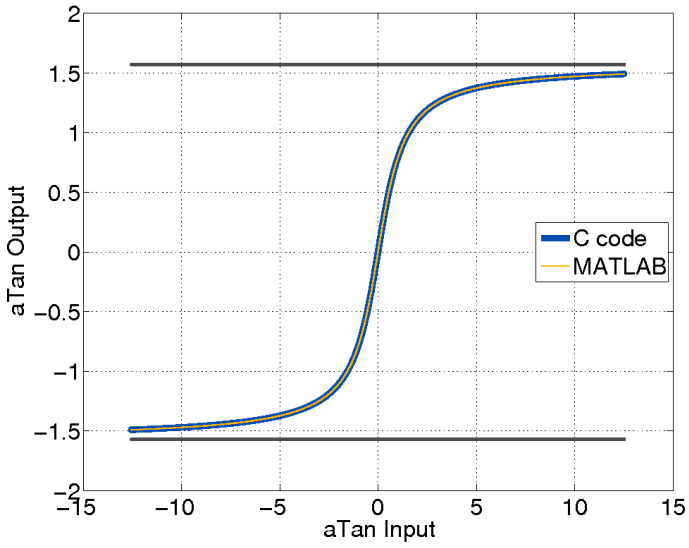

Figure 5.20: For SPI prototype integration into the CDS real-time control computer system, the arctangent had to be implemented as a C code inline function. This plot validates that the real-time C code output follows the offline Matlab code accurately.

5.6.2 SPI Prototype Control

The SPI prototype was controlled entirely from the CDS using the Experimental Physics and Industrial Control System (EPICS) and interfaced through the Motif Editor and Display Manager (MEDM) screens (Carwardine, 1995) and (Evans, 1999).

The Matlab Simulink signal flow model diagram used by the prototype SPI is shown in **Figure 5.21**. Here the input channels that are monitored include the balanced photodetector pair from the interferometer, the demodulated sine and cosine signals, the return QPD x, y, and sum channels as well as the launch QPD channels. The ADC card records the interferometer channels through an anti-aliasing filter. All of the electrical signals are fed out of the vacuum wall through DB-25 vacuum feedthroughs. The QPD circuitry drives differential, balanced signals while the interferometer photodetector circuitry signals are all single ended and ground referenced.

The model provides real-time control of the length sensing mode, whether mid-fringe locking or fringe counting, calibration of signals, and determination of the phase, ϕ (in fringe counting mode) that allows the calculation of equivalent displacement. While the model defines signal flow paths, the MEDM screens provide the interface to operate the instrument.

The SPI prototype uses three MEDM screens enabling real-time user control and monitoring. The first screen is an overview screen that displays the differential length, pitch, and yaw between the two platforms (**Figure 5.22**). It also allows the length sensing mode to be switched from mid-fringe locking (SR) to fringe counting mode (LR) and displays which mode is currently operating by highlighting the appropriate measurement with a blue box. The differential seismometer signal is shown as well as the PZT control level, which is useful while in the mid-fringe locking mode to determine if the platforms are close to their control authority limits. Finally, the calibrated pitch and yaw are plotted as x and y components with a few seconds of persistence allowing real-time monitoring of the angular motion.

While the overview screen displays most of the critical information, it does not allow for control of the SPI beyond selection of the length sensing mode. The MEDM setup screen provides much more control by allowing gains, filters, and signal flow to be adjusted (**Figure 5.23**). This screen provides the interface to calibrate the signals

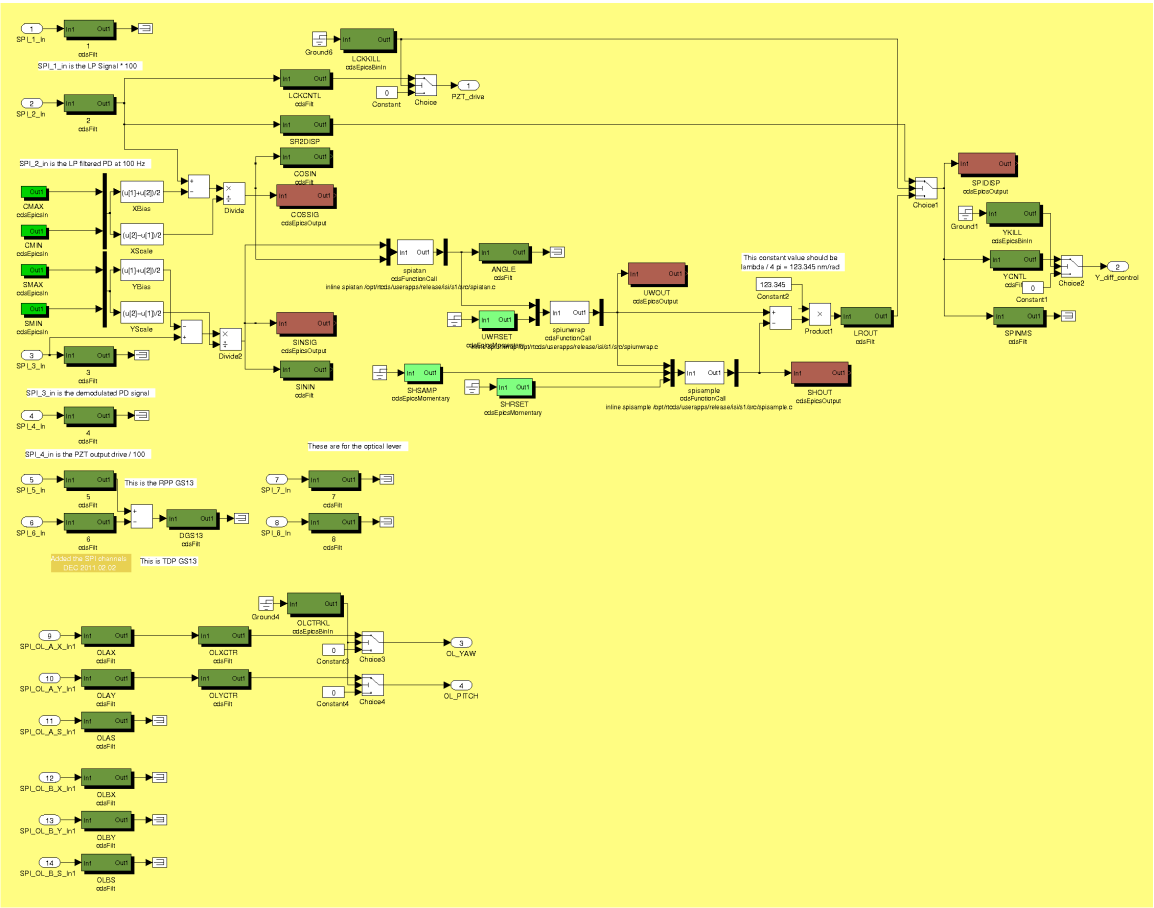

Figure 5.21: The SPI computer signal flow is defined in a Matlab Simulink model, which is then compiled by the RCG to run on the real-time Linux front-end computer.

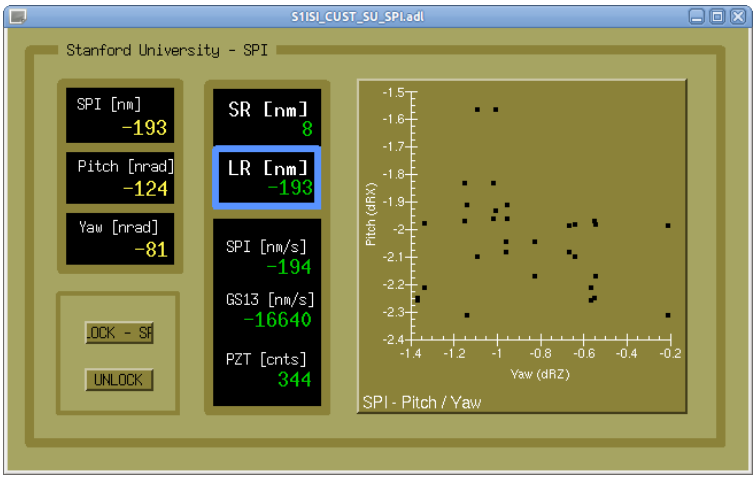

Figure 5.22: SPI prototype user interface is provided through MEDM screens. This overview screen provides the most relevant information from the SPI, such as calibrated real-time signals.

and the GS-13 seismometers. It also includes switches allowing the SPI signals to be propagated out to the higher level Interferometer Sensing and Control (ISC) channels. Finally, the status of the signals in the fringe counting mode are monitored. The sine and cosine terms are plotted against each other raw (tracing an ellipse) and normalized (tracing a circle). If the interferometer's contrast changes the normalization will not be valid and it will become obvious on this plot. The algorithms such as phase angle ϕ calculations and unwrap values are also monitored and can be reset or their output zeroed. This screen provides the main interface for the SPI prototype length sensing control.

The final MEDM screen provides the calibration and monitoring of the QPDs and associated optical levers (**Figure 5.24**). Both the launch and return beam's pitch, yaw, and power are calibrated and displayed. Control filters are also included and can be engaged in the output before the information is sent into the ISC channels.

These MEDM screens provide the interface for calibrating, controlling, and directing the signals originating from the SPI. Since the aLIGO CDS specific problems, such as the custom arctangent, unwrap, and sample and hold code have already been solved in the prototype, implementation of an SPI into aLIGO should be simplified.

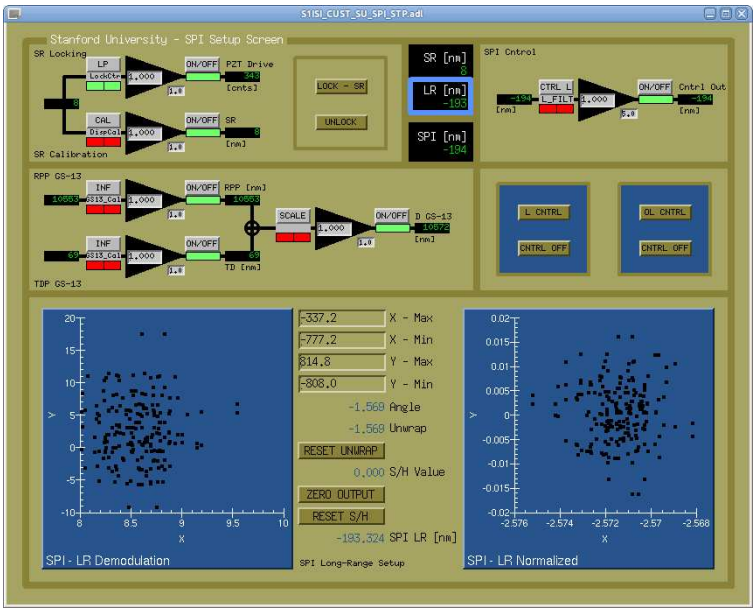

Figure 5.23: SPI prototype MEDM setup screen allows control of calibrations, gains, and signal flow paths. The interferometric length sensing modes are also selected, monitored, and controlled from here.

5.7 Independent Instrumentation

In order to quantify the SPI differential length measurement, two Geotech GS-13 seismometers were installed along the SPI's sensitive axis. One was located on the host platform while the other was installed on the remote platform. These seismometers are extremely sensitive in the 1 to 10 Hz frequency band but are also, by nature, susceptible to tilt-horizontal coupling errors. The error from this coupling is explored in more detail when the prototype's results are analyzed in Chapter 6. By subtracting the signals from both sensors, the differential velocities between the platforms can be recorded. This velocity measurement is then mathematically integrated resulting in a displacement measurement.

Platform motion of the RPP and Tech Demo as recorded by the seismometers is plotted in **Figure 5.25**. The noise floor was also computed for the GS-13 seismometers and is plotted for reference. The noise floor was determined by calculating the uncorrelated noise across multiple sensors and so does not include tilt-horizontal

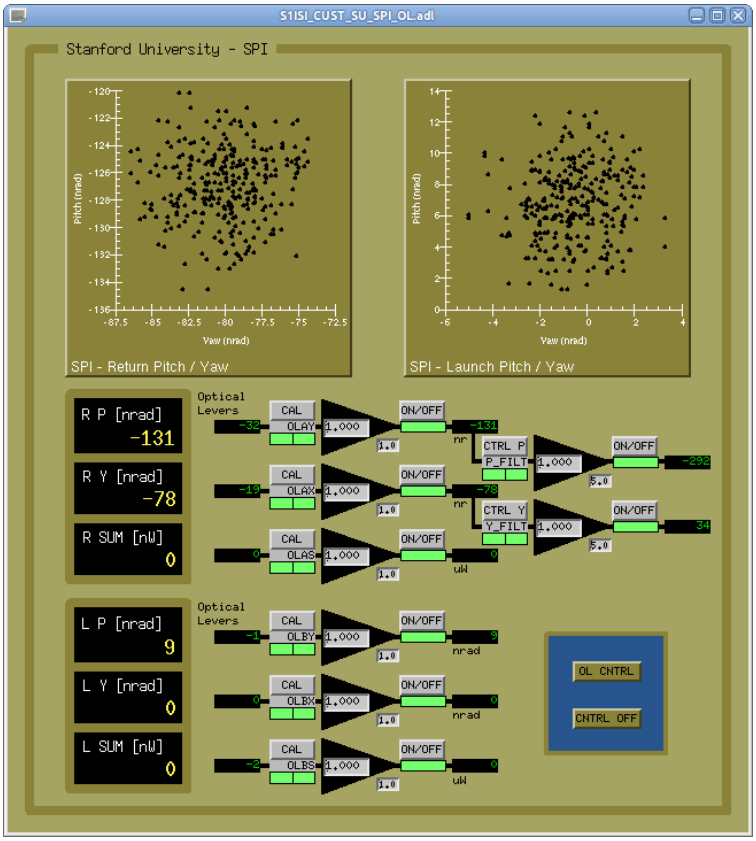

Figure 5.24: The SPI prototype optical levers sense the differential pitch and yaw between the platforms. The angular data is displayed and controlled on this MEDM interface screen.

coupling errors inherent to horizontal seismometers.

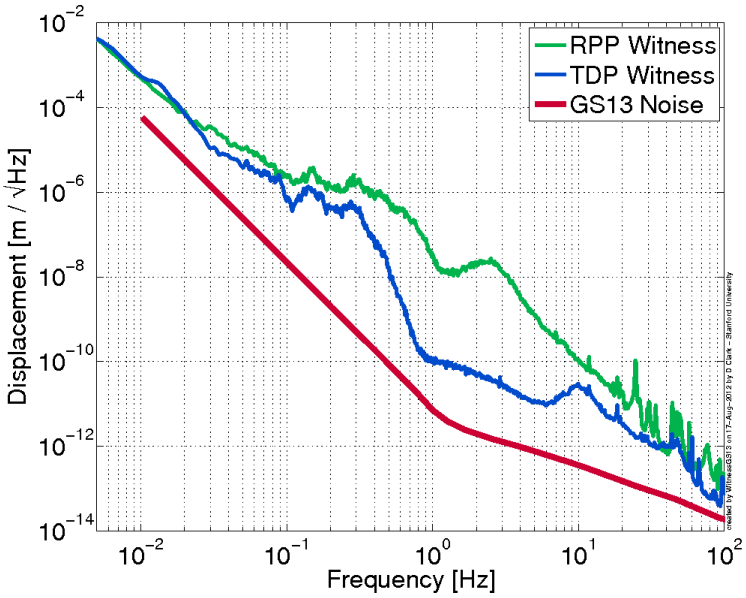

Figure 5.25: GS-13 seismometers were installed on the host (Tech Demo) and remote (RPP) platforms. The plotted motions were recorded with both platforms under local control. The GS-13 noise floor is also plotted but does not include errors introduced by tilt-horizontal coupling.

Chapter 6

Differential Platform to Platform Control

To help validate the proof of concept for the Seismic Platform Interferometer (SPI), the differential displacement between the two platforms was measured and controlled. These tests were carried out in the Stanford ETF between two adjacent in-vacuum ISI platforms. The details of the control flow, feedback loop filter design and results are documented in this chapter.

6.1 Control Flow

The SPI signal was used to control the differential length (L), pitch (P), and yaw (Y) between the host and remote platforms in the ETF. Since both platforms are controlled locally by the Control and Data acquisition System (CDS), the entire control law was implemented digitally. The control flow is represented in **Figure 6.1** showing that each platform is controlled locally relative to its individual sensors. The SPI signal is then sent into the Interferometer Sensing and Control (ISC) streams, which are high level channels used to command locations for particular platforms and their associated optics. These ISC signals can then be acted upon by the platforms through the addition of the ISC information to their blended sensors in the local control filters. In the case of the SPI prototype testing, the L, P, and Y signals were

used to control the remote RPP.

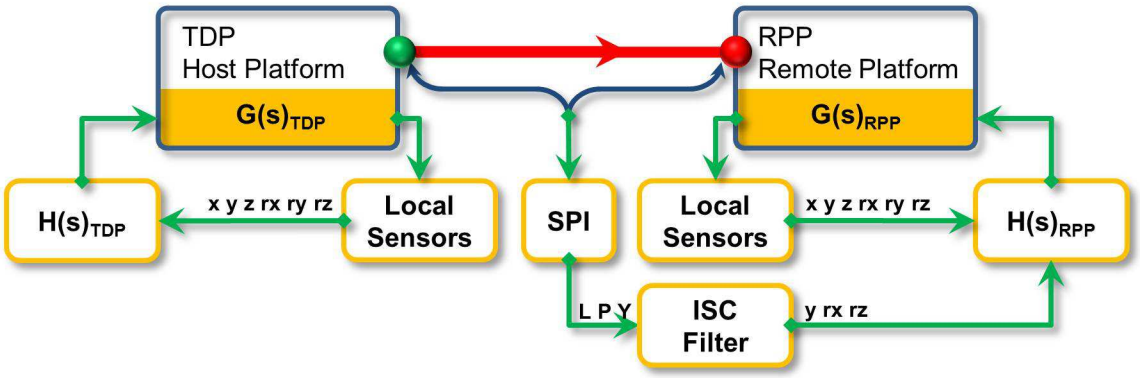

Figure 6.1: The RPP and TDP are under local feedback control using their respective sensors. The SPI signals are fed into the Interferometer Sensing and Controls (ISC) channels where they are then acted upon by the RPP.

By controlling the RPP, the Tech Demo becomes the reference point to which the RPP position is controlled through the SPI. While many configurations for control are possible, this particular configuration was chosen because it represented a more challenging condition in which to test the SPI sensing capabilities. While neither the RPP nor the Tech Demo are aLIGO ISI platforms, they do provide an adequate testbed. When these platforms are under local control, their performance along the local y axis was plotted in **Figure 5.25**. It becomes obvious, referencing this, that the performance of the Tech Demo is superior to the RPP. This is expected as the TDP is a two-stage active system whereas the RPP is single-stage. This forms the basis for the Tech Demo becoming the reference standard to which the RPP is controlled through the SPI.

6.2 Control Design

Following the block diagram in **Figure 6.1**, driven transfer functions were recorded for each of the SPI signals. These were accomplished by driving signals open loop into the ISC channels while recording the response in the SPI output. These transfer functions, although somewhat noisy due to ground motion excitation of the platforms,

allow the ISC control filters to be designed.

For implementation in aLIGO the target frequency band is $5 \cdot 10^{-3}$ to 5 Hz. However, since the GS-13 seismometers are extremely accurate from 1 to 10 Hz, for the prototype implementation it is desirable to be able to show improvement in the most sensitive range of the seismometers so the control band was chosen to be from $5 \cdot 10^{-3}$ to as high as 40 Hz, which is different than the aLIGO band.

The controllers were designed and analyzed using Bode plots comparing the plant (the driven transfer functions from the ISC channel to the SPI signal), the open loop ($plant \cdot controller$) response, the closed loop ($\frac{plant}{1-plant \cdot controller}$) response, and the controller sensitivity ($\frac{1}{1-plant \cdot controller}$). These are displayed in **Figures 6.2**, **6.3**, and **6.4** for the length, pitch, and yaw dimensions respectively. The filter design is based on a desire for a gain of greater than 10 for frequencies below 0.5 Hz. An even higher gain is desired if stability can be maintained. A high upper unity gain frequency (UUGF), which is the crossover frequency for a magnitude of 1, of about 20 to 50 Hz was implemented in the length controller. In order to obtain the proper phase margin to the UUGF, a form of plant-inversion was used. Several notches were added at higher frequencies to reduce resonances and noise. Even with this, the filters are expected to introduce excess noise into the RPP at higher frequency. For actual implementation of the SPI in aLIGO, the SPI control loops are expected to have an UUGF around 0.5 Hz and have minimal authority on the local isolation loops at 5 Hz and above. This should help prevent sensor noise from the SPI being projected onto the platform (**Figure 5.18**). While we intentionally designed a high UUGF for our testing, the aLIGO filters will likely be much more conservative.

The control filters are plotted in **Figure 6.5**. These filters were then implemented in their digital form in the CDS by using the Tustin (bilinear) approximation at a sampling rate of 4,096 Hz (Franklin et al., 1997).

$$H_T(z) = H(s)|_{s=\frac{2}{T}\frac{z-1}{z+1}} \tag{6.1}$$

The controllers that were implemented include:

$$H_{\text{length}}(z) = \frac{85.37z^8 - 507.2z^7 + 1171z^6 - 1156z^5 - 17.7z^4 + 1170z^3}{z^8 - 7.536z^7 + 24.87z^6 - 46.92z^5 + 55.38z^4 - 41.88z^3} \\ \frac{-1157z^2 + 493z - 81.82}{+19.82z^2 - 5.366z + 0.6367} \tag{6.2}$$

$$H_{\text{pitch}}(z) = \frac{2.388z^7 - 11.78z^6 + 20.85z^5 - 11.15z^4 - 11.94z^3}{z^7 - 6.271z^6 + 16.78z^5 - 24.81z^4 + 21.88z^3} \\ \frac{+20.7z^2 - 11.31z + 2.23}{-11.5z^2 + 3.328z - 0.4086} \tag{6.3}$$

$$H_{\text{yaw}}(z) = \frac{-0.9887z^8 + 5.856z^7 - 13.47z^6 + 13.18z^5 + 0.3476z^4 - 13.46z^3}{z^8 - 7.495z^7 + 24.57z^6 - 46.03z^5 + 53.9z^4 - 40.39z^3} \\ \frac{+13.19z^2 - 5.578z + 0.9191}{+18.92z^2 - 5.063z + 0.5928} \tag{6.4}$$

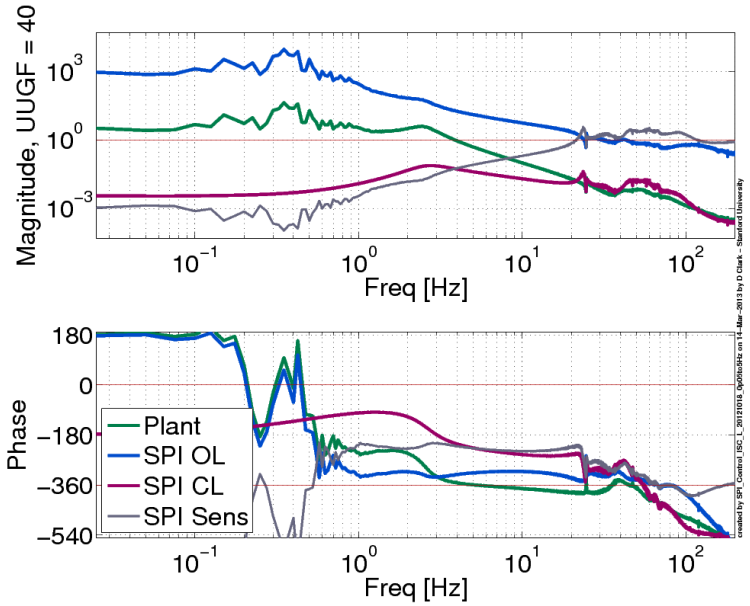

Figure 6.2: The control filter design Bode plot describing the differential length (L, or y in the local basis) as sensed by the SPI. In these plots, the OL response refers to the $plant \cdot controller$, the CL means $\frac{plant}{1-plant \cdot controller}$, while Sens is $\frac{1}{1-plant \cdot controller}$.

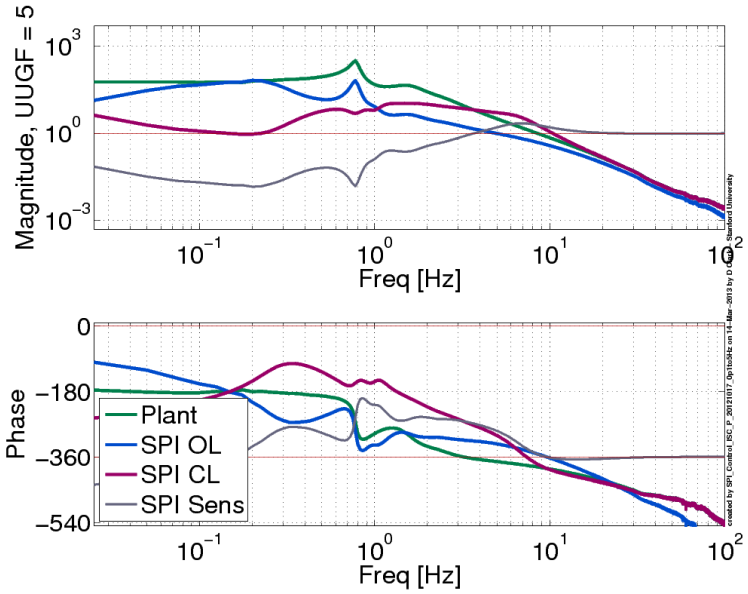

Figure 6.3: Differential pitch (P, or rx in the local basis) control filter design Bode plot as sensed by the SPI.

6.3 Control Results

The performance of the SPI controlled RPP was monitored by GS-13 seismometers in length, L, (y local basis). The differential pitch and yaw axes have no independent witness sensors. The full control of length, pitch, and yaw dimensions was achieved by first increasing the gain on the pitch and yaw loops. Once these loops were controlled, the gain of the length controller was then increased to the design point.

6.3.1 Length Results

Seismometers located on each platform provide better analysis opportunities than just the in-loop SPI length signal in the differential length dimension. The uncontrolled measurement of the differential length is shown in **Figure 6.6** where P2P refers to SPI measurements between the Tech Demo and the RPP. From this figure it is apparent that the differential GS-13 seismometer signals match the L signal over a wide frequency range. At frequencies above 25 Hz the SPI is limited by the laser

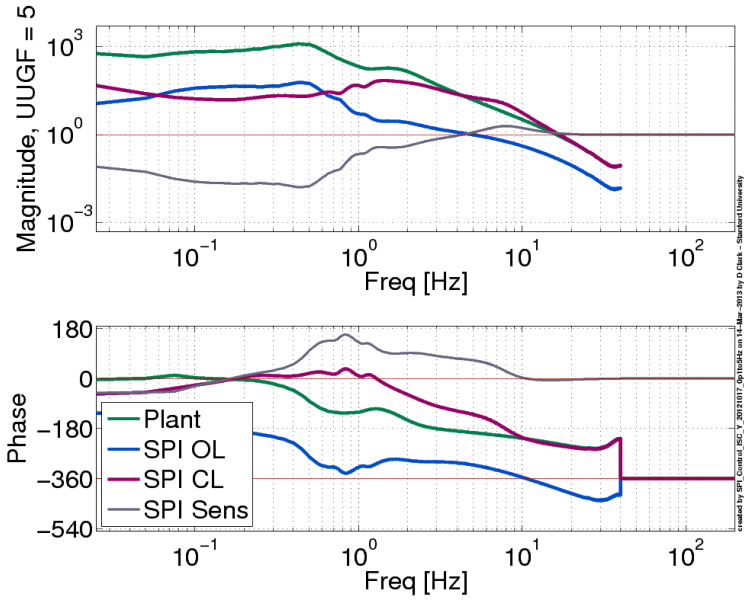

Figure 6.4: Differential yaw (Y, or rz in the local basis) control filter design Bode plot as sensed by the SPI.

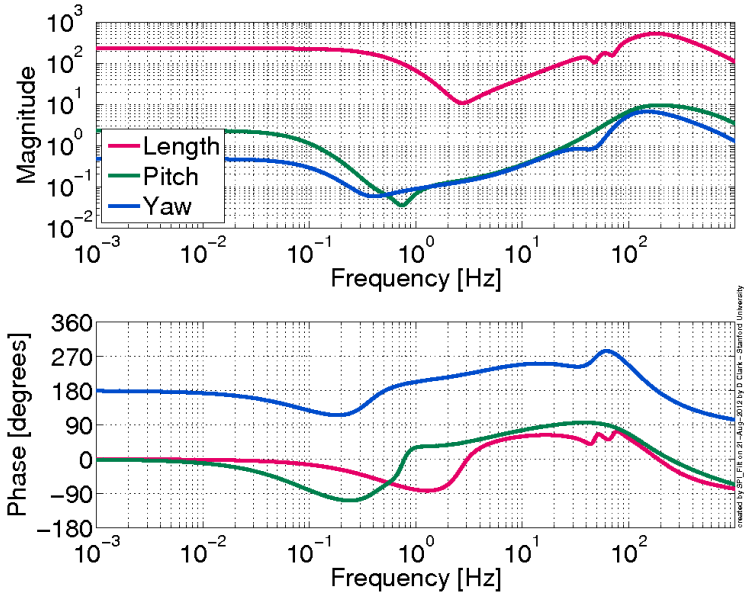

Figure 6.5: The digitally implemented filters as used for RPP control using SPI signals.

frequency noise as characterized in Section 5.5.2. At low frequency, below about 0.15 Hz, the seismometers quickly digress following what is likely differential tilt-horizontal coupling behavior.

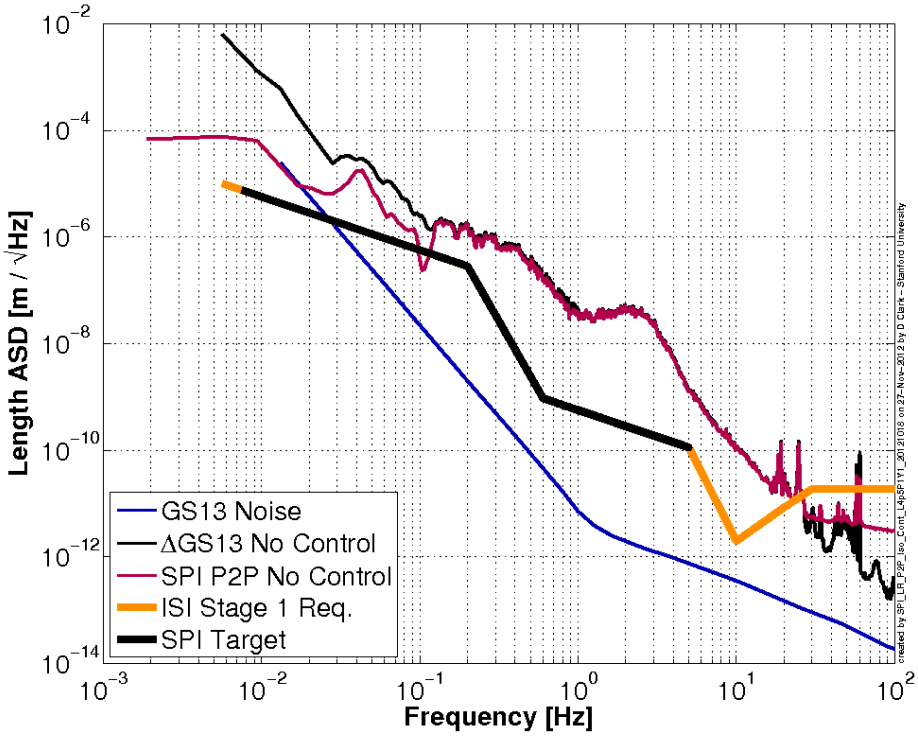

Figure 6.6: The differential GS-13 signal (ΔGS13) is compared to the SPI length signal (SPI P2P No Control), which both measure the displacement between the RPP and Tech Demo platforms. The high frequency end (above 25 Hz) of the SPI length, L, signal is at the frequency noise floor of the laser, inhibiting better measurements. The low frequency end (below 0.15 Hz) of the GS-13 signals quickly approach the instrument predicted noise floor and are also likely coupling tilt motion into the signal.

Once the RPP was servo controlled to track the Tech Demo by the SPI length signal, the GS-13 seismometers recorded a decrease in the motion (**Figure 6.7**). These GS-13s independently measure an order of magnitude improvement from 100 mHz to 5 Hz with the SPI enabled length control active. The in-loop SPI length measurement, however, indicates a greater reduction than just what the GS-13 seismometers indicate (**Figure 6.8**). Knowing the ISC control filters used to implement the control,

an estimation of the predicted motion attenuation levels can be calculated. This is shown in **Figure 6.9**, which shows a clear discrepancy between the expected differential GS-13 motion and the actual recorded motion when under control. It can be accepted that at frequencies below about 20 mHz the GS-13s are noise limited but this does not explain the majority of the discrepancy.

Since the geometry of the placement of the seismometers makes them sensitive to pitch motion (rx locally), an estimate for the tilt-horizontal coupling of differential pitch motion was established. By considering the tilting of the seismometers, as recorded by the SPI pitch signal, an estimate of the effect of tilt-horizontal coupling was plotted in **Figure 6.10**. This corresponds closely to the measured differential GS-13 signal and explains most of the discrepancy between the expected and actual differential GS-13 signals except for in the 0.13 to 0.45 Hz band. While it is believed that only the differential pitch between the platforms should couple into the differential GS-13 signal at low frequency, if we include the measured pitch of the Tech Demo along with the SPI differential pitch signal we get a closer match. Adding calibration lines might provide further insight into how the apparent Tech Demo pitch motion, along with the SPI pitch motion provides a closer match than when the SPI pitch motion was used alone.

The differential GS-13 seismometer signal closely matches the SPI length signal at frequencies above 2 Hz but dramatically follows the tilt coupling at frequencies below that. While the seismometers provide a nice, independent measurement, they are still susceptible to tilt-horizontal coupling and quickly approach their noise floor at low frequencies. They are excellent at validating the SPI length performance at frequencies above 2 Hz but their usefulness is limited at low frequencies. This is exactly why an instrument such as the SPI is needed!

Finally, sometimes it is useful to visualize the decrease in platform motion as the root mean square (RMS) motion in a particular frequency band. This is plotted in **Figure 6.11** where the RMS curve is the integration of the amplitude spectral density (ASD) data from high frequencies. The improvement in the total RMS motion down to 0.00187 Hz is visible in a reduction from $7.82 \cdot 10^{-6}$ m to $1.77 \cdot 10^{-9}$ m.

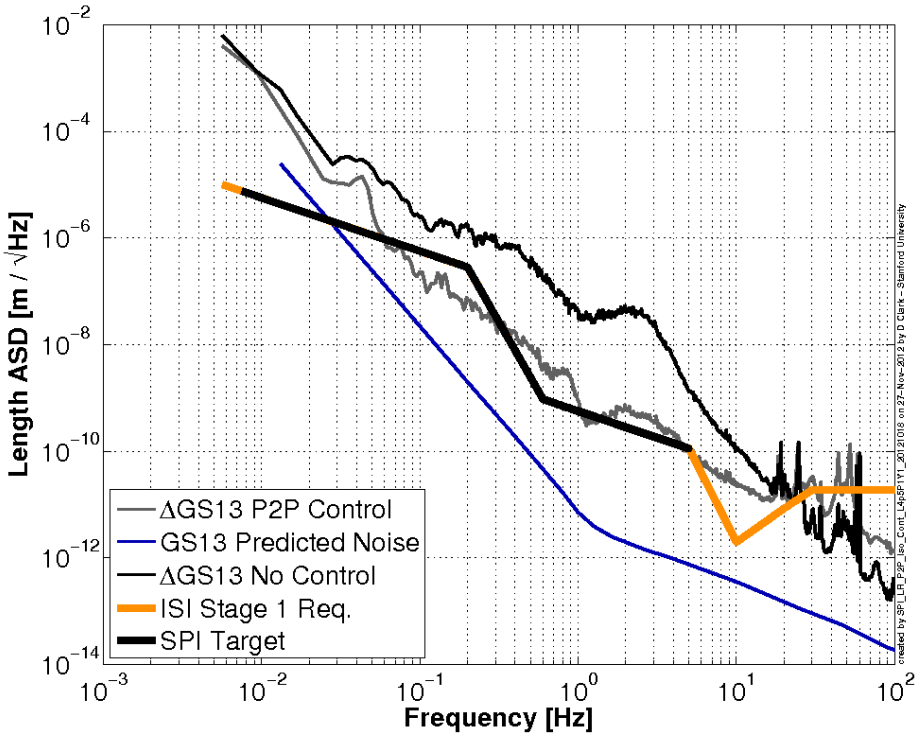

Figure 6.7: The differential GS-13 signal measuring the length between the RPP and the Tech Demo platforms is reduced when the RPP is controlled using the SPI L signal.

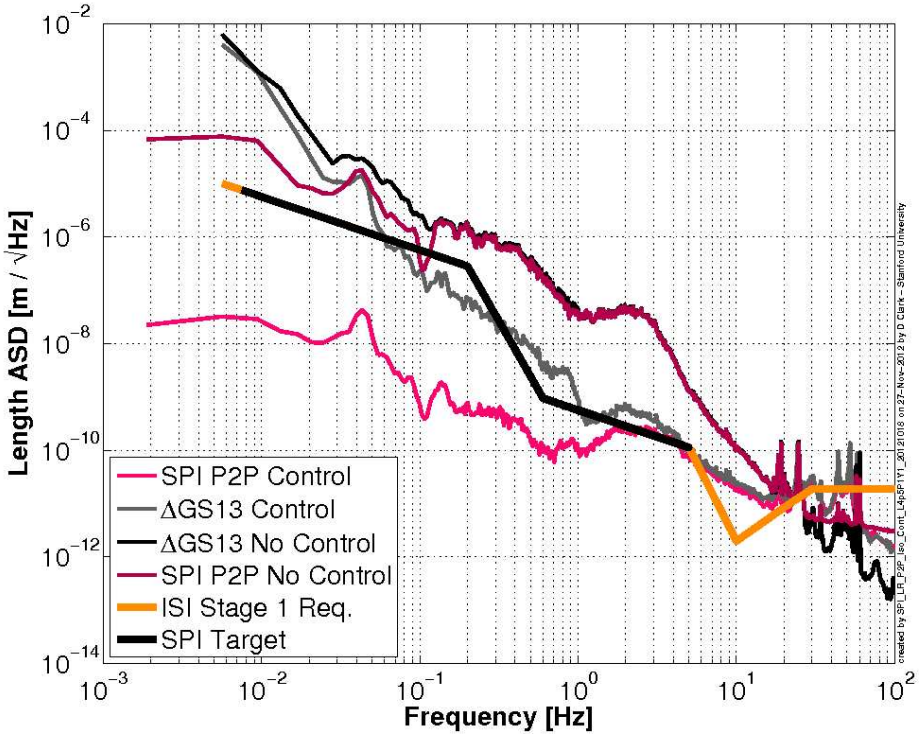

Figure 6.8: The in-loop SPI length signal (labeled SPI P2P Control) when the RPP platform is controlled shows better performance than the differential GS-13 signals indicate.

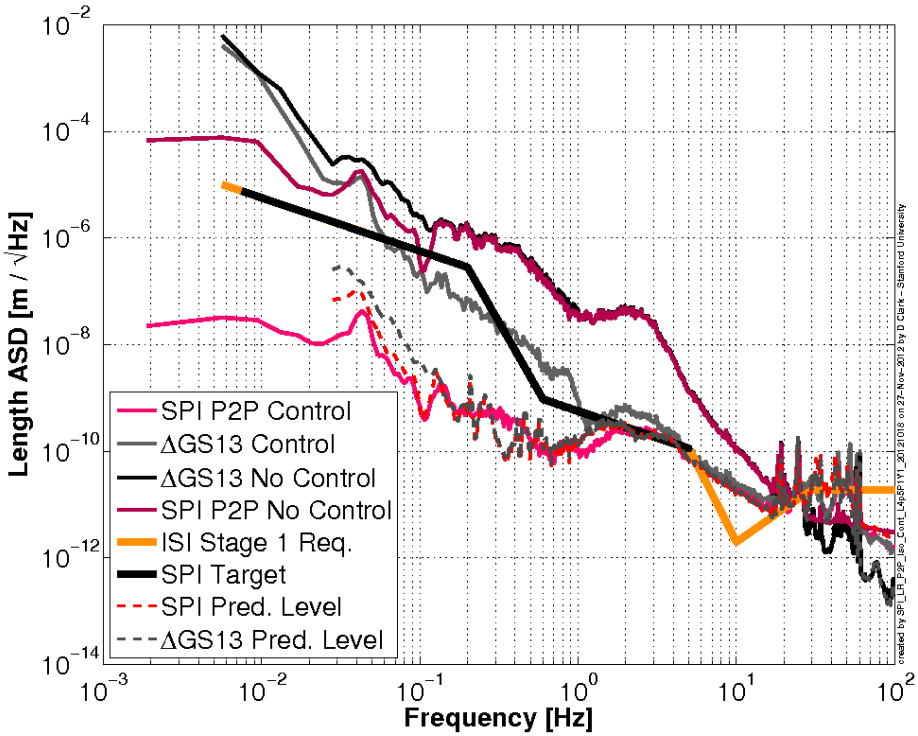

Figure 6.9: By knowing the implemented control filters, an estimate for the expected motion attenuation can be made. This shows that the recorded SPI length measured motion is close to what would be expected. The GS-13 signals, however, show a clear discrepancy.

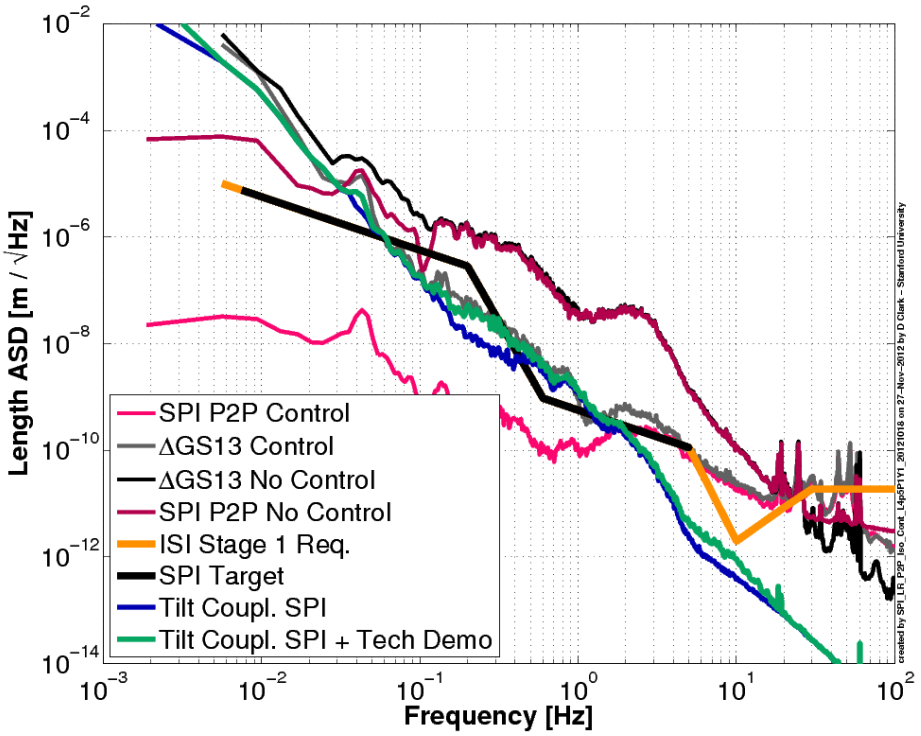

Figure 6.10: The discrepancy noted in **Figure 6.9** in the GS-13 signals seems to be related to tilt-horizontal coupling. Since the differential tilt (pitch) of the platforms is measured by the SPI pitch signal, an estimate for the tilt-horizontal coupling effect on the differential GS-13 signal is plotted in blue. The ΔGS-13 signal closely follows this except for the range of 0.13 to 0.45 Hz. If the pitch of the Tech Demo platform is added to the SPI pitch, the expected tilt-horizontal coupling matches the ΔGS-13 signal even closer, the reason of which is not clearly understood.

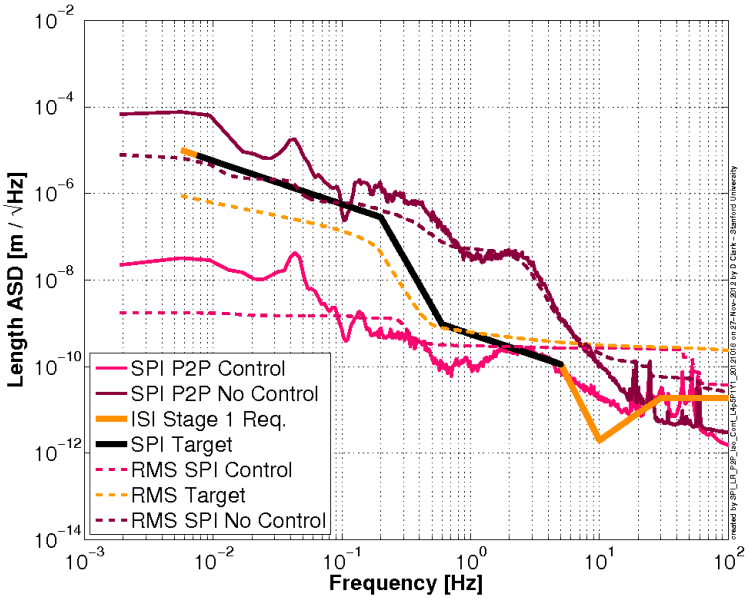

Figure 6.11: The in-loop SPI length signal and RMS motion integrated from high frequency both with, and without, control. The amplitude spectral densities are plotted along with their corresponding RMS levels in dotted lines. At the lowest frequency, the RMS of the SPI length signal is clearly better. The excess motion introduced at high frequency from the SPI onto the RPP can also be seen in the elevated RMS levels when under control from 10 to 50 Hz.

While the overall RMS reduction is impressive, some excess noise is being introduced at high frequencies. This is visible in the 10 to 50 Hz region. While reducing the loop gain would reduce this added noise, it would also reduce the low frequency performance. Ideally, one would want to reduce the gain only in this frequency range, however, this is not possible without additional loss of phase. For aLIGO implementation, two possibilities exist, 1) the additional differential platform motion might be acceptable since the SUS pendulums quickly provide absolute isolation above their first natural frequencies around 0.5 Hz and 2) the control authority could be relaxed some at higher frequencies, thus reducing the induced noise, by realizing that the platform controlled motion is already several factors below the requirement at 0.5 Hz.

6.3.2 Pitch and Yaw Results

Since the pitch and yaw dimensions do not have independent sensors, the only method to compare performance is by monitoring the in-loop SPI signals. Caution must be taken with an in-loop sensor, because the control filter can act on sensor noise, driving an in-loop sensor signal below its actual noise floor. This gives the impression of better performance than is actually achieved.

Traces for the aLIGO SPI requirement, anticipated sensor noise from Section 5.5.10, and the measured beam launch angles are plotted for comparison in **Figures 6.12** and **6.13**. Since the platform to platform laser beam is servo driven to the center of the sensor QPD, laser beam amplitude fluctuations do not affect the signal. This is not the case for the launch beam sensor where the signal was corrected for fluctuations in the laser beam amplitude before being plotted for reference. Referencing **Figure 6.12**, for example, it is assumed that the pitch laser beam wander below 0.2 Hz is imposed on the platform by the control loops. This is assumed because at these frequencies the in-loop SPI pitch signal is below the levels measured by the launch QPD. The actual differential platform angles are thus likely to be tracking along with the laser beam launch stability, which would need to be improved in order to meet the SPI target at frequencies above 0.4 Hz in both the pitch and yaw directions.

Just as with SPI length measurements, it can be useful to refer to the RMS angle

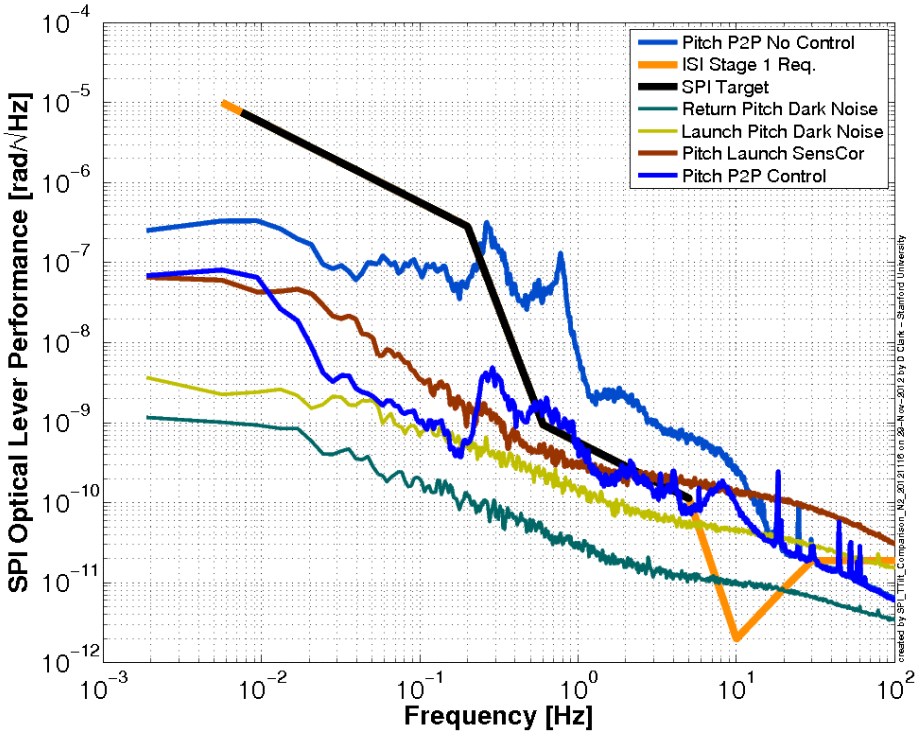

Figure 6.12: In-loop SPI differential pitch sensor signal both with, and without, SPI enabled RPP control. The projected noise floor, aLIGO SPI target, and the measured launch angles are plotted for reference.

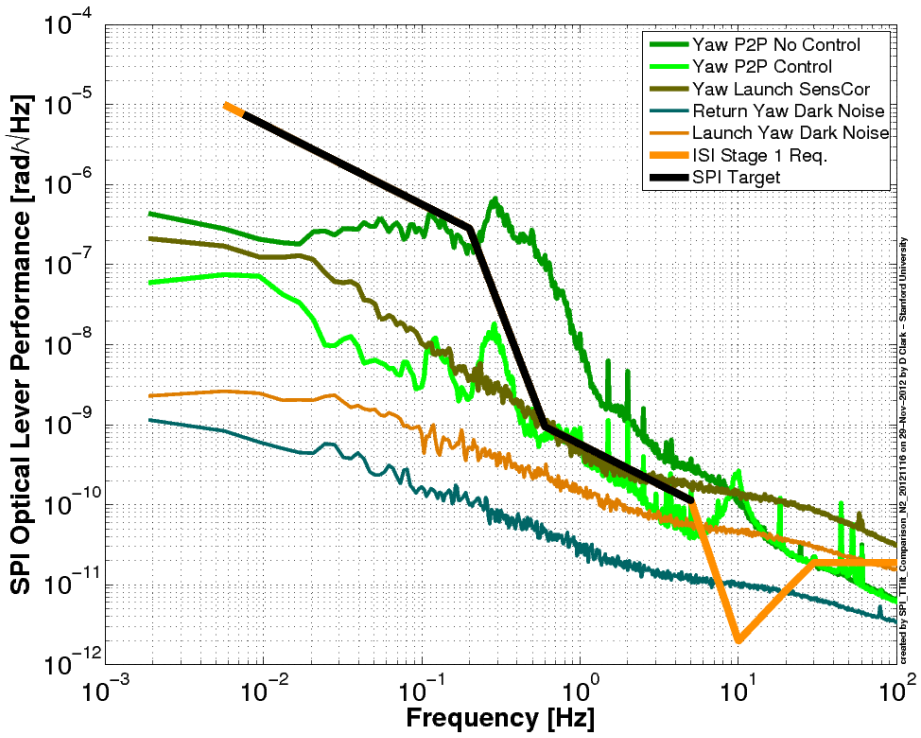

Figure 6.13: In-loop SPI differential yaw sensor signal both with, and without, SPI enabled RPP control. The projected noise floor, aLIGO SPI target, and the measured launch angles are plotted for reference.

levels in a particular frequency range. These are plotted in **Figures 6.14** and **6.15**, being integrated right-to-left from high frequency. The RMS improvement down to 0.00187 Hz is visible in a reduction from $9.31 \cdot 10^{-8}$ rad to $8.11 \cdot 10^{-9}$ rad for pitch and from $2.28 \cdot 10^{-7}$ rad to $9.44 \cdot 10^{-9}$ rad in yaw.

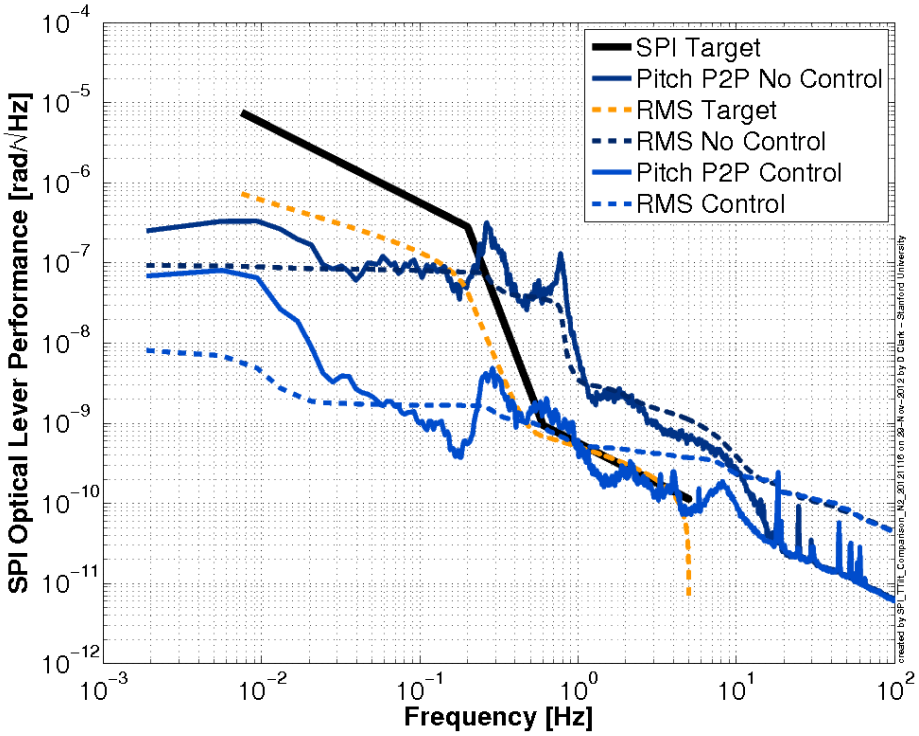

Figure 6.14: The RMS values for the differential pitch signals are plotted by taking a right to left integration of the ASD signals.

Finally, the differential pitch and yaw between the RPP and the Tech Demo are plotted in **Figures 6.16** and **6.17** respectively. In these plots, the SPI pitch or yaw without control is compared to an estimate of the differential motion when controlled using the SPI sensor. The estimate was obtained by taking the worst-case measurement for the in-loop SPI signal and the measured launch stability. This provides a best-guess estimate for the actual platform motion, even if the control gain reduces the in-loop sensor signal below its noise floor.

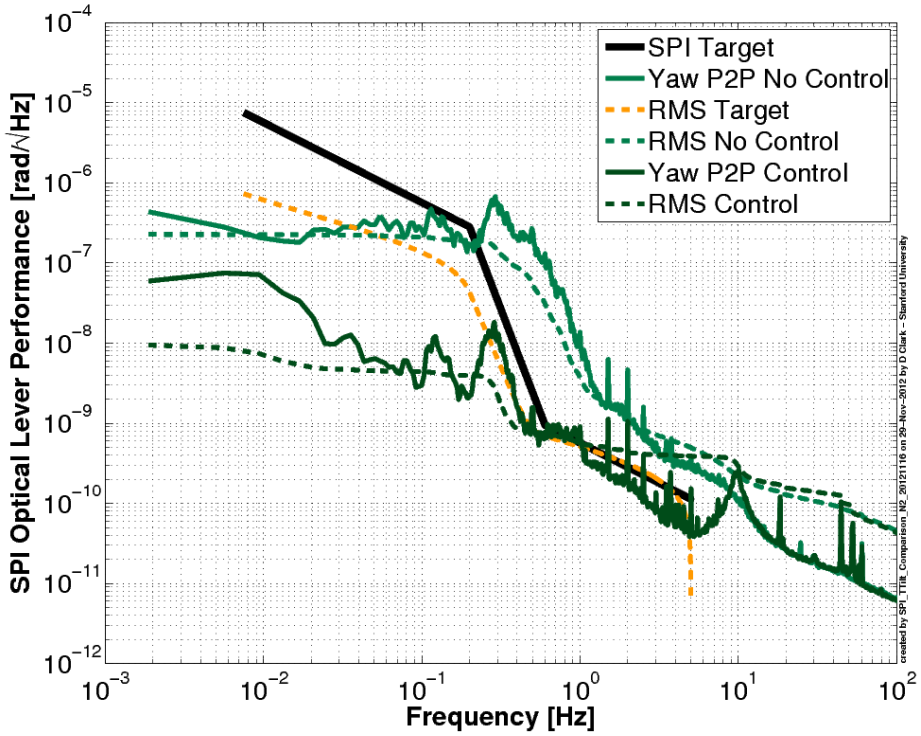

Figure 6.15: The RMS values for the differential yaw signals are plotted by taking a right to left integration of the ASD signals.

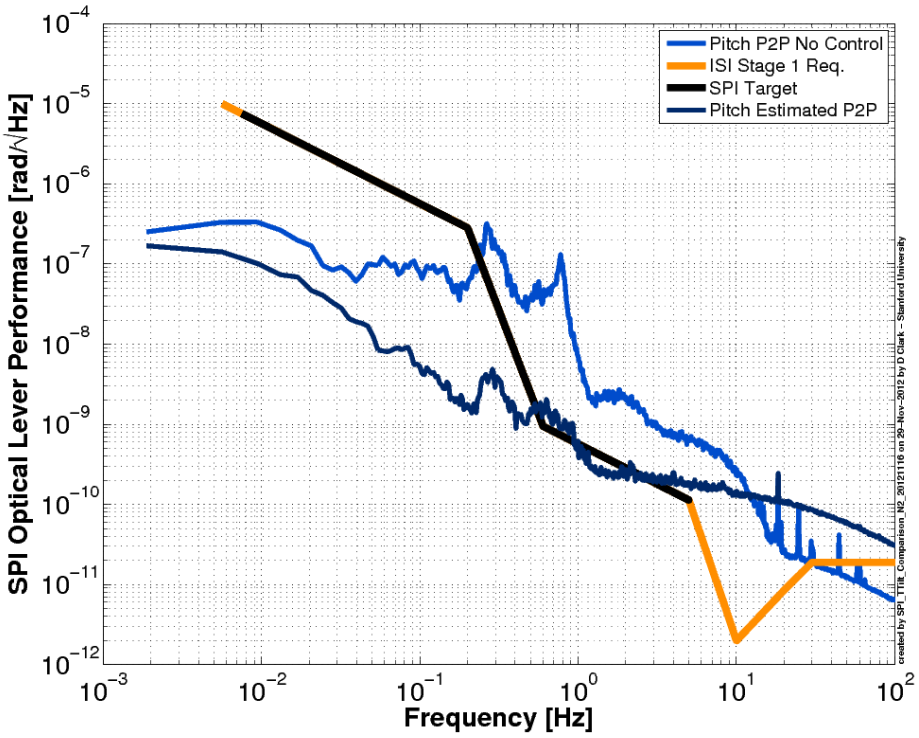

Figure 6.16: The SPI pitch sensor measures the differential pitch between the Tech Demo and RPP. A trace of the nominal motion without SPI enabled RPP control is compared to the estimated platform motion when under SPI enabled control. The estimate was obtained by taking the maximum at each frequency of the SPI in-loop pitch measurement while the RPP was under SPI control and the measured launch stability.

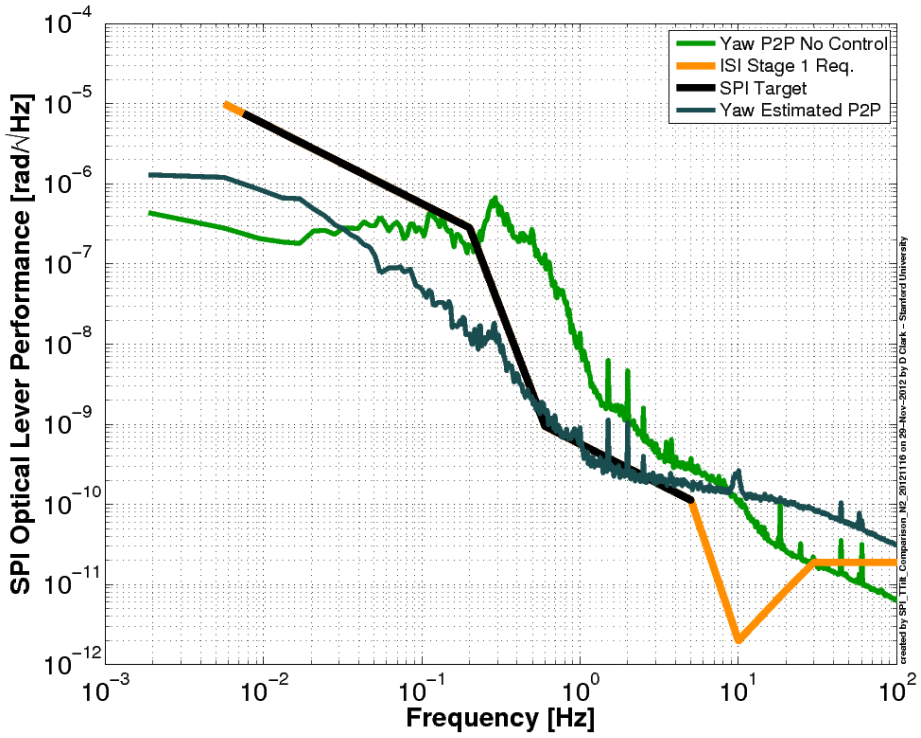

Figure 6.17: The SPI yaw sensor measures the differential yaw between the Tech Demo and RPP. A trace of the nominal motion without SPI enabled RPP control is compared to the estimated platform motion when under SPI enabled control. The estimate was obtained by taking the maximum at each frequency of the SPI in-loop yaw measurement while the RPP was under SPI control and the measured launch stability.

6.4 Control Summary

The SPI provided the differential signals required to control the length, pitch, and yaw between the RPP and the Tech Demo. This control allowed the RPP's performance to improve beyond its own sensors by being able to reference the higher performance Tech Demo motion through the SPI (**Figure 6.18**). The prototype SPI and the implemented control loops show an order of magnitude increase in performance of the differential length motion as recorded by the GS-13 seismometers from 100 mHz to 5 Hz.

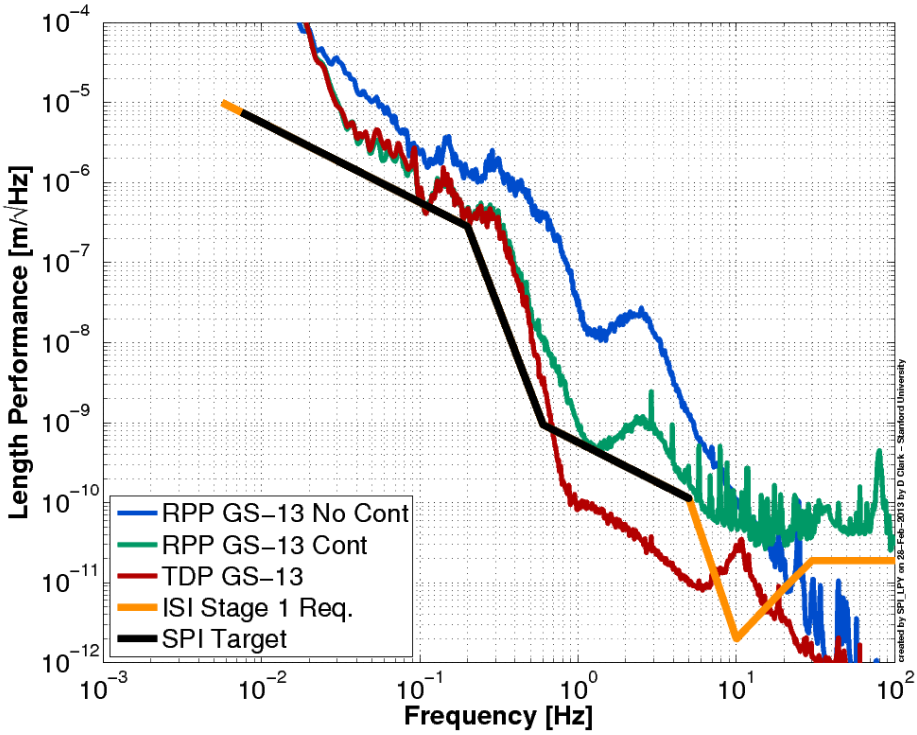

Figure 6.18: In general, the ΔGS-13 motion is almost entirely dominated by the RPP motion. The RPP motion at low frequencies is decreased when under SPI enabled control because the RPP can reference the superior sensors on the TDP. The RPP motion is elevated at higher frequencies because of SPI sensor noise being projected onto the platform.

A glimpse of the RMS reductions that control these three degrees of freedom can be seen in **Figure 6.19**. In this figure, the differential length, pitch, and yaw were

under control until $t = 0$ when the control loops were turned off. The signals then measure a quickly dying transient and continue to measure the differential motion between the platforms without control.

The fringe counting mode of the SPI length sensor also demonstrated a large dynamic range from meeting the sensor noise floor requirements to large displacements. A recording of the length between the RPP and the Tech Demo during a vacuum system vent is shown in **Figure 6.20** where the total measured displacement is as large as several millimeters.

While the prototype did not meet the target at all frequencies, performance is anticipated to improve with implementation between aLIGO platforms. This is because the aLIGO platforms have lower initial motions than those of the RPP. For aLIGO, the SPI would likely incorporate different control filters with lower frequency roll-off to prevent SPI noise from being projected onto the platforms. Perhaps the largest area of concern is the SPI optical lever beam launch stability. As was shown in **Figures 6.12** and **6.13**, while the controllers can suppress the in-loop noise, the actual differential motion is likely dominated by the beam stability, which does not meet the SPI target above 0.4 Hz. This is investigated further in Appendix G.

The control of the RPP to follow a differential length, pitch, and yaw between the RPP and the Tech Demo demonstrated an increase in performance in all controlled directions. This helps validate the SPI as a sensor that will be useful in counteracting the tilt-horizontal coupling induced errors in the aLIGO ISI platforms. The RMS improvements indicate at least an order of magnitude in the reduction of the differential motions (**Table 6.1**).

Table 6.1: Improvements in the differential length, pitch, and yaw by controlling the RPP to track the Tech Demo platform in the Stanford ETF. The RMS values are valid for the frequency range from 0.001875 Hz to 100 Hz.

	Length	L	**Pitch**	P	**Yaw**	Y
No Control	$7.82 \cdot 10^{-6}$	m	$9.31 \cdot 10^{-8}$	rad	$2.28 \cdot 10^{-7}$	rad
SPI Control	$1.77 \cdot 10^{-9}$	m	$8.11 \cdot 10^{-9}$	rad	$9.44 \cdot 10^{-9}$	rad
Reduction	$4,418$	times	11	times	24	times

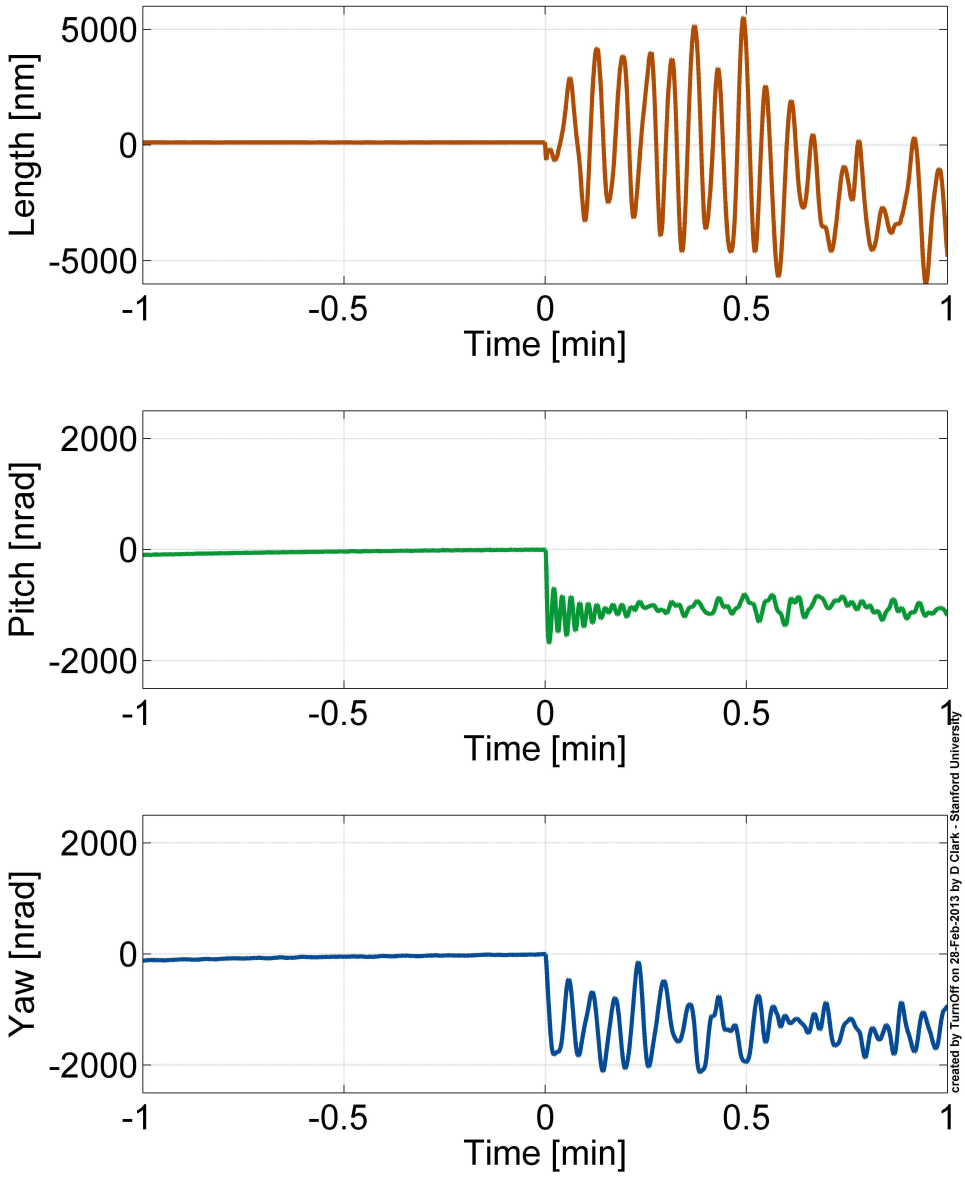

Figure 6.19: The differential platform motion is controlled to be small. When the control loops driving the RPP to track the Tech Demo platform are turned off, the differential motion dramatically increases.

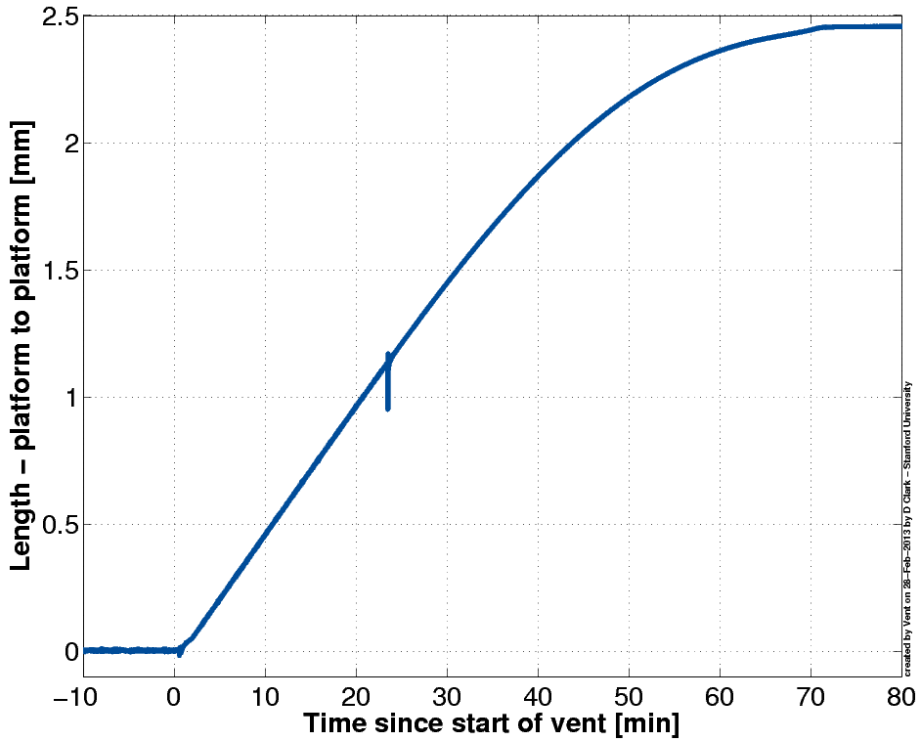

Figure 6.20: Demonstration of the large dynamic range capabilities of the SPI length sensor. The ETF vacuum system vent results in the distance between platforms increasing. The glitch in the signal at $t \approx 23$ minutes was likely caused by a brief cycling off and then on again of the damping loops on the Tech Demo platform.

Chapter 7

Conclusions and Future Work

The Seismic Platform Interferometer (SPI) prototype proved to be a useful sensor measuring the differential length, pitch, and yaw between adjacent in-vacuum isolation platforms. I recommend it be implemented as an upgrade to aLIGO. The SPI will allow aLIGO to counteract the effect of the tilt-horizontal coupling of the horizontal seismometers used in the aLIGO Internal Seismic Isolation (ISI) subsystem. This helps ensure that the seismic isolation systems are able to operate at their design goals and provide a stable surface for the rest of the interferometer optical suspension systems at low frequency and has already been identified as a possible added-on enhancement for aLIGO (Fritschel, 2013).

Before implementation in aLIGO, several concerns need to be addressed as described below in Section 7.1. Other ideas on possible improvements or unique applications for the SPI are described in the rest of the chapter. Finally, conclusions of the thesis are given in Section 7.6.

7.1 Future Work for SPI Implementation in aLIGO

While the SPI prototype was fully operational in the Stanford ETF, some considerations must be addressed before it can be implemented in aLIGO. Perhaps the most

fundamental is resolving the optical lever launch stability. Another is preparing the SPI to meet the aLIGO vacuum and layout requirements. While these areas need consideration, careful engineering and testing should allow integration of the SPI into aLIGO.

7.1.1 Optical Lever Beam Launch Stability

Comparing the noise budgets of the length, pitch, and yaw degrees of freedom as displayed in **Figures 5.18** and **5.19**, it becomes clear that all of the noise sources adding to the total instrument noise floor are below the target SPI sensitivity except for the optical lever launch stability. In **Figure 5.19**, the pitch and yaw stability levels are by far the biggest contributing factor. When the RPP was controlled by the SPI signal, the pitch and yaw control gain was high, causing a significant reduction in the in-loop motion (**Figures 6.16** and **6.17**). Just because the in-loop signal is attenuated does not mean the actual platform motion is controlled to those levels. In fact, it is reasonable to expect that the high gain of the controllers is imposing the natural wander of the launch light onto platform motion. This, in effect, is causing the RPP to track with the errant wandering of the launched light from the host platform. **Figure 6.10** shows that the GS-13s are detecting a signal well in excess of the predicted platform to platform motion at frequencies between 0.050 and 2 Hz. This signal from the GS-13s is possibly caused by imposed tilt motion from launch light wander coupling into the seismometers from tilt-horizontal coupling.

One of the noise sources for the prototype SPI launch angle sensor appears to be coupling of interfered light from the length sensor. Even with care taken to use anti-reflection (AR) coated optics and misalignment of back reflections, **Figure 7.1** shows correlation of the length interference fringes into the launch beam optical lever measurements. We found one scattered light source in the interferometer and directed it into a beam stop. This is an elusive noise source which definitely is detrimental to the launch angle measurement and is discussed in more detail in Appendix G.

In order for the SPI to operate at the target sensitivity, the launch light stability will need to be improved. Several possibilities exist to help stabilize this. One option

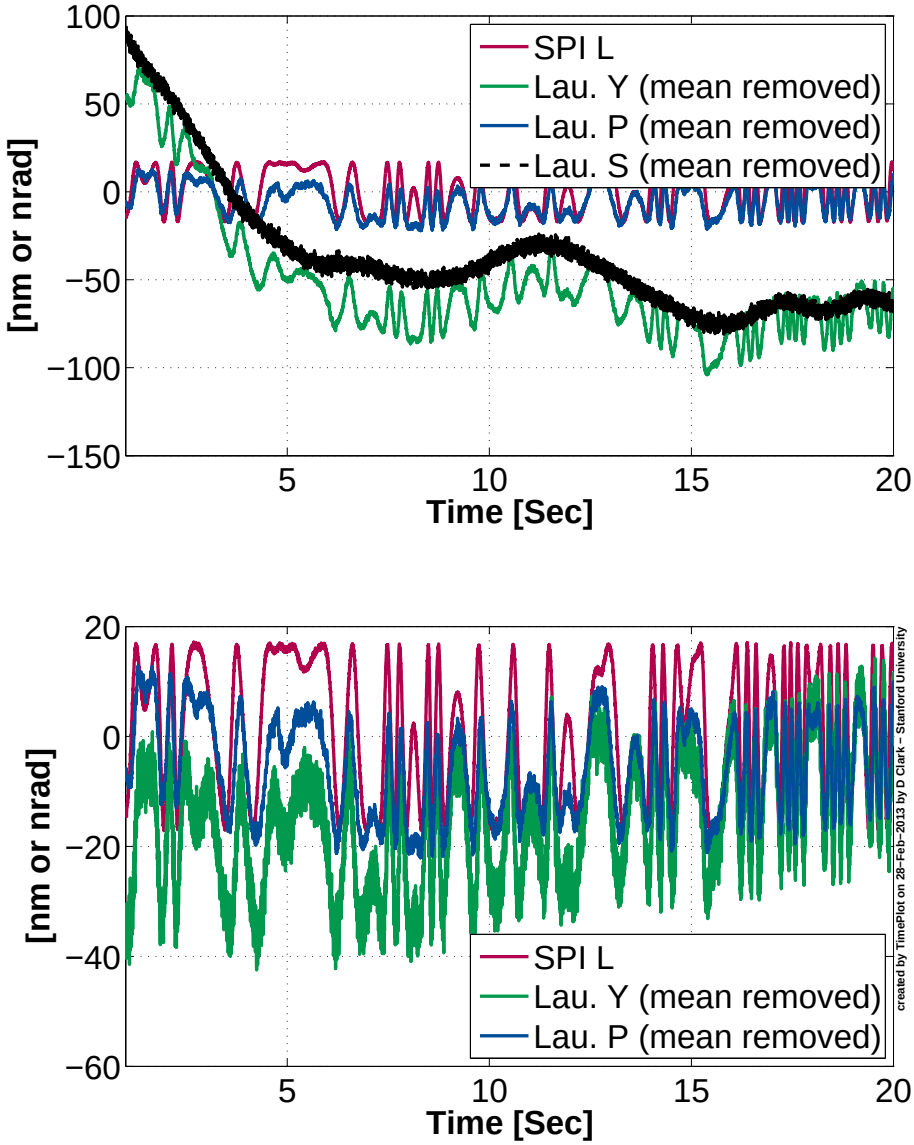

Figure 7.1: In this figure, the length signal as measured by the interferometer is appearing on the launched pitch and yaw signals. This is visible in the high correlation between the SPI L trace and the Lau. Y and Lau. P traces. The mean value for all of the angle sensors have been removed for plotting. In the upper plot, the yaw signal appears to be correlated to the QPD sum signal (Lau. S). The expected coupling of the sum power on yaw has been removed in the lower plot.

is to stabilize the light in an optical cavity before launching from the host platform. By locating such a cavity before the first non-polarizing beam splitter in **Figure 5.5**, the light output would be common to both interferometer arms so the cavity stability would need to be good enough such that the frequency stability of the laser was not degraded by the cavity. Construction of such a cavity is complicated by the low frequency nature of the SPI as a sensor. If a good cavity were constructed, however, it might be possible to stabilize the laser frequency as well as the launch light angle.

A second option would be to separate the optical lever pitch and yaw sensing light beam from the interferometer length sensing beam. The advantage is that a cavity used to stabilize the launch light angle would not need to meet a frequency requirement because the optical lever sensors are immune to frequency changes in the received light. A possible drawback is the need for a second beam of light linking adjacent platforms. This would involve a second mirror on the remote platform, increasing the necessary footprint.

It might be adequate to measure the launch light stability on the host platform and subtract the launched light angle in real-time from the returned light angle. Pitch and yaw would then be controlled from this difference in signal. This method would require precise calibration of the two sensors and a second QPD circuit on the host platform. The SPI prototype anticipated and incorporated this.

Finally, using an amplified spontaneous emission (ASE) light source (chosen because of its short coherence length) the measured optical launch signals improved (Appendix G). This indicates that the mechanical stability of the launch optical posts might meet the requirements while the source of the excess noise is more subtle.

7.1.2 Advanced LIGO Vacuum Compatibility

At the time of construction, the aLIGO vacuum system was known as the largest ultra-high vacuum in the world with pressures reaching into the 10^{-9} Torr ($1.3 \cdot 10^{-7}$ Pa) range. In order to maintain such a vacuum system, the LIGO Vacuum Review Board (VRB) has set very stringent requirements on what is allowed into the system

(Coyne, 2009a). Materials that are common in other fields are often not approved for use in aLIGO. Also, because of the extremely high incident laser power on the optics inside aLIGO (over 800 kW), hydrocarbons and other contaminants that are inside the vacuum system can be baked onto the optics and very quickly compromise the ultra-low absorption of the mirrors. The optical profile of the optical components is critical in aLIGO and contaminants on the optical surface resulting in localized heating is one concern that disturbs the optical profile (Lantz, 1999).

7.1.2.1 Optical Components

Advanced LIGO (aLIGO) already utilizes a large array of optical components in the vacuum envelope. No problem is anticipated in obtaining UHV and aLIGO compatible beam splitters, mounts, or optics. Possible areas of caution include the surface finish of commercial mounts and holders because anodized aluminum, for example, is common in optics but is not aLIGO approved. Another area of concern is with lubricants that often are placed on threads and actuators.

7.1.2.2 Optical Fiber Feedthrough

One critical aspect of the SPI prototype concerns how to launch the laser light optically from the host platform of the Tech Demo. An aLIGO vacuum compatible feedthrough for polarization maintaining (PM) fiber at 1.5 μm wavelength could not be located commercially. As a result one was fabricated by taking a metal clad PM fiber that was soldering it into a Kovar ferrule, which, in turn, was soldered into a stainless flange used on the vacuum system (Appendix G). The feedthrough system was then leak checked down to 10^{-9} $\frac{\text{Torr}\cdot\text{L}}{\text{s}}$ ($1.33 \cdot 10^{-10}$ $\frac{\text{Pa}\cdot\text{m}^3}{\text{s}}$), the lowest sensitivity of the leak tester, without any discernible leak. The fiber and flange were then placed into service in the ETF and subsequently used for the experiments.

Such a feedthrough system is theoretically aLIGO vacuum compatible, although it would be necessary to establish reviewed assembly, testing, and implementation procedures.

7.1.2.3 Optical Fiber

Metal and polyimide optical fiber claddings are two coatings thought to be aLIGO vacuum compatible. The first several cm of fiber interior to the vacuum envelope after the feedthrough are metal coated. For the prototype, the rest of the delivery fiber is standard PM patch cord with a vinyl buffer which is not aLIGO compatible. A several meter length of polyimide PM fiber was purchased and tested although the loss factor was high because the sample obtained had a core sized for 1.3 μm light. Polyimide clad fiber is likely to be the most cost effective and easiest to obtain aLIGO vacuum compatible PM optical fiber.

7.1.2.4 Photo-Detectors and Associated Electronics

Most electronics internal to the aLIGO vacuum system are housed in pressure containing pods. This allows the electrical components to operate in air at one atmosphere without contaminating the vacuum system. Advanced LIGO (aLIGO) vacuum compatible electrical feedthrough connectors are already in use and readily available.

One area of concern involves the photo-detectors themselves. While the rest of the readout circuit is contained in a pod and would not pose a contamination hazard, the photodetectors must be located in the vacuum (unless optical windows are used which would significantly increase the complexity and cost). The photodetector units include anti-reflective coatings on windows in front of the detectors. These windows would have to be removed or otherwise modified to vent the void between the window and the detector. Any gas trapped in a void has the potential to include contaminants or create a virtual leak extending the pump-down time to operating vacuum levels.

7.1.3 A Compact Sensor Concept

Apart from the SPI remote mirror, the components are all located on the host platform. One concept for a compact sensor is included in **Figure 7.2**. In the design, areas of optimization include:

- Minimization of the total "footprint" area occupied on the host optical platform

- Maximization of the stiffness of the mounting structure
- Accessibility to the adjustments necessary for alignment and setup
- Length and stability of the interferometer reference arm
- Maintaining the integrity of the metrology loops

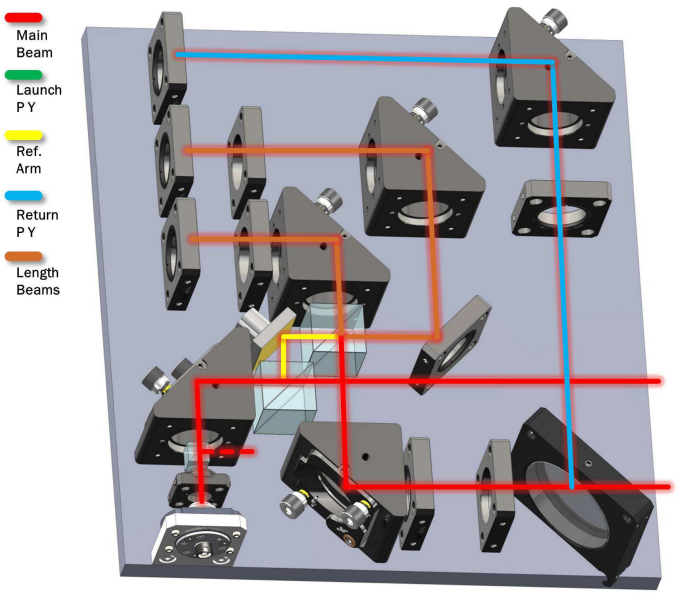

Figure 7.2: A solid model of a possible configuration of an SPI sensor for use in aLIGO. Small footprint and structural stiffness were goals in the design layout.

The SPI housing frame could be constructed from a material such as aluminum or a low coefficient of thermal expansion (CTE) material such as Invar. Even though materials such as stainless steel have a lower CTE than aluminum, the higher conductivity of aluminum means that temperature gradients are less likely to be as strong. The minimization of temperature gradients is important in order to maintain optical alignment and reduce errors caused by differential strains. Another material option that might be more difficult to implement but provide improved performance is silicon. Most of the optics, when possible, would be clamped on both sides increasing the

stiffness and reducing errors caused by Abbé offset (although a top mounting plate shell is not shown in the diagram). Care must also be taken in the clamping arrangement design to minimize stressing optical components with changes in temperature. The SPI should have three feet, or some other, kinematic method to clearly define the contact points of the frame to the optical table. This would help reduce stresses from being transmitted to the SPI unit from the platform.

While this concept is not meant to represent a final design, it provides an example of an aLIGO implemented SPI sensor. Just as with the SPI prototype, the remote platform is equipped with a single mirror.

7.1.4 Platform Formation Control

For the SPI prototype, the choice to control just the RPP was clearly the most advantageous for testing. In aLIGO the situation is more complicated. Several options exist for controlling a fleet of multiple platforms to "fly in formation." Some possibilities were explored in **Section 4.5**. Whatever the method, the control flow quickly becomes more complex as the SPI sensing of length, pitch, and yaw between many platforms is added. A well defined control scheme would help in the control implementation in aLIGO.

7.1.5 Laser Source

The aLIGO based SPI sensors need stable, in-vacuum light sources. The SPI prototype utilized a single 10 mW light source operating at 1,533 nm. For aLIGO, the corner station might house as many as nine SPI sensors. Cost reduction for aLIGO implementation might be realized through using a single laser source and vacuum feedthrough with in-vacuum splitting and routing to the necessary use points. Even if the laser frequency was modulated directly for the fringe counting mode (another option is modulating the PZT in the reference arm as was discussed in Section 5.4.1.2 and used in the prototype), the light could still be delivered and used at each of the sensors. The necessary demodulation could still be possible by referencing the laser frequency drive signal.

Finally, while the laser used for the SPI prototype was run experimentally at vacuum levels in the Stanford ETF, contamination possibilities to the aLIGO vacuum system would likely prohibit such a deployment. By mounting the laser externally, accessibility is improved allowing easy inspection and replacement.

7.2 Mode Switching

The SPI prototype used two methods to measure the differential length between platforms. These included the mid-fringe locking and the fringe counting methods. Since the mid-fringe locking method had limited range, the fringe counting method was used for the SPI prototype performance testing. Throughout the testing, the fringe counting method displayed adequate performance well-exceeding the sensitivity target.

Although PZT nonlinearity and noise become a concern with mid-fringe locking and the range is reduced, this method might further improve the noise floor of the SPI. Especially applicable might be the use of Lithium Niobate or similar materials with less nonlinearity and noise than those exhibited by the PZT crystals (Kawamata et al., 2007). This assumes the current limiting noise sources such as frequency and temperature stability in the reference arm could also be reduced.

If mid-fringe locking did result in improved performance, a system for automatic switching from the fringe counting to mid-fringe locking methods could be implemented. This would allow large motions at a reduced sensitivity level in the fringe counting mode and then, once differential motions were reduced, would automatically switch over to a mid-fringe lock resulting in higher sensitivity.

One possibility for implementing such a system would be to always run the fringe-counting components. This means that the SPI reference arm would be continuously modulated at 10 kHz. The output of the fringe counting method would allow the control loops to drive the differential platform length to a position on the interferometer characteristic curve to the mid-fringe point (**Figure 5.8**). Once the platform length was held here by the SPI enabled length control, the mid-fringe locking controller could be engaged. This then holds the operating point of the interferometer

at the mid-fringe by tracking length changes in the sensing arm with the reference arm PZT. The control authority for holding the mid-fringe is then related to the differential length between platforms and would be used for platform to platform control. The control signal to the PZT in the mid-fringe locking mode would also be monitored to determine where the PZT was relative to its limits of motion. If a large seismic disturbance was sensed, as the PZT control motion reached a limit of travel the interferometer control would automatically disengage the mid-fringe locking PZT control signal and switch the SPI sensing back to the fringe-counting mode.

While the current fringe counting method for length detection of the SPI prototype meets the design criteria, it might be possible to increase the sensitivity further through the use of automatic mode switching. If this were attempted, it would likely be necessary to decrease other, limiting noise factors. Automatic mode switching could combine the advantages of the fringe counting and the mid-fringe locking sensing modes in a way that is independent of external manual supervision.

7.3 Laser Frequency Control

The laser exhibited low frequency noise as discussed in Section 5.5.2. However, when the first order slope and mean are not removed from the data, the noise performance worsens. Most of this was discovered to be attributed to the temperature induced change in length of the arms of the interferometer, although this does not explain all the behavior of the measured signal. A possible source causing fluctuations in the frequency stability could be temperature drift in the laser itself. If this were the case, tighter temperature stability of the laser might improve performance. The optical fiber could also introduce phase noise in the light. Even though polarization maintaining (PM) fiber was used throughout the light delivery chain to reduce noises such as fiber induced phase noise and polarization wander, changing the fiber routing and increasing isolation to mechanical disturbances might also increase performance. Finally, while mitigation against frequency noise generation is the most elegant, the frequency noise of the light used in the interferometer could be enhanced through

active control. While standard cavities work well at higher frequencies, the low frequency nature of the SPI sensor means designing and implementing such a cavity with good low frequency performance is not trivial. An atomic absorption line such as acetylene could be used at low frequencies but Doppler broadening becomes problematic. Techniques such as Doppler free atomic absorption might be applicable to stabilize the SPI laser frequency at the expense of added complexity (de Labachelerie et al., 1994), (de Labachelerie et al., 1995), and (Nakagawa et al., 1996).

For aLIGO, it might be possible through careful temperature shielding of the laser and adequate routing and suspension of the light delivery fiber to maintain a frequency noise low enough to meet the SPI target sensitivity. Even though the frequency noise of the laser is projected to be the limiting noise source from HAMs 4 to 5, the SPI prototype, as tested, exhibited noise that met the requirement.

7.4 An SPI Sensor for the 4 km Arms

The SPI was envisioned to control position of the seismic isolation platforms in the aLIGO vertex to each other. Perhaps this could be extended to the 4 km long arm cavities as well. This might aid the main interferometer in startup because the SPI could provide sensing and control at the platform level when motions are too great for the main interferometer's Fabry-Perot cavity control system to maintain lock. Situations such as elevated ground motions after an earthquake might make such a system very useful.

By taking the measured noise sources of the SPI into consideration, it is the frequency noise of the laser that scales proportionally with the length of the sensing arm of the SPI that is the limiting factor. The noise floor of such a sensor relative to the sensitivity target for a 4 km arm is plotted in **Figure 7.3**. From this figure, it can be inferred that the SPI could provide useful sensing information below 0.5 Hz. A practical mount position for a long-arm SPI could be on the HEPI support structure since HEPI controls the low frequency positions.

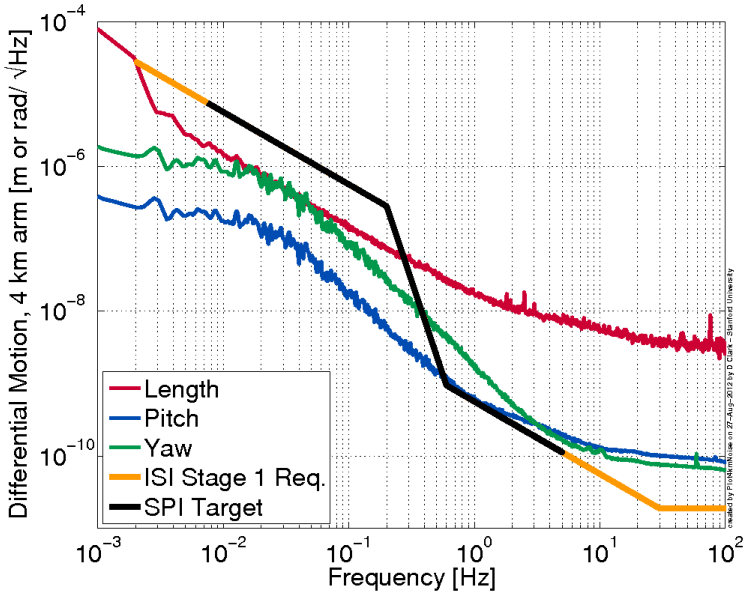

Figure 7.3: The sensitivity floor of the prototype SPI as predicted for measuring the differential length, pitch, and yaw for the aLIGO 4 km long arms.

7.5 Available Commercial Sensors

Several commercial sensors could also be used for length sensing between adjacent ISI platforms. These would still be subject to the aLIGO vacuum requirements.

AttoCube manufactures a Fabry-Perot interferometric sensor. The fiber coupled sensor (FPS3010) has a maximum working distance of about 1 m but is available for use in vacuum. It is unclear to what extent it would need to be modified to meet aLIGO vacuum requirements. The ASD was calculated from a 14 hour data collection to a fixed target provided by AttoCube. Assuming this noise is equivalent to the sensor noise if it were installed on the ISI platforms, this sensor would meet the length sensing requirements of the SPI (**Figure 7.4**).

Agilent (formerly Hewlett-Packard) has long been known for high precision laser interferometric instruments. The company provided an ASD plot of the frequency stability of an Acousto-Optic Modulated (AOM) laser and Remote Optical Combiner (ROC). Assuming that the frequency noise of the laser is the limiting noise source, this was converted to equivalent displacement noise for the distance from HAM 4 to

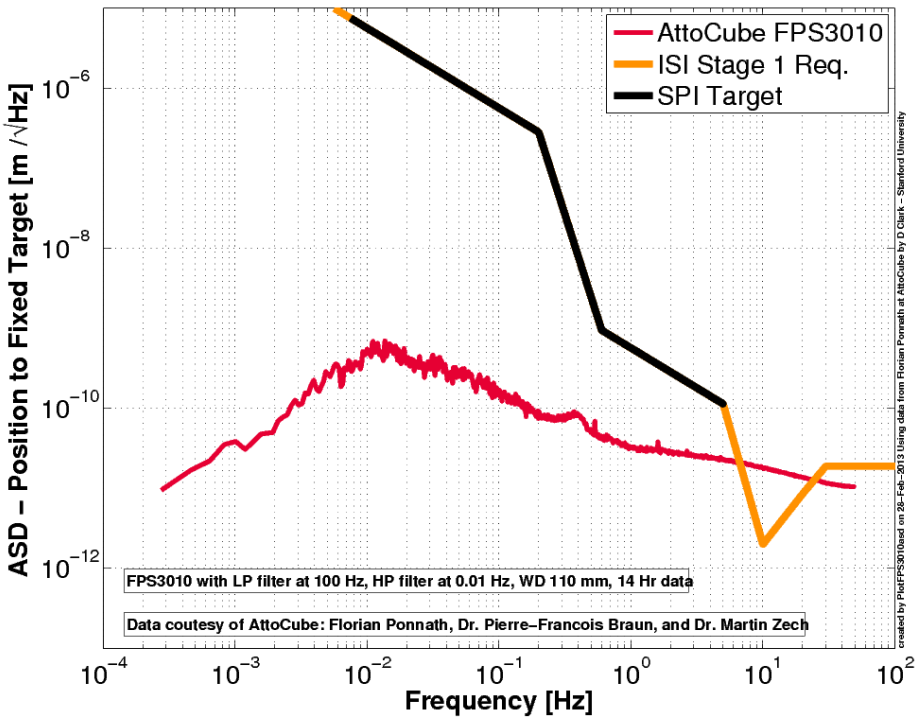

Figure 7.4: The AttoCube interferometric sensor noise floor. Note the time series data had a high pass filter at 0.01 Hz so the low frequency noise has been attenuated. Data courtesy of AttoCube: Dr. Pierre-Francois Braun and Dr. Martin Zech, AttoCube contact: Florian Ponnath.

5 and shown in **Figure 7.5**.

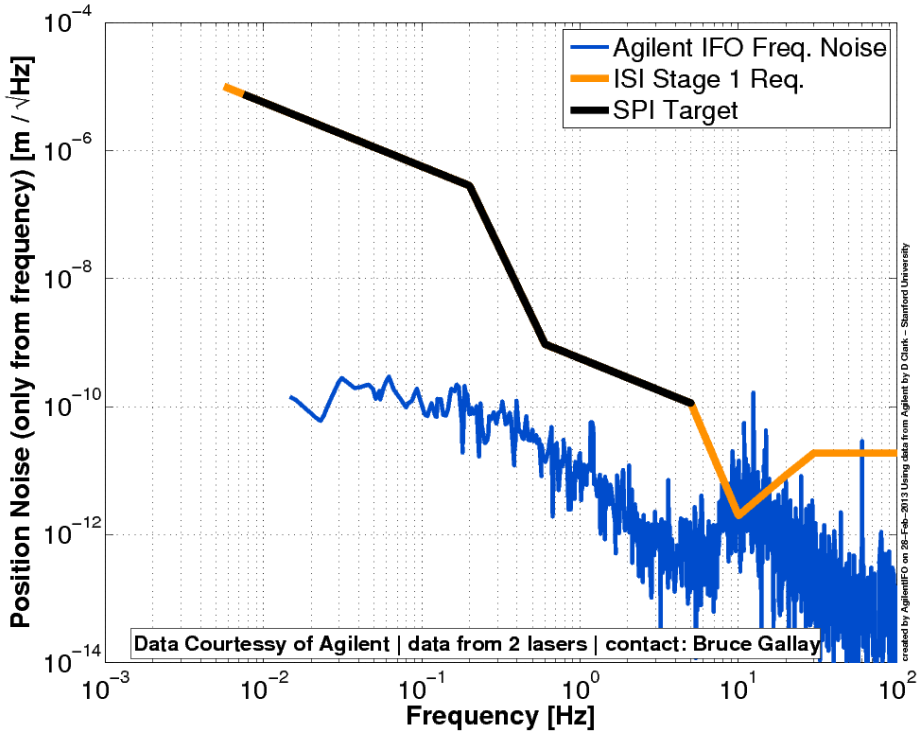

Figure 7.5: The Agilent laser noise for the HAM 4 to 5 location compared to the SPI requirements. Data courtesy of Agilent Technologies, Inc. Contact: Bruce Gallay.

Compared to the prototype SPI noise budget (which is dominated by the laser frequency noise), both the AttoCube and the Agilent interferometric sensors display lower noise floors in the SPI frequency range (**Figure 7.6**). While the SPI already meets the length sensing requirements, a commercial sensor could provide even more performance though at increased cost. The AttoCube has excellent length sensing noise performance when used within the working distance limit of about 1 m. Since the AttoCube only measures displacement, pitch and yaw would have to be sensed independently. The Agilent interferometer system can incorporate angular sensing of pitch and yaw in addition to displacement but fiber coupling into the vacuum system would increase the cost of integration into aLIGO.

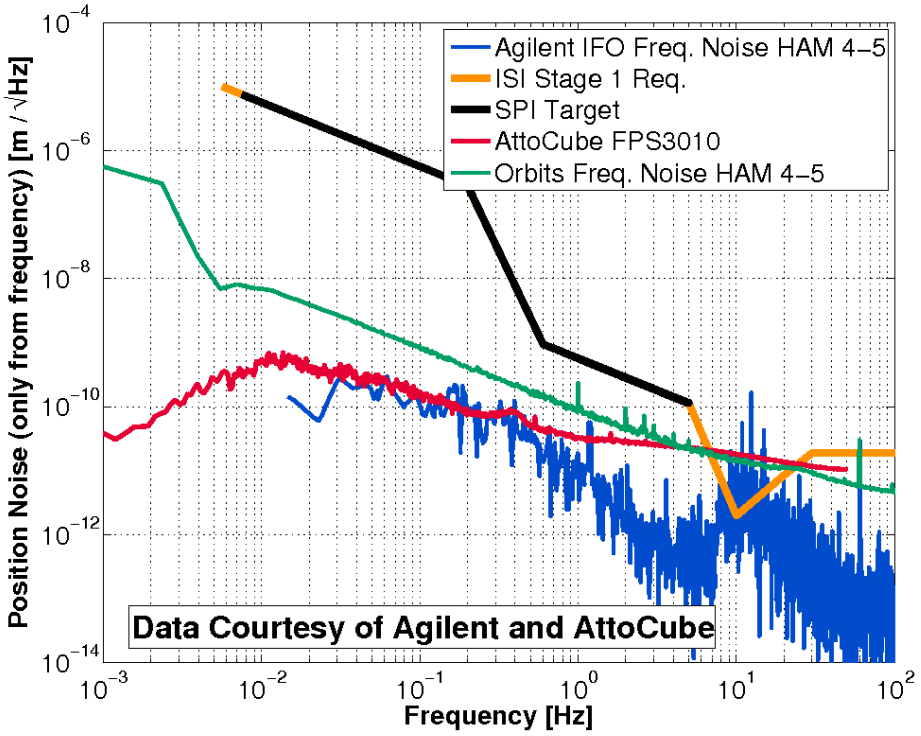

Figure 7.6: Both the AttoCube and Agilent interferometric sensors compared to the SPI requirements and the prototype SPI noise equivalent for the HAM 4 to 5 distance. Data courtesy of AttoCube and Agilent respectively.

7.6 Conclusions

Advanced LIGO (aLIGO) uses several techniques to obtain seismic motion attenuations from the ground to the interferometer optics. This can be as great as 10 orders of magnitude at 10 Hz. One level in the isolation chain is the Internal Seismic Isolation (ISI) platforms. These platforms are single or double stage structures that are controlled relative to inertial space in all six degrees of freedom. A problem arises in that the horizontal seismometers used in the active control of the ISI platforms have difficulty distinguishing horizontal acceleration from acceleration due to gravity coupled into the sensor through tilt. This tilt-horizontal coupling is one factor that limits the low frequency performance of the ISI system.

Two possible methods to improve the performance of the ISI system include: 1) measuring the tilt and subtracting its effect, and 2) measuring and controlling the differential motion between adjacent platforms by the Seismic Platform Interferometer (SPI).

One way to measure tilt involves spatially separated vertical seismometers. In this method two or more vertical seismometers are placed in a configuration where the common mode signal is vertical motion and the differential signal is proportional to the tilt. Once the tilt is known, it can be used to correct the horizontal seismometer signals on the ISI platform. If this were implemented in aLIGO, many accurate vertical seismometers would be necessary. A prototype vertical seismometer designed to be immune to air pressure variations was built and tested. While the prototype would need improved noise performance for use in aLIGO, the working prototype demonstrated the concept.

Because the differential motion between adjacent platforms is the critical concern at low frequencies, controlling this motion will improve the interferometer performance. An auxiliary sensor called the Seismic Platform Interferometer (SPI) was constructed. The SPI measures the differential length, pitch, and yaw between adjacent ISI platforms and was tested in the Stanford ETF. The noise floor was quantified and compared to the requirements for such a sensor. The length sensing noise is well below the requirement. Pitch and yaw sensing seem to be limited by the launch

stability of the light used by the optical levers above about 0.5 Hz.

The SPI was then used to control the differential length, pitch, and yaw between the RPP and Tech Demo in the Stanford ETF by actuators on the RPP. Control reduced the differential length motion between the two platforms by an order of magnitude between 100 mHz and 0.5 Hz as measured by independent GS-13 seismometers. The actual improvement is likely much better at low frequency than the seismometers measured because the GS-13s themselves are subject to tilt-horizontal coupled noise.

The SPI prototype demonstrated the ability to sense and control differential motion of two in-vacuum isolation platforms. With little modifications or improvements, the SPI should be implemented in aLIGO at frequencies below 5 Hz. This will enable an increase in the low frequency performance of the ISI systems by correcting for excess low frequency motion caused by tilt-horizontal coupling in the ISI systems' horizontal feedback seismometers.

Appendix A

Geotech GS-13 Seismometer Improvements for use in aLIGO

The Geotech Instrument's GS-13 seismometer is a single degree of freedom instrument that has one of the lowest noise floors of seismometers in the 1 to 10 Hz frequency band. Even outside this frequency band, the performance still remains impressive. Because of this performance, these instruments are used on both the aLIGO single stage HAM and two-stage BSC seismic isolation systems. The anticipated GS-13 seismometer count for use in aLIGO is 180 installed units. Several challenges involving the integration of these instruments have arisen and were investigated in the following sections. The redesign of internal flexures is described in Section A.1. The damping of the GS-13 offload spring resonances is documented in Section A.2. Finally, μ-metal shielding tests and pre-amplifier resistor noise experiments are reported in Sections A.3 and A.4 respectively.

A.1 Constraint Flexure Redesign

A.1.1 Background

A new flexure was developed to constrain the proof mass for the GS-13 seismometer. This flexure is a direct replacement for the six "delta-rod" flexures which currently

come with the instrument. These flexures constrain the proof mass of the seismometer to move along the seismometer's sensitive axis. This configuration of the delta-rods over-constrains the proof mass as only the five degrees of freedom need to be constrained (the three rotational and two translation). A second order twist about the sensitive axis is also allowed in response to axial motion. This constraint configuration requires careful alignment in manufacturing but it is a worthwhile inconvenience in exchange for robustness and symmetry in design. The new flexures are designed to be much more rugged than the original delta-rods so that normal handling of the seismometers will not damage them even when transported with the proof mass unlocked. By retrofitting the seismometers with these new flexures, the need to install a custom remote locker / unlocker motor is eliminated. The problem of the fragile nature of the delta-rod flexures has been described by the technicians and scientists responsible for aLIGO installation and integration as the "least reliable part of the entire ISI subsystem" (Lantz, 2009c). This section describes the design of the new flexures, the flexure testing to demonstrate the shock-loading, the noise performance of instruments with the new flexures, the testing of the self-damping system to protect the seismometer in the sensitive axis direction, and some background on other flexure designs that were considered but not chosen. The new flexures cost less to manufacture than the internal remote locking motors and associated electronics and result in a much more robust instrument (O'Reilly, 2008).

A.1.2 Design Objectives

The design objectives that were considered to define the new flexure design are listed as follows. These were the main drivers when considering alternative designs and influenced the final design specifications.

- Remove the remote, in-vacuum, test-mass locking / unlocking motor. This is driven by reliability issues and extra costs associated with motor hardware, electronics and labor for both primary installation and future maintenance and repair.

- The replacement flexures should survive at least a 20 g half sine-wave load with

even larger load capability being desired. The 20 g objective was chosen because the Trillium T-240, a low frequency seismometer, is specified to withstand that g loading without proof mass locks. We anticipate with careful packaging that we can design to 20 g loading and ship the seismometers without locking the proof mass.

- The replacement flexure must have the same attachment mounting points as the existing delta-rods so that installation will not require any modifications to the rest of the seismometer.

- The instrument's natural frequency must remain at or below 1 Hz as provided by the original delta-rods. This is necessary to ensure that the modified instrument meets or exceeds its original performance.

- The flexures should not degrade the seismometer's noise performance.

- The flexure should be designed for manufacturability. Choices of geometry, material, machining methods, and hardening procedure should all be consistent with ease of production and installation.

A.1.3 Design Background

The GS-13 has a proof mass of 5 kg. This mass is constrained to move in the instrument's sensitive axis by 6 flexures that form two equilateral triangles (or a Δ configuration) in two parallel planes offset from each other (**Figure A.1**). If not properly aligned, this system over-constrains the proof mass, so tolerances of the system be held high to ensure that the over-constraint does not increase the natural frequency and introduce unwanted stresses and "binding" as a result of the proof mass movement. The proof mass has a motion of ± 3 mm along its sensitive axis. The arrangement is such, however, that there is also a slight motion radially towards the sensitive axis at the attachment points on the order of 60 μm. This means that the replacement flexure must provide appropriate compliance not only along the instrument's sensitive axis but also radially in from the proof mass.

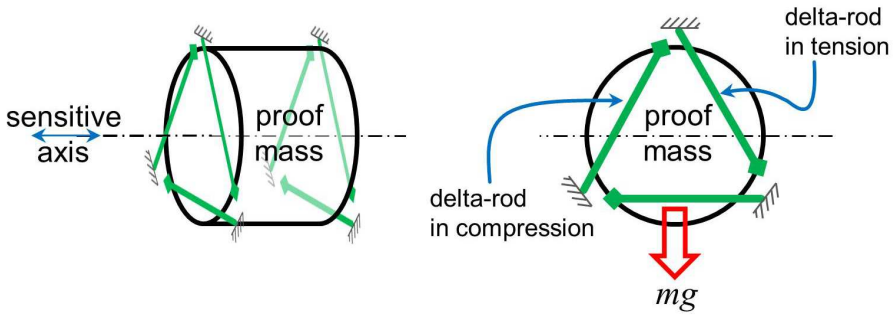

Figure A.1: The GS-13 seismometer proof mass is constrained by 6 delta-rods. These form two equilateral triangles and effectively constrain the proof mass to motion along the sensitive axis. Since 6 delta rods are used to constrain 5 degrees of freedom, the design is not kinematic and problems associated with over constraints arise if adequate precision is not achieved in the mounting and structure.

The original delta-rod can be seen in the lower flexure position of the seismometer in **Figure A.2**. The rod consists of a 0.53 mm (0.021 in.) diameter round wire with properties which appear similar to A228, a type of spring steel. This wire provides flexing in both directions and is stiffened in the middle by a brass sheath. The existing flexure arrangement was calculated to go into Euler buckling around 3.4 g of static loading. This buckling range was verified in testing with a load cell and clamp arrangement.

Because the design requires a greater compliance along one axis than the other, the round wire design was not optimal for the design specifications. Instead, a crossed flexure design was pursued (depicted in **Figure A.3**). This requires 4 flexing points each of which allows rotation in only one direction. Two of these flexing elements are then stacked in series at one end allowing flexing in two directions. Another stacked pair is then located on the other end of the replacement flexure bringing the total flexural elements on a single flexure to four. Thus the translation of the proof mass is constrained through the six flexures.

The original delta-rods failed in Euler buckling with a slenderness ratio of 90 (**Figures A.17** to **A.20**). If the slenderness ratio is reduced to below 40, the chance of Euler buckling is greatly reduced or eliminated (Juvinall and Marshek, 2000).

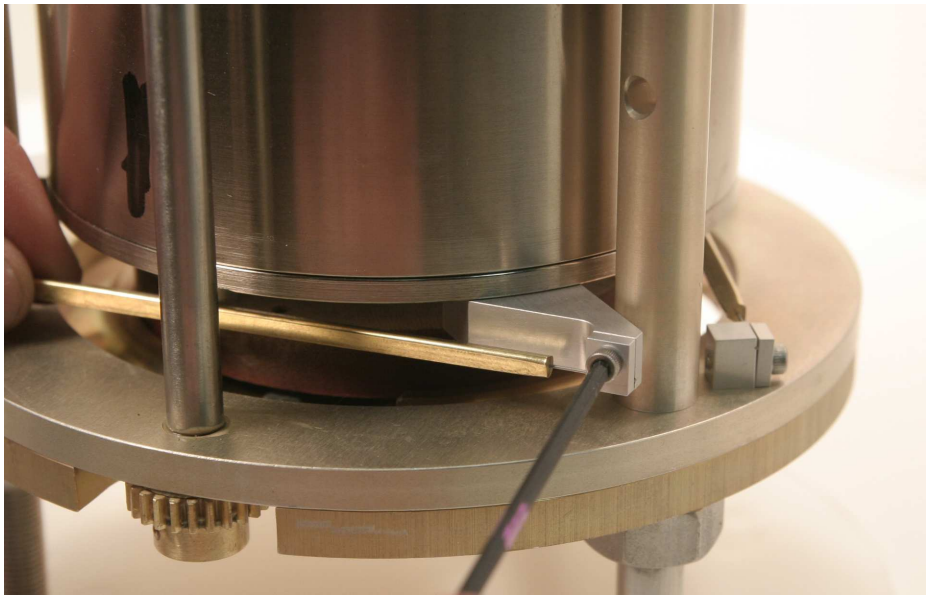

Figure A.2: GS-13 original delta-rod.

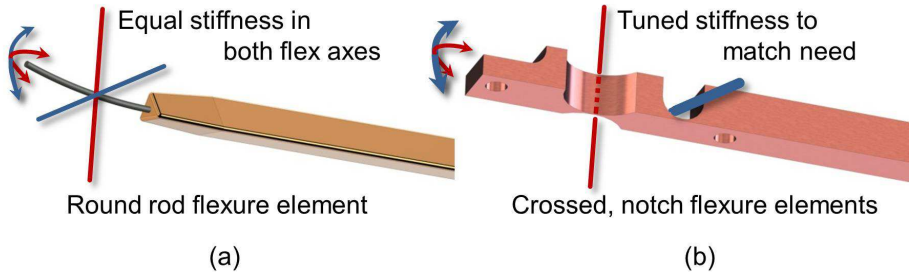

Figure A.3: Original delta-rod round end flexure element has equal stiffness in both flex axes (a). New crossed flexure concept allowing matching of rotational stiffness to instrument requirement (b). Identical flexure elements are located on both ends of the rod to allow the necessary degrees of freedom.

However, if the existing delta-rod flexing wire were reduced in length to a point where buckling will not occur, at a 20 g load on the instrument, the stresses induced by the proof mass motion will exceed the yield stress of the material. This indicates that a round flexure element is not an optimal solution.

The designs investigated mainly focused on circular or elliptical notch flexure elements. These elements are much more resistant to buckling, are relatively easy to machine (especially circular notches), and seem to be well suited for this application (Smith, 2000).

A.1.4 Recommended Flexure Design

The recommended flexure design, which is the design currently installed in aLIGO is described as follows. Later, Section A.1.5 documents a few prior designs that were subsequently abandoned.

A.1.4.1 Material Selection

A beryllium copper alloy C17200 (also known as alloy 25) was chosen as the base material for the design with an H temper (TD04). Several reasons made this material desirable, including high yield stress, availability, minimal interaction with magnetic fields around the proof mass and the ability to easily age it after machining. Work at Stanford had previously used BeCu for precision flexures with good results (Section 3.1). After aging (2 hours air bake at 330 °C) this material is brought to the tempered properties of HT (TH04) with ultimate yield stresses of 1.10 to 1.38 GPa (160 to 200 ksi). The fatigue properties of the BeCu alloy are excellent with a 10^8 cycle limit at 310 MPa (45 ksi).

A.1.4.2 Geometry and Design

The final design consists of four flexing points. Two precise round-notch flexures in the sensitive axis with 0.250 in. (6.35 mm) radii each with a minimum web thickness of 0.004 in. (101.6 μm). There are also two 0.125 in. (3.18 mm) radii half-round notch flexures with webs of 0.015 in. (381 μm) for the direction perpendicular to the

sensitive axis. The ends of each flexure have a geometry such that they fit into both ends of the existing mounting structure and can be attached with the existing screws. Because of form factor constraints, the design for the top three and bottom three flexures are slightly different. This is necessary because the upper flexures need to fit between existing flex strips used by cantilevers for the proof mass offload springs.

The size of the 0.250 in. (6.35 mm) radius flexure elements was chosen because with a larger radius, less stress is induced when the flexure undergoes bending. However, at large radii the element loses its buckling robustness as it more closely approximates a column. The optimal point is thought to be very close to this chosen radius and has been shown to be adequate in subsequent acceptance testing.

The large radii notch flexure has a web thickness of 0.0040 ± 0.00025 in. (101.6 ± 6.35 μm), which is the critical dimension dominating the entire flexure's stiffness. This stiffness is critical because it defines the natural frequency of the instrument and, ultimately, the sensitivity. The smaller radii notch flexure web thickness is much larger at $0.0150 \pm \frac{+0.0025}{-0.0005}$ in. ($381 \pm \frac{+63.5}{-12.7}$ μm) with dimensions that are not as critical. The static loading for this flexure design was predicted through the calculations to be 33 g with the CAD drawings for both flexures shown in **Figure A.4**.

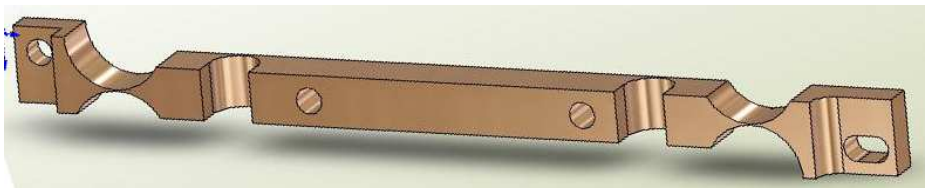

Figure A.4: CAD rendering of the GS-13 replacement BeCu flexure.

A.1.4.3 Manufacturing Process

The design of the BeCu flexure was optimized for manufacturing on a 3-axis CNC milling machine. Because of this, round notch flexures were used instead of elliptical elements. The manufacturing process is straightforward with no individual part flips. The process used for the prototype flexures is described as follows with multiple flexures milled out of the same piece of stock reducing setup time. Completed prototype flexures as machined at Stanford on fixture plate are shown in **Figure A.5**.

Over 1,200 production flexures were then machined under contract at High Precision Devices and installed in the aLIGO sensors (Champagnie, 2010).

1. Face the BeCu stock to 0.250 in. (6.35 mm). This is a reduction from the actual thickness of the stock, which was 0.270 in. (6.86 mm).

2. Drill the central mounting holes and mount stock to fixture plate with socket-head cap screws (SHCS).

3. Mill down the left and right edge creating the proper overall flexure length.

4. Mill the mounting recess on each end. This was accomplished using a standard and ball end-mill to create the proper contour.

5. Drill the left end mounting hole and mill the right end mounting slot.

6. Fix these mounting points to the fixture plate with SHCS.

7. With a 0.250 in. (6.35 mm) diameter ball end mill machine the two smaller round-notch flexure elements. The depth of this cut is critical to the specified $0.0150 \pm \frac{+0.0025}{-0.0005}$ in. ($381 \pm \frac{+63.5}{-12.7}$ μm).

8. Drill and then precision ream or bore the 0.250 in. (6.35 mm) radius holes that define the larger round notch flexures. The web thickness for this operation needs to be closely controlled to 0.0040 ± 0.00025 in. (101.6 ± 6.35 μm).

9. Mill around the contour of the flexure to release it from the stock.

10. Clean any machining lubricants in preparation for aging.

11. Age the cleaned flexures in a preheated oven at 330 °C in air for 2 hours. After they are removed and allowed to cool they can be installed.

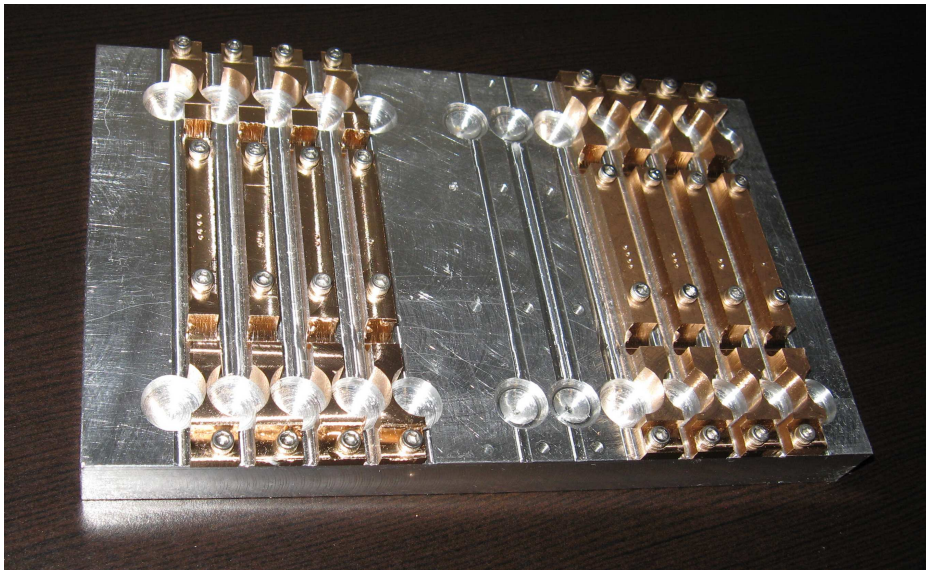

Figure A.5: Machined BeCu replacement flexures on fixture plate. The 8 flexures (4 upper and 4 lower) were machined from one plate of BeCu stock.

A.1.4.4 Installation Procedure

The installation of the flexures was accomplished with the following procedure:

1. Ensure the manual proof mass lock is engaged.

2. Remove the GS-13 can after removing the three bottom nuts and gaskets with a 9/16 in. wrench.

3. Unscrew and completely remove the $4-40$ screws and clamps on each end of the 6 delta-rods.

4. Remove the 6 delta-rods.

5. For seismometers with proof mass offload springs, the springs may need to be untensioned and the outer-most cantilever base flex strips removed to facilitate placement of new top flexures.

6. Position new flexures in place. Make sure to distinguish between upper and lower flexure variations. Tighten the screws on the left end of the flexures

which attach the flexures to the frame (round hole in flexure). Leave the screws on the the right end of the flexure loose (slotted hole in flexure).

7. If needed readjust the natural frequency (ω_n) adjustment knob to be in the neutral position with the knob indicating '0'. Do this by loosening the $4-40$ screws that clamp onto the torsion spring wire that is attached to the knob. Then re-tighten these screws.

8. Slightly release and carefully re-engage the proof mass lock.

9. Tighten all $4-40$ screws that hold the flexures in place (**Figure A.6**).

10. Replace the can and associated hardware.

11. Unlock the proof mass and test the instrument for freedom of movement.

12. Test the instrument's noise floor against other instruments and time response with weight-lift technique as described in the GeoTech manual and aLIGO documents (Hanson et al., 2009a), (Hanson et al., 2009b), and (Vargas et al., 2010). Prototype tests are also described in more detail in Section A.1.6.

A.1.5 Other Designs Considered

A.1.5.1 Maraging Steel Flexures

A flexure design made out of maraging steel C350 was first attempted. This design utilized small, 0.125 in. (3.175 mm), diameter round notch flexure elements in both the vertical and horizontal directions. The design was promising by having a predicted static load rating of 45 g. Unfortunately, this design had several drawbacks including: (a) difficulty in acquiring stock material in any geometry other than round rod, (b) relatively poor machinability, and (c) extensive hardening procedure including over 100 hours bake in an argon backfilled oven. The ultimate problem, however, was that the flexures become magnetic when installed on the seismometer. With the flexures in place, it was noted that sometimes when the proof mass traveled to one limit of motion the maraging steel flexures would be attracted to the proof mass and were

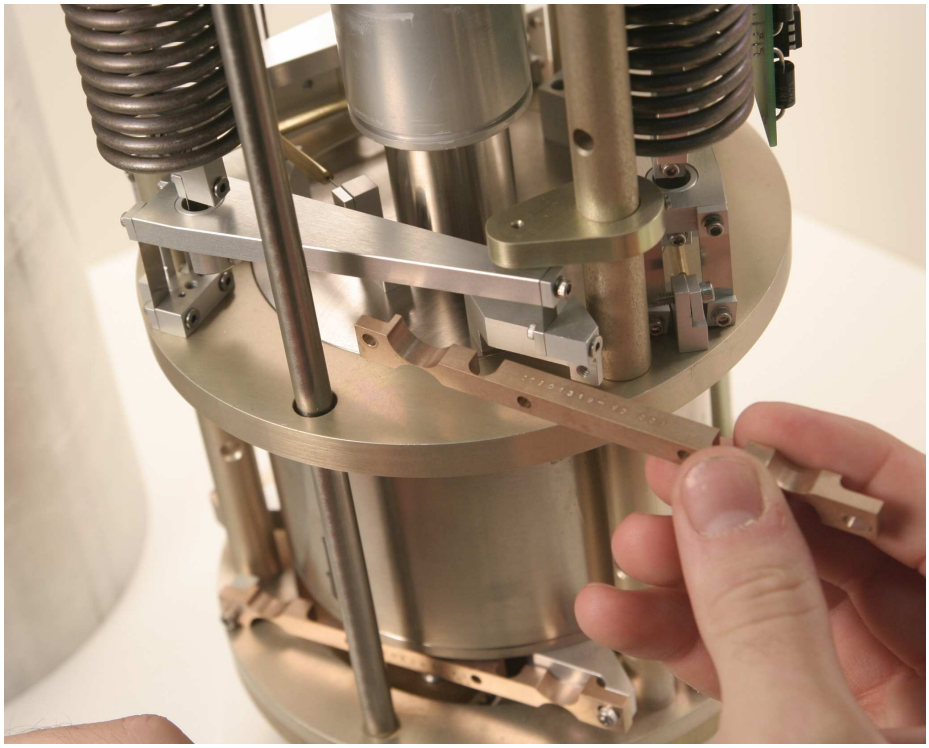

Figure A.6: Installation of an upper BeCu replacement flexure on a GS-13.

"captured" magnetically by it. This is not acceptable for the seismometer as free, uninterrupted motion is critical to the instrument's operation. **Figure A.7** shows a maraging steel prototype flexure installed in a test seismometer.

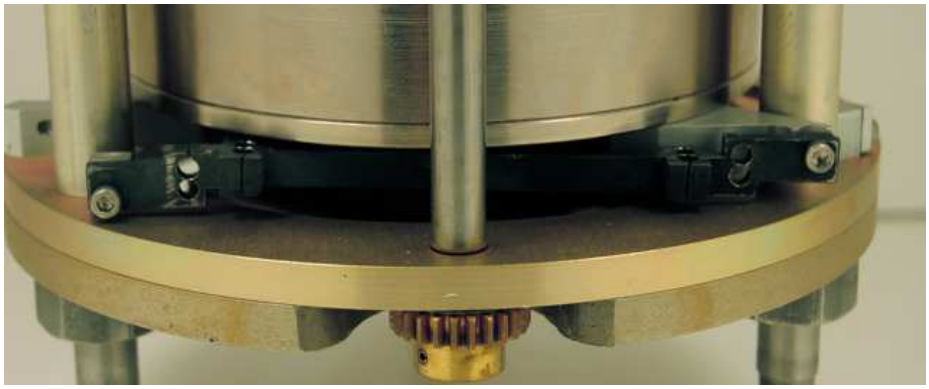

Figure A.7: Picture of installed C350 maraging steel prototype flexure in a test seismometer. This flexure had good mechanical performance but the magnetic properties would sometimes cause the proof mass to become "captured" in the lower extreme of travel. This is due to the magnetic attraction of the seismometer's permanent magnet to the maraging steel flexure.

A.1.5.2 BeCu / Brass Flexure

Another design that was pursued involved brass parts that were soldering together by thin 0.006 in. (152 μm) BeCu flexible strips to create the flexure. The material cost was very low for this design but the maximum strength obtained could not meet the goal of 20 g static loading. Several prototypes were made, and it became apparent that maintaining the required tolerances while soldering together the nine individual pieces (5 brass elements and 4 flexure joints) would be very difficult in a production setting. **Figure A.8** shows the design and **Figure A.9** shows a prototype installed on a test seismometer.

Figure A.8: CAD of the brass and BeCu flex strip flexure assembly. The flexure is composed of 5 brass sections and 4 BeCu flexible strips soldered together.

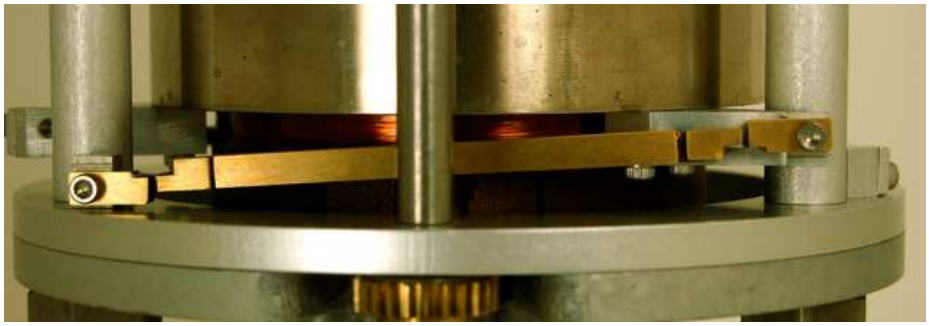

Figure A.9: Brass / BeCu flexure installed in the lower position on a test seismometer. While the materials cost was low for this design, it was not as robust and was more difficult to assemble to the required tolerances than either the maraging steel design (Section A.1.5.1) or the BeCu design (Section A.1.4).

A.1.6 Testing

A.1.6.1 Performance Validation

The testing of the GS-13 equipped with the recommended BeCu flexures was carried out by doing several tests comparing it to two GS-13 seismometers that had the original delta-rods. The first test consisted of comparing the response of the two instruments with a weight-lift procedure. In this procedure the proof mass of the instrument is pushed down to the lower limit of travel and then released while the time response of the system is recorded. **Figure A.10** shows three separate response plots for each of three GS-13 instruments. The first row, displayed in red, corresponds to the seismometer equipped with the new flexure design. The natural frequency of the seismometer and the Q factor can both be measured and compared through this test. The seismometer equipped with the new flexures had a natural frequency of 0.94 Hz and a Q factor of 41.5. This compares to natural frequencies of 1.01 Hz and 1.09 Hz respectively for each of the stock GS-13 seismometers with both of them having identical Q factors of 28.6. In order to maintain instrument sensitivity, it is important that the natural frequency be at or below that which the original delta-rods provided while maintaining a Q factor at or above what a stock seismometer gives.

The second portion of the performance testing involved placing the seismometer on the Stanford Technology Demonstrator Platform (Tech Demo). **Figure A.11** shows the table top where the seismometer's performance is compared against 6 feedback GS-13s, 2 stock witness GS-13s, 2 witness Streckeisen STS-2s, and a Trillium T-240 seismometer.

The results of this test are plotted in **Figure A.12**. Here it is important to note that the signal of the GS-13 with the modified flexures corresponds with that of the witness STS-2, and closely to the two witness GS-13 seismometers. The noise floor also closely matches one of the witness GS-13 seismometers and is actually better at higher frequency than the other stock GS-13. For this test, the chamber was at air pressure with chamber doors closed with only the stage two damping loops engaged. The noise was estimated using Hua's multichannel coherent subtraction method using the 6 feedback GS-13s, the 3 low frequency seismometers (2 STS-2s, 1 T240) and the

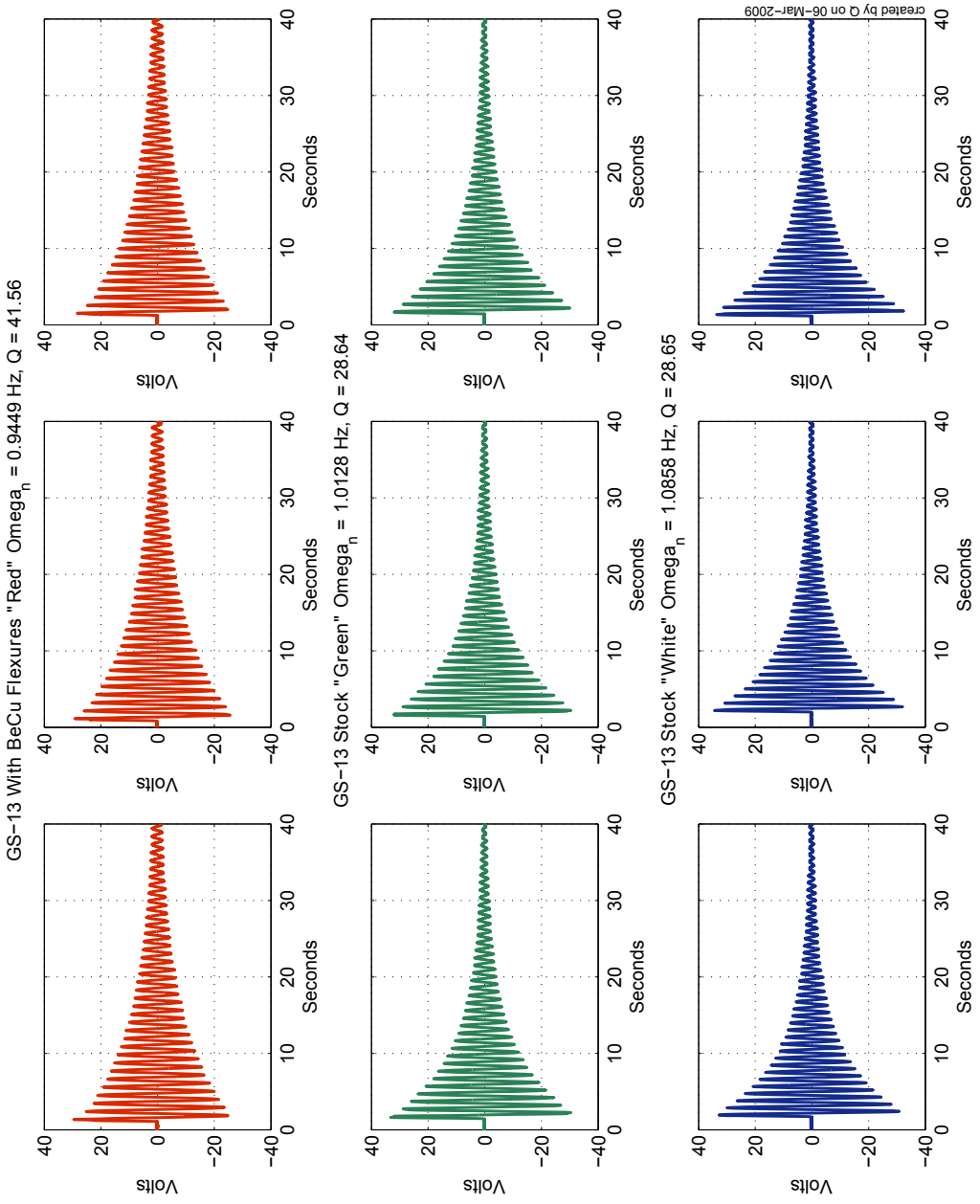

Figure A.10: Time response of GS-13 seismometer output to a step input of the proof mass. Three instruments were compared with three different collections indicating that the seismometer with the replacement flexures ("Red") had both a lower natural frequency, ω_n and a higher Q factor than the other two seismometers equipped with the original delta-rods.

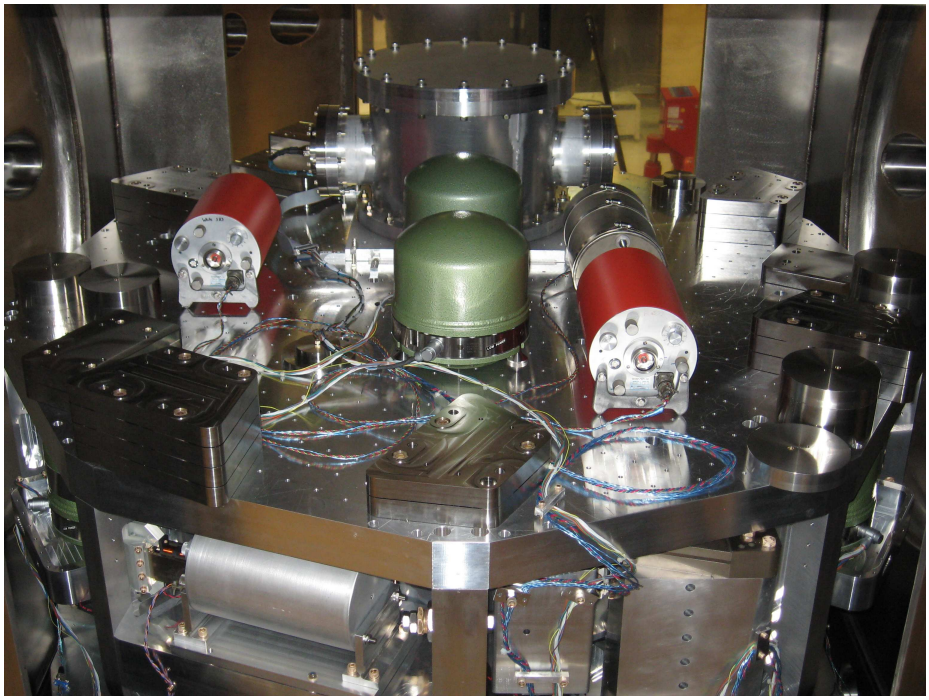

Figure A.11: The test GS-13 equipped with the prototype replacement flexures is compared to 2 other stock witness GS-13 seismometers, 2 witness Streckheisen STS-2 seismometers, a Trillium T-240 seismometer, and 6 feedback GS-13 seismometers in order to estimate any reduction in signal or increase in noise.

other 2 witness GS-13s as references (Hua, 2005). The results of this test are helpful in showing that the new flexure design does not degrade the instrument performance.

A.1.6.2 Robustness Testing

The flexures were also tested to establish their overall strength and resilience. The flexure has two main modes of failure. The first is due to exceeding the overall yield stress of the material and the second is buckling. As the round-notch flexure's radius increases with the loading, the web height, and the bending stiffness held constant, the buckling failure mode is dominant. Conversely, if the notch radius is decreased the yield stress limit is quickly reached.

While the design calculations assume the static loading case, tests were done for both static and dynamic loading. It is not clear how static loading calculations can be extrapolated to get dynamic, shock loading situations. For the static load tests, the flexures were placed in a fixture equipped with a load cell and compressed while recording the compression force. Static load tests were only done in compression because the buckling failure mode is only present in this configuration. **Figure A.13** shows one such test of a flexure to failure.

In the test plotted in **Figure A.13**, the flexure failed at a static equivalent loading of about 19 g force of equivalent static loading. In two other tests resulting in failure, flexures have failed at 18 g and 23 g. However, multiple prototype flexures withstood 27 g (the force at which the load cell saturated). The actual failure point is very dependent on the initial offset of the flexure and the stress loading from flexure bending. All of the static tests were carried out with the flexure at the maximum range of travel that it could experience when installed increasing the likelihood of failure. Buckling was the cause of failure in all flexures that failed. This indicates that a round notch radius larger than the current 0.250 in. (6.35 mm) would not be advantageous.

The second method of testing involved drop tests of an S-13 seismometer, equipped with an accelerometer, onto a concrete floor or swung into a concrete wall. (The S-13 seismometer is mechanically very similar to the GS-13 but is less expensive containing a coil with a reduced generator constant.) Before testing, the seismometer

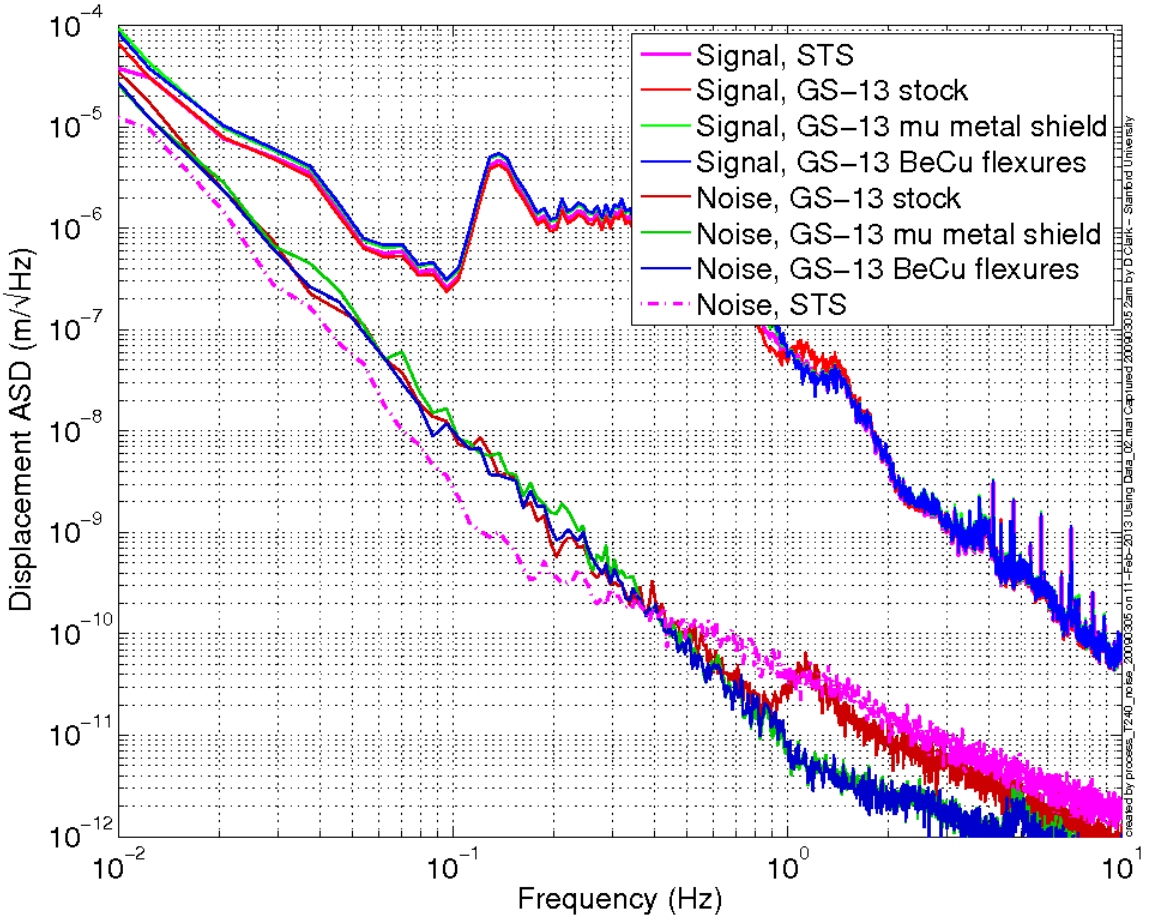

Figure A.12: Three GS-13 seismometers were compared along the x axis to a Streckheisen STS-2 witness seismometer on the damped Tech Demo platform at 1 am. The signal amplitude (upper curves) and an estimated noise floor (lower curves) of the inertial sensors are compared. The response and noise of the GS-13 seismometer with the BeCu flexures was acceptable compared to the other instruments containing the original delta-rods.

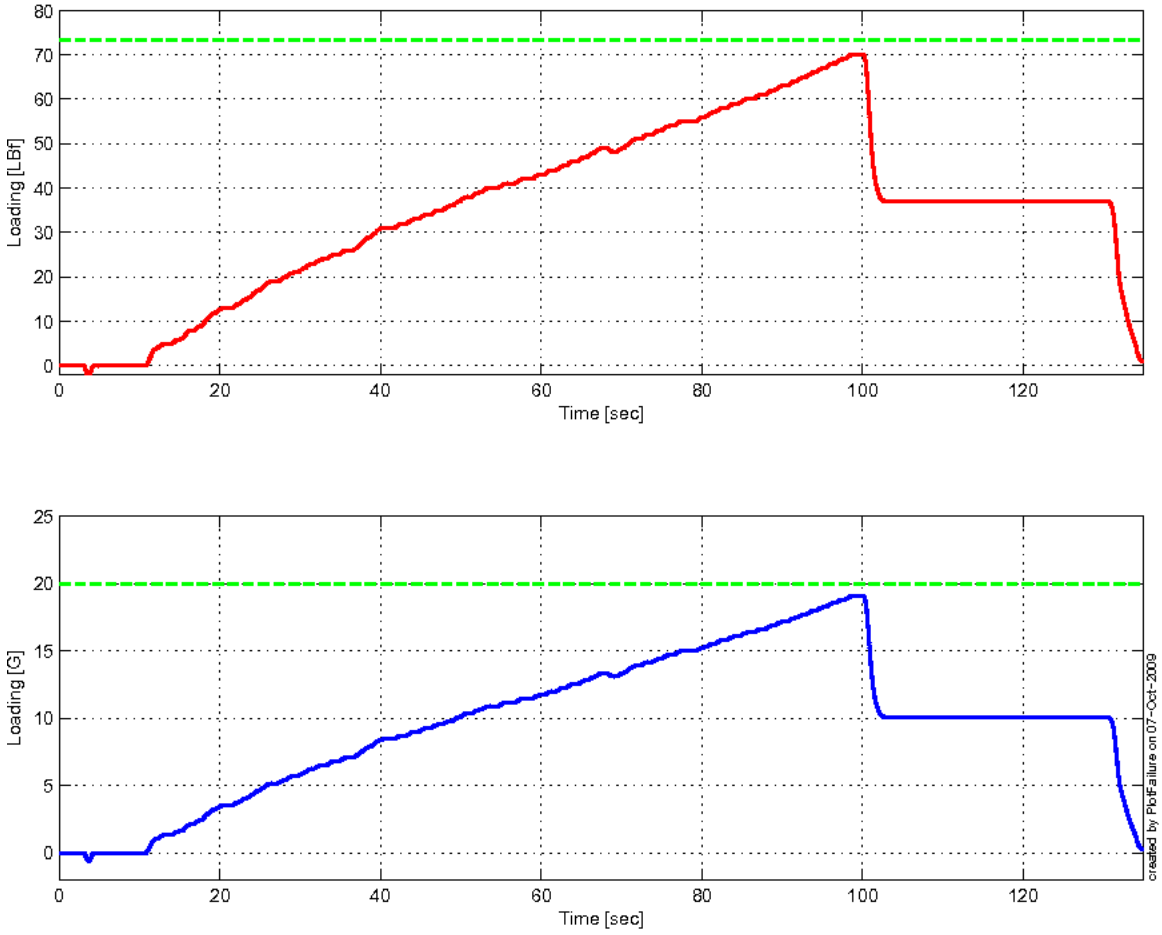

Figure A.13: Static loading of a BeCu replacement flexure to failure. This flexure only withstood the equivalent of 19 g static loading before buckling. The buckling is evident because the thin web section folded back on itself for a length of about 1.5 mm after which the flexure still held a compressional load.

was mounted inside its vacuum pod. The added mass of the pod helps reduce the accelerations that the seismometer is subjected to for any given drop which makes the test more representative of field conditions. For the situations when the instrument is not in the pod, the proof mass locking knob would be accessible and should be used so drop tests without the pod were not conducted. The instrument was then dropped from various heights onto different surfaces: a solid wood lab table, a stainless steel cleanroom table, cardboard, and ultimately the concrete floor. Of the drop surfaces, the stainless steel table provided the most compliance and thus the most energy absorbing and best surface for the instrument. The worst case was a 25.4 mm drop onto the concrete floor which had maximum peak accelerations on the order of 55 g. For this drop, the peak loading duration was very small measuring between 2 and 5 milliseconds (ms). **Figure A.14** shows the corresponding accelerations recorded for these drops onto concrete without any detectable degradation of the flexures.

The test seismometer was then swung into a 1 in. (25.4 mm) thick high-density polyethylene (HDPE) plastic plate on a concrete wall along the instrument's sensitive axis as shown in **Figure A.15**. While the instrument is subjected to large accelerations, in practice the motion of the internal proof mass is damped. This is because the aLIGO preamp board installed in the seismometer allows excess voltage that is generated by rapid movements of the seismometer's proof mass (along the sensitive direction) to be dissipated across diodes. One of the goals of the test was to measure the amount of current the instrument produces on impact and make sure that this does not exceed the levels that can be safely handled by the preamplifier and seismometer. **Figure A.16** shows the results of one of the swing tests and shows that the maximum current is around 60 mA which is well below the maximum that can be absorbed.

A.1.7 Recommended Use

The recommendations for the implementation of the more rugged BeCu flexure design as described in Section A.1.4 are threefold.

1. It is recommended that the manual proof mass lock be left in place on the

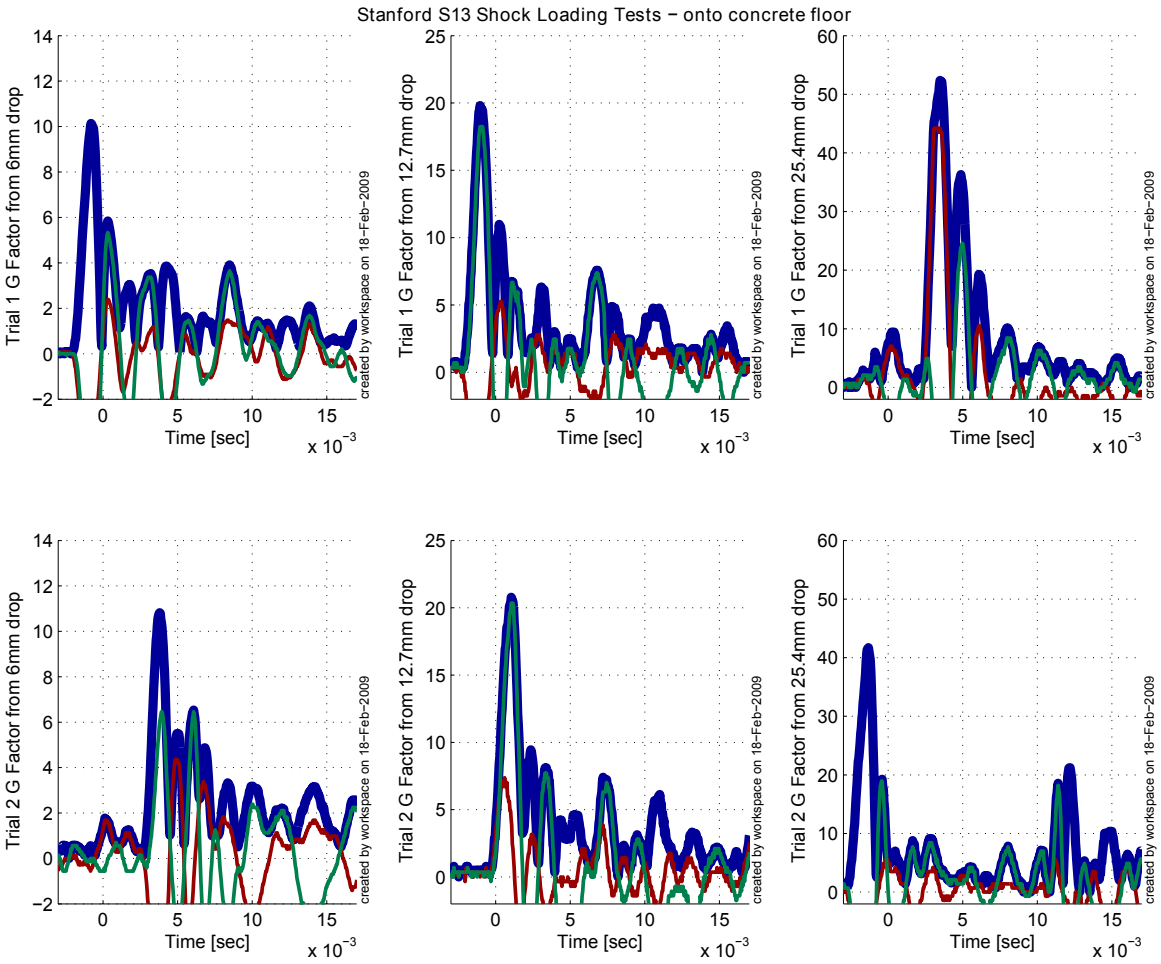

Figure A.14: Impact drop tests of the test seismometer onto concrete floor from differing heights. Both x and y directions are plotted. The thick blue line represents the addition of both directions in quadrature.

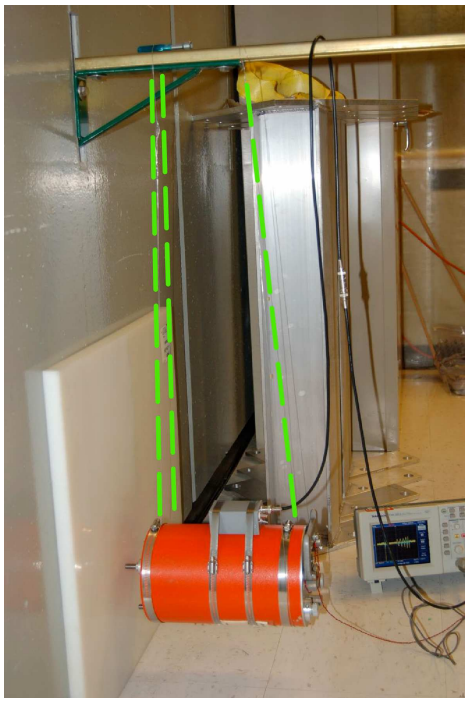

Figure A.15: A test seismometer is slung by wires (highlighted in light green) and allowed to swing into the wall while measuring the resulting deceleration on the instrument case.

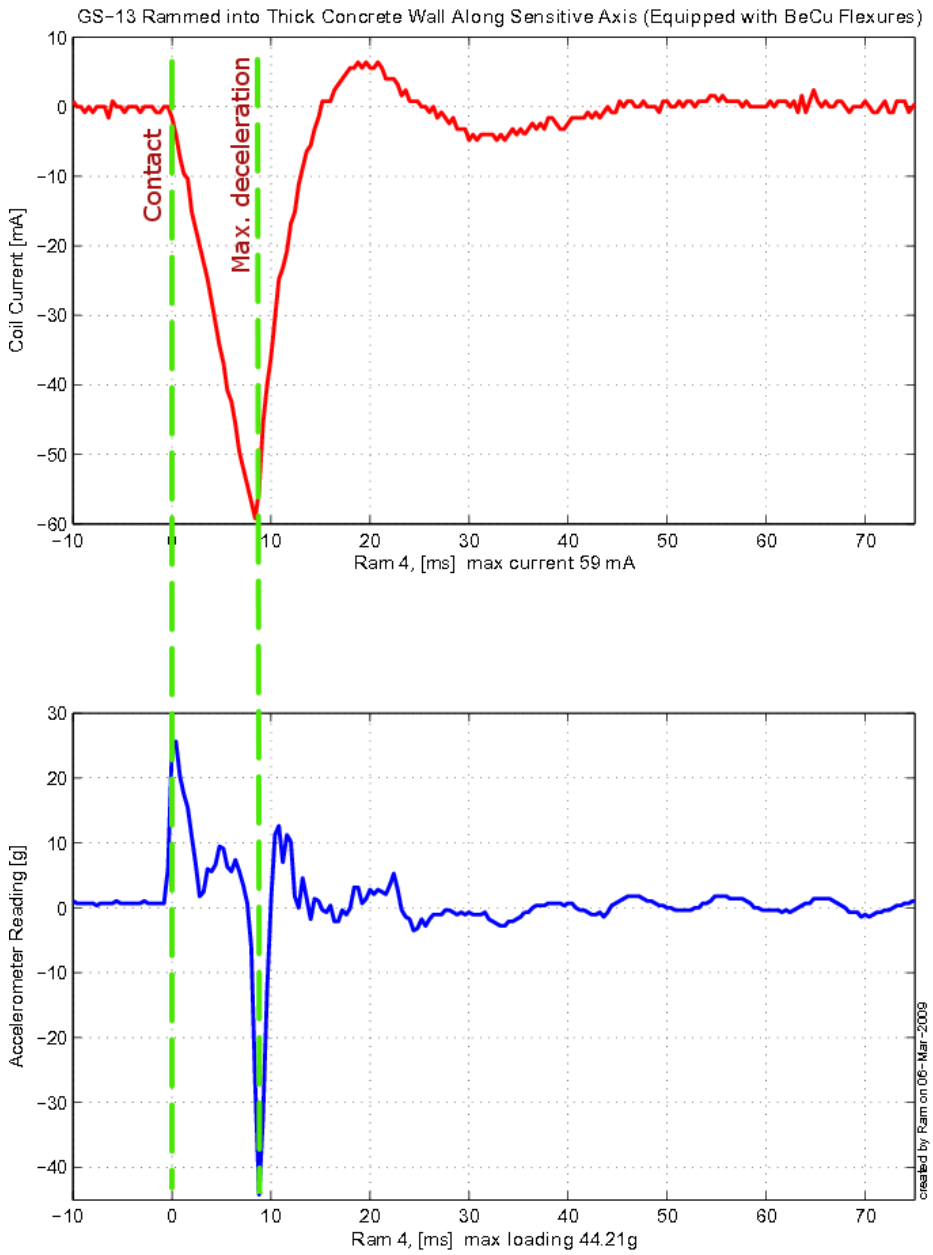

Figure A.16: The maximum acceleration on the seismometer case and resulting current flow of the test instrument on a 1 m pendulum being swung into the wall.

instrument. This manual locker will be accessible, and should be used, up to the point when the seismometer is installed in the vacuum pod. At the time of podding the manual lock should then be placed in the unlocked position.

2. When the podded seismometer is shipped, the seismometer and pod should be placarded to orient the instrument's nameplate and 'top' to be down. This is recommended for both horizontally and vertically configured instruments. The internal geometry of the seismometer is such that if placed in this orientation the proof mass settles into a cone which helps reduce the effect of impacts to the instrument providing a greater degree of protection to the instrument and flexures.

3. Finally, once the instrument is podded, further work would best be carried out on a semi-compliant work surface. In brief testing, a stainless steel cleanroom table provided much better shock damping than solid wood or concrete surfaces. Care in handling should be in accordance with standard care taken when using and handling sensitive scientific instruments.

A.1.8 Conclusion

The BeCu flexure design, as described in this report, has been adopted by aLIGO. Its use replaces the costly and sometimes unreliable in-vacuum proof mass locking motors. Testing indicates that the flexure maintains the original seismometer's sensitivity and noise floor while creating a much more robust instrument. It is also important that Section A.1.7 be followed to ensure proper, sustained instrument performance.

A.2 Offload Spring Damping

The GS-13 seismometer is equipped with 3 coil springs. These springs counteract the mg force due to gravity on the proof mass when operated in the vertical configuration. Even when the instrument is configured for horizontal sensitivity (the configuration

GS - 13 Flexure Elements

Definitions

Material Properties (www.matweb.com)

$E_{BeCu} := 125GPa$ $S_{y.BeCu} := 1103MPa$ Up to 900MPa

$E_{A228} := 210GPa$ $S_{y.A228} := 1590MPa$ Up to 2750MPa

$E_{steel} := 205GPa$ $S_{y.steel} := 310MPa$

$E_{nispan} := 165GPa$ $S_{y.nispan} := 760MPa$ Up to 200GPa in E

$E_{mara} := 27600ksi$ $S_{y.mara} := 294ksi$

Givens

$m_{proof} := 5\ kg$

$l_{clamp.total} := 10.1cm$

$force_{flexure} := \frac{m_{proof} \cdot g \cdot 2}{2 \cdot 3} = 3.674\ lbf$

$factor_{safety} := 1.5$

$force_{design} := force_{flexure}\ 20\ factor_{safety} = 110.231\ lbf$

$l_{rod} := 8.9\ cm$

$l_{flex} := 6\ mm$ for fixed free

$l_{eff} := l_{flex}\ 2 = 0.472\ in$

$disp_{max} := 3mm$

$disp_{transverse} := 6\ 10^{-5} m$

Figure A.17: MathCAD calculations for the BeCu flexure design - sheet 1.

Existing Flexure

Basis

$d := .021in$

$$I_{existing} := \frac{\pi \left(\frac{d}{2}\right)^4}{4} = 9.547 \times 10^{-9}\ in^4$$

Euler Buckling Load

Calculate the slenderness ratio. Euler's formula works if ratio is above 140. Buckling does not occur if less than 40.

$$r_{slenderness.eff} := \frac{l_{eff}}{\sqrt{\frac{I_{existing}}{\left(\frac{d}{2}\right)^2 \pi}}} = 89.989$$

$$EBF := \frac{\pi^2 E_{steel} I_{existing}}{l_{eff}^2} = 12.551\ lbf$$

$$SafetyFactor_{EBF} := \frac{EBF}{force_{flexure}} = 3.416$$

Traditional Load by Superposition

the two following equations should match

$l_{hingedApproximation} := l_{clamp.total} - l_{flex} = 0.095\,m \quad l_{rod} + l_{flex} = 0.095\,m$

$$\theta_{max} := \operatorname{asin}\left(\frac{disp_{max}}{l_{hingedApproximation}}\right) = 1.81\ deg$$

$$M_{equiv} := \frac{E_{steel} I_{existing} \theta_{max}}{l_{flex}} = 3.163 \times 10^{-3}\ ft\ lbf$$

$$\sigma_{bend} := \frac{M_{equiv} \frac{d}{2}}{I_{existing}} = 41.742\ ksi$$

$$F_{max} := \left(S_{y.steel} - \sigma_{bend}\right) \left(\frac{d}{2}\right)^2 \pi = 1.115\ lbf$$

$$k_{existing} := \frac{M_{equiv}}{\theta_{max}} = 0.021\ \frac{in\ lbf}{deg}$$

$$\frac{F_{max}}{force_{design}} = 0.01 \quad .01\ 30 = 0.3$$

$$SafetyFactor_{trad.exist} := \frac{S_{y.steel}}{\sigma_{bend}}$$

$SafetyFactor_{trad.exist} = 1.077$

Figure A.18: MathCAD calculations for the BeCu flexure design - sheet 2.

Good New Flexure

Round Notch Flexure - BeCu - Inline Motion

Design Variables

$d_{notch} := .5in \qquad b := .25in \qquad t := .004in$

Stiffness Calculations

$a_x := \frac{d_{notch}}{2}$

$K_{\theta zMz} := \frac{2\, E_{BeCu}\, b\, t^{\frac{5}{2}}}{9\, \pi\, \sqrt{a_x}} = 0.073 \text{ N m}$

$k_{existing} = 0.136 \text{ N m} \qquad \theta_{act} := \text{asin}\left(\frac{disp_{max}}{3.25in}\right) = 2.083 \text{ deg}$

Strength Calculations

$K_t := 1 + \frac{t}{2\, a_x}^{\frac{9}{20}} = 1.004$

$M := K_{\theta zMz}\, \theta_{act} = 2.665 \times 10^{-3} \text{ N m}$

$\sigma_{notch} := K_t \frac{6\, M}{t^2\, b} = 35.506 \text{ ksi}$

$t_{max.BeCu.yield} := \left(\frac{S_{y.BeCu}}{\theta_{act}}\right)^2 \frac{9\, \pi^2\, a_x}{K_t^2\, E_{BeCu}^2\, 16} = 0.081 \text{ in}$

$\theta_{yield} := \frac{S_{y.BeCu}}{\sqrt{t}} \sqrt{\frac{9\, \pi^2\, a_x}{K_t^2\, E_{BeCu}^2\, 16}} = 9.384 \text{ deg}$

$MaxS := S_{y.BeCu} - \sigma_{notch} = 124.471 \text{ ksi}$

$F_{axial} := MaxS\, t\, b = 124.471 \text{ lbf}$

$\frac{F_{axial}}{force_{flexure}} = 33.875$ Force to failure with flexure in offset position

$\frac{S_{y.BeCu}\, t\, b}{force_{flexure}} = 43.539$ Force to failure with flexure in neutral position

Figure A.19: MathCAD calculations for the BeCu flexure design - sheet 3.

Round Notch Flexure - BeCu - Out of Sensitive Axis Direction

Design Variables

$d_{notch} := .25in$ $b := .25in$ $t := .015in$

Stiffness Calculations

$a_x := \frac{d_{notch}}{2}$

$K_{\theta zMz} := \frac{2\, E_{BeCu}\, b\, t^{\frac{5}{2}}}{9\, \pi \sqrt{a_x}} = 2.823\, N\, m$

$k_{existing} = 0.136\, N\, m$

Strength Calculations

$K_t := 1 + \frac{t}{2\, a_x}^{\frac{9}{20}} = 1.027$

$\theta_{radial} := \tan\left(\frac{2.0629\, 10^{-8} m}{2in}\right) = 2.327 \times 10^{-5}\, deg$

$M := K_{\theta zMz}\, \theta_{radial} = 1.147 \times 10^{-6}\, N\, m$

$\sigma_{notch} := K_t \frac{6\, M}{t^2\, b} = 1.111 \times 10^{-3}\, ksi$

$t_{max.BeCu.yield} := \left(\frac{S_{y.BeCu}}{\theta_{radial}}\right)^2 \frac{9\, \pi^2\, a_x}{K_t^2\, E_{BeCu}^2\, 16} = 3.109 \times 10^{8}\, in$

$\theta_{yield} := \frac{S_{y.BeCu}}{\sqrt{t}} \sqrt{\frac{9\, \pi^2\, a_x}{K_t^2\, E_{BeCu}^2\, 16}} = 3.35\, deg$

$MaxS := S_{y.BeCu} - \sigma_{notch} = 159.976\, ksi$

$F_{axial} := MaxS\, t\, b = 599.908\, lbf$

$\frac{F_{axial}}{force_{flexure}} = 163.268$ Force to failure with flexure in offset position

$\frac{S_{y.BeCu}\, t\, b}{force_{flexure}} = 163.269$ Force to failure with flexure in neutral position

$\frac{48ksi}{30\%} = 160\, ksi$ $\frac{60.5ksi}{160ksi} = 0.378$

$\frac{1\, 10^8}{1Hz} = 3.169\, yr$ $\frac{37.8kN}{mm^2} = 5.482 \times 10^3\, ksi$

$\frac{2\, 10^5}{1Hz} = 2.315\, day$ $15.4 \frac{2000\, lbf}{in^2} = 30.8\, ksi$

Figure A.20: MathCAD calculations for the BeCu flexure design - sheet 4.

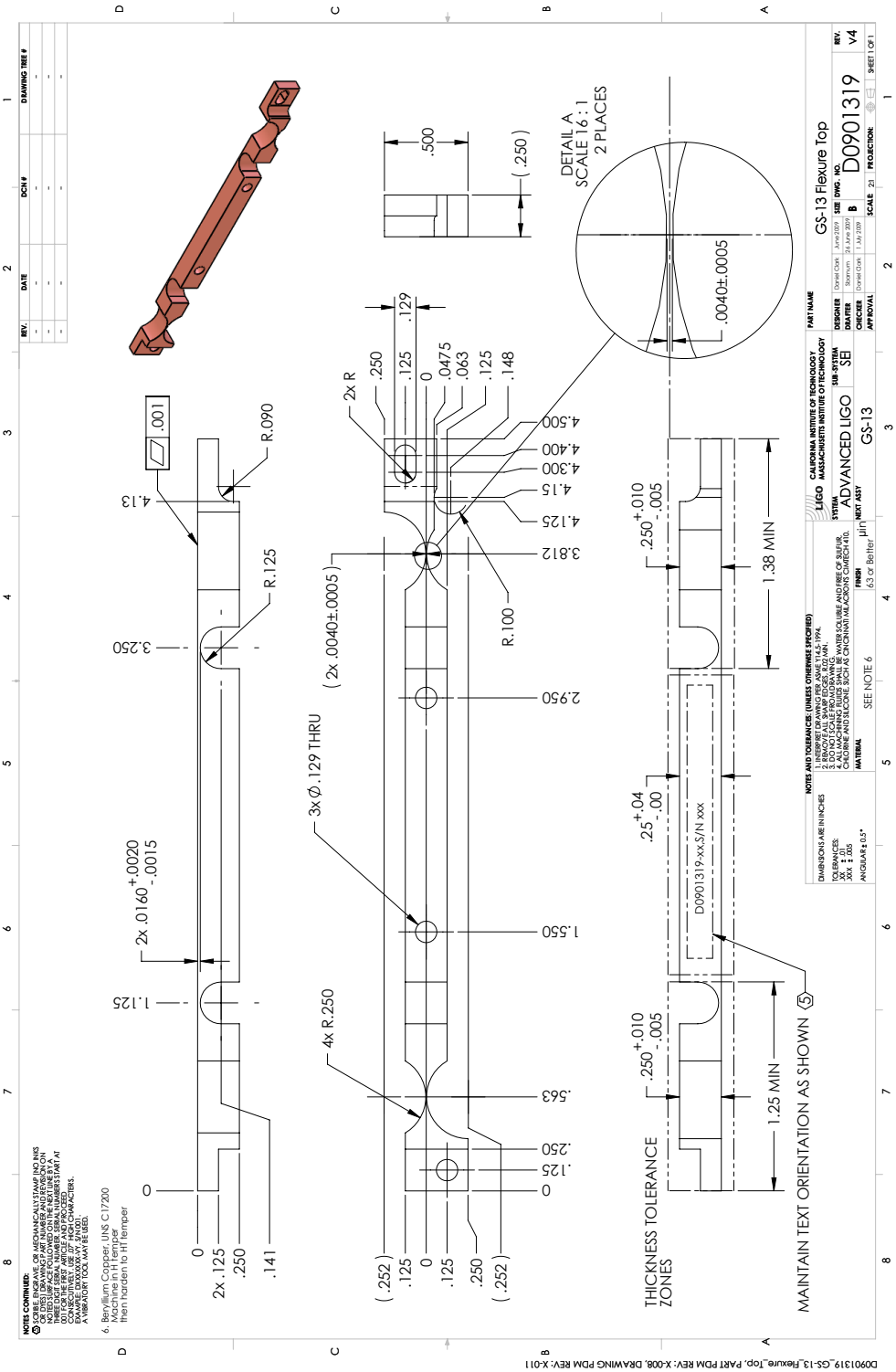

Figure A.21: CAD drawings of the BeCu GS-13 replacement upper flexure design.

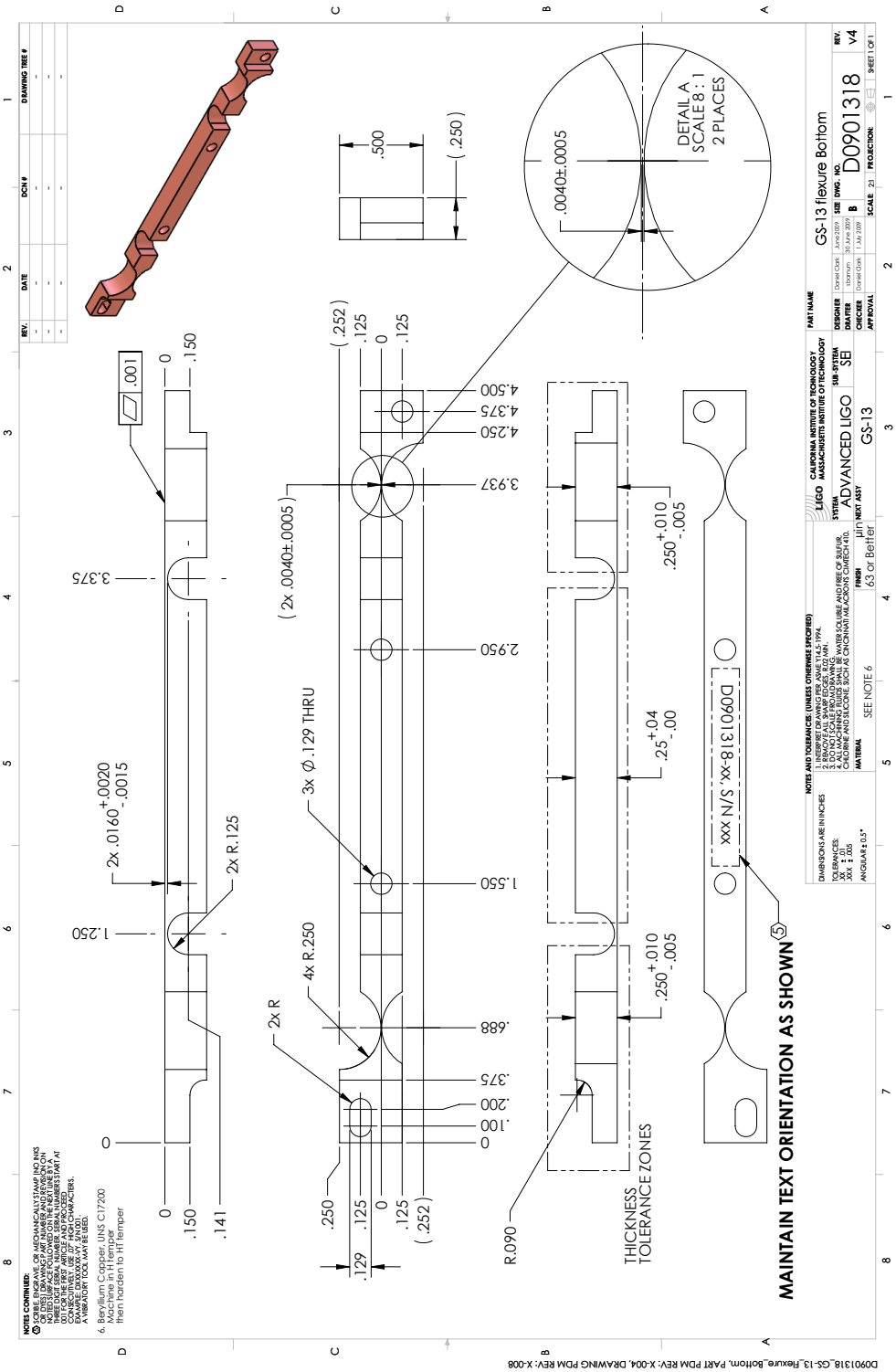

Figure A.22: CAD drawings of the BeCu GS-13 replacement lower flexure design.

when the springs are disconnected from the proof mass), the moving mass of these springs still couples into the active isolation system sensors. Note that for aLIGO, the springs are not installed in the horizontal units so this is only a concern in the vertical seismometers (Lantz, 2009b). The resonance of these springs was verified by placing a HeNe laser with a beam passing one of the coils of a vertically configured GS-13. The laser beam, partially occluded by the spring, was subsequently monitored on a photodetector. A spectrum analyzer was used to record the 103 Hz frequency resonance of the spring (**Figure A.23**).

In order to decrease the effect of this resonance on the rest of the ISI subsystem, a DuPont Viton® o-ring of the correct size to span the gap between adjacent coils was placed on the coil spring near the fixed attachment point (**Figure A.24**). Viton® was used because it has excellent damping properties at room temperature and is relatively easy to procure (Jones, 2001). The Viton® damped spring was measured while it was subjected to forced excitation and exhibited a dramatic decrease in the Q factor of the resonance.

For validation, all 6 of the in-vacuum GS-13 feedback seismometers used for stage two of the Stanford Tech Demo were removed and modified to include damping o-rings. 18 o-rings were installed and the seismometers were re-installed on the isolation platform. **Figure A.25** displays results as measured on the Tech Demo before and after the installation of the damping o-rings. Several resonances are seen in this plot due to the fact that not all of the springs resonate at the same natural frequency. Once the damping o-rings have been installed, the effect of the GS-13 spring resonances fall below the noise floor for the measurement to the point where they were no longer detectable. This means that these resonances will not introduce excess motion in the isolation platform from control loops which use these sensors.

Long term creep or "compression set" of the o-rings was not tested although a demonstration o-ring damped spring unit did not seem to degrade over several years. If the creep strain relaxation could be compared to the analysis of the Initial LIGO seismic isolation stacks, it is roughly estimated that this will not be an issue for several decades (Giaime, 1995), (Giaime et al., 1996).

For aLIGO isolation systems, the vertical seismometers are to have a damping

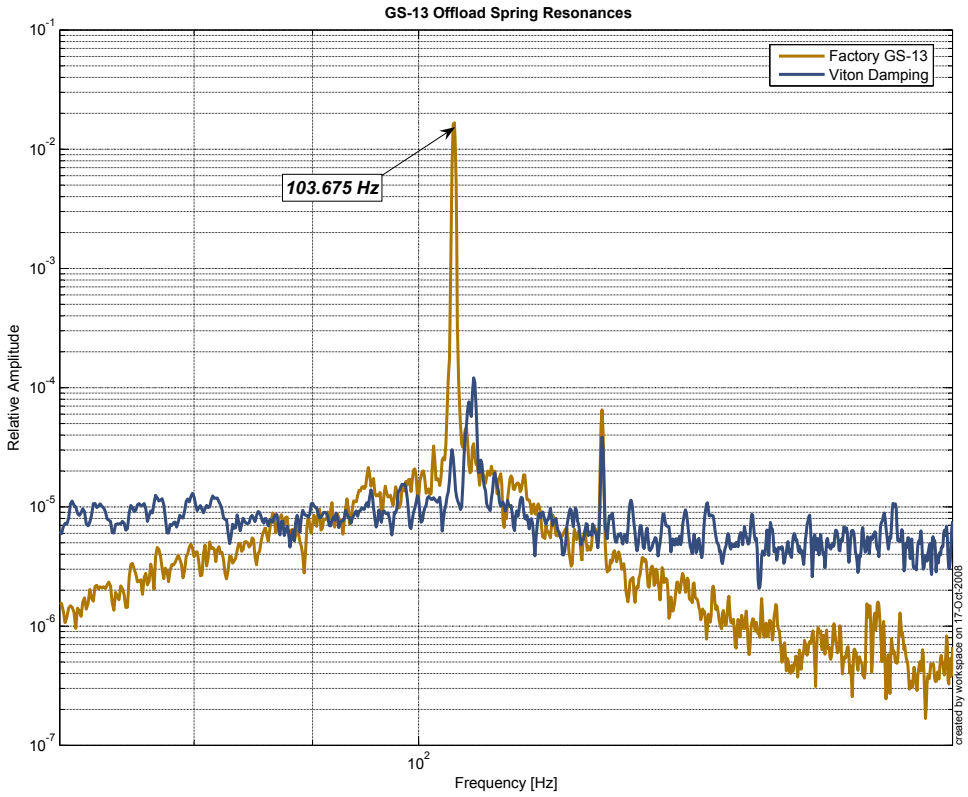

Figure A.23: The GS-13 seismometer proof mass offload springs have an internal resonance that couples into the measurement. A laser vibrometer measured this spectra revealing the frequency and Q of the peak. Adding a Viton® o-ring reduces the Q.

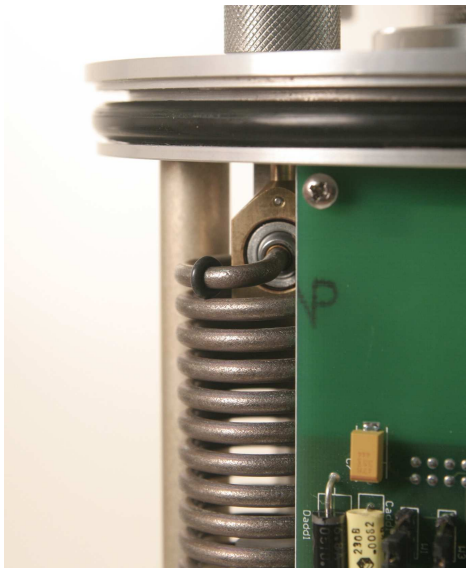

Figure A.24: Placement of Viton® o-ring to damp the internal resonance of the GS-13 offload spring.

o-ring installed on the offload springs (Hanson et al., 2009b), (Hanson et al., 2009a). While this is helpful for the vertical seismometers, aLIGO was able to procure the horizontal seismometers without the offload springs installed (Lantz, 2009b). (The offload springs are not necessary for the operation of horizontal sensors.) Thus this addresses and eliminates this resonance mode from affecting the isolation platform performance.

A.3 μ-Metal Shielding Tests

A concern is that the GS-13 seismometers can be affected by local magnetic fields. In aLIGO the GS-13s are located within several centimeters of the corresponding, degree of freedom, voice-coil actuators. Concern was raised that stray fields could raise the noise floor of the instrument. Two independent tests were performed on the Stanford Tech Demo with GS-13 seismometers podded inside a μ-metal enclosure.

Tests which compared the shielded GS-13 seismometer to another unshielded witness and 6 unshielded feedback seismometers, indicated that the noise floor was not

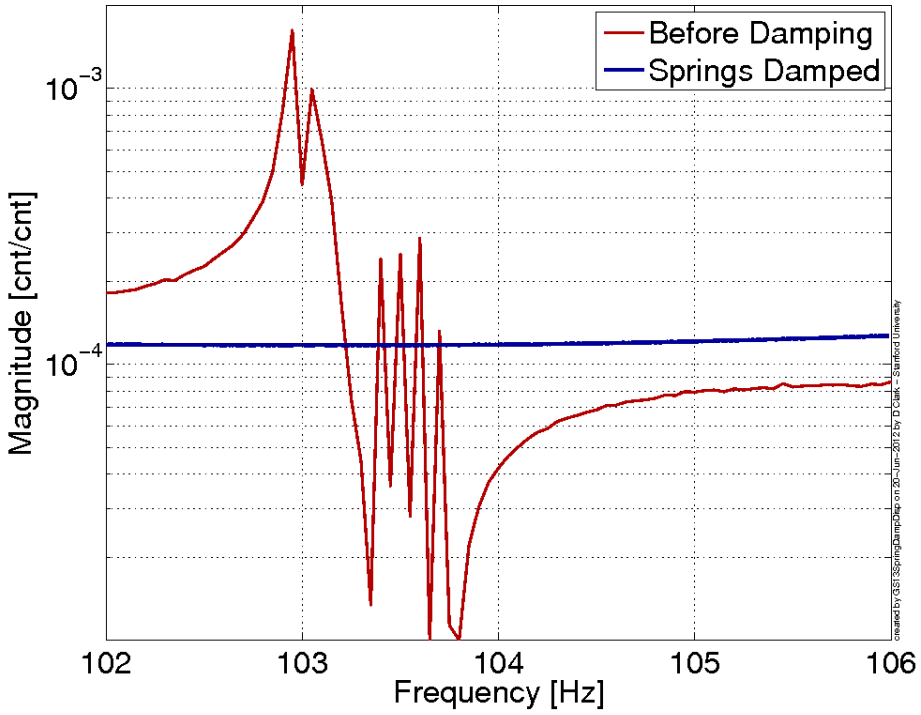

Figure A.25: Driven transfer function of the TDP. Spring resonances were clearly visible in the GS-13 response. Placement of Viton® o-rings damped the internal resonances of the GS-13 offload springs.

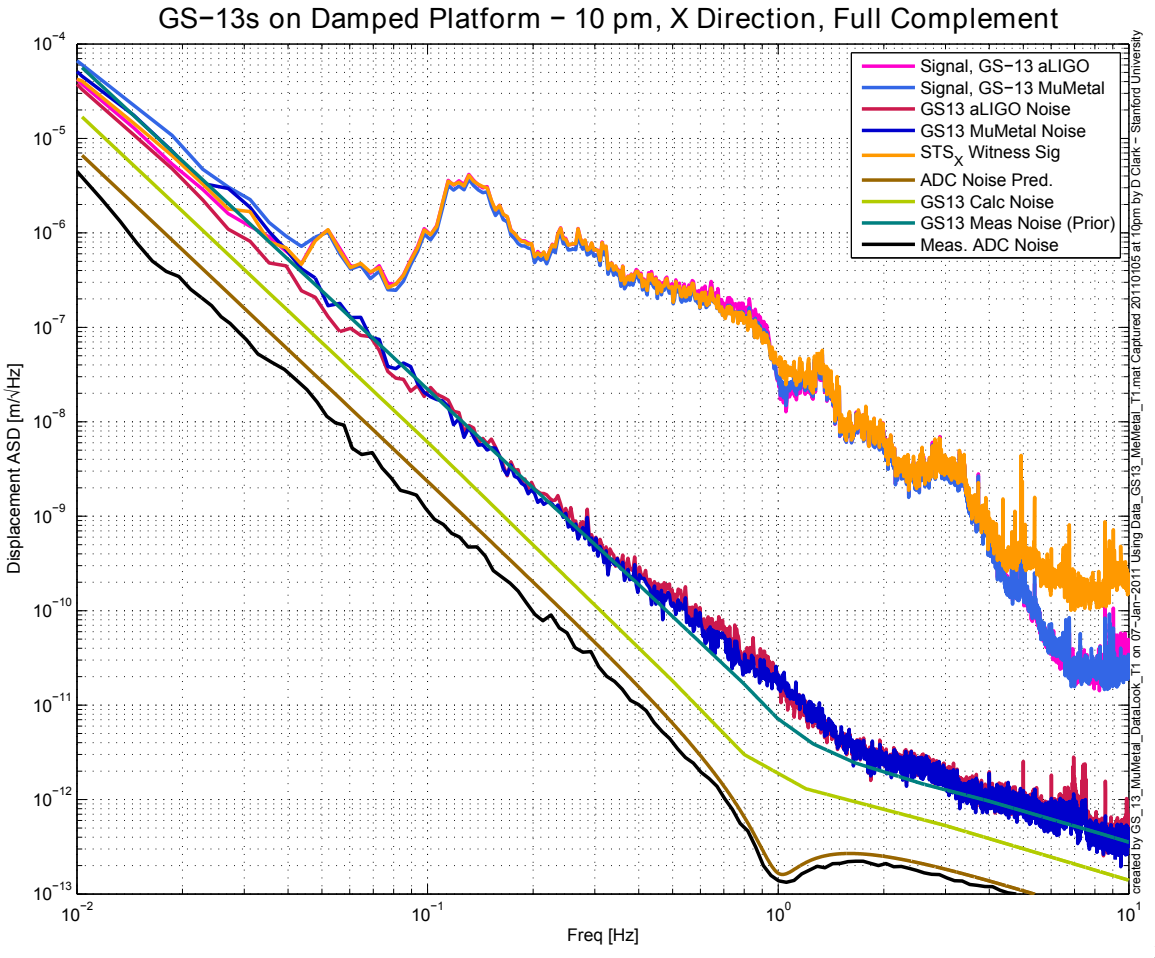

Figure A.26: Frequency response of a μ-metal shielded GS-13 seismometer on the Stanford Tech Demo.

detectably reduced by adding the shielding. **Figure A.26** shows the seismometer's signal and noise floor comparing the shielded to witness GS-13s. The curves on the bottom are the predicted and measured ADC, and preamplifier electronics noise respectively. It is interesting to note that the noise of the GS-13 does not meet the expected noise floor given by the preamplifier electronics when unlocked and operating. If the proof mass is locked down, however, then the noise is closer to the expected values. In part, this could be due to the fact that motion generates a bias voltage across the coil. As shown in Section A.4, a bias creates excess noise.

In the tests done as shown in **Figure A.26** on the platform, the μ-metal shielding does not seem to reduce the noise floor when operating on the Stanford Tech Demo. However, tests at MIT showed that the μ-metal shielding does reduce the magnetic coupling of the instrument (Biscans and Matichard, 2010). For the tests at Stanford, it is important to note that the μ-metal test GS-13 seismometer was located on the table surface and much more distant from the voice-coil actuators (a magnetic field source) than the feedback GS-13s. Because of their closer proximity to the voice-coils, the feedback GS-13s could possibly benefit from μ-metal shielding that was not predicted from the tests at Stanford.

A.4 aLIGO GS-13 Preamp Resistor and Bias Measurements

The GS-13s that are to be used in aLIGO are equipped with updated, internal preamplifiers (Hanson et al., 2009b). These boards use standard thin-film surface mount resistors. A test was conducted to determine if any performance gain could be achieved by replacing the standard resistors with precision Vishay VSMP1206 49R9, 953R, and 9K2 resistors. On the preamp board, R1 and R2 were replaced and a resistor was soldered across the seismometer's coil input to approximate the DC resistance of the sense coil. The voltage noise was measured at low frequency and at two different bias voltage levels across the effective coil resistor. The following **Figure A.27** indicates that the noise increases by a factor of 5 with a 25 mV bias was applied levels. While

differences in the noise were noted with changes in the bias, the precision resistors are not discernibly better than the ones already in use on the aLIGO preamplifiers.

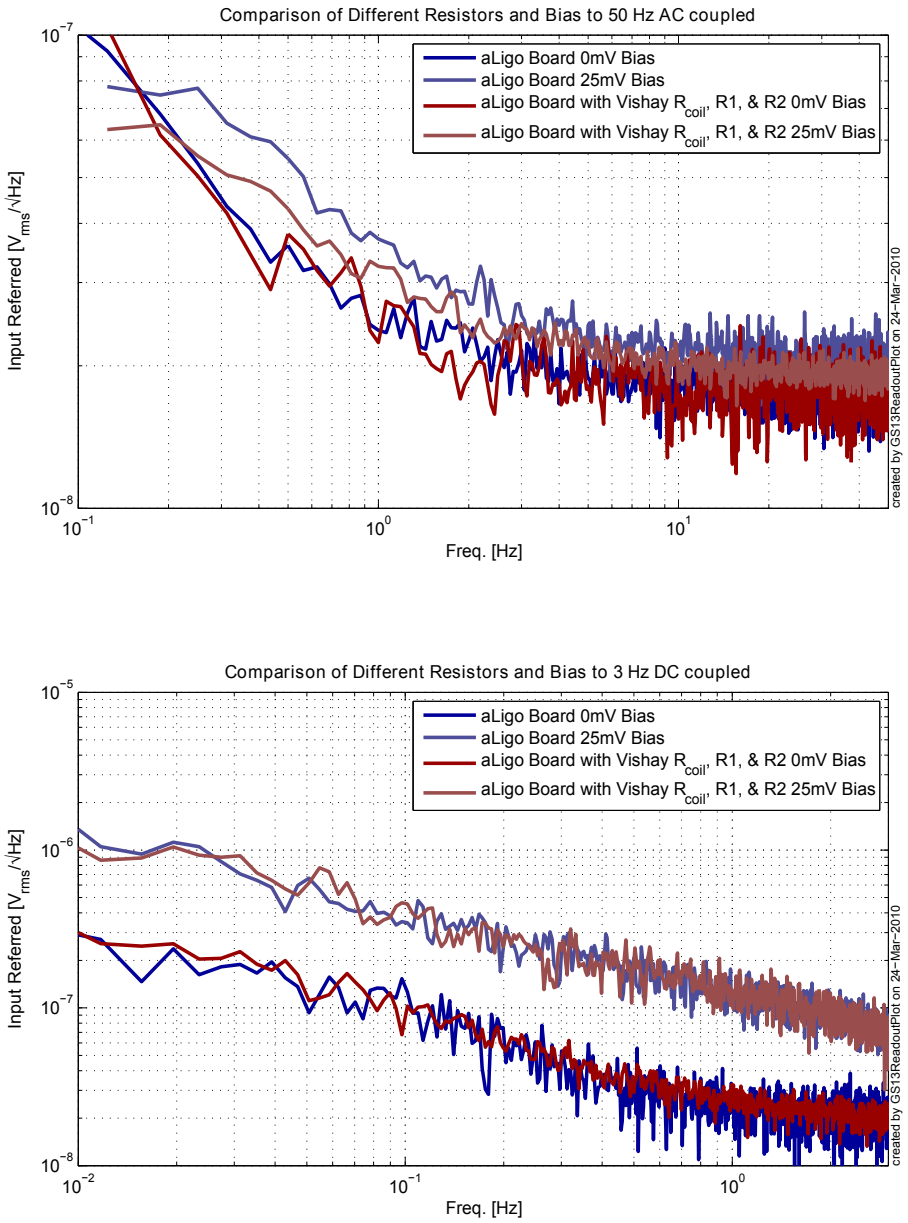

Figure A.27: Noise measurements of the aLIGO GS-13 preamplifier with different resistors. No noticeable effect was seen with the precision resistors over the ones that are currently being used for the preamplifiers.

Appendix B

Trillium T-240 Seismometer Characterization

Initial research and development for the LIGO BSC Internal Seismic Isolation (ISI) subsystem relied on the Streckheisen STS-2 seismometer for velocity sensing of the stage one platform. The STS-2 seismometers were already tested and qualified when concerns over availability, lead times, remote mass locking reliability, and support led to interest in validating the Trillium T-240 as an acceptable replacement. The T-240 is a long period (240 second), low noise, tri-axial seismometer specified to have performance comparable to the STS-2. Unlike the STS-2, the T-240 does not require proof mass locking which reduces complexity for in-vacuum use. A test T-240 instrument was installed on the Stanford ETF Technology Demonstrator Platform (Tech Demo) to determine its sensitivity and noise level relative to two witness Streckheisen STS-2s (**Figure B.1**).

B.1 T-240 TDP Installation

The T-240 was readied for placement on the Tech Demo by building a pod so that the interior could be held at atmospheric pressure while inside the vacuum system. The instrument was attached to the pod through the use of threaded studs. These studs had a right handed M10 x 1.0 thread on one end and a left handed $5/16 - 24$

Figure B.1: The Trillium T-240 seismometer (right) next to the Streckheisen STS-2 seismometer (left). The T-240 is slightly taller but occupies a smaller diameter (as viewed from above). While the instrument diameters are similar, the T-240's feet are contained within the outer diameter of the instrument.

threads on the other end. These studs, with equal turns on each end, interfaced with the threaded mounting holes in the seismometer and pulled the instrument down onto the plate. Three mounting protrusions cast into the instrument housing become the constraint point with the plate. The pod was then attached to the platform and in-vacuum wiring connected the instrument to a flange through the vacuum wall (**Figure B.2**). A readout box was built from a prototype STS-2 readout box, which amplifies the instrument's output, selects the coordinate basis system, allows for calibration signals to be sent, commands re-centering of the masses, allows for mass position readout, and allows for RS-232 serial communications to the instrument (the DB-25 feedthrough pinout is displayed in **Figure B.3**).

B.2 Comparison of Signal and Noise to the STS-2

The vacuum system was pumped down to the 10^{-5} Torr ($\approx 10^{-3}$ Pa) level with the damping loops on the Tech Demo engaged. Data was recorded from both the two

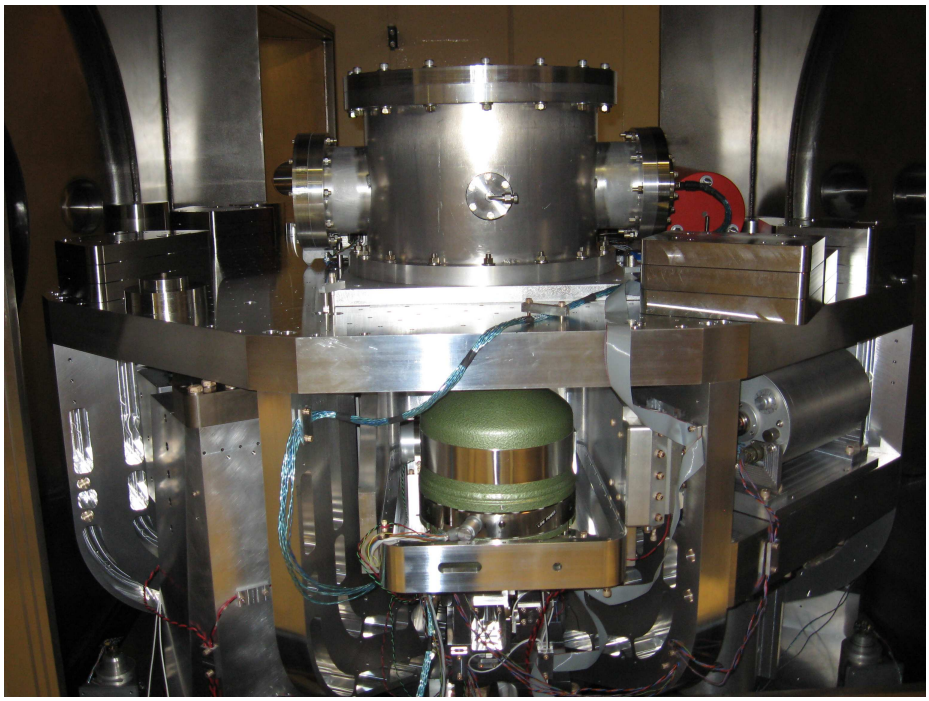

Figure B.2: The Trillium T-240 instrument, housed inside the pod, is located at the top center of the platform.

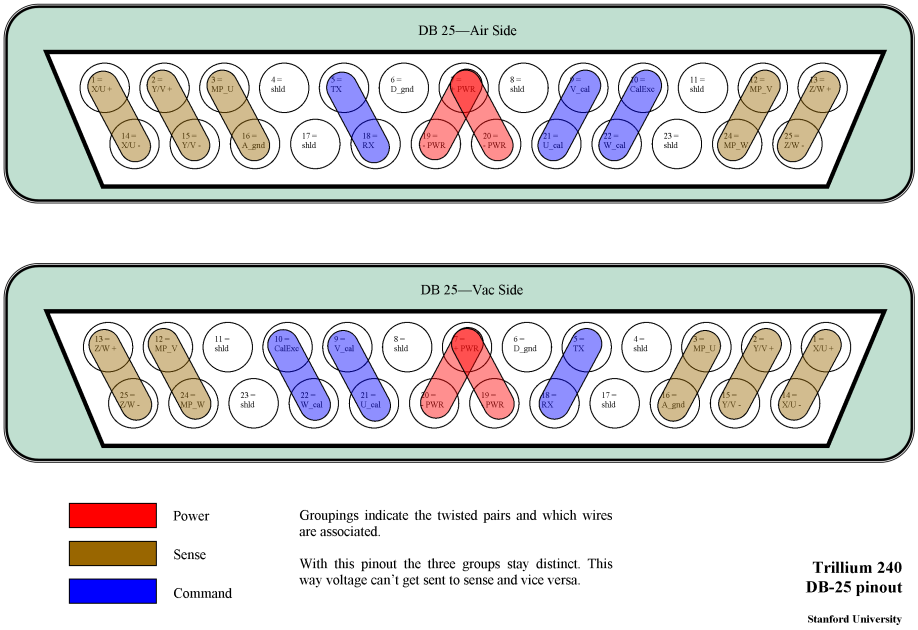

Figure B.3: Pinout for the vacuum and air side of the DB-25 connectors used for the power and signal for the Trillium T-240 seismometer in the Stanford ETF

witness STS-2 seismometers and the T-240 over several hours. This data was analyzed using Hua's multichannel coherent subtraction method (specExplain), which looks for uncorrelated noise between instruments (Hua, 2005). The uncorrelated part of a signal (such as readout electronic noise for example) was then ascribed as the noise floor of the instrument while the correlated parts of the signal (such as translation, or rotation of the instrument) was plotted as the instrument's signal. It is important to realize that while the correlated signal is ascribed as the instrument signal it does not distinguish between common mode sources that affect all instruments, such as tilt-horizontal coupling and common electrical noise in all sensors, such as 60 Hz line noise.

The correlated signal and the uncorrelated noise is displayed in **Figure B.4**. The spread between the two traces for any given instrument represents the signal to noise ratio. While the T-240 signal is comparable to that from the STS-2, the noise floor is noted to be slightly elevated in some degrees of freedom.

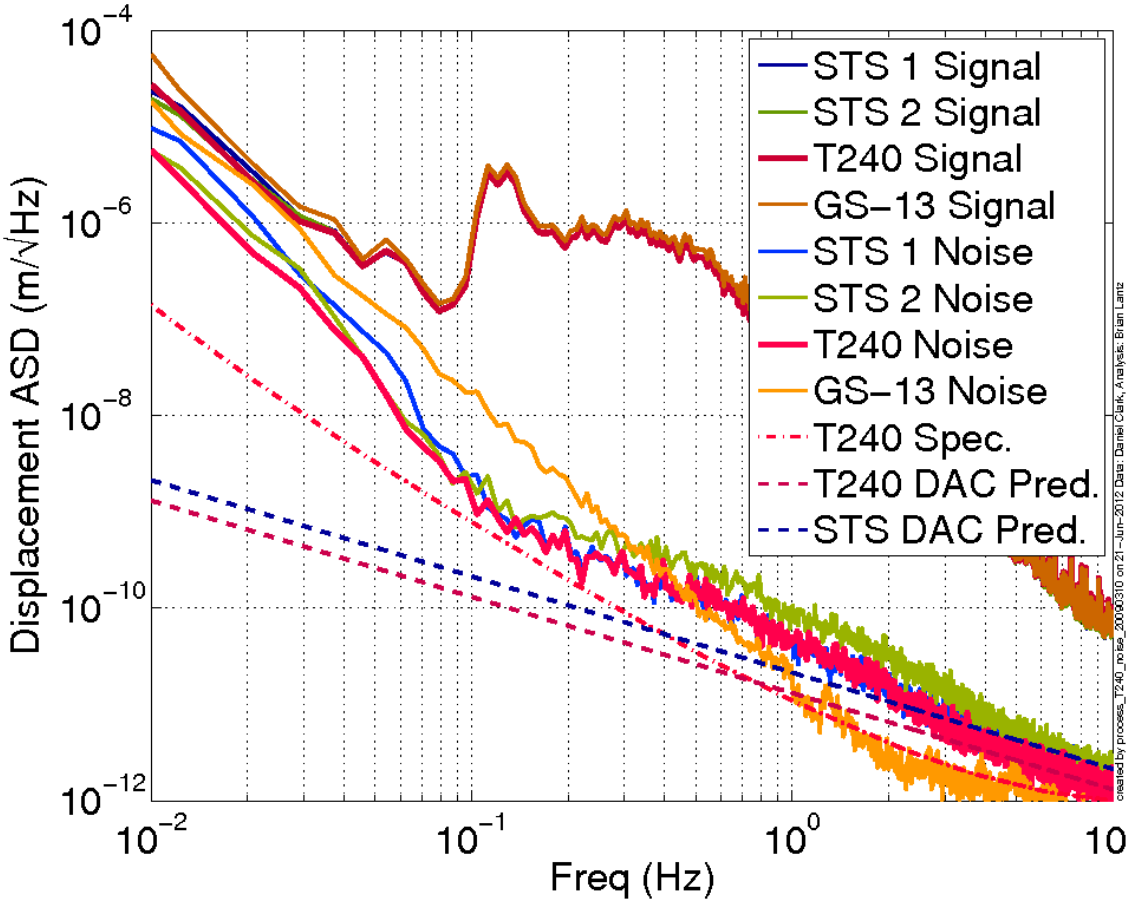

Figure B.4: The spectrum and noise floor of the test instruments on the Tech Demo, x axis on 2009-03-10 at 2100 hrs. The noise floor is estimated for the DAC given the different instrument gains and is plotted along with the T-240 specification. The Trillium T-240 does not seem to have an elevated noise floor in comparison with the two witness STS-2 seismometers in this case. For the y axis, the noise is also comparable between the STS-2s and the T-240. The z axis, though, showed a slight increase (up to a factor of 2 worse) at some frequencies..

B.3 Conclusion

Despite the slightly higher noise floor of the T-240 in some tests as compared with the STS-2, the overall performance is similar. Other non-performance factors such as the slightly smaller physical diameter and lack of proof mass locks make the T-240 an appealing instrument for aLIGO use. The T-240 was subsequently chosen for use on the aLIGO ISI platforms. Some of the 45 instruments required are already installed and provide the necessary low frequency inertial sensing.

Appendix C

Damping of HAM ISI Blade Springs

The aLIGO HAM Internal Seismic Isolation (ISI) subsystem utilizes three maraging steel blade springs countering the mg force of the single active platform stage. Brian Lantz (Stanford) and Jeff Kissel (Louisiana State University (LSU)/LLO) had recognized that a problematic resonance around 150 Hz in the ISI was caused by the blade springs that High Precision Devices had modeled in finite element analysis (FEA) at 155 Hz (Lantz, 2009a).

Andy Stein (MIT) then checked the FEA analysis of the blade springs and reported the calculated resonance to be 153 Hz (Stein, 2009). Because resonances such as these can easily couple into the control feedback signal, it is advantageous from a controls perspective to either increase the resonance frequency or reduce the resonant Q factor. There are methods used to filter out such resonances in the control loops but the control system as a whole is much more robust if the offending resonances can be removed from the plant. Often it is easier to reduce the Q by an order of magnitude than it is to stiffen the system and increase the frequency of any particular resonance by a corresponding order of magnitude. This appendix describes a method implemented to damp this 153 Hz resonance of the HAM ISI blade spring.

C.1 Damper Design

A Tuned Mass Damper (TMD) was used to provide the reduction in Q for the first blade spring resonance. A TMD is a parasitic mass-spring-damper resonant system that is placed on the primary structure. The TMD resonance is tuned to match that of the structural mode to be damped. It is then placed on the structure such that the primary structure's resonance excites the TMD which then parasitically couples energy out of the system and into the TMD damping mechanism. Several aspects make a TMD well suited to damping the HAM ISI blade springs. These include factors such as:

- The resonance is well defined at one particular frequency (since the geometry of the blade springs and weight they support are closely controlled).
- The overall size could be reduced since the TMD is a resonant system which helps couple the energy at the tuned frequency into a loss mechanism.
- The TMD should not adversely affect the blade spring performance at lower frequencies.

Since aLIGO operates at ultra-high vacuum (UHV) levels, strict requirements are in place specifying which materials are allowed (Coyne, 2009a). Of these materials, DuPont Viton® has desirable damping qualities at room temperature and around 100 Hz (Jones, 2001). Viton® is also on the aLIGO approved list of materials if used in limited quantities, obtained from approved vendors, and processed as per LIGO cleaning procedures (Coyne, 2009b). As a result, Viton® was chosen as the loss method for the TMDs.

Ideally, the mass-spring system of the TMD should have a $Q \approx 10$ while matching the 153 Hz mode of the blade springs (Clark and Lantz, 2009). To measure this, a HeNe laser and photodetector were set up as a vibrometer and connected to a spectrum analyzer. The analyzer was configured to drive a shaker platform and record the transfer function of the platform to vibrometer. Prototype TMDs were built and tested on this setup to ensure the parameters were met.

To mount the device, a mechanical bolted connection to the blade springs would be ideal but the FEA analysis provided by Andy Stein suggested that even a small attachment hole in the blade spring results in large stress concentration factors (Stein, 2009). Since the blade spring is a maraging steel, magnets were tested and it was found that they provided an adequate connection.

After several prototyping iterations, the final design was a small mass about 0.150 kg attached to the end of a stainless steel strip. This strip is clamped to a base where the attachment magnets are placed, constrained laterally in slight pockets. Beneath the stainless strip a Viton® o-ring is placed that is backed by a small stainless plate. The mechanism for loss in this design is that motion of the mass creates a slight compression and shear in the Viton® o-ring at the base resulting in the energy of the system being dissipated as heat. **Figure C.1** displays a CAD diagram of the TMD and a CAD drawing in **Figure C.4**.

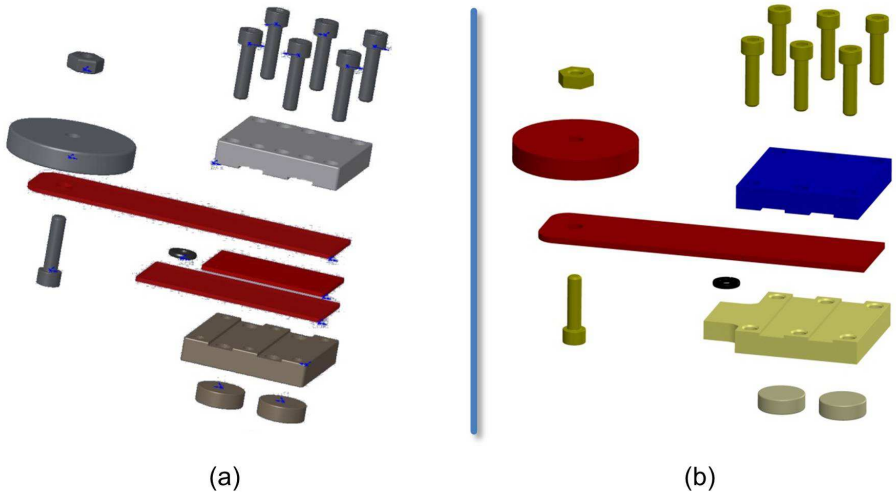

Figure C.1: Tuned Mass Dampers for reducing the Q of the first internal resonance of the HAM ISI blade springs. The exploded diagram shows the assembly of the units used in eLIGO HAM 6 (a). For aLIGO BSCs, the TMD design was revised to include a base plate made from 440 stainless reducing parts count and eliminating the need for nickel plating (b).

C.2 Installation and Results

Six TMDs were manufactured and installed during Enhanced LIGO (eLIGO) commissioning on the HAM 6 chambers in the Livingston and Hanford observatories (Clark, 2009), (Clark, 2010). **Figure C.2** shows the installation in the already assembled HAM ISI. Transfer function of the ISI before and after the TMD installation in **Figure C.3** shows that the resonant peaks of the blade springs have been damped below the noise floor of the sensors.

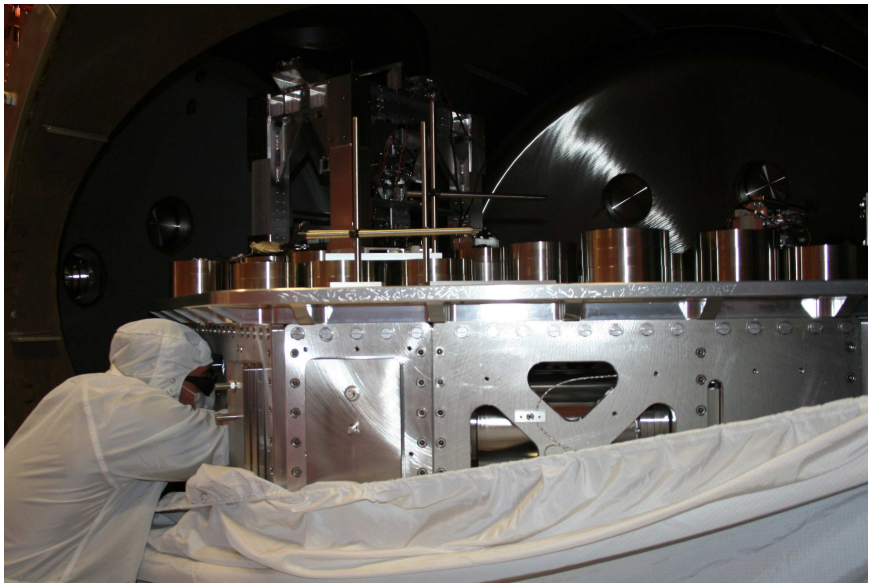

Figure C.2: Installation of the TMDs into the eLIGO HAM 6 ISI at the Hanford observatory.

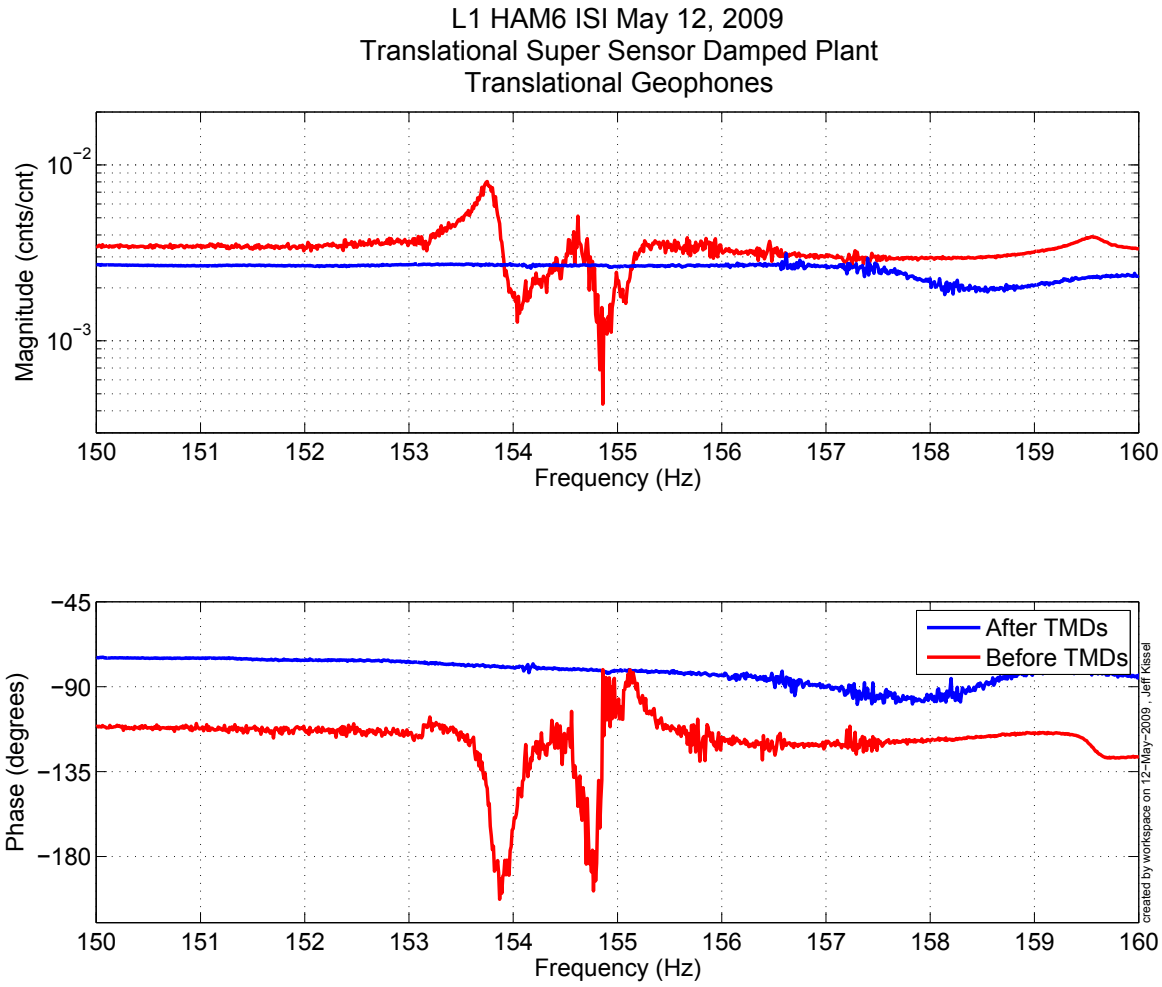

Figure C.3: Driven transfer function of the HAM ISI plant before and after the installation of the TMDs. The response shown is from a Cartesian z drive to the GS-13 sensors in the same basis. This verifies that the three blade spring resonances have been sufficiently damped so that they no longer appear in the plant transfer function.

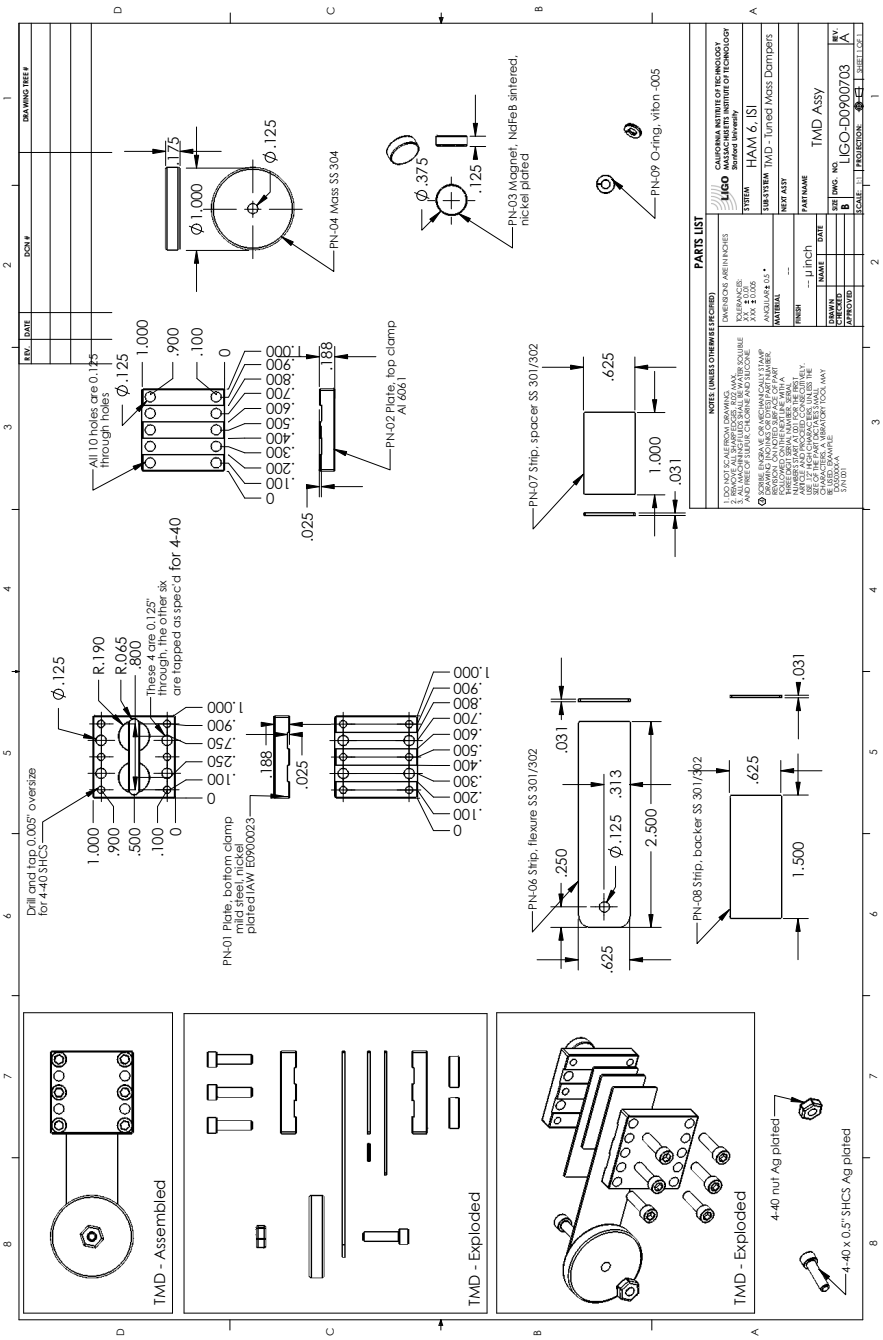

Figure C.4: As built drawings for the eLIGO HAM 6 TMDs. Revised drawings for the aLIGO TMDs for both the HAM and BSC ISIs are documented in (Hillard, 2009) and (Hillard, 2011) respectively.

Appendix D

Ground Disturbance Studies

D.1 Stanford High Energy Physics Laboratory, End Station III

The ground motion of the End Station 3 laboratory building was documented to determine if the building was adequate for certain experimental setups. The ground motion was measured utilizing horizontal and vertical Geotech S-13 (S-13) seismometers with a preamplifier and a Stanford Research Systems SR-785 spectrum analyzer. Measurements were taken at different time periods in the day and with different configurations of the building air handler / HVAC system. The measurement location was on level 1 (3 stories below grade in the high bay) along the west wall about a third of the length of the building toward the south from the north wall. There is a utility trench running north-south along the west wall. The measurements were conducted just east of the trench to ensure measurement of the slab motion. The resulting root of the mean square spectral density in displacement units is plotted in **Figure D.1**.

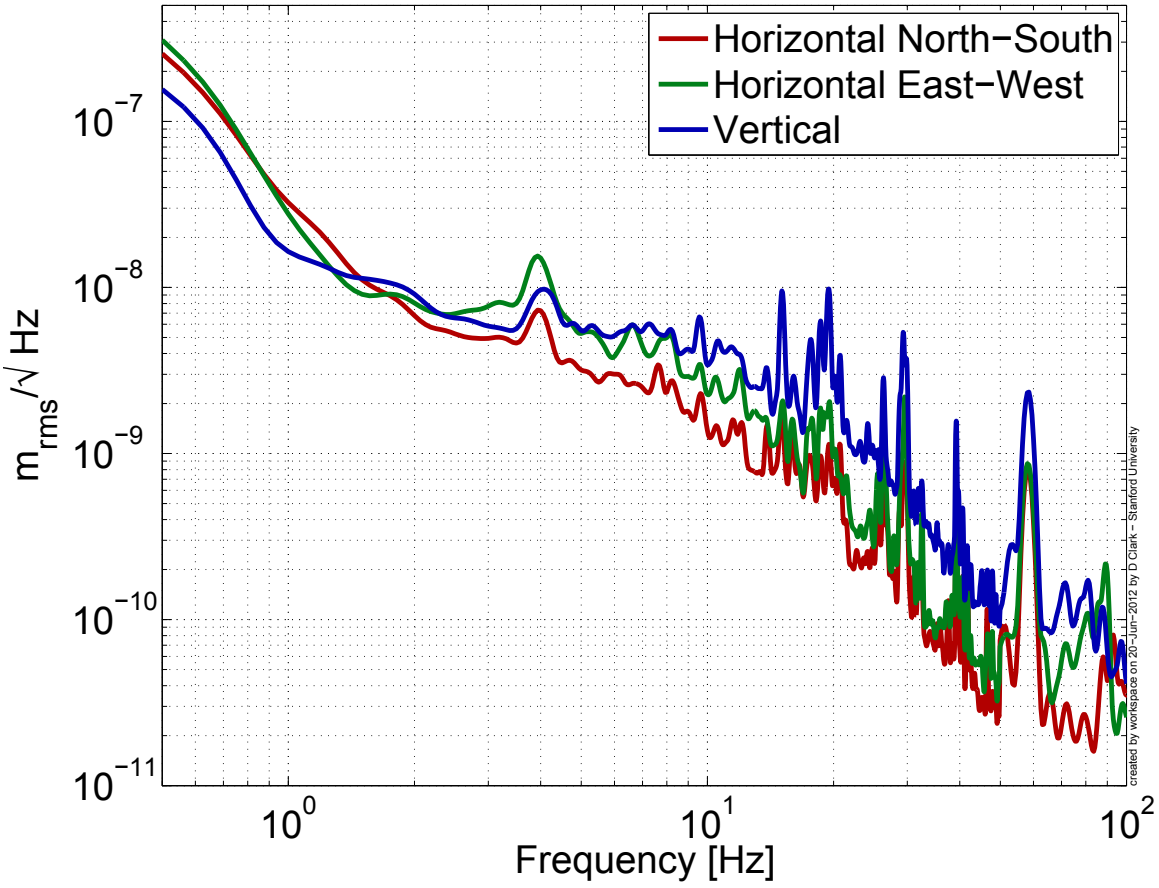

Figure D.1: Stanford Hansen Experimental Physics Laboratory End Station III ground motion recorded at 0140 hrs on 2007-03-20. The building HVAC was turned off but the chilled water and ventilation fans for the clean rooms were left running.

D.2 Stanford Nano Technology Center Basement

D.2.1 Data Recording

Data was recorded at two different locations in the basement of the Nano building (renamed the Spilker Building in 2012) during construction (**Figure D.6**). In the analysis, Location 1 is anticipated for the transmission electron microscope (TEM), while 2 is where the E-Beam is expected to be placed. Location 1 is also referred to in some plots as the "floor" while 2 is often called "the pit". Data was recorded using 4 Geotech S-13 seismometers. The resulting signal was then recorded through an ADC at a rate of 240 Hz (resulting in a Nyquist frequency of 120 Hz). The upper frequency of interest is 100 Hz.

Data was collected from 2008-12-27 to 2009-01-06. From the data collected, the good length, least disturbance data was recorded on 2009-01-05 and 2009-01-06. The channels and seismometers were located as follows in Table D.1.

Table D.1: Location of the S-13 seismometers for measuring ground disturbances in the Stanford Nano Fabrication Facility (Spilker Bldg.)

Label	S/N	Description
V1	2837	Vertical instrument at test location
V2	2842	Vertical instrument at other location
NS	2848	North / South oriented horizontal S-13
EW	2839	East / West oriented horizontal S-13

D.2.2 Data Analysis

The recorded data was calibrated and plotted as displacement vs. frequency in **Figures D.2** and **D.3** for both of the measurement sites. The data was also separated in one-hour long sections and plotted individually, allowing the ground motion throughout the night to be observed (**Figures D.4** and **D.5**). All of these measurements were purposely taken during times of relatively low anthropogenic noise (during academic break and at night). The data was recorded during the construction phase of

the building before any of the building infrastructure (elevators, HVAC, etc.) or shell was installed.

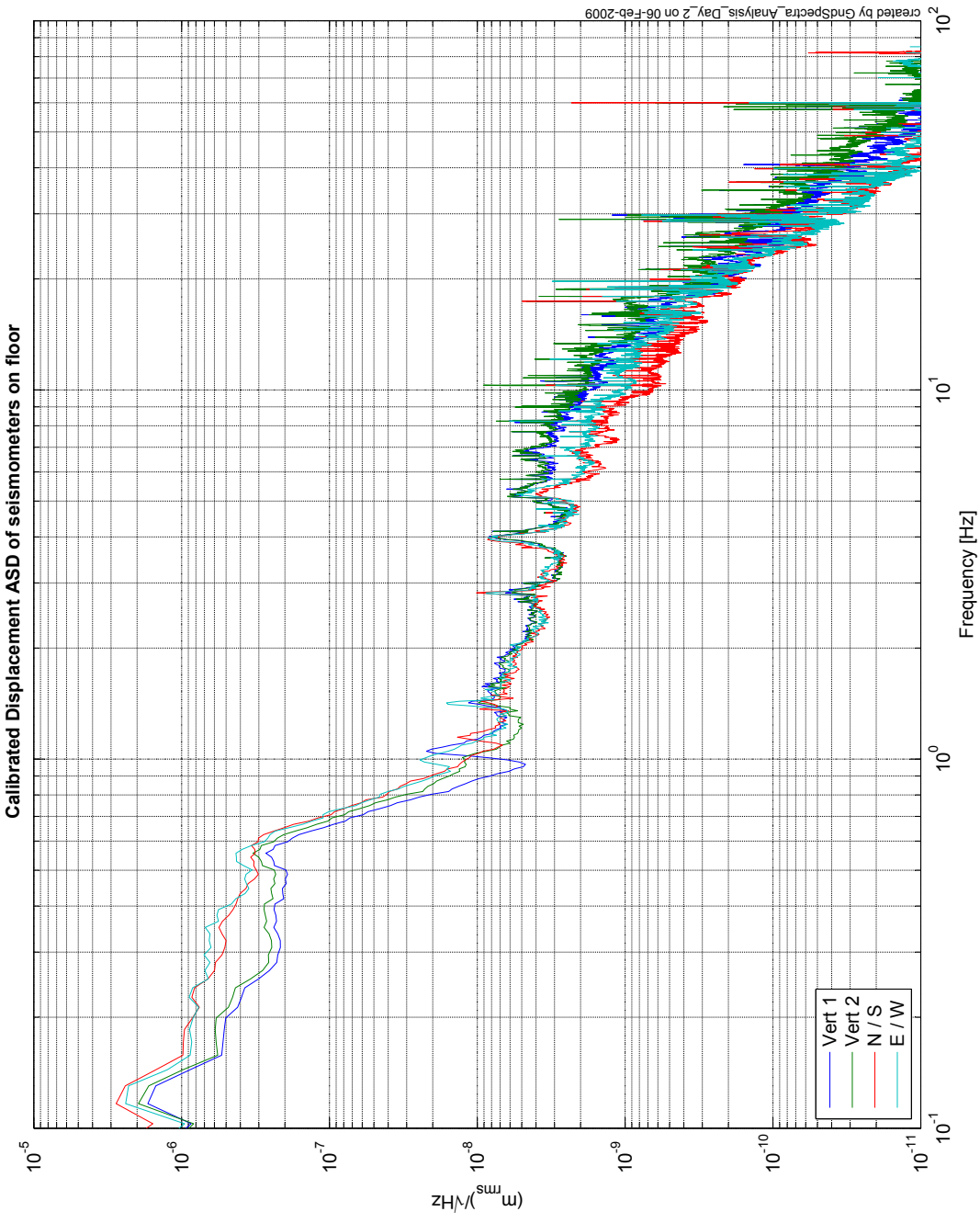

Figure D.2: Spilker Building E-Beam location motion recorded at night, 2009-01-05 (also referred to as the "floor").

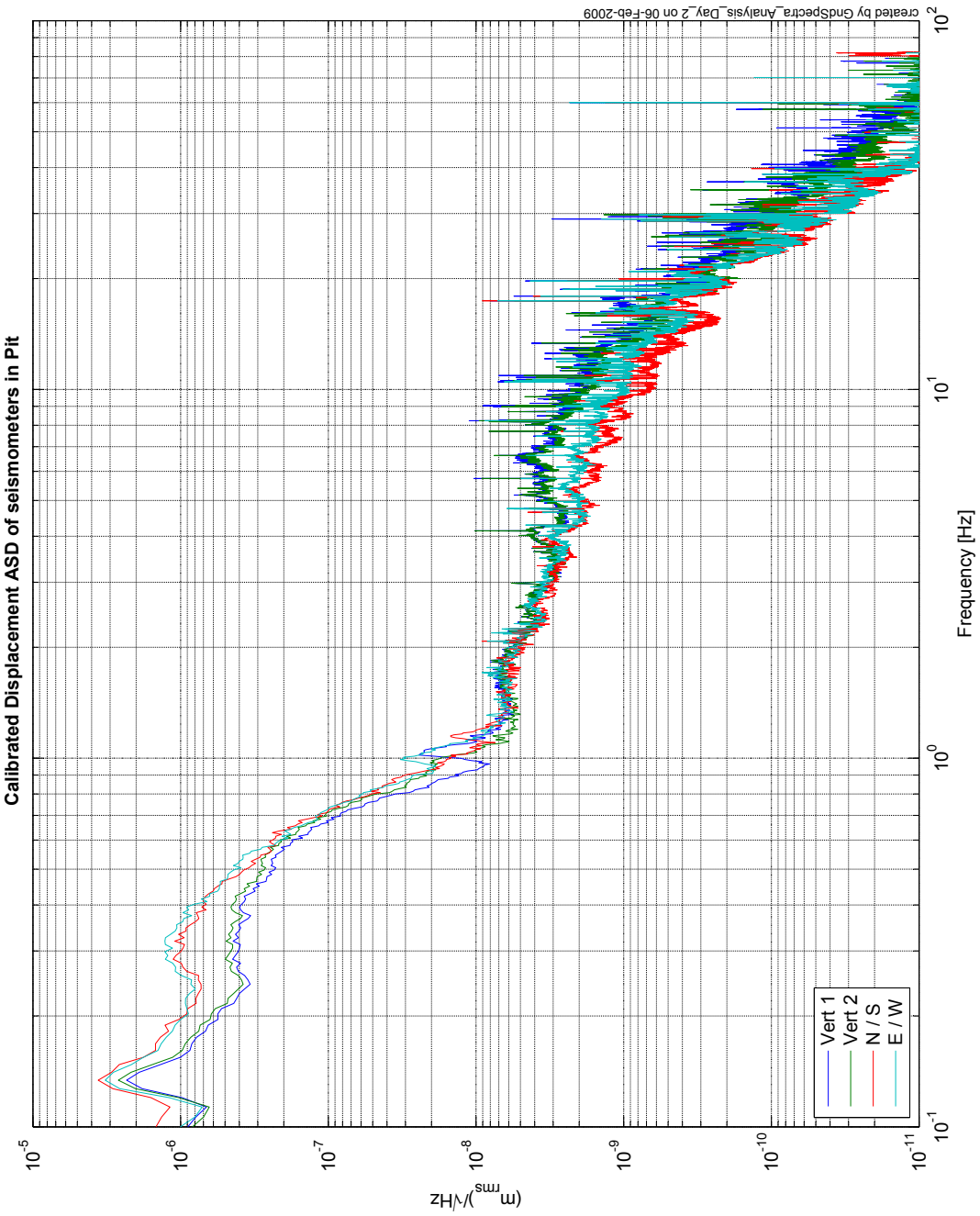

Figure D.3: Spilker Building TEM location motion recorded at night, 2009-01-06 (also referred to as the "pit").

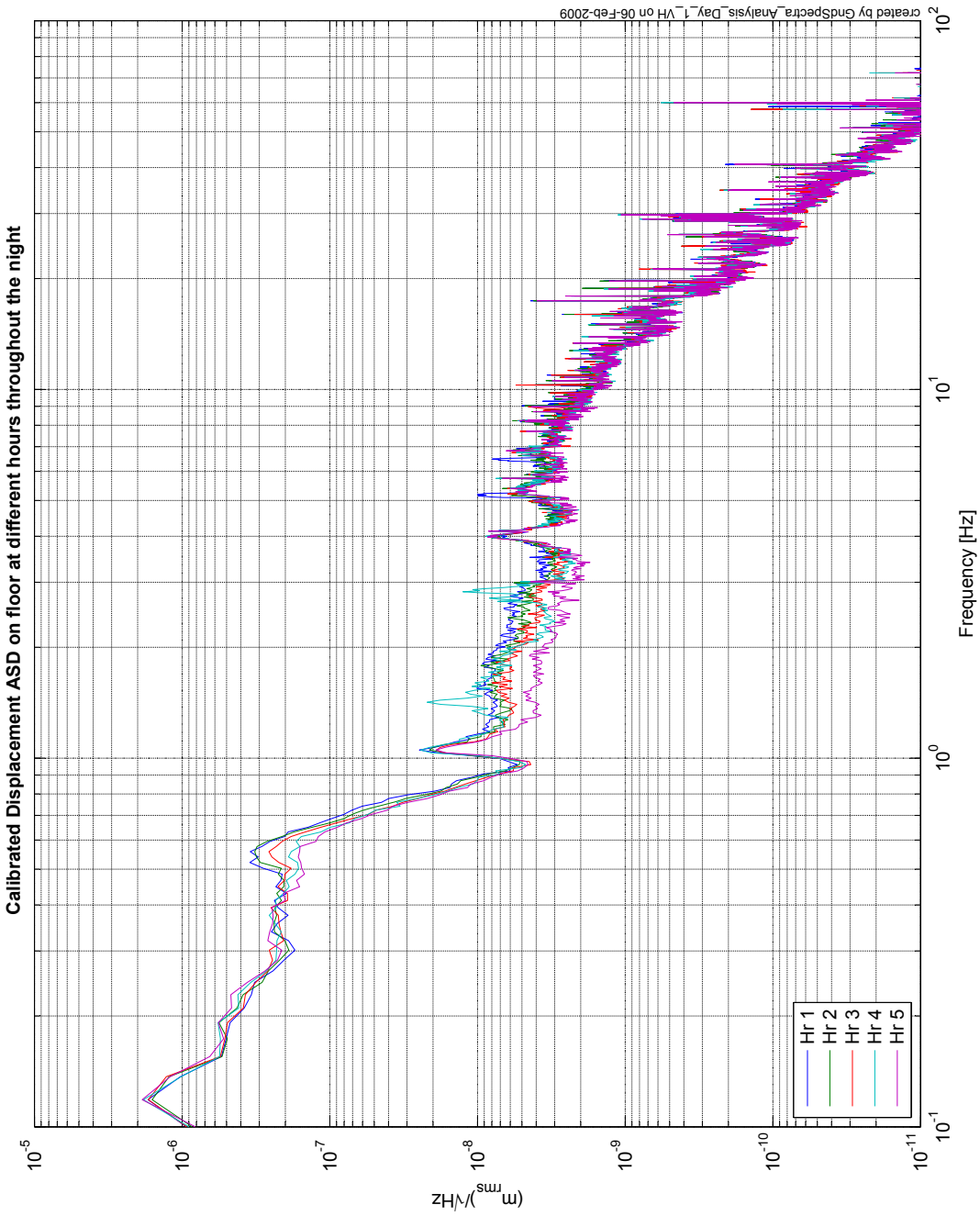

Figure D.4: Spilker Building E-Beam location vertical "floor" motion at different hours of the night, 2009-01-05 (also referred to as the "floor").

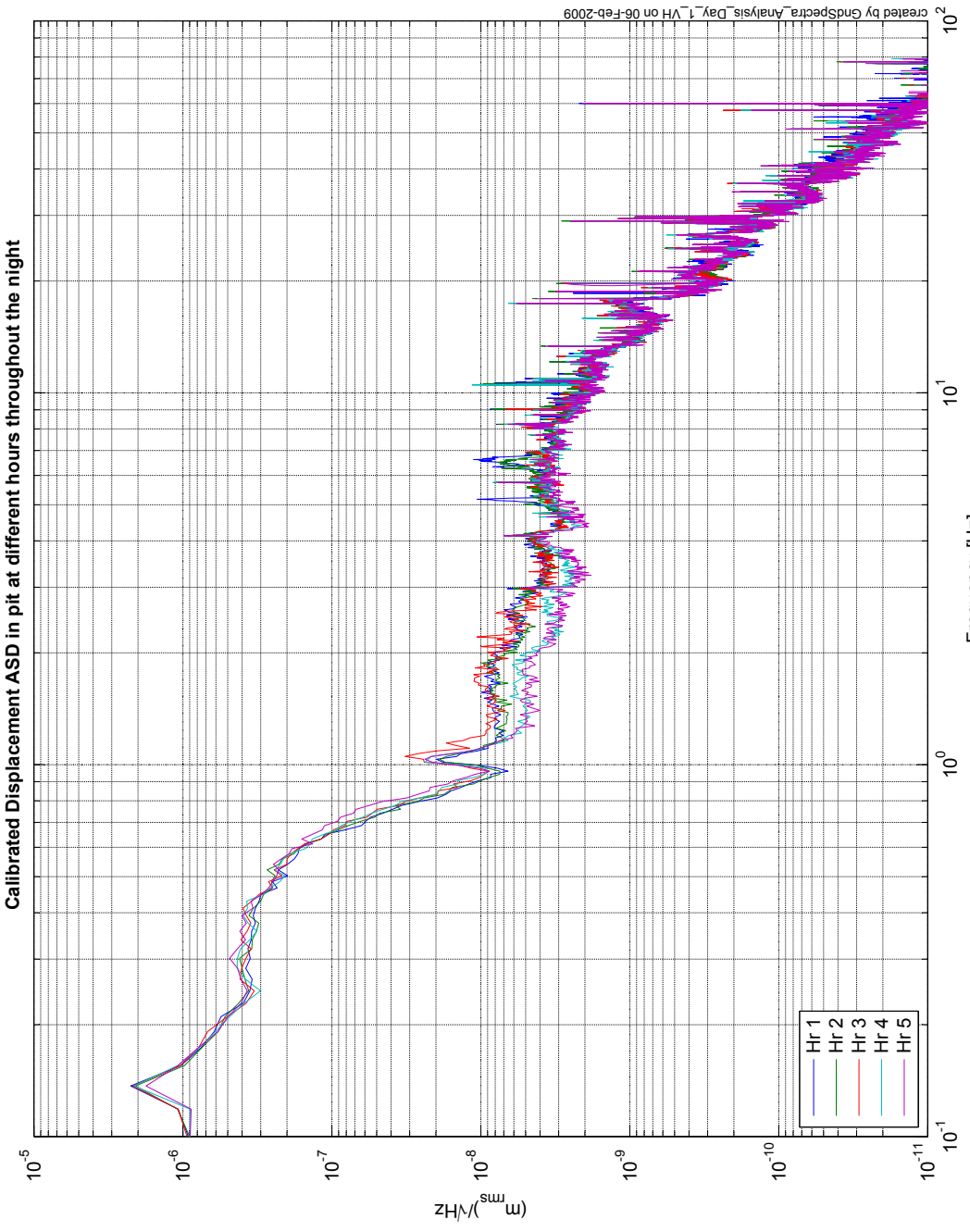

Figure D.5: Spilker Building TEM location vertical "pit" motion at different hours of the night, 2009-01-06 (also referred to as the "pit").

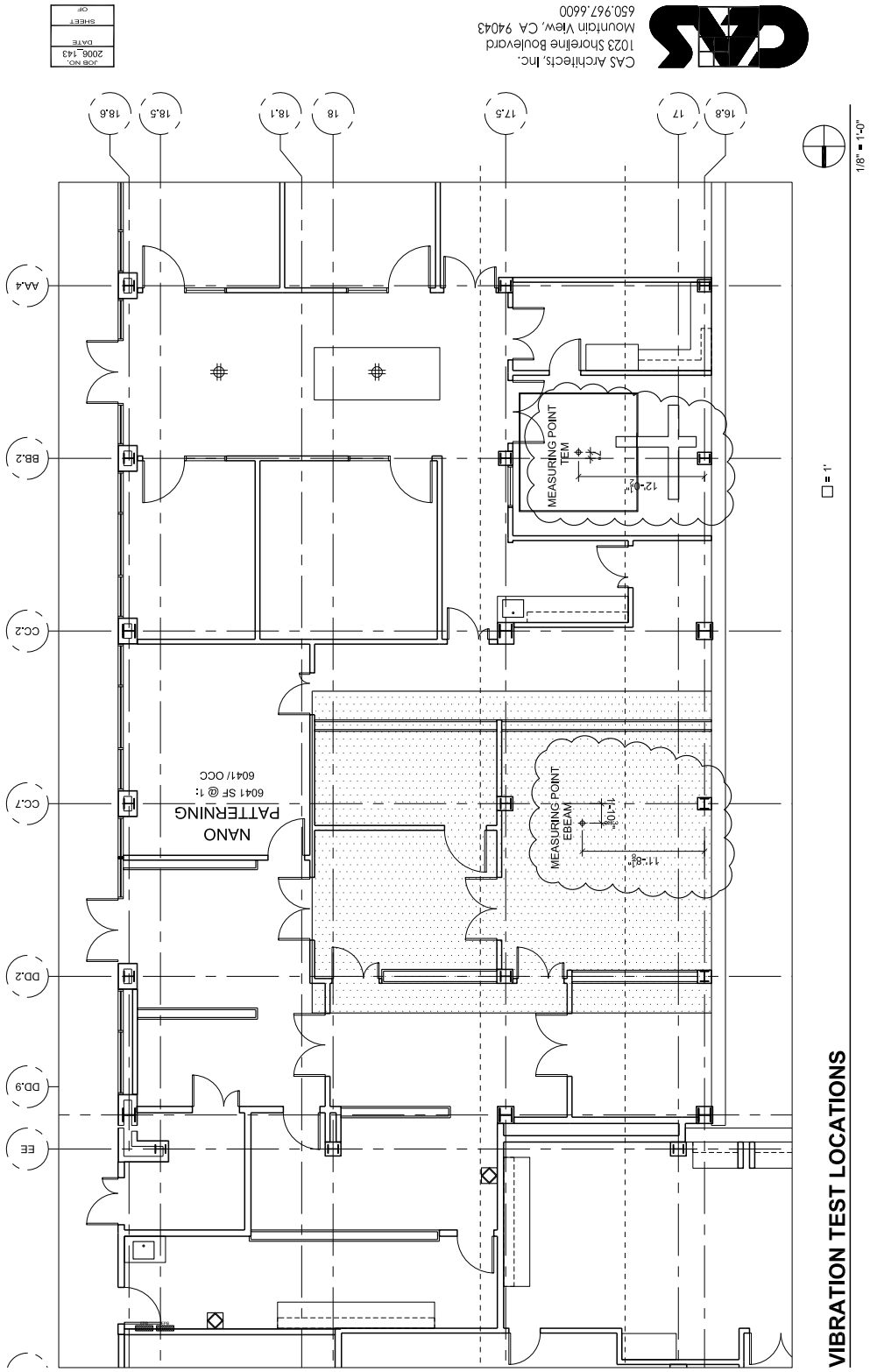

Figure D.6: Location of the E-Beam and TEM instruments floor motion study in the Spilker Building during construction.

Appendix E

Circuits and Schematics

A number of custom circuits were designed and built in support of this thesis. Several of these circuits are documented in this appendix providing a reference for their design and layouts. These include the balanced photodetector circuit used to read the Seismic Platform Interferometer's SPI output, the quad photodetector used for the optical levers of the SPI and temperature sensors used to monitor the Technology Demonstrator Platform (Tech Demo) temperature during laser frequency noise measurements.

E.1 Balanced Photodetector

The interferometric detection consists of a balanced detection scheme. This allows the monitoring of both outputs from the recombination beamsplitter simultaneously. When the interferometer is at the mid-fringe, the light on each photodetector is equal resulting in an output voltage value close to zero. Since the laser wavelength used is in the 1.5 μm band, two individual InGaAs detectors were used. The detectors pass current at the rate of $1\text{A}/\text{W}_{\text{incidentLight}}$ which means that at a maximum laser output of the SPI of 10 mW the current flow is 10 mA which is within the source and sink range for the transimpedance amplifier chosen (LT1124). The balanced detector as used in the SPI prototype was constructed by Alireza Mirandi of Stanford University.

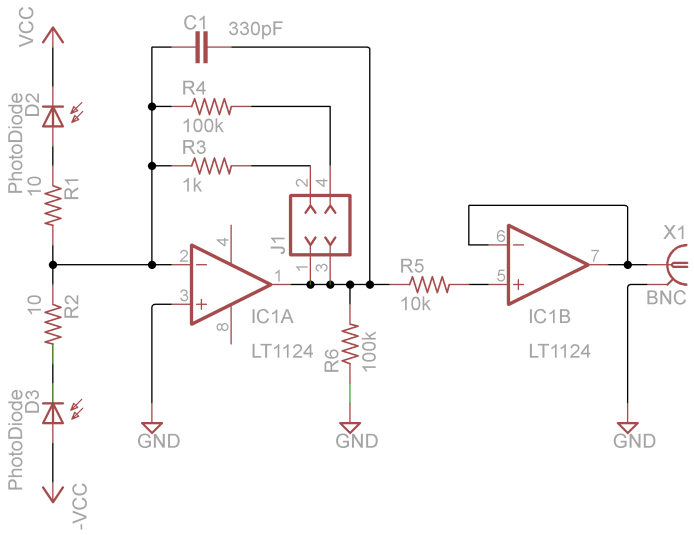

Figure E.1: SPI balanced photodetector schematic.

E.2 Quad Photodetector

Two quad photodetectors (QPDs) are used in the SPI. One QPD measures the pitch and yaw stability of the launch beam while a second QPD measures the differential pitch and yaw of the two platforms. The QPD circuit is composed of:

- InGaAs quadrant photo detector composed of A, B, C, and D quadrants
- Transimpedance pre-amplifiers for each quadrant with active low-pass filtering
- Math amplifier section with active low-pass filters
- Differential line drivers for signal output

The QPD quadrants are arranged in alphabetical order from A through D clockwise starting with A in the northwest quadrant. The math section of the QPD circuit combines the quadrants to determine the yaw, pitch, and total power as follows:

$$Sum_{power} = A + B + C + D \tag{E.1}$$

$$Pitch_{vertical} = (A + B) - (C + D) \tag{E.2}$$

$$Yaw_{horizontal} = (A + D) - (B + C) \tag{E.3}$$

Figures E.2, **E.3** and **E.4** contain the schematics for the QPD sensors with **Figure E.5** displaying the printed circuit board (PCB) layout. The component values for the resistors and capacitors in the schematic and on the PCB are tabulated in **Tables E.1** and **E.2** respectively.

Table E.1: Resistor component values (in Ω) for the SPI QPD schematic. Ryzx value is determined by the intersection of row YZ and column X. A zero indicates a jumper wire placed in that position where a blank indicates no Ryzx component in schematic.

R	0	1	2	3	4	5	6	7	8	9
0X										
1X										
2X				1 k		1 k				
3X										
4X							1 k	100		
5X	1 k	100	1 k	1 k	1 k	1 k	1 k			
6X		0	60.4 k	1 k	1 k	1 k	60.4 k			
7X							2 k			0
8X	0		0				0	2 k	0	2 k
9X	2 k	0	2 k	1 k						
10X										
11X							0	50	2 k	0
12X	2 k	60.4 k	60.4 k	60.4 k	0	50	0	0	60.4 k	2 k
13X	2 k	2 k	2 k	60.4 k	1 k	50	60.4 k	0	50	2 k
14X	2 k	2 k	2 k	1 k	2 k	100	50	2 k	2 k	50
15X	2 k	2 k	1 k	1 k	1 k	1 k				

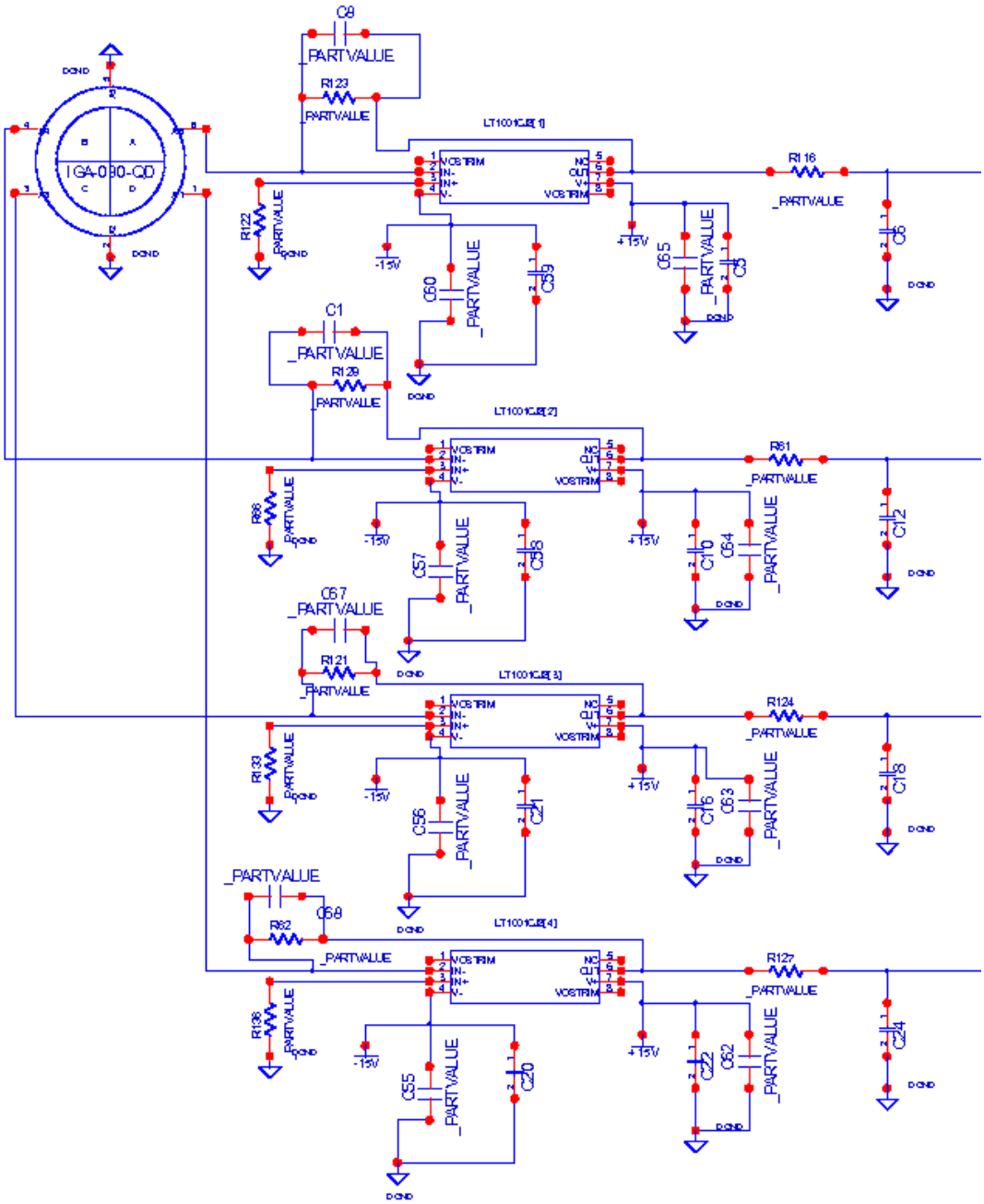

Figure E.2: SPI QPD schematic part 1 of 3.

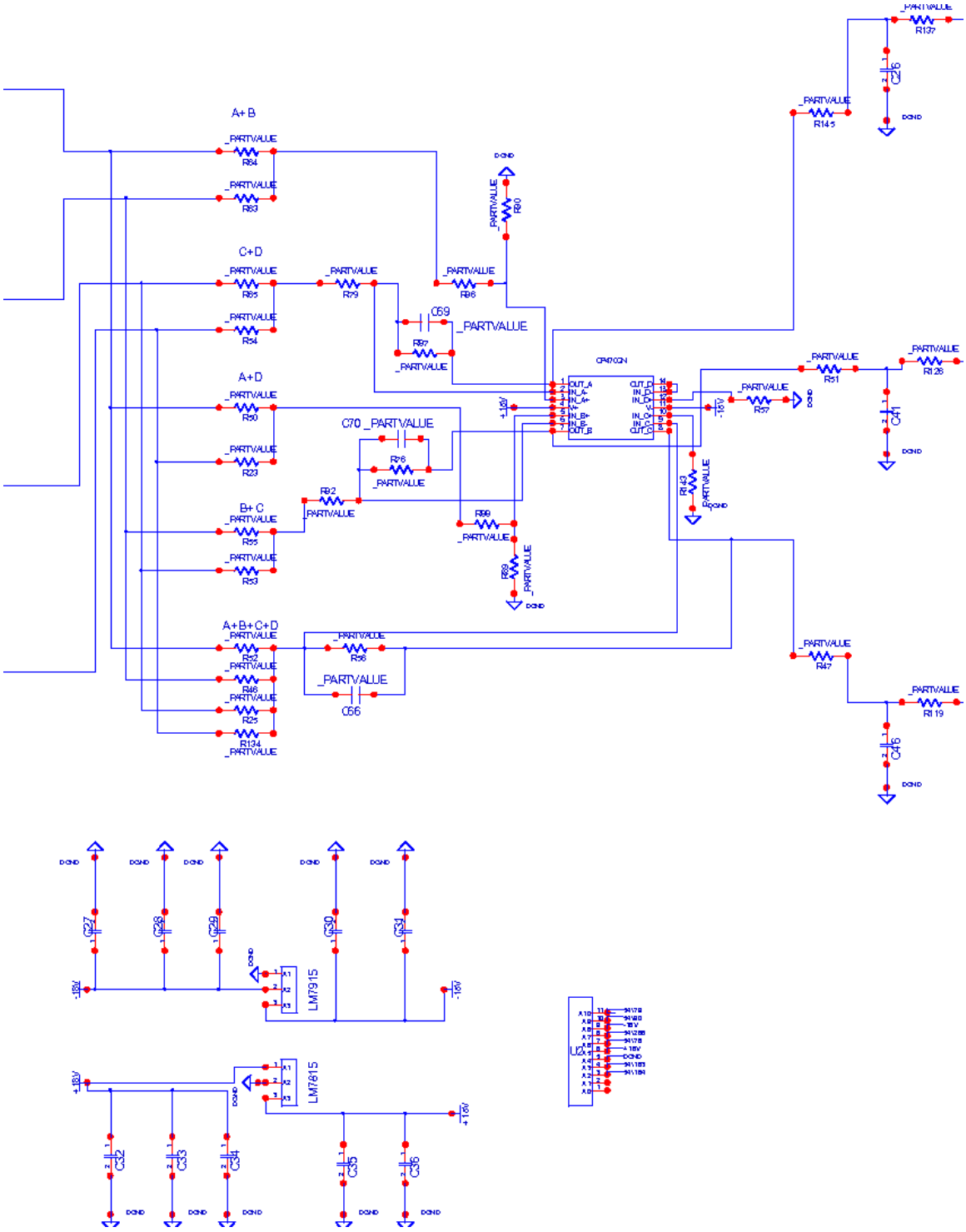

Figure E.3: SPI QPD schematic part 2 of 3.

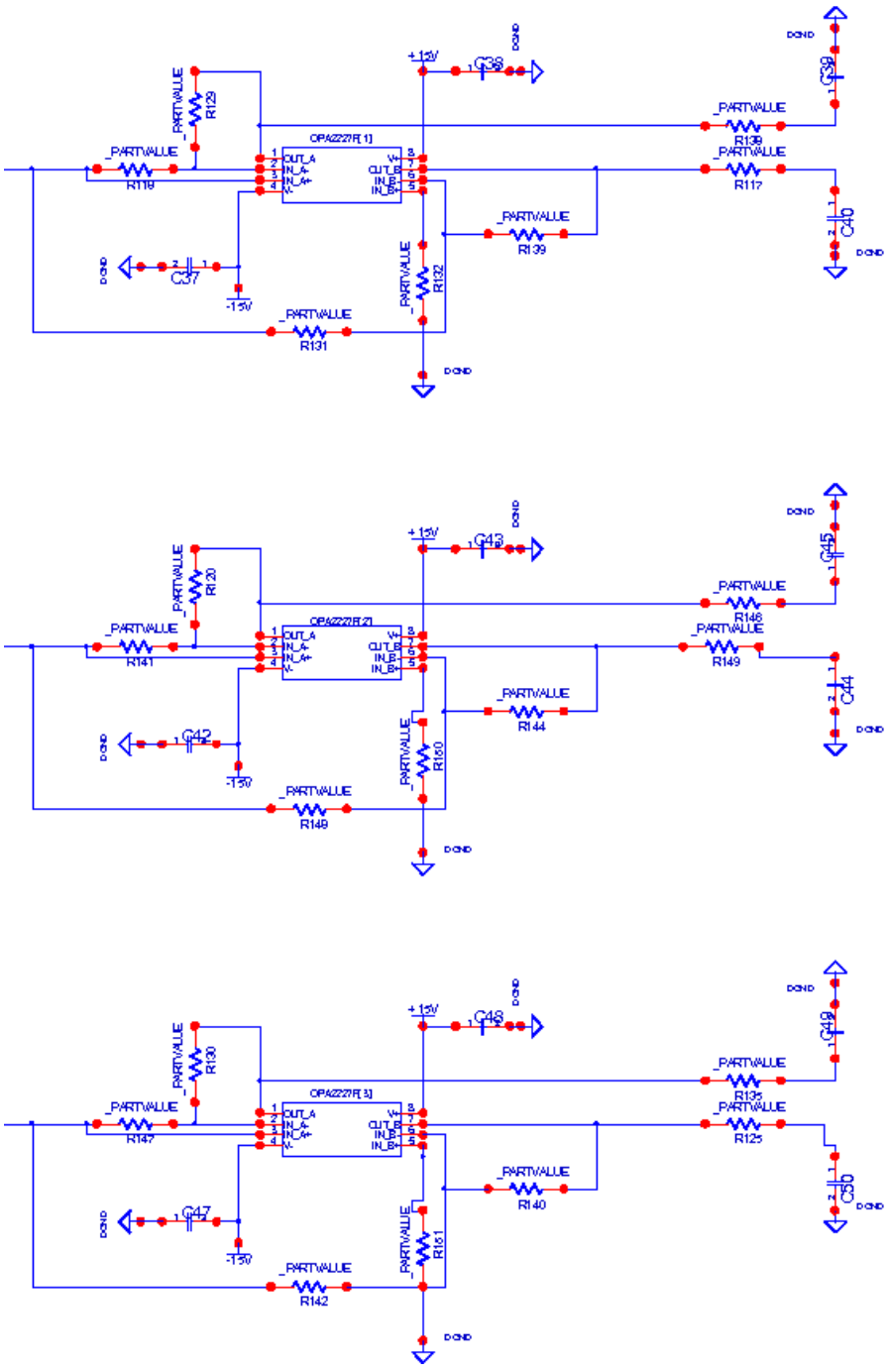

Figure E.4: SPI QPD schematic part 3 of 3.

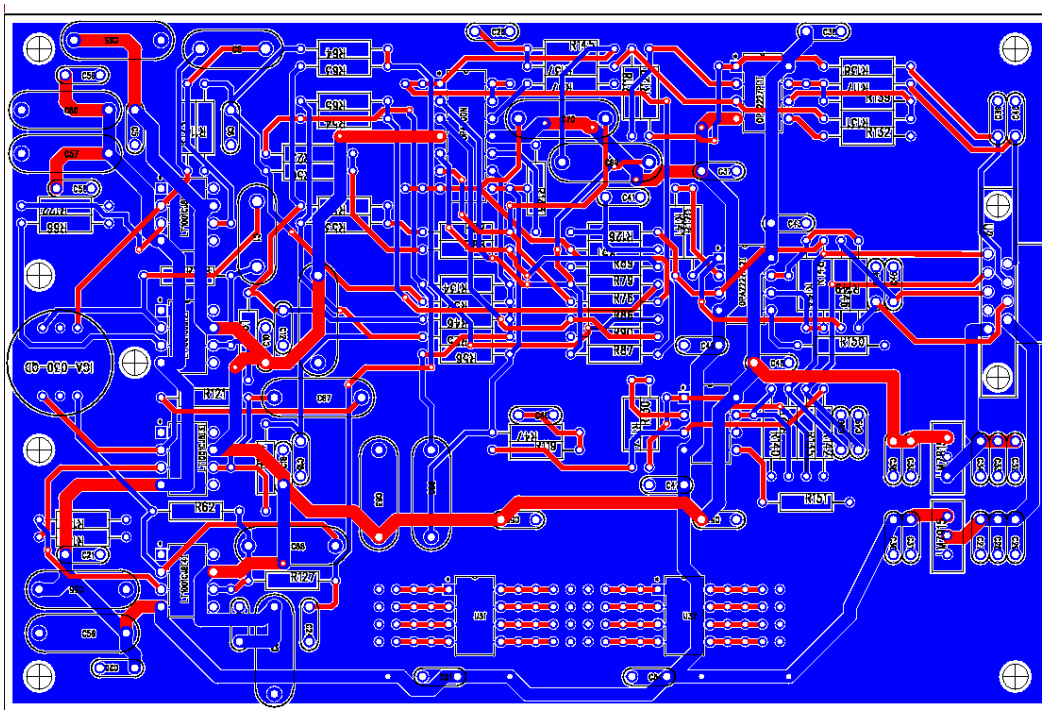

Figure E.5: SPI QPD board layout.

Table E.2: Capacitor component values (in μF) for the SPI QPD schematic. Cyzx value is determined by the intersection of row YZ and column X. The capacitor type is noted as P for polypropylene, C for ceramic disc, and T for tantalum. A zero indicates no component placed in that position where a blank indicates no Cyzx component in schematic.

C	0	1	2	3	4	5	6	7	8	9
0X		0.01 P				0.01 P	0		0.01 P	
1X	0.01 P		0				0.01 P		0	
2X	0.01 P	0.01 P	0.01 P		0		0	0	100p C	15 T
3X	10 T	100p C	0	100p C	15 T	10 T	100p C	1 T	1 T	0
4X	0	0	1 T	1 T	0	0	0	1 T	1 T	0
5X	0					2.2	2.2	2.2	0.01 P	0.01 P
6X	2.2		2.2	2.2	2.2	2.2	0.1 P	0.01 P	0.01 P	0.1 P
7X	0.1 P	0.1 P								

E.3 Temperature Sensors

Preliminary measurements of the frequency noise of the laser led to strong suspicions of temperature noise coupling into the experiment. Because the measurement of the laser frequency noise was accomplished by measuring the apparent length change of a fixed mismatched arm interferometer on the Tech Demo, temperature could affect the measurement by changing the laser frequency or it could couple in by actually changing the interferometer arm length used on the Tech Demo. In order to quantify how much frequency noise to actually attribute to the laser, it became desirable to monitor the temperature changes on the Tech Demo optics platform.

The requirements for such a sensor dictated high sensitivity on the order of 0.1 $\mu^{\circ}\mathrm{C}/\sqrt{\mathrm{Hz}}$. Due to past experience with precision thermistor bridges, (Higuchi et al., 2008), a Wheatstone bridge type thermistor layout was chosen. In order to increase sensitivity, two thermistors were placed in the bridge and the bridge was linearized by feeding the initial amplifier signal back into one leg of the bridge (**Figure E.6**). A precision voltage reference was used to maintain a constant drive across the bridge, reducing noise coupling from the power supply. 100 kΩ thermistors were used with a β value of 4,143K. This meant that the self heat generated by the bridge is:

$$P_{self-heat} = \frac{(10\,\mathrm{V})^2}{100\,\mathrm{k}\Omega} = 1\,\mathrm{mW} \tag{E.4}$$

While the sensitivity at the bridge output is then:

$$V_{out} = 10\,\mathrm{V} \cdot \frac{0.04}{^{\circ}\mathrm{C}} = \frac{400\,\mathrm{mV}}{^{\circ}\mathrm{C}} \tag{E.5}$$

If we assume a low frequency, input referred RMS noise of 2 $\mu\mathrm{V_{pk\text{-}pk}}$ for the LTC1151 chopper stabilized op-amps, then the noise floor for detection is:

$$\frac{2\,\mu\mathrm{V_{pk\text{-}pk}}}{400\,\mathrm{mV}/^{\circ}\mathrm{C}} = 5\,\mu^{\circ}\mathrm{C} \tag{E.6}$$

The Johnson noise for the $100k$ Ω resistors is:

$$N_{Johnson} = \sqrt{4 \cdot k \cdot 100\,\mathrm{k}\Omega \cdot 300\,\mathrm{K}} = 4 \times 10^{-8}\,\mathrm{V}/\sqrt{\mathrm{Hz}} \tag{E.7}$$

Since the input range of the ADC is ±10 V and since it can accept a balanced input, the circuit was designed to drive a balanced line improving noise rejection. A single pole passive low-pass filter is located directly after the bridge linearization with capacitors in the feedback loop of each of the subsequent amplifiers to further low-pass filter the output. The low-pass frequency for the passive filter is 18.8 Hz. The gain stage has low-pass corner frequencies at 636 Hz, 106 Hz, and 13.8 Hz depending on the setting of J3. 79.6 Hz is the low-pass frequency for the line drivers.

The basic circuit, as **Figure E.6** shows, consists of (generally from left to right):

- Power conditioning and bridge voltage drive stabilization
- Wheatstone configured bridge with two active thermistor elements
- Bridge linearization operation amplifier
- Passive, single pole, low-pass filter
- Gain amplifier with single order active low-pass filtering
- Line drivers for + and - driving of balanced signal incorporating single order, active low-pass filters

The circuit gain is determined by a gain setting jumper of J3 with setting for gains of 1.25, 2.5 and 12.5 respectively. The output is also switchable from balanced to unbalanced so that, when balanced, there is an additional effective gain of 2. This results in the following output sensitivities as documented in **Table E.3**. The electrical schematic is displayed in **Figure E.6** and the circuit board layouts are shown in **Figures E.7** and **E.8** respectively.

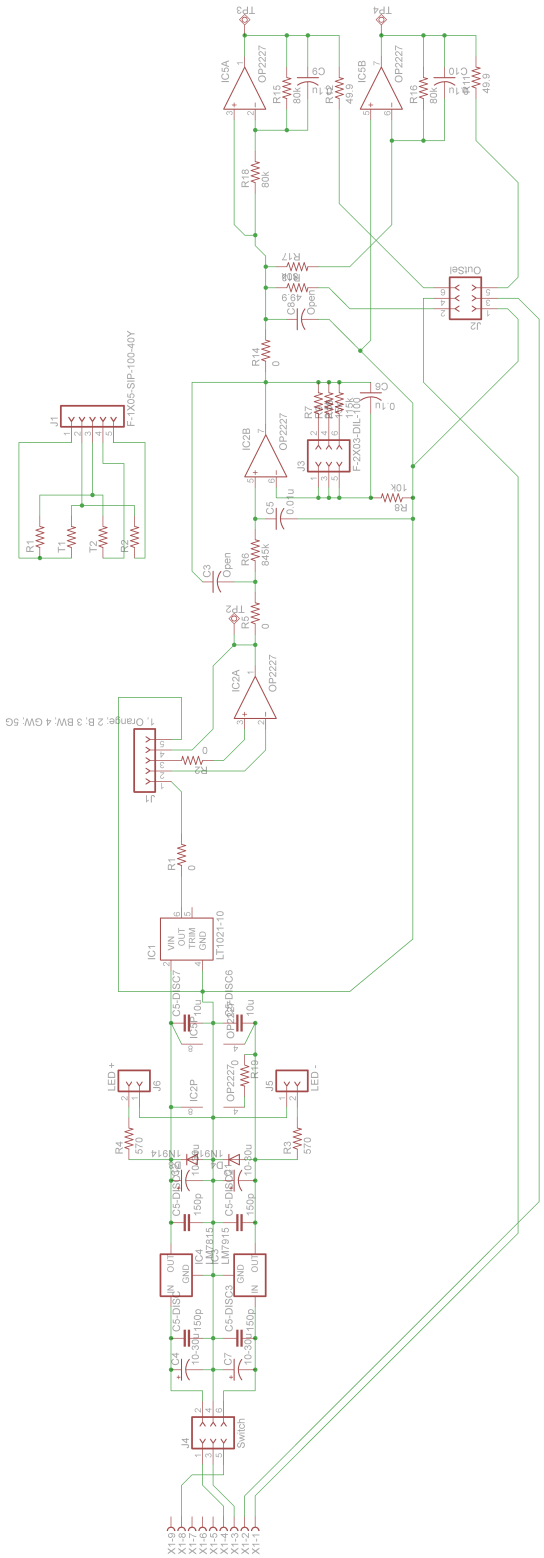

Figure E.6: Temperature sensor electrical schematic for bridge (inset) and the main pre-amplifier and line driver board.

Table E.3: Sensitivities for the temperature sensors dependent on the gain and line driver settings.

Setting	**Amp. Gain**	**LP Freq. Hz**	**Line Drive**	**Sensitivity**	**ADC Full Scale**
J3	Gain	Hz	Unbal. / Bal.	°C/V	±°C
1	1.25	636	Unbal.	2.0	10
			Bal.	1.0	5.0
2	2.5	106	Unbal.	1.0	5.0
			Bal.	0.5	2.5
3	12.5	13.8	Unbal.	0.2	1.0
			Bal.	0.1	0.5

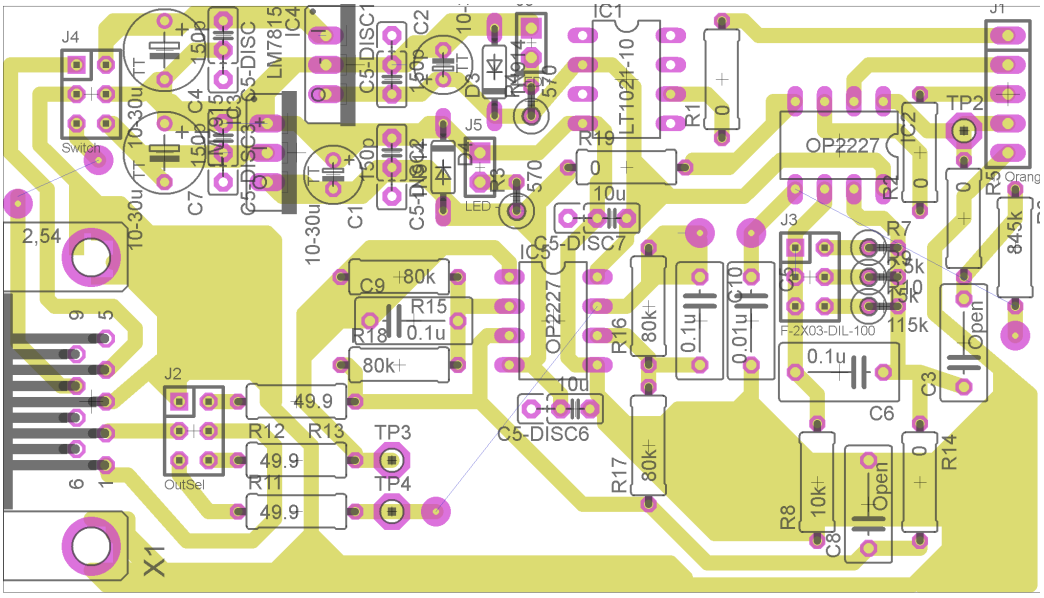

Figure E.7: Temperature sensor pre-amplifier and line driver single layer circuit board layout.

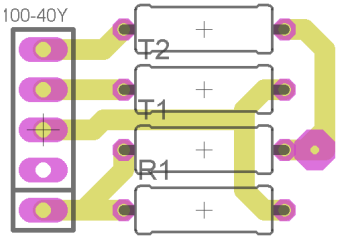

Figure E.8: Temperature probe circuit board layout combining the thermistors and bridge resistors at the same location to reduce errors introduced from the sensor wire resistance.

Appendix F

Stanford Rapid Prototype Platform

The Stanford ETF houses two active seismic isolation platforms. One of these platforms, the Rapid Prototype Platform (RPP) was re-instrumented and placed under inertial damping and control to allow testing and validation of the Seismic Platform Interferometer (SPI) prototype. This appendix provides the RPP documentation.

The RPP was first developed to demonstrate the feasibility of control in all six degrees-of-freedom of a relatively stiff system. Over the years, development work transitioned to the more advanced Technology Demonstrator Platform (Tech Demo) in the ETF and the RPP was unused. For the SPI, two active platforms are necessary in order to validate the design. This meant that the RPP, separated by 8.9 m edge-to-edge from the Tech Demo, needed to be recommissioned to the point where it could serve as a remote platform.

F.1 Mechanical System

The RPP contained two active stages with each stage supported by maraging steel triangular blade springs and flexures. Because of some geometry constraints around the beam tube connecting the RPP to the Tech Demo, the remote SPI mirror on the RPP had to be located on the upper (1^{st}) stage of the RPP. This meant that the

lower (2^{nd}) stage was not being used and subsequently was removed (**Figure F.1**). The RPP was then reduced to a single stage with added mass to offset the weight the second stage had provided. This was done to increase the center of mass position of the RPP to be closer in line with the actuation plane and to simplify the damping control loops by removing the extra resonances generated by the second stage.

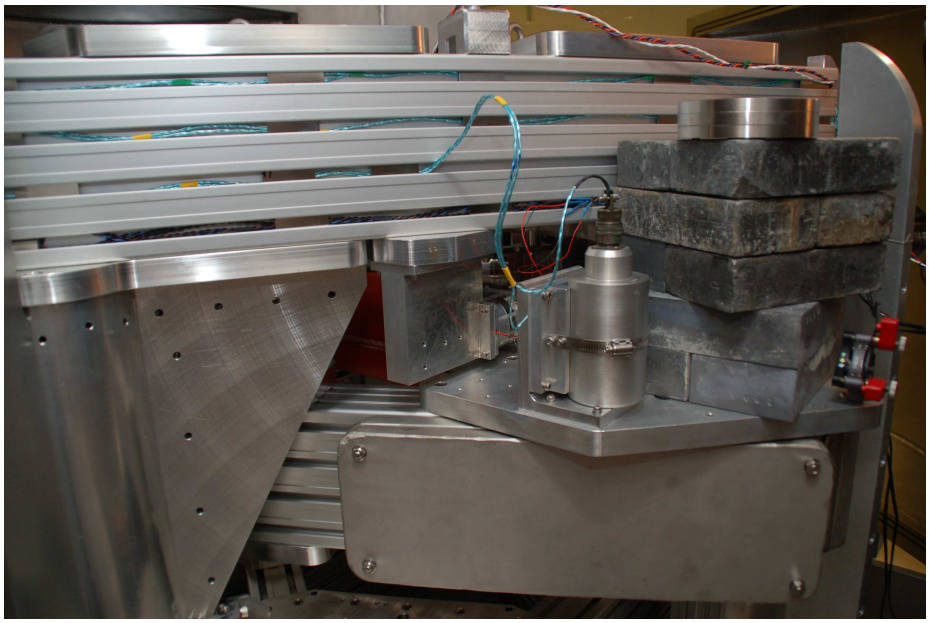

Figure F.1: Picture of the Rapid Prototype Platform (RPP) upper stage with balancing mass and the SPI remote mirror. A vertical L-4C seismometer used for active damping and inertial control is also seen. Barely visible is a horizontal voice coil actuator and a stage 0 to 1 flexure and blade spring.

F.2 Instrumentation and Electronics

Since the RPP was not currently being used, many of the sensors, cables, and associated electronics had been removed. Since the SPI did not require that the RPP be re-commissioned to the same performance as before, only L-4C seismometers and voice coil actuators on the single active stage were required. After machining new seismometer mounting plates, the seismometers were installed. The voice coil actuators (BEI Kimco Magnetics LA14-17-000A) were already in position but locked

down. Once the platform was brought close to level these actuators were unlocked. New in-vacuum wiring was run to all sensors and actuators.

Once outside the vacuum system, the L-4C signals were amplified by the HEPI Pier Interface Chassis LIGO-D080521 which adds a gain of 11 to the signal (Abbott, 2009). These inertial signals were then attached to an aLIGO ADC through a custom built Stanford Anti-Aliasing Chassis. The anti-aliasing board provided passive, single pole, low-pass filters at about 100 Hz to each channel.

The output of the digital to analog converter (DAC) is connected to a custom built Anti-Imaging Chassis which also filters the output at about 100 Hz. The Anti-Imaging Chassis also takes the DAC output and converts it from a differential to a single ended signal through an instrumentation amplifier. This is important because the coil driver requires a single ended input. The coil driver is a LIGO prototype unit that is capable of driving 10 A of current per channel to the coils.

F.3 Computer Control

A new custom model was created to run in the aLIGO computer system, on a separate core, that handles the damping and control of the RPP. This model also handles the introduction of Interferometer Sensing and Control (ISC) command signals from the SPI and runs at 4,096 Hz.

The general signal flow through the computer is documented below with the Matlab SimuLink diagram shown in **Figure F.2**

1. L-4C inertial sensor signals are introduced and calibrated to the "ideal geophone" response in the L4CINF

2. The L-4C signals are split and re-oriented to the ETF global basis in the L4C2CART transformation matrix before being displayed and recorded by the L-4C monitors (**Table F.1**)

3. The damping and inertial controllers are implemented directly in the actuator basis

4. Interferometer Sensing and Control (ISC) command signals are introduced and re-oriented to the Cartesian basis in the ISC2CART matrix (**Table F.3**)

5. The signals are then passed into a blocking stage based on the watchdog

6. The CART2ACT matrix converts the ISC signals from the Cartesian basis into the actuator basis so that they can be added with the signals from the controller (**Table F.2**)

7. Signals from the RPP damping and inertial control are added to the ISC command signals

8. After passing through the master switch, the signals are sent to the DAC

The transformation matrices rely on the relative orientation of the sensors and actuators to each other and also to the global ETF coordinate system. **Figure F.3** displays the relevant positions as used in creating the matrices.

Table F.1: L-4C inertial seismometer to global ETF Cartesian basis transformation matrix.

L4C2CART	H_1	H_2	H_3	V_1	V_2	V_3
x	0.333	0.333	−0.667	−0.025	0.015	0.009
y	−0.577	0.577	0	−0.004	−0.019	0.023
rz	1.123	1.123	1.123	0	0	0
z	0	0	0	0.333	0.333	0.333
rx	0	0	0	−0.219	−1.239	1.459
ry	0	0	0	1.558	−0.968	−0.589

The interaction with the real-time control model is done through Experimental Physics and Industrial Control System (EPICS) Motif Editor and Display Manager (MEDM). A screen capture of the RPP master control overview screen is displayed in **Figure F.4**.

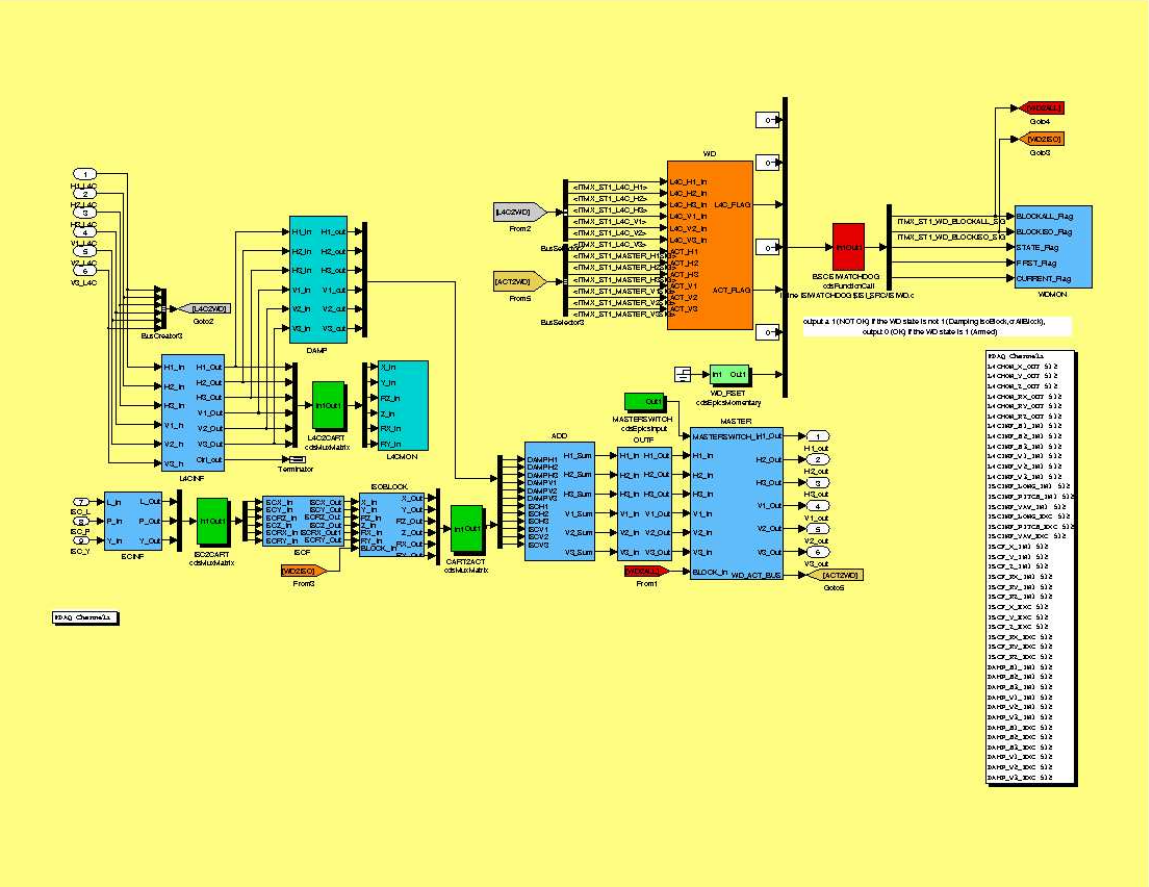

Figure F.2: Simulink model for the computer control of the RPP system. The signals introduced on the left are composed of L-4C and the ISC commands. The outputs to the voice coil actuators are on the right.

Table F.2: ETF Cartesian basis to actuator basis transformation matrix.

CART2ACT	x	y	rz	z	rx	ry
H_1	0.333	−0.577	1.667	0	0	0
H_2	0.333	0.577	1.667	0	0	0
H_3	−0.667	0	1.667	0	0	0
V_1	0	0	0	0.333	−2.273	1.870
V_2	0	0	0	0.333	−0.483	−2.903
V_3	0	0	0	0.333	2.756	1.033

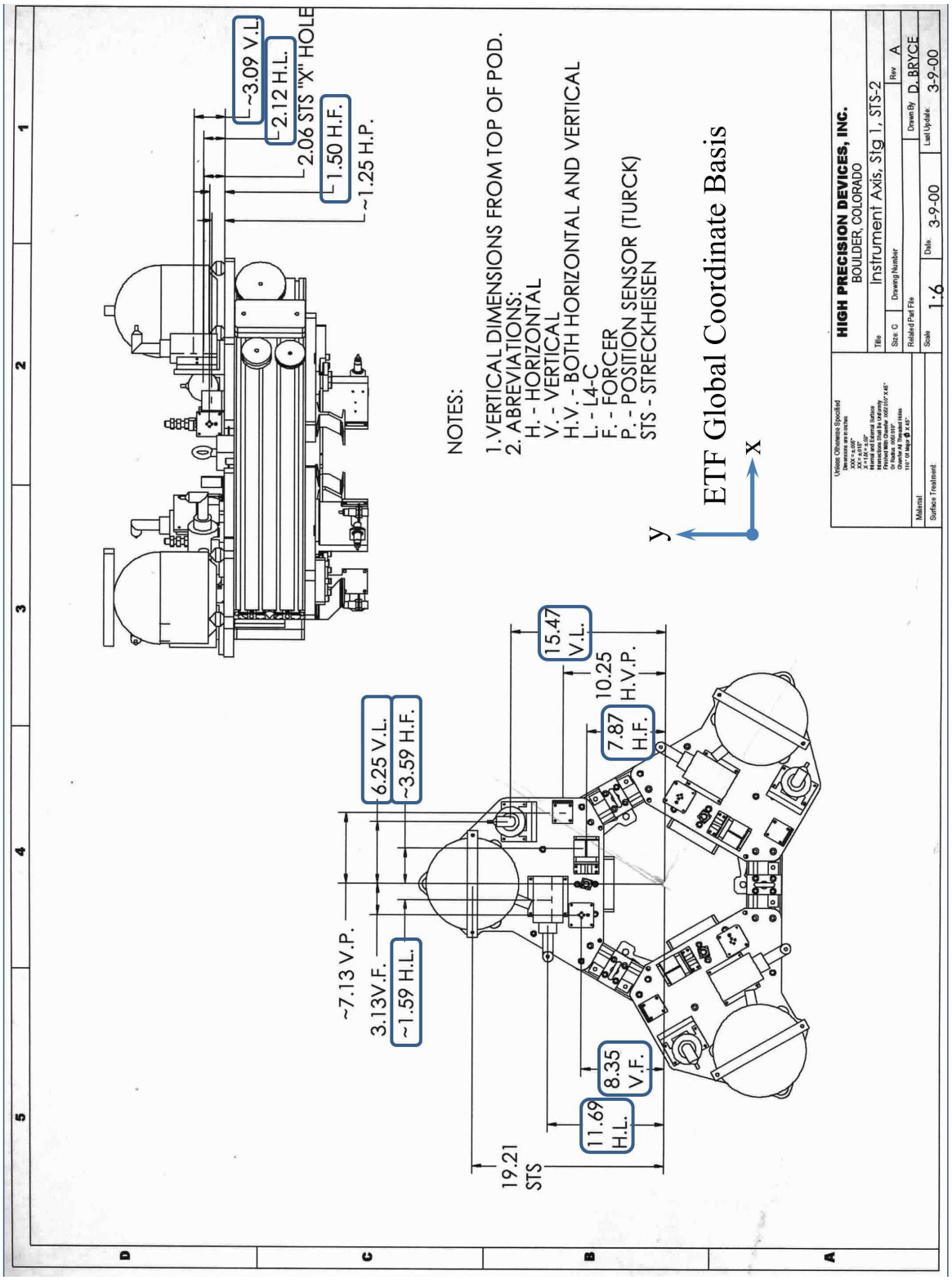

Figure F.3: Location of the L-4C seismometers and the actuators for the RPP. This information is used in creating the transformation matrices as displayed in **Table F.1**, **F.2**, and **F.3**.

Table F.3: Interferometer Sensing and Control (ISC) input to ETF global Cartesian basis transformation matrix.

ISC2CART	*Length*	*Pitch*	*Yaw*
x	0	0	0
y	1	0	0
rz	0	0	1
z	0	0	0
rx	0	1	0
ry	0	0	0

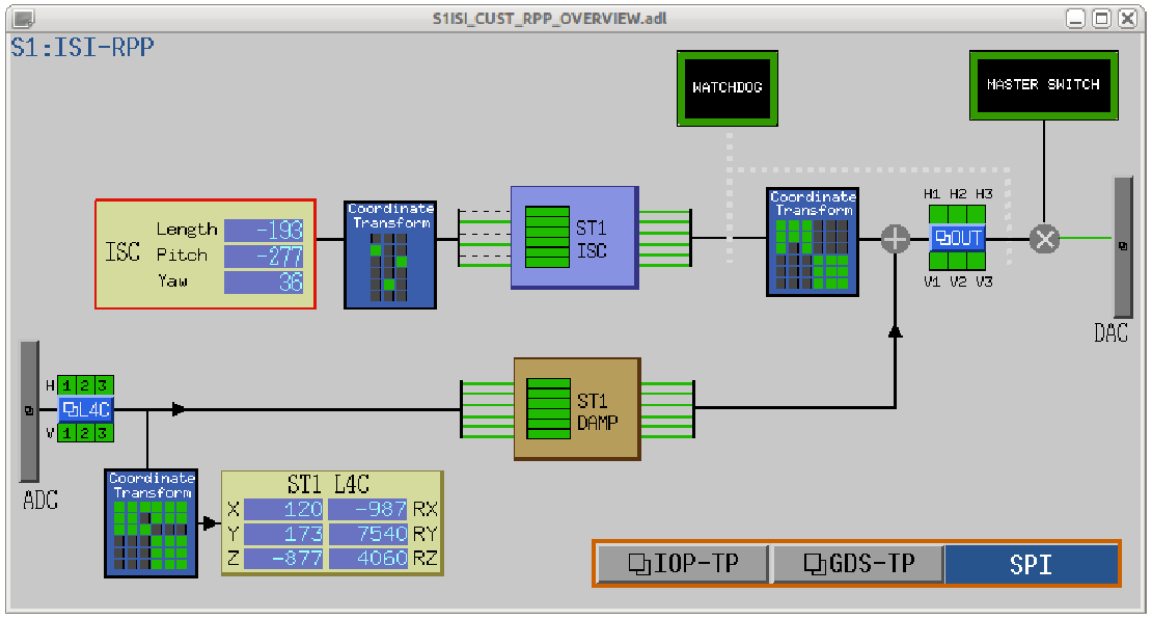

Figure F.4: RPP master control screen. Clicking on any of the control areas brings up related displays where the settings can be changed.

F.4 Control Loops

The main control need for the RPP is to damp the natural resonances of the platform, to provide a little inertial isolation, and to provide a way for the SPI to control the platform's position through the ISC control. The plant transfer functions are plotted for all degrees of freedom in **Figure F.5**. The damping controllers' horizontal and vertical Bode plots are shown in **Figures F.6** and **F.7** respectively. These controllers are shown for the H_1 and V_1 degrees of freedom in **Figure F.8**. The control loops were implemented and **Figure F.9** shows the platform motion in selected directions both with and without control.

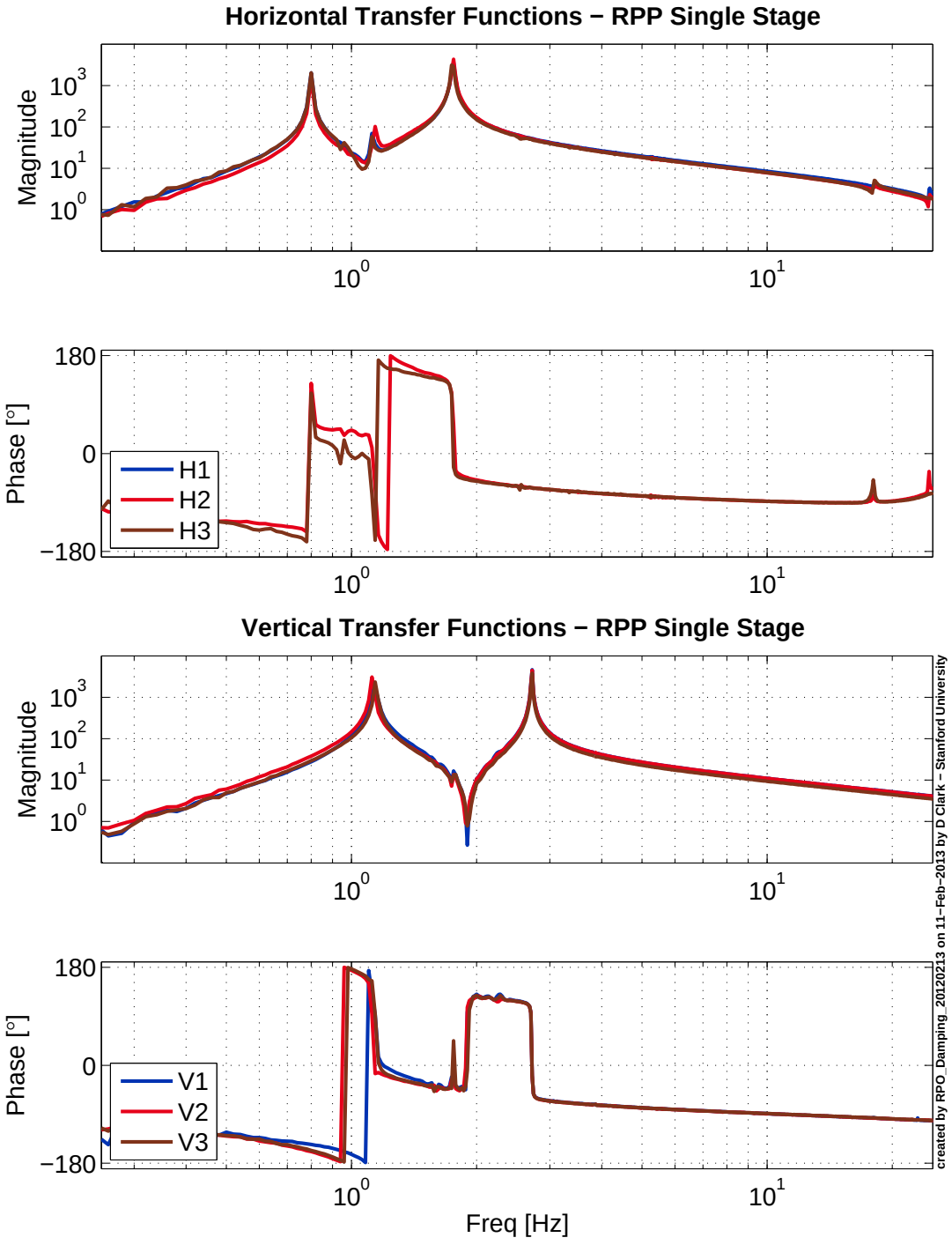

Figure F.5: RPP plant transfer functions showing the natural platform resonances in the actuator basis.

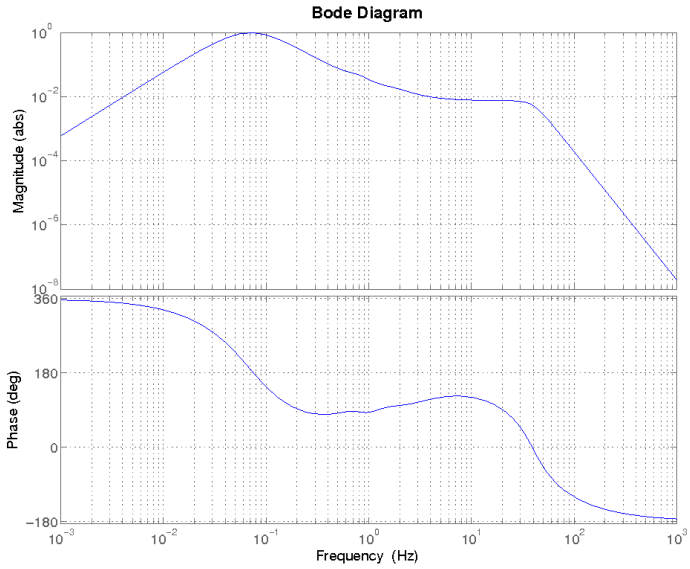

Figure F.6: RPP horizontal damping and inertial controller Bode plot.

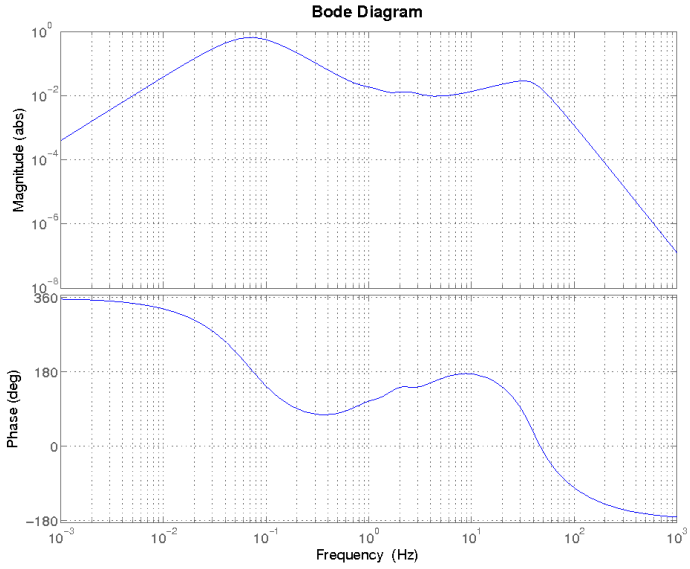

Figure F.7: RPP vertical damping and inertial controller Bode plot.

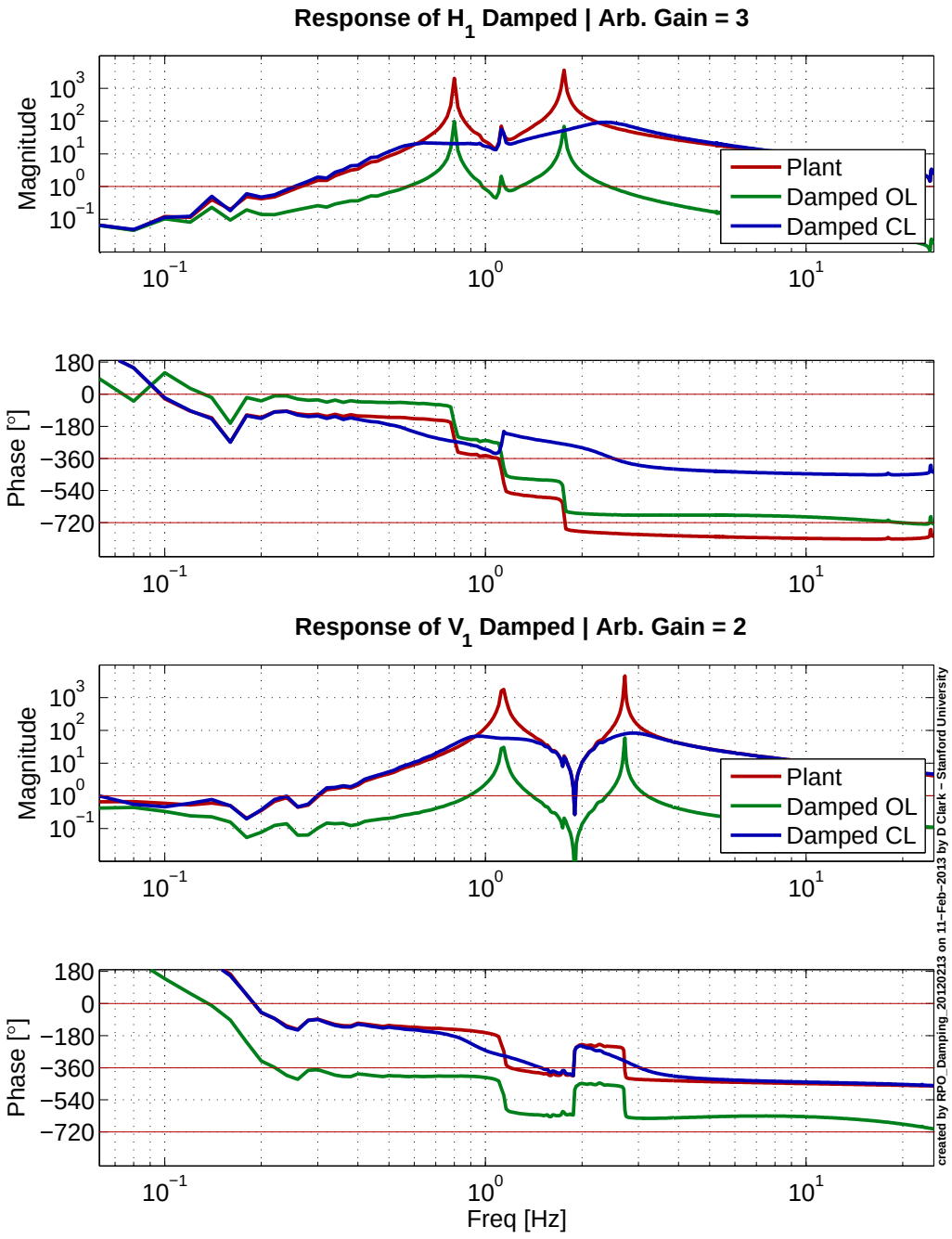

Figure F.8: RPP H_1 and V_1 degrees of freedom plant and controller Bode plots. The damped traces are calculated based on the controller implemented. Measured responses are shown in **Figure F.9**.

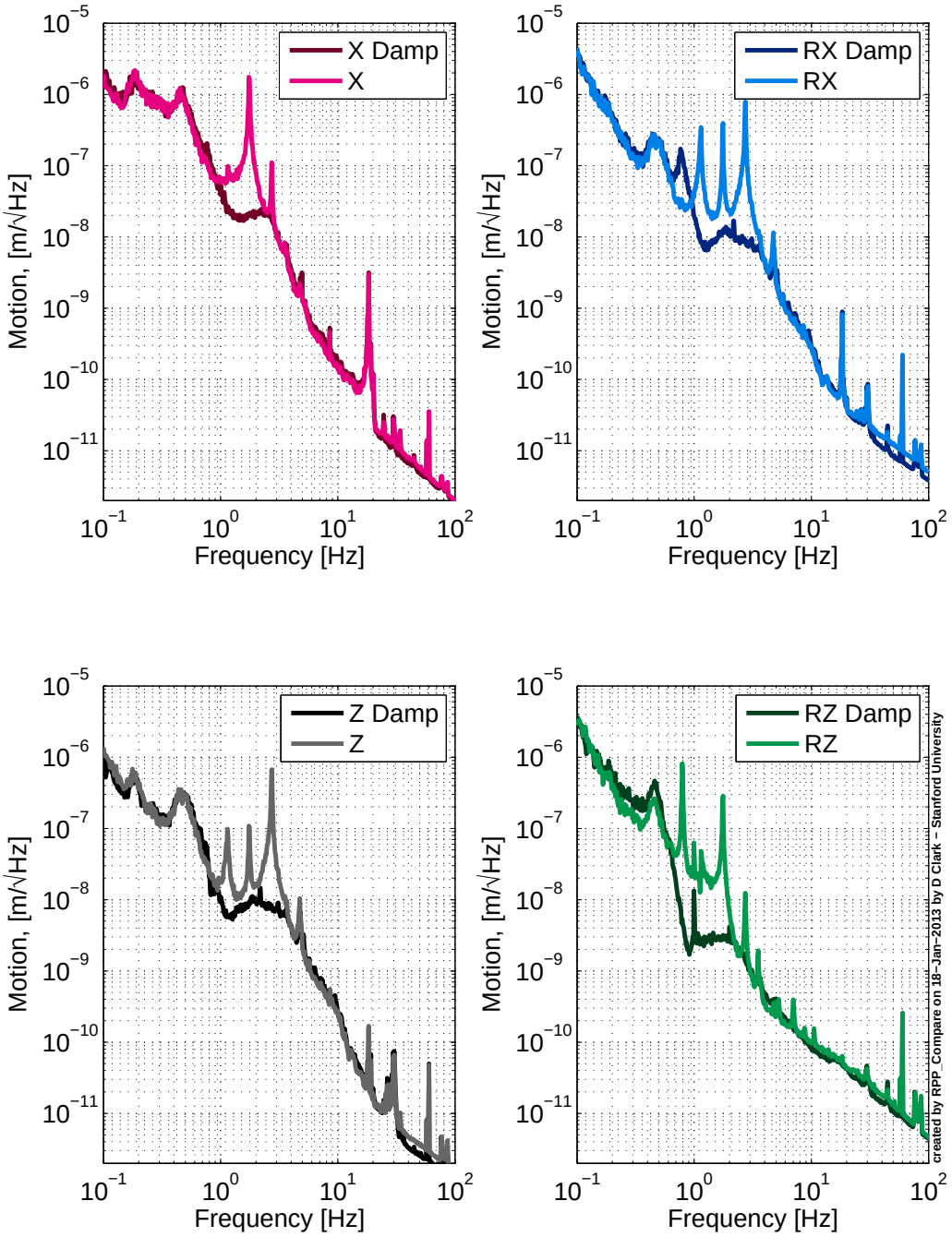

Figure F.9: Comparison platform motion of selected RPP channels with, and without, inertial damping control.

Appendix G

Fiber Tests

The laser light used by the Seismic Platform Interferometer (SPI) first needs to be introduced into the vacuum chamber. Of the possible methods, a vacuum feedthrough and fiber optic delivery was chosen for the SPI prototype. This was preferred because it allowed simple coupling of the light to the host platform for the optical levers. A fiber feedthrough also avoids possible challenges due to changes in the index of refraction of air. (An optical window allows light to pass through air external to the vacuum system and could result in additional phase noise in the light due to changes in n.)

G.1 Feedthrough Design

Ideally an optical, vacuum feedthrough would meet the following requirements:

- Be aLIGO ultra-high vacuum (UHV) compatible (utilizing metal-to-metal seals) and utilize materials on the approved vacuum materials list (Coyne, 2009a)
- Be able to operate at the aLIGO UHV levels
- Allow transmission of 1.5 μm light in polarization maintaining (PM) fiber without substantially reducing the transmitted power (desire less than a 25% (≈ -1.25 dB) power insertion loss)

- Not significantly add phase noise to the transmitted light (the phase noise added must remain below the SPI laser frequency requirement)
- Have minimal polarization wander (polarization wander is subsequently converted into power fluctuation in the SPI so it must remain below the SPI relative intensity noise (RIN) requirement)
- Interface with standard vacuum hardware such as the ConFlat® flanges already in use in the aLIGO vacuum system
- Have an FC/APC connector on the air side enabling connection to the laser pigtail

Since no commercially available feedthroughs that met the above requirements were located, a prototype was built and tested in the Stanford ETF.

G.2 Feedthrough Prototype

A 1.5 μm PM fiber vacuum feedthrough was constructed and tested for the SPI prototype. This feedthrough utilized an OZ Optics hermetically sealed and metalized fiber pigtail assembly number: MEPMJ-3A-1550-8/125-1-60-30-0-1.06. This pigtail had an FC/APC connector on the air side and a short section (approximately 10 cm) of metalized fiber on the vacuum side of a PM fiber. A gold plated Kovar® ferrule was pre-assembled on the metalized fiber creating a hermetic seal having a specified He leak rate of $< 10^{-5}\ \frac{\text{ATM}\cdot\text{cc}}{\text{s}}$, $7.6 \cdot 10^{-6}\ \frac{\text{Torr}\cdot\text{L}}{\text{s}}$ ($1.01 \cdot 10^{-6}\ \frac{\text{Pa}\cdot\text{m}^3}{\text{s}}$) (OZ-Optics, 2009).

The OZ Optics assembly was then soldered into a stainless steel KF vacuum flange using zinc-chloride ($ZnCl_2$) as a flux for ADD-HERE™ solder. ADD-HERE™ is a silver-bearing acid flux solder sold for HVAC repair work, which has a high (75 %) Pb content.

The assembly was then leak checked with no indicated leak down to the system sensor floor of $10^{-9}\ \frac{\text{Torr}\cdot\text{L}}{\text{s}}$ ($1.33 \cdot 10^{-10}\ \frac{\text{Pa}\cdot\text{m}^3}{\text{s}}$). Finally, an in-vacuum section of PM fiber patch cord was spliced on using a PM fusion splicer, completing the feedthrough.

Ideally, polyimide coated fiber would be used for in-vacuum. The prototype used a jacketed fiber patch cord which is not aLIGO vacuum compatible because while 1.3 μm PM fiber is available off-shelf with a polyimide coating, 1.5 μm fiber is "special order". A picture of the feedthrough components are shown in **Figure G.1**.

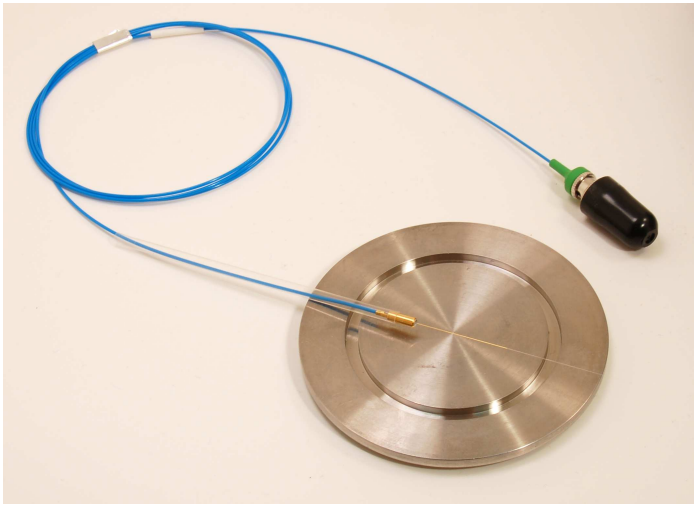

Figure G.1: KF flange and PM metalized fiber feedthrough. Note the metalized portion of the fiber extending approximately 5 cm beyond the ferrule.

In principle, the prototype feedthrough (less the in-vacuum spliced fiber portion) is aLIGO vacuum compatible because of the metal-to-metal sealing methods. While this prototype utilized materials and methods designed to meet the strict aLIGO requirement, no cleaning, baking or out-gas testing was performed.

G.3 Feedthrough Testing

The optical performance of the light launched from the fiber was tested with the following experiments. While changes such as polarization wander could not be measured directly with the optical configuration, inference can be made as to their overall effect. The main tests involved comparing the RIN (or power stabilities) and pointing stabilities of light passing through the feedthrough both with and without a polarizer.

The experiments without the polarizer provide a baseline noise floor for that particular configuration. This way, when the polarizer is added, polarization wander is

converted into amplitude fluctuations. A limit can then be assumed for the polarization wander by comparing the RIN from experiments with and without the polarizer.

Since no alternative feedthrough was available, direct comparison testing had to be conducted between data collected with the feedthrough and without the feedthrough (installing a section of PM patch fiber in place of the feedthrough). Since the patch cord could not enter the vacuum system these comparison tests were conducted in air but with the same optical layout as later vacuum tests. The relative intensity noise (RIN) of the launched light, as shown in **Figure G.2**, displays the lowest level without the feedthrough or polarizer. This means that polarization wander is generated by the fiber (comparing the no polarizer, no feedthrough case to the polarizer, no feedthrough case). It is also worth noting that in this test it seems that polarization wander is not made significantly worse by the feedthrough (comparing the polarizer, no feedthrough to the polarizer, feedthrough case).

The tests of the fiber feedthrough indicate that it does not significantly reduce the performance over what is achieved from PM fiber itself.

G.4 Fiber Testing

The fiber noise in terms of RIN and pointing stability was then measured at vacuum using the optical setup as described in schematic form in **Figure G.3**. The RIN for the in-vacuum measurements is shown in **Figure G.4**. This indicates that there is some polarization wander in the light because the traces show a different RIN when the polarizer is in place. If one assumes that all of the amplitude fluctuations are caused by polarization wander, then this wander can be plotted as a function of angle as in **Figure G.5**.

The quad photodetector (QPD) also measured the pitch and yaw of the launched light (**Figures G.6** and **G.7**, respectively). Polarization changes of the light do not seem to have an effect on the pitch stability. In contrast, the polarizer used to maintain a steady polarization of the light entering the SPI from the fiber seems to impart a lot of yaw noise. This is not well understood. Another noteworthy item is that if an ASE source is used (with a very short coherence length) instead of a

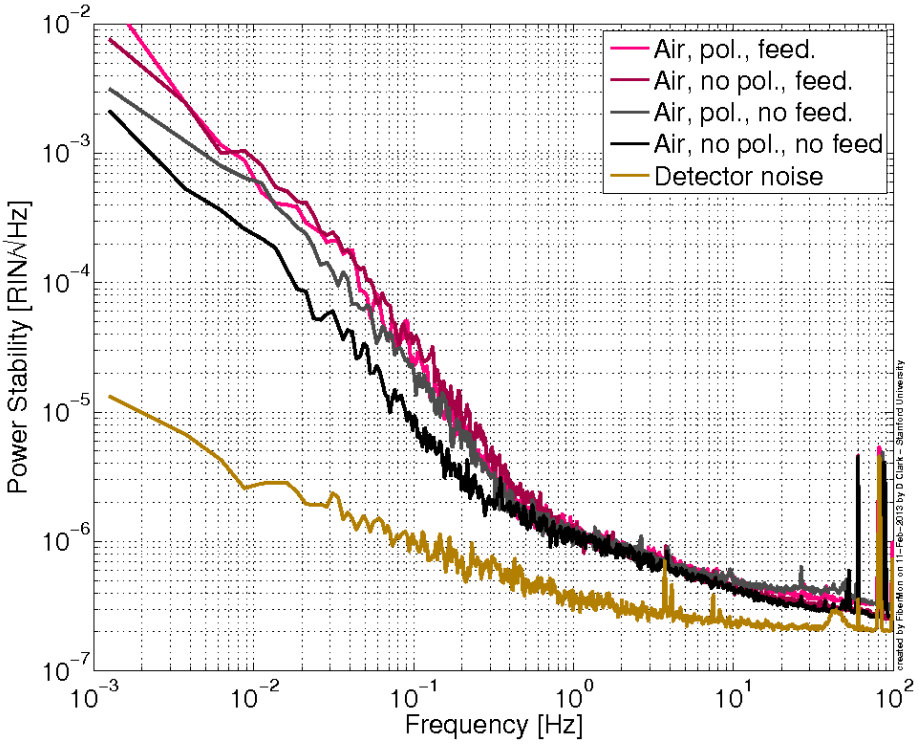

Figure G.2: The RIN of the fiber feedthrough tested. The intensity noise is lowest without the feedthrough or polarizer. While the RIN is less without the feedthrough, there does not seem to be a significant difference in the cases with the polarizer. Two traces to compare, the no polarizer and no feedthrough case to the no polarizer with feedthrough case may indicate excess RIN coming from a source other than polarization wander in the feedthrough. Also plotted is the dark noise as measured on the detector showing the measurement noise floor.

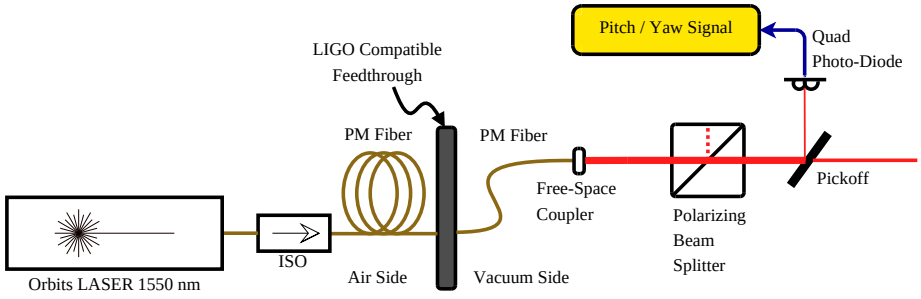

Figure G.3: Schematic diagram of the setup used to test the optical noise and performance of the PM optical fiber as used in the SPI.

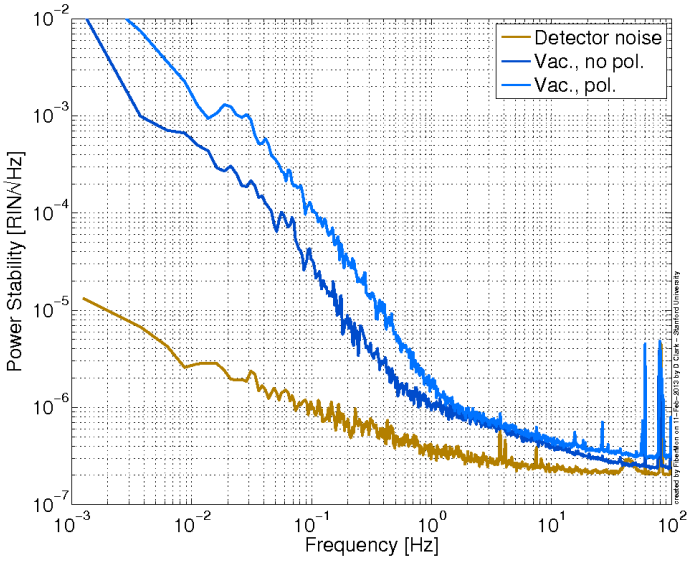

Figure G.4: RIN of the light from the PM fiber in vacuum both with, and without, a polarizer. The difference in the traces indicates that there is some polarization wander imposed on the light as it is propagating along the fiber.

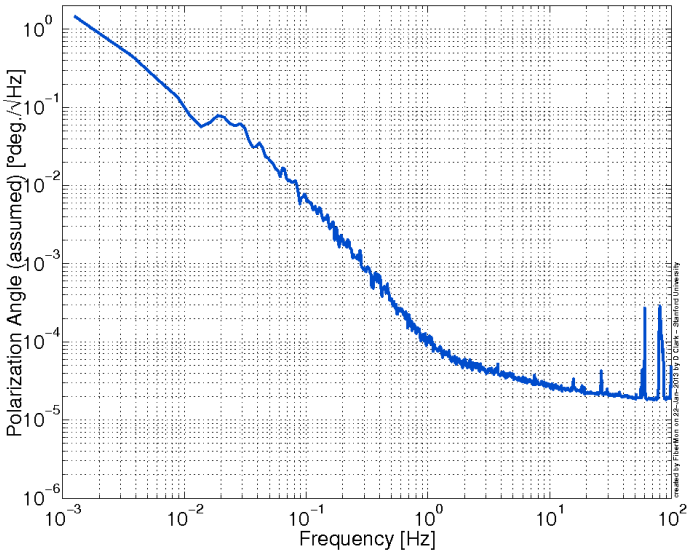

Figure G.5: If all of the difference in the RIN of the light from the fiber with the polarizer is attributed to polarization wander, this graph shows the angle of that wander with respect to frequency for a one hour data run in vacuum. In collecting this data, the fast-axis of the PM fiber was oriented 45 ° with respect to the polarizer reducing the nominal power to $\frac{\sqrt{2}}{2}$ of the fiber output power. This helps linearize the coupling of power to angle and simplifies this approximation.

laser (which has an extremely long coherence length), the pointing stability is greatly improved at low frequency. The source of this is elusive but could be related to backscatter of parasitic interferometers similar to what was shown in **Figure 7.1**. A parasitic interferometer could be supported by a laser but might not be established using light from an ASE source.

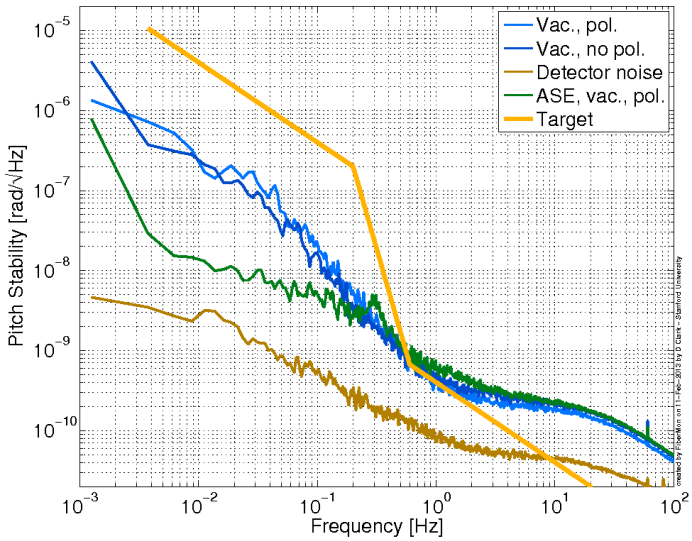

Figure G.6: The pitch pointing stability of the light from the fiber does not seem to be affected significantly by changes in the light's polarization. This is indicated by the close matching of the two traces. The detector noise is the recorded level from the detector and associated electronics with no incident light on the QPD.

In **Figure G.8**, the pitch and yaw time series are plotted for one minute of collected data. This provides an idea of the RMS values for the pointing stability of the light launched from the fiber. One issue with the QPD is that if the beam is not centered on the detector, power fluctuations show up as pointing instability. The in-vacuum Lisajous plots have been corrected for power by: $Angle = QPD_{\text{angle}} - Power_{\text{incident on QPD}} \cdot \beta$ where β is a scale factor found by the least squares fit of the $Power_{\text{incident On QPD}}$ and the QPD_{angle}. The angles corrected are shown in **Figure G.9**. Other plots of the full test data follow in **Figures G.10, G.11, G.12,** and **G.13**.

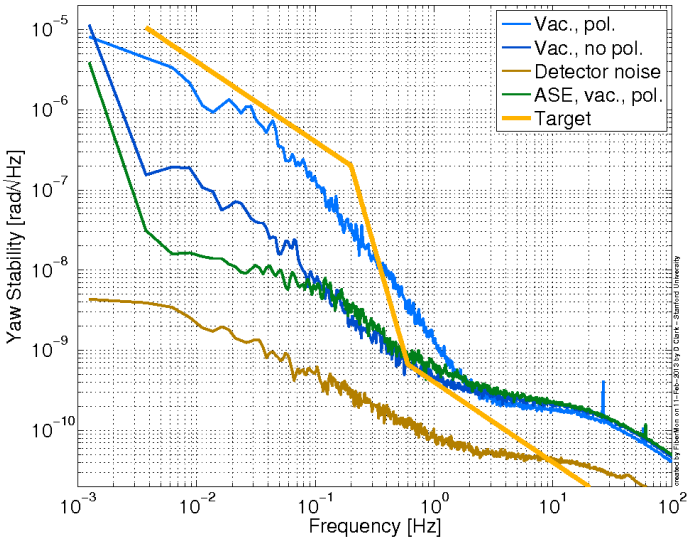

Figure G.7: The yaw stability of the fiber is a strong function of the polarizer. When in place, the polarizer causes a significant increase in the apparent pointing noise at low frequency.

G.5 Future Experimental Work

While the above tests estimate the optical performance of the PM fiber as used for the SPI, there are many other noise sources that could be investigated. Some of the noise that is seen in the aforementioned data could be a result of the following potential noise sources, any of which could be studied in detail:

- Electronic noise, perhaps more of a factor when there is incident light on the QPD.
- Temperature changes in the fiber, optical table, laser, and mounts that might change the light pointing, the geometry, or the location of the sensor.
- Parasitic interferometers perhaps are formed in some of the optical elements that may be contributing to higher yaw noise levels with the polarizer in place.
- Non-Gaussian beam shaping that could also couple into the optical lever measurements and become problematic.

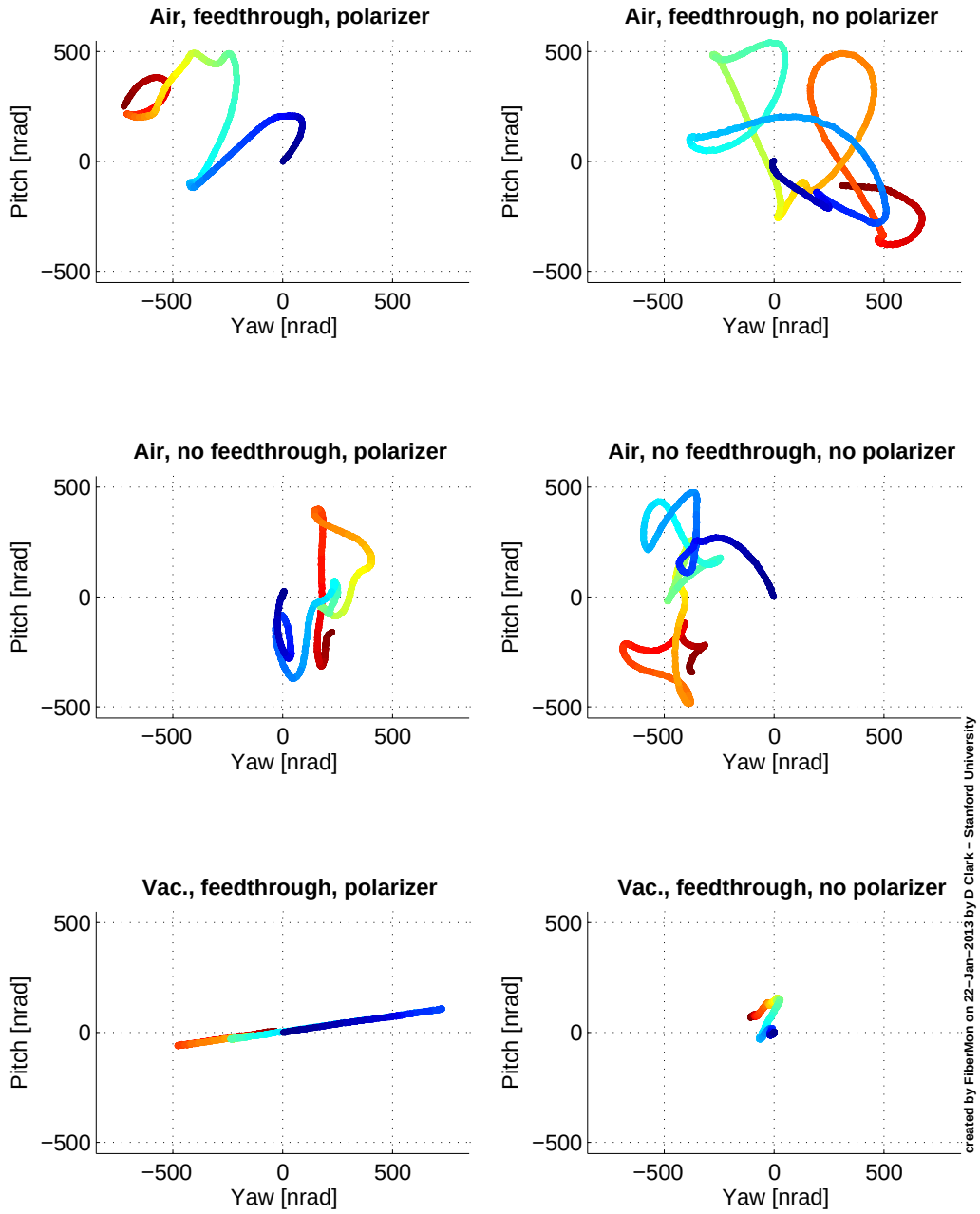

Figure G.8: Scatter plots of one minute of QPD data. The detrimental effects of air on the pointing stability are quite clear. In the in-vacuum cases (comparing the lowest two plots), using the same optical setup as when in air, it is also obvious that the polarizer tends to increase the yaw recorded motion. The lever arm from the launch point to the QPD is ≈ 0.65 m.

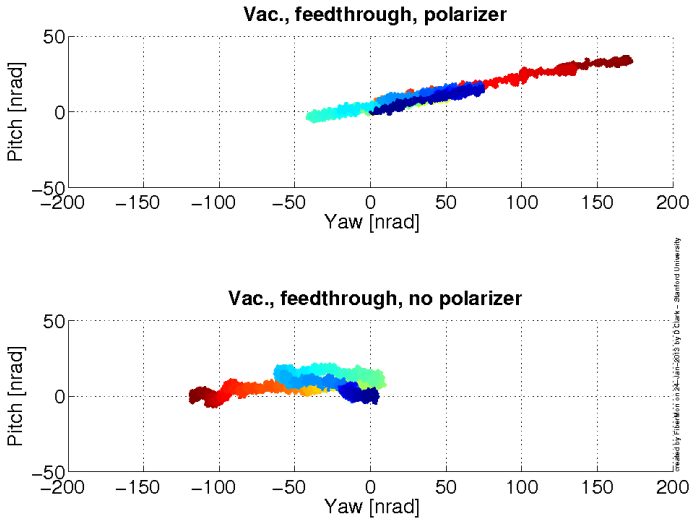

Figure G.9: Scatter plots of one minute of QPD data. The coupling of light amplitude fluctuations have been compensated resulting in much less apparent motion.

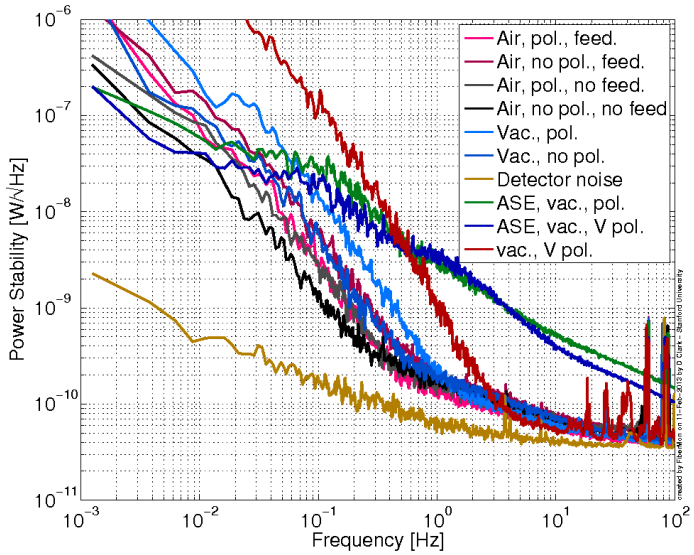

Figure G.10: Complete data set of the power stability measured in W on the QPD.

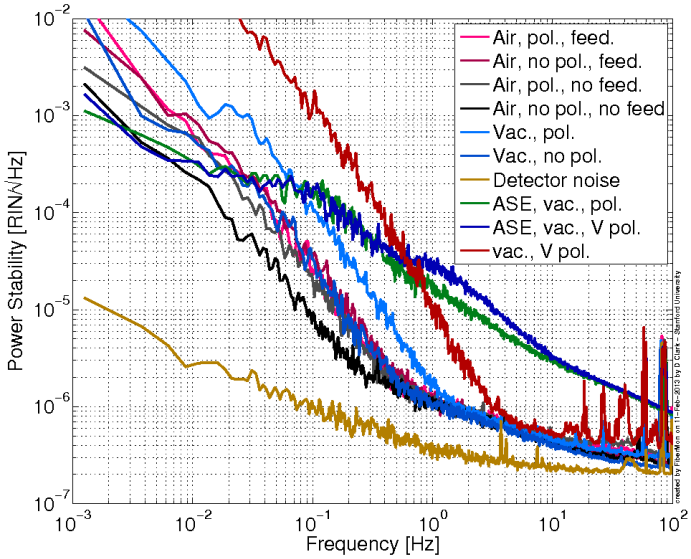

Figure G.11: Complete data set of the power stability measured as RIN on the QPD.

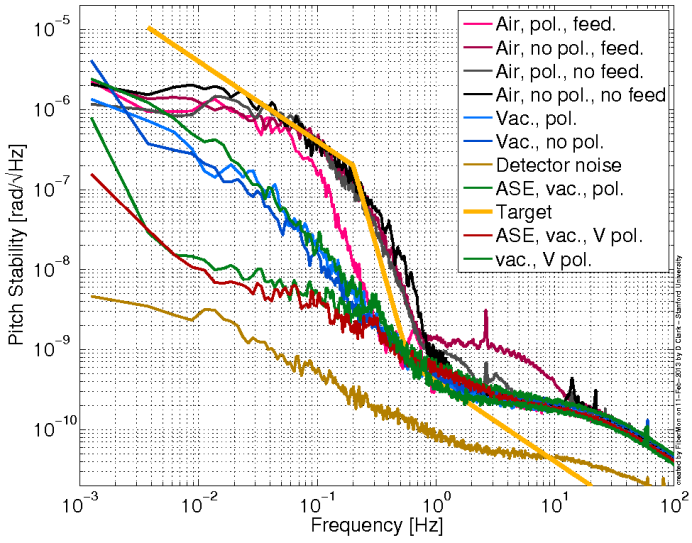

Figure G.12: Complete data set of the pitch stability of the launched light.

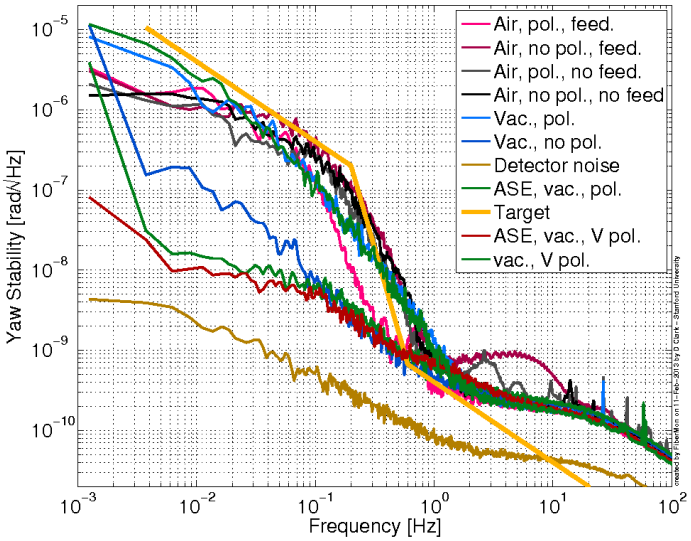

Figure G.13: Complete data set of the yaw stability of the launched light.

Finally, while some estimates have been made as to the fiber induced pointing and polarization stability, measurements on the optical phase noise added by the fiber would be of interest but were not pursued. The experiments measuring the frequency noise of the laser were conducted with the fiber and feedthrough. In that case, all of the frequency noise was assumed to be from the laser itself while in reality a portion of it could be phase noise induced in the fiber delivery.

Bibliography

Abbott, B. (2009). Hepi pier interface module. Technical Report D080521, LIGO Laboratory.

Abbott, R., Adhikari, R., Allen, G., Baglino, D., Campbell, C., Coyne, D., Daw, E., DeBra, D., Faludi, J., Fritschel, P., Ganguli, A., Giaime, J., Hammond, M., Hardham, C., Harry, G., Hua, W., Jones, L., Kern, J., Lantz, B., Lilienkamp, K., Mailand, K., Mason, K., Mittleman, R., Nayfeh, S., Ottaway, D., Phinney, J., Rankin, W., Robertson, N., Scheffler, R., Shoemaker, D. H., Wen, S., Zucker, M., and Zuo, L. (2004). Seismic isolation enhancements for initial and advanced ligo. *Classical and Quantum Gravity*, 21(5):S915.

Ahn, B.-H., Trageser, M. B., Metzger, E. H., Pondrom, W. L., Hadfield, M. J., Carroll, R., Coccoli, D. J., Feldman, J., Helfant, S., Albert, W. C., Simpson, J. H., Potter, J. E., McKern, R., and DeBra, D. B. (1984). Inertial technology for the future. *IEEE Transactions on Aerospace and Electronic Systems*, AES-20(4):414–444.

Aso, Y., Ando, M., Otsuka, S., and Tsubono, K. (2006). Active vibration isolation using a suspension point interferometer. *Journal of Physics: Conference Series*, 32(1):451.

Baker, J. G., Centrella, J., Choi, D.-I., Koppitz, M., and van Meter, J. (2006). Gravitational-wave extraction from an inspiraling configuration of merging black holes. *Phys. Rev. Lett.*, 96:111102.

Barbour, N. and Schmidt, G. (2001). Inertial sensor technology trends. *IEEE Sensors Journal*, 1(4):332–339.

Barton, M., Robertson, N., Willems, P., Fritschel, P., and Shoemaker, D. (2008). Cavity optics suspension subsystem design requirements. Technical Report T010007, LIGO Laboratory.

Belfi, J., Beverini, N., Bosi, F., Carelli, G., Virgilio, A. D., Maccioni, E., Ortolan, A., and Stefani, F. (2012). A 1.82 m^2 laser gyroscope for nano-rotational motion sensing. *Applied Physics B*, 106:271–281.

Bilger, H. R., Stedman, G. E., Poulton, M. P., Rowe, C. H., Li, Z., and Wells, P. V. (1993). Ring laser for precision measurement of nonreciprocal phenomena. *IEEE Transactions on Instrumentation and Measurement*, 42(2):407–411.

Biscans, S. and Matichard, F. (2010). Mumetal magnetic shield review. Technical Report E1000646, LIGO Laboratory.

Black, E. D. and Gutenkunst, R. N. (2003). An introduction to signal extraction in interferometric gravitational wave detectors. *American Journal of Physics*, 71(4):365–378.

Blair, D. G. (1991). *The Detection of Gravitational Waves*. Cambridge University Press.

Bork, R., Abbott, R., Barker, D., Heefner, J., and Laboratory, L. (2001). An overview of the ligo control and data acquisition system. San Jose, California,. 8th International Conference on Accelerator & Large Experimental Physics Control Systems.

Bosi, F., Cella, G., Virgilio, A. D., Ortalan, A., Porzio, A., Solimeno, S., Cerdonio, M., Zendri, J. P., Allegrini, M., Belfi, J., Beverini, N., Bouhadef, B., Carelli, G., Ferrante, I., Maccioni, E., Passaquieti, R., Stefani, F., Ruggiero, M. L., Tartaglia, A., Schreiber, K. U., and Gebauer, A. (2011). Measuring gravitomagnetic effects by a multi-ring-laser gyroscope. *Physical Review D*, 84:122002–1–23.

Carwardine, J. A. (1995). An introduction to plant monitoring through the epics control system. Advanced Photon Source, Argonne National Laboratory.

CDA (1962). Beryllium copper, publication 54. Technical Report CDA Publication No 54, 1962, Copper Development Association.

Center, N. G. S. F. (2009). Laser interferometer space antenna spacecraft description - lisa-sc-dd-0001. Technical report, Greenbelt Maryland,.

Champagnie, J. (2010). C1000245-v1 high precision devices (hpd) quote/job p09070d. Technical Report C1000245, LIGO Laboratory.

Cheng, Y., Winterflood, J., Ju, L., and Blair, D. G. (2002). Tilt sensor and servo control system for gravitational wave detection. *Classical and Quantum Gravity*, 19:1723–1729.

Chin, E. J., Lee, K. T., Winterflood, J., Ju, L., and Blair, D. G. (2005). Low frequency vertical geometric anti-spring vibration isolators. *Physics Letters A*, 336:97–105.

Clark, D. (2009). Ham 6 isi tmd installation instructions. Technical Report E0900119, LIGO Laboratory.

Clark, D. (2010). Ham-isi blade spring tuned mass damper assembly procedure. Technical Report E1000835, LIGO Laboratory.

Clark, D. and Lantz, B. (2009). Discussion of tuned mass damper parameters. Technical Report T0900143, LIGO Laboratory.

Coyne, D. (2009a). Ligo vacuum compatible materials list. Technical Report E960050, LIGO Laboratory.

Coyne, D. (2009b). Vacuum compatibility, cleaning methods and qualification procedures. Technical Report E960022, LIGO Laboratory.

Coyne, D., Giaime, J., Jones, L., Lantz, B., and Mason, K. (2006). Design requirements for the in-vacuum mechanical elements of the advanced ligo seismic isolation system for the ham chamber. Technical Report E030180, LIGO Laboratory.

de Labachelerie, M., Nakagawa, K., Awaji, Y., and Ohtsu, M. (1995). High-frequency-stability laser at 1.5 um using doppler-free molecular lines. *Op*, 20(6):572–574.

de Labachelerie, M., Nakagawa, K., and Ohtsu, M. (1994). Ultranarrow c2h2 saturated-absoption lines at 1.5 um. *Optics Letters*, 19(11):840–842.

DeBra, D. (1998). Design considerations for drag free satellites. In *AIP Conference Proceedings*, volume 456, page 199.

DeBra, D. (1999). Drag-free spacecraft as platforms for space missions and fundamental physics. *Classical and Quantum Gravity*, 14(6):1549.

Dergachev, V. and DeSalvo, R. (2012). A high precision mechanical ground rotation sensor. Technical Report G1200895, LIGO Laboratory.

DeSalvo, R. (2009). Review: Accelerometer development for use in gravitational wave-detection interferometers. *Bulletin of the Seismological Society of America*, 99(2B):990–997.

DeSalvo, R., Marka, S., Numata, K., Sannibale, V., Takamori, A., Tariq, H., Ugas, E. J., Yoda, T., Aso, Y., and Bertolini, A. (2005). Study of quality factor and hysteresis associated with the state-of-the-art passive seismic isolation system for gravitational wave interferometric detectors. *Nuclear Instruments and Methods in Physical Research A*, 538:526–537.

Dimopoulos, S., Graham, P. W., Hogan, J. M., and Kasevich, M. A. (2007). Testing general relativity with atom interferometry. *Physical Review Letters*, 98(11):111102.

Dimopoulos, S., Graham, P. W., Hogan, J. M., Kasevich, M. A., and Rajendran, S. (2008). Atomic gravitational wave interferometric sensor. *Physical Review D*, 78(12):122002.

Dunn, R. W., Mahdi, H. H., and Al-Shukri, H. J. (2009). Design of a relatively inexpensive ring laser seismci detector. *Bulletin of the Seismological Society of America*, 99(2B):1437–1442.

Einstein, A. (1916). Sitzber. deut. akad. wiss. *Kl. Math. Physik. u. Tech*, page 688.

Einstein, A. (1918). Sitzber. deut. akad. wiss. *Kl. Math. Physik. u. Tech*, page 154.

Evans, Kenneth, J. (1999). An overview of medm. In *International Conference on Accelerator and Large Experimental Physics Control Systems*, pages 466–468, Trieste, Italy.

Forward, R. L. (1964). Measurement of static force field gradients (us patent).

Forward, R. L. (1965). *Detectors for Dynamic Gravitational Fields*. PhD thesis, University of Maryland, College Park.

Forward, R. L. (1978). Wideband laser-interferometer gravitational-radiation experiment. *Physical Review D*, 17(2):379–390.

Franklin, G. F., Workman, M. L., and Powell, D. (1997). *Digital control of dynamic systems*. Addison-Wesley Longman Publishing Co., Inc.

Fritschel, P. (2009). Advanced ligo systems design. Technical Report T010075, LIGO Laboratory.

Fritschel, P. (2013). Potential advanced ligo post-project upgrades. Technical Report T1300176, LIGO Laboratory.

Giaime, J. (1995). *Studies of Laser Interferometer Design and a Vibration Isolation System for Interferometric Gravitational Wave Detectors*. PhD thesis, Massachusetts Institute of Technology.

Giaime, J. and Lantz, B. (2003). Advanced seismic isolation technology demonstrator. Technical Report G030235, LIGO Laboratory.

Giaime, J., Saha, P., Shoemaker, D., and Sievers, L. (1996). A passive vibration isolation stack for ligo: Design, modeling, and testing. *Review of Scientific Instruments*, 67(1):208 –214.

Goodman, J. W. (2005). *Introduction to Fourier Optics*. Roberts & Company, 3 edition.

Hanson, J., O'Reilly, B., Kissel, J., Grabeel, G., and Ramet, C. (2009a). Gs-13 inspection checklist. Technical Report F0900070, LIGO Laboratory.

Hanson, J., O'Reilly, B., Kissel, J., Ramet, C., and Mitchell, R. (2009b). Gs-13 modification and pod assembly procedure. Technical Report T080086, LIGO Laboratory.

Hardham, C. (2005). *Quiet Hydraulic Actuators for LIGO*. PhD thesis, Mechanical Engineering.

Harry, G. M. and LSC (2010). Advanced ligo: The next generation of gravitational wave detectors. *Classical and Quantum Gravity*, 27(8).

Higuchi, S., Clark, D. E., Lantz, B., and DeBra, D. B. (2008). Thermistor bridge performance in the 10^{-4} to 1 hz range and its applications in gravitational wave detection projects. In *ASPE 2008 Annual Conference Proceedings*. ASPE, ASPE.

Hillard, M. (2009). Tuned mass damper assembly. Technical Report D0900703, LIGO Laboratory.

Hillard, M. (2011). aligo bsc, tuned mass damper assy. Technical Report D1101793, LIGO Laboratory.

Hua, W. (2005). *Low Frequency Vibration Isolation and Alignment System for Advanced LIGO*. PhD thesis, Electrical Engineering.

Hua, W. and Lantz, B. (2005). Progress in seismic isolation and alignment on the technology demonstrator at the stanford etf - lsc meeting, march 20-23, 2005, livingston la. Technical Report G050168, LIGO Laboratory.

Hulse, R. A. and Taylor, J. H. (1975). Discovery of a pulsar in a binary system. *The Astrophysical Journal Letters*, 195(12):L51–L53.

Hurst, R. B., Stedman, G. E., Schreiber, K. U., Thirkettle, R. J., Graham, R. D., Rabeendran, N., and Wells, J.-P. R. (2009). Experiments with an 834 m[sup 2] ring laser interferometer. *Journal of Applied Physics*, 105(11):113115.

Ibrahim, R. A. (2008). Recent advances in nonlinear passive vibration isolators. *Journal of Sound and Vibration*, 314:371–452.

IndIGO (2011). Ligo-india, indian initiative in gravitational wave observations. Technical report, IndIGO Consortium.

Jones, D. I. G. (2001). *Handbook of Viscoelastic Vibration Damping*. John Wiley & Sons, LTD.

Ju, L., Blair, D. G., and Zhao, C. (2000). Detection of gravitational waves. *Reports on Progress in Physics*, pages 1317–1427.

Juvinall, R. C. and Marshek, K. M. (2000). *Fundamentals of Machine Component Design*. John Wiley & Sons, LTD.

Kawamata, A., Hosaka, H., and Morita, T. (2007). Non-hysteresis and perfect linear piezoelectric performance of a multilayered lithium niobate actuator. *Sensors and Actuators A: Physical*, 135(2):782 – 786.

Kissel, J. S. (2009). L1ham6 - y direction.

Kohl, M. L. and Levine, J. (1993). Measuring low frequency tilts. *Journal of Research of the National Institute of Standards and Technology*, 98:191–202.

Kohl, M. L. and Levine, J. (1995). Measurement and interpretation of tidal tilts in a small array. *Journal of Geophysical Research*, 100:3929–3941.

Lantz, B. (2005). Lessons from the etf technology demonstrator. Technical Report G050271, LIGO Laboratory.

Lantz, B. (2009a). Advanced ligo single stage ham vibration isolation table. Technical Report G070156, LIGO Laboratory.

Lantz, B. (2009b). Ligo review of 'compliance to ligo modifications on gs-13'. Technical Report C0900025, LIGO Laboratory.

Lantz, B. (2009c). Personal communication between B. Lantz (isi-subsystem lead) and D. Clark, 2009.

Lantz, B. (2009d). Sensor noise estimates for advanced ligo seismic isolation systems. Technical Report T0900450, LIGO Laboratory.

Lantz, B. (2010). Revised ham-isi performance targets for advanced ligo srm chambers. Technical Report T1000216, LIGO Laboratory.

Lantz, B., Schofield, B., Clark, D. E., and DeBra, D. (2009). Requirements for a ground rotation sensor to improve advanced ligo. *Bulletin of the Seismological Society of America*, 99(2B):980–989.

Lantz, B. T. (1999). *Quantum Limited Optical Phase Detection in a High Power Suspended Interferometer*. PhD thesis, Massachusetts Institute of Technology.

Levine, J., Meertens, C., and Busby, R. (1989). Tilt observations using borehole tiltmeters. *Journal of Geophysical Research*, 94:574–601.

Loukianov, D. P. (1999). Laser and fiber-optic gyros: the status and tendencies of development. In *RTO SCI International Conference on "Integrated Navigation Systems"*, volume RTO MP-43.

LTC (1995). Lt1021 precision voltage reference. Semiconductor Datasheet C, Linear Technology Corporation, 1630 McCarthy Blvd., Milpitas, CA 95035.

Mantovani, M. and DeSalvo, R. (2005). One hertz seismic attenuation for low frequency gravitational waves interferometers. *Nuclear Instruments and Methods in Physical Research A*, 554:546–554.

Matichard, F. (2012). Advancing mit-ligos tilt-free seismometer project. Technical Report E1200969, LIGO Laboratory.

Metzger, E. H. (1986). Development experience of a moving base gravity gradiometer and discussion of future applications. Colorado Springs, CO,. 14th Annual Gravity Gradiometry Conference, Department of the Air Force.

Metzger, E. H. (1987). Bell aerospace gravity gradiometer survey system (ggss). volume 1, Colorado Springs, CO,. Fifteenth Annual Gravity Gradiometry Conference.

Nakagawa, K., de Labachelerie, M., Awaji, Y., and Kourogi, M. (1996). Accurate optical frequency atlas of the 1.5 um bands of acetylene. *Japan Optical Society*, 13(12):2708–2714.

O'Reilly, B. (2008). Personal communication between B. O'Reilly and D. Clark, april 21, 2008.

OZ-Optics (2009). Hermetically sealable patchcords with metal solder. website product specifications. http://www.ozoptics.com/ALLNEW_PDF/DTS0036.pdf.

Richman, S. J., Giaime, J. A., Newell, D. B., Stebbins, R. T., Bender, P. L., and Faller, J. E. (1998). Multistage active vibration isolation system. *Review of Scientific Instruments*, 69(6):2531–2538.

Robertson, N. A., Drever, R. W. P., Kerr, I., and Hough, J. (1982). Passive and active seismic isolation for gravitational radiation detectors and other instruments. *Journal of Physics E: Scientific Instruments*, 15:1101–1105.

Rowe, C. H., Schreiber, U. K., Cooper, S. J., King, B. T., Poulton, M., and Stedman, G. E. (1999). Design and operation of a very large ring laser gyroscope. *Applied Optics*, 38(12):2516–2523.

Saulson, P. (1994a). *Fundamentals of Interferometric Gravitational Wave Detectors*. World Scientific, Salem, MA.

Saulson, P. R. (1990). Thermal noise in mechanical experiments. *Physical Review D*, 42(8):2437–2445.

Saulson, P. R. (1994b). *Fundamentals of Interferometric Gravitational Wave Detectors*. World Scientific Publishing Company.

Schreiber, K. U., Hautmann, J. N., Velikoseltsev, A., Wassermann, J., Igel, H., Otero, J., Vernon, F., and Wells, J.-P. R. (2009). Ring laser measurements of ground rotations for seismology. *Bulletin of the Seismological Society of America*, 99(2B):1190–1198.

Schreiber, K. U., Velikoseltsev, A., Rothacher, M., Klgel, T., Stedman, G. E., and Wiltshire, D. L. (2004). Direct measurement of diurnal polar motion by ring laser gyroscopes. *Journal of Geophysical Research: Solid Earth*, 109(B6):n/a–n/a.

Shoemaker, D. (2009). Advanced ligo reference design. Technical Report M060056, LIGO Laboratory.

SMC (2004). Ni-span-c alloy 902, pub. number smc-086. Technical Report SMC-086, Special Metals Corporation.

Smith, S. T. (2000). *Flexures, Elements of Elastic Mechanisms*. Gordon and Breach.

Stedman, G. E. (1997). Ring-laser tests of fundamental physics and geophysics. *Reports on Progress in Physics*, 60:615–688.

Stein, A. (2009). Fea of ham isi spring - for tuned mass damper. Technical Report T0900199, LIGO Laboratory.

Stochino, A., Abbot, B., Aso, Y., Barton, M., Bertolini, A., Boschi, V., Coyne, D., DeSalvo, R., Galli, C., Huang, Y., Ivanov, A., Marka, S., Ottaway, D., Sannibale, V., Vanni, C., Yamamoto, H., and Yoshida, S. (2009). The seismic attenuation system (sas) for the advanced ligo gravitational wave interferometric detectors. *Nuclear Instruments and Methods in Physical Research A*, 598:737–753.

Stochino, A., DeSalvo, R., Huang, Y., and Sannibale, V. (2007). Improvement of the seismic noise attenuation performance of the monolithic geometric anti-spring filters for gravitational wave interferometric detectors. *Nuclear Instruments and Methods in Physical Research A*, 580:1559–1564.

Taylor, J. H. and Weisberg, J. M. (1982). A new test of general relativity: Gravitational radiation and the binary pulsar psr 1913+16. *The Astrophysical Journal*, 253:908–920.

Taylor, J. H. and Weisberg, J. M. (1989). Further experimental tests of relativistic gravity using the binary pulsar psr 1913+16. *The Astrophysical Journal*, 345:434–450.

Vargas, M., Hillard, M., Matichard, F., and Mitchell, R. (2010). Bsc gs-13 pod assembly procedure. Technical Report E1000564, LIGO Laboratory.

Varvella, M., Calloni, E., Fiore, L. D., Milano, L., and Arnaud, N. (2004). Feasibility of magnetic suspension for second generation gravitational wave interferometers. *Astroparticle Physics*, 21:325–335.

Venkateswara, K. (2011). Uwtiltmeterprogress. Technical Report G1101080, LIGO Laboratory.

Weber, J. (1969). Evidence for discovery of gravitational radiation. *Physical Review Letters*, 22(24):1320–1324.

Weber, J. (1970). Gravitational radiation experiments. *Physical Review Letters*, 24(6):276–279.

Weiss, R. (1972). Electronically coupled broadband gravitational antenna. *Quarterly Progress Report, Research Laboratory of Electronics (MIT)*, (105):54.

Wen, S. (2006). Ligo sei entry 604 - http://ligo.phys.lsu.edu:8080/sei/604.

Wen, S. (2009). *Improved Seismic Isolation for the Laser Interferometer Gravitational Wave Observatory with Hydraulic External Pre-Isolator System*. PhD thesis, Faculty of the Louisiana State University and Agricultural and Mechanical College in partial fulfillment of the requirements for the degree of Doctor of Philosophy in The Department of Physics and Astronomy by Shyang Wen BS, National Taiwan University.

Wielandt, E. and Streckeisen, G. (1982). The leaf-spring seismometer: Design and performance. *Bulletin of the Seismological Society of America*, 72(6A):2349–2367.

Winterflood, J. (2001). *High Performance Vibration Isolation for Gravitational Wave Detection*. PhD thesis, University of Western Australia, Department of Physics.

Winterflood, J., Barber, T., and Blair, D. G. (2002a). Using euler buckling springs for vibration isolation. *Classical and Quantum Gravity*, 19:1639–1645.

Winterflood, J., Barber, T. A., and Blair, D. G. (2002b). Mathematical analysis of an euler spring vibration isolator. *Physics Letters A*, 300:131–139.

Zhou, Z. B., Winterflood, J., Ju, L., and Blair, D. G. (2001). Investigation of a laser walk-off angle sensor and its appliation to tilt measurement in gravitational wave detectors. *Physics Letters A*, 280:197–203.

Glossary

ADC analog to digital converter. 30, 109, 120, 221, 237, 243

aLIGO Advanced LIGO. xxii, xxiii, xxxviii, 7–14, 16, 18, 24–31, 33, 34, 36, 38, 47–49, 51, 62, 69, 72, 76, 81–83, 85, 87–89, 91, 96, 109, 112, 115, 118, 122, 128, 129, 140, 148, 151, 152, 154–156, 158, 159, 161, 162, 164, 166, 167, 169, 170, 174, 176, 178, 188, 192, 199, 201, 204–206, 212–214, 243, 253–255

AOI angle of incidence. 37

AR anti-reflection. 152

ASD amplitude spectral density. 134, 162

ASE amplified spontaneous emission. 154, 256, 259

BSC Beam Splitter Chamber. xxii, xxiii, 8, 9, 13–18, 33, 72, 76, 81, 169, 207

CAD computer aided drafting. xxii, xxiii, xxxvi–xxxviii, 13, 15, 16, 20, 175, 181, 197, 198, 215

CDS Control and Data acquisition System. 10, 96, 109, 118–120, 122, 127, 129

CPS capacitive position sensor. 14

CTE coefficient of thermal expansion. 53, 66, 69, 111, 157

CW continuous wave. 8

DAC digital to analog converter. 243, 244

EDM electro-discharge machined. 55, 59

eLIGO Enhanced LIGO. xxxix, 215, 216

EPICS Experimental Physics and Industrial Control System. 10, 120, 244

ETF Engineering Test Facility. xxiii, 17, 19, 25, 54, 86, 90, 115, 127, 151, 155, 159, 166, 167, 207, 241, 243, 244, 254

FEA finite element analysis. 213, 215

GAS Geometric Anti-Spring. 59

HAM Horizontal Access Module. xxii, xxiii, 8, 9, 13, 14, 16–18, 23, 31, 33, 72, 73, 76, 79, 81, 83, 90, 104, 115, 161, 162, 169, 213, 214, 216
HDPE high-density polyethylene. 188
HEPI Hydraulic External Pre-Isolator. xxii, 12–15, 17, 31, 161, 243
HVAC heating, ventilation, and air conditioning. 65, 219, 222

IFO interferometer. 85, 91, 112
ISC Interferometer Sensing and Control. 31, 122, 127–129, 133, 243, 244, 248
ISI Internal Seismic Isolation. xxii, xxiii, 12–14, 16–18, 21, 23, 27, 31, 47, 48, 73, 75, 76, 81, 83, 85, 87, 127, 128, 148, 151, 162, 166, 167, 199, 207, 212–214, 216

JILA Joint Institute for Laboratory Astrophysics. 24, 35

L-4C Sercel L-4C. 14, 242, 243
LIGO Laser Interferometer Gravitational-wave Observatory. xix, xxi, 1, 7, 8, 10–13, 22, 24, 25, 35, 59, 72, 154, 199, 207, 214, 243
LISA Laser Interferometer Space Antenna. 5, 6
LLO LIGO Livingston Observatory. xxiii, 13, 23, 213
LSU Louisiana State University. 213

MEDM Motif Editor and Display Manager. 10, 120, 122, 244
MIT Massachusetts Institute of Technology. 41, 204, 213
MZ Mach-Zehnder. 85, 91, 93, 103

PCB printed circuit board. 231
PM polarization maintaining. 26, 88, 89, 110, 155, 156, 160, 253–256, 260
PSL Pre-Stabilized Laser. 8
PZT piezo-electric transducer. 96, 98, 105, 109, 120, 158–160

QPD quad photodetector. 91, 100–102, 108, 110, 117, 120, 122, 140, 154, 230, 231, 256, 259, 260

RCG Real-time Code Generator. 118
RIN relative intensity noise. 105, 108, 254–256
RLG ring laser gyroscope. 36–38
RMS root mean square. 134, 140, 143, 147, 148, 259
RPP Rapid Prototype Platform. xxiii, 17, 19, 25, 86–88, 91, 112, 118, 123, 128, 129, 131, 133, 143, 147, 148, 152, 158, 167, 241–244, 248

S-13 Geotech S-13. 219
SISO single-input single-output. 17
SM single mode. 110
SNR signal to noise ratio. 28
SPI Seismic Platform Interferometer. xix, 25, 71–73, 75, 76, 78–83, 85–91, 93, 98, 100, 102–104, 108–112, 115, 118, 120, 122, 123, 127–129, 131, 133, 134, 140, 143, 147, 148, 151, 152, 154–162, 164, 166, 167, 229, 230, 241–243, 248, 253, 254, 256, 260
SUS suspensions. xxii, xxiii, 12, 13, 17, 20, 31, 140

Tech Demo Technology Demonstrator Platform. xxiii, xxxviii, 17, 19, 25, 86–88, 91, 93, 102, 103, 111, 112, 118, 123, 128, 131, 133, 134, 143, 147, 148, 155, 167, 182, 199, 201, 203, 204, 207, 208, 229, 236, 241
TEM transmission electron microscope. 221
TMD Tuned Mass Damper. 214–216

UHV ultra-high vacuum. 7, 8, 26, 81, 91, 155, 214, 253
UUGF upper unity gain frequency. 129

VRB Vacuum Review Board. 154